



UNIVERSITY *of the*
WESTERN CAPE

THE PETROGENESIS OF THE INTERMEDIATE TO MAFIC ROCKS OF THE
YZERFONTEIN SUBSUITE, AND THEIR RELATIONSHIP TO-, AND
PARAGENESIS OF HYDROTHERMAL VEINING, CAPE GRANITE SUITE,
SALDANIA BELT, SOUTH AFRICA

by

Sharmoney Wilson

Supervisor: Dr. Russell Bailie

Dissertation is submitted in partial fulfilment of the requirements for the degree of
Master of Science in Applied Geology at the University of the Western Cape, Bellville,
South Africa

2020

Declaration

By submitting this dissertation, I declare that the entirety of the research presented is my own, original work, that I am the sole author thereof, and that reproduction and publication thereof by the University of the Western Cape will not infringe any third-party rights. It has not previously in its entirety or in part been submitted for any other qualification.



.....
Signed

07/05/2020

.....
Date



UNIVERSITY *of the*
WESTERN CAPE

Abstract

The 535 Ma post-orogenic Yzerfontein Pluton is a composite pluton that comprises rocks of mafic, intermediate and felsic compositions belonging to the shoshonitic series. The Yzerfontein Pluton forms part of the Cape Granite Suite of the Late-Proterozoic to Early-Cambrian Pan-African Saldania Belt. In this study, major- and trace-element data for the various rocks of the pluton, which act as hosts to extensive hydrothermal veining, are presented and integrated with the petrographic examination of the host rocks in order to constrain their petrogenesis. The relative enrichment in large ion lithophile elements (LILE), such as Cs, Rb, Sr, Ba, and Pb, and the depletion of high field strength elements (HSFE), such as Th, U, Nb and Hf, are indicative of a subduction-related history associated with a significant crustal contribution. A crustal influence is also further indicated by negative Nb anomalies. The rocks have high $^{87}\text{Sr}/^{86}\text{Sr}_{(0)}$ values (0.705388 – 0.714788), and relatively low to intermediate $^{143}\text{Nd}/^{144}\text{Nd}_{(0)}$ values (0.512237 – 0.512307) for a time (t) of 535 Ma. They also have negative $\epsilon\text{Nd}_{(t)}$ values between -2.75 and -0.62. These weakly negative $\epsilon\text{Nd}_{(t)}$ values close to 0 indicate a weakly to mildly enriched source for the rocks of the Yzerfontein Pluton. Subduction was the main source for the enrichment of the mantle wedge along the active continental margin.

The mafic to felsic rocks display a compositional variation which may be attributed to fractional crystallisation, mainly of pyroxenes and amphiboles, and to a lesser extent plagioclase and K-feldspar, as demonstrated by fractional crystallisation modelling. Major and trace element trends on binary plots do not suggest an association or compositional affinity of the Yzerfontein Pluton with the Vredenburg I-type granites of the Cape Granite Suite. These inferences are also corroborated by the absence of an intrusive contact between the Yzerfontein Pluton and the I-type granites, at least at emplacement level.

The paragenetic sequence of hydrothermal veining has also been demonstrated based on overgrowth, replacement, and growth zoning relationships, as well as cross-cutting relationships. These techniques suggest that the first stage of hydrothermal activity involved the precipitation of quartz, pyrite and calcite. This was followed by the continued precipitation of quartz and pyrite from hydrothermal solutions, as well as tourmaline and jasper. During stage 3, quartz, pyrite and tourmaline continued to precipitate from solution, together with epidote. Finally, during stage 4, the precipitation of all minerals from hydrothermal veins ceased, except for quartz, which resulted in the formation of barren quartz veins. Alteration associated with this paragenetic sequence is mainly propylitic and phyllic, with supergene alteration involving mainly limonite and malachite.

Fluid inclusion microthermometry revealed the presence of two types of aqueous fluids, including 1.) type I fluid inclusions which contain a liquid phase and a small vapour phase \pm an opaque phase, and 2.) type II fluid inclusions which contain a liquid phase, a solid halite phase, and a vapour phase \pm an opaque phase. Type I fluids have been constrained to total homogenization temperatures of 125 – 320°C, homogenization pressures of 0.52 – 10.68 MPa

and low salinities ranging from 3.06 – 11.34 wt. % NaCl_{equiv.}, which correspond to trapping conditions of 186°C at 0.56 kbar with associated depths of ~2 km, as calculated from their P-T isochore graph. Type II fluid inclusions have been constrained to total homogenization temperatures of 158 – 210°C, homogenization pressures of 139.24 – 553.45 MPa and high salinities of 35.37 – 44.48 wt.% NaCl_{equiv.}, which correspond to trapping conditions of 260 – 379 °C at 1.39 – 5.55 kbar with associated depths of ~5 – 22 km.

The stable isotope values of the veining characterised by type I fluid inclusions, together with their low to high homogenization temperature, low pressure and low salinity, tend to suggest a dominantly meteoric origin for these fluids. The stable isotope values and microthermometry of calcite-bearing veins containing type II fluid inclusions tend to suggest that mixing of fluids of meteoric and magmatic origin must have been responsible for producing these moderate temperature and very high pressure and salinity fluids, with the meteoric component dominating. The magmatic component to the type II fluid inclusions is proposed to be derived from the influx of magmatic water from either the S- or I-type granites of the Cape Granite Suite. Overall, the dominantly meteoric origin of the fluids explains why the hydrothermal veins are of a sub-economic to very poorly mineralised nature, and that there was not extensive fluid flow and hydrothermal alteration to generate a well-mineralised system. Furthermore, the fluid/rock ratios of the hydrothermal fluids are inferred to have been relatively low, as illustrated by the low degree of alteration that is largely localised to areas directly adjacent to the veins and also from the dominantly propylitic alteration present.



Acknowledgements

I would firstly like to thank God for guiding me and giving me the knowledge and understanding to successfully complete my thesis. I am thankful to my supervisor Dr. Russell Bailie for being patient, supportive, understanding and for always being available. The guidance, knowledge and insight that you have provided over the last few years have been priceless and indispensable to say the least. I would also like to thank my supervisor for his availability to assist me in the field and helping me to efficiently select my geological samples. I would also like to thank the National Research Foundation (NRF) and the Wheatfield Estate Foundation Trust (WEFT) for funding this project and my accommodation over the last few years.

I would like to express my gratitude to Janine Botha and Richard Harrison at the University of the Western Cape (UWC) for assisting me with the crushing and milling of my samples and the making of my thin sections, which I actively participated in. I would like to extend a great thanks to the staff at the Central Analytical Facility (CAF) at the University of Stellenbosch, specifically Riana Rossouw for performing Laser-Ablation Inductively Coupled Plasma Mass Spectrometry (LA-ICP-MS) on my samples, and Mareli Grobbelaar for performing X-Ray Fluorescence (XRF) on my samples. I would also like to thank the staff at the Department of Geological Science at the University of Cape Town (UCT), specifically Dr. Petrus le Roux for analysing some of my samples for their radiogenic isotope values, and Prof. Chris Harris for analysing some of my samples for their stable isotope values.

I am grateful to Stephan Dunn who performed microthermometry on samples of the Yzerfontein Pluton at the University of Stellenbosch, with the help of Vutomi Salinda. The microthermometric data obtained also formed part of the Honours research project of Vutomi Salinda. I am thankful that you have shared the microthermometric data with me, as it is a significant contribution to my thesis. I would also like to thank Dr. Juergen Reinhardt and Dr. Tshipeng Mwenze for assisting with my petrographic identifications, as well as confirming certain petrographic observations. A special thanks to Prof. Duncan Miller, one of my thesis examiners, for assisting in professional language edits to my thesis, as well as Prof. Chris Harris, my second examiner, who provided me with detailed comments and ways to improve the interpretation and igneous geochemistry parts of my thesis. I would also like to acknowledge Stephane Tsakou for his help and support, and for sacrificing his time to go into the field with me.

I am grateful for the guidance and support of my parents Patricia Wilson and Gary Wilson, my siblings Carlin, Vanita, Roschele, Curtis and Rico-Dean and my dear friends Andrea, Yasmeen, Mihlali, Nehemiah, Carmenlite and Musa – I appreciate every effort you made to be there for me during this experience. I am also thankful to my mentor Stemray Lesch for his invaluable support and guidance during my entire university experience.

Table of Contents

Declaration.....	ii
Abstract.....	iii
Acknowledgements.....	v
Declaration.....	ii
Abstract.....	iii
Acknowledgements.....	v
List of Figures	ix
List of Tables	xiii
Chapter 1: Introduction	15
1.1. Background and Locality	15
Chapter 2: Regional Geology	18
2.1. Regional Geological Setting	18
2.1.1. The western branch of the Saldania Belt	19
2.1.2. The Cape Granite Suite	22
2.2. Local geological setting.....	24
2.2.1. The Yzerfontein Pluton	24
2.2.2. Timing of magmatic emplacement	24
Chapter 3: Research Methodology and Analytical Techniques	26
3.1. Field work.....	26
3.2. Geochemical Sampling.....	26
3.3. Analytical Methods	26
3.3.1. Optical Petrography.....	26
3.3.2. X-Ray Fluorescence (XRF).....	27
3.3.3. Laser-Ablation Inductively Coupled Plasma Mass Spectrometry (LA-ICP-MS)	27
3.3.4. Radiogenic Sr- and Nd-isotope analysis	28
3.4. Stable isotopes.....	28
3.5. Fluid Inclusion Studies.....	29
3.5.1. Fluid Inclusion Petrography	30
3.5.2. Microthermometry	30
Chapter 4: Lithological and Petrographic Relationships	32
4.1. Introduction	32
4.2. Classification of host rock	32
4.3. Alteration of host rocks.....	32
4.4. Mafic Rocks	33

4.4.1.	Leucocratic Gabbro	33
4.4.2.	Melanocratic Gabbro	35
4.4.3.	Poikilitic Monzogabbro	37
4.5.	Intermediate Rocks	41
4.5.1.	Syenodiorite and Monzonite	41
4.5.2.	Syenite.....	47
4.6.	Felsic Rocks	49
4.6.1.	Quartz Microsyenite	50
4.6.2.	Monzogranite.....	51
Chapter 5: Hydrothermal veins and breccias.....		53
5.1.	Introduction	53
5.2.	Internal vein textures.....	53
5.3.	Hydrothermal vein assemblages.....	54
5.3.1.	Quartz-dominated veins	55
5.3.2.	Tourmaline-dominated veins.....	61
5.3.3.	Breccias and brecciated veins	62
5.3.4.	Jasper-dominated veins	64
5.3.5.	Epidote-dominated veins.....	68
5.3.6.	Calcite-dominated veins	70
5.3.7.	Barren quartz veins.....	70
5.4.	Compositional changes in hydrothermal veins.....	72
5.5.	Paragenetic sequence of hydrothermal events.....	74
5.5.1.	Overgrowth, replacement and growth zoning relationships.....	74
5.5.2.	Cross-cutting relationships	80
Chapter 6: Whole-rock geochemistry		83
6.1.	Introduction	83
6.2.	Major, trace and rare earth element (REE) geochemistry.....	83
6.2.1.	Rock classification	83
6.2.2.	Major element variation	90
6.2.3.	Trace element variation	91
6.2.4.	Rare earth elements (REE)	93
6.3.	Radiogenic isotope geochemistry	94
Chapter 7: Fluid Inclusion Analysis and Stable Isotope Geochemistry.....		97
7.1.	Fluid Inclusion Analysis: Introduction	97
7.2.	Fluid Inclusion Petrography	97

7.3. Microthermometry	99
7.3.1. Terminology	99
7.3.2. Fluid Inclusion Types	99
7.4. Stable Isotope Geochemistry	106
7.4.1. Introduction	106
7.4.2. Isotope geothermometer.....	108
7.4.3. $\delta^{18}\text{O}$ isotope results	109
7.4.4. δD isotope results	110
7.4.5. $\delta^{13}\text{C}$ isotope results.....	110
7.4.6. Origin of the fluids	110
Chapter 8: Discussion.....	114
8.1. Introduction	114
8.2. Petrogenesis.....	114
8.2.1. Petrogenetic processes	114
8.2.2. Source characterisation	124
8.2.3. Petrogenetic model for the rocks of the Yzerfontein Pluton.....	127
8.3. Tectonic Setting	128
8.4. Relationship with the I-type granites of Cape Granite Suite	130
8.5. Trapping conditions, origin and paragenesis of hydrothermal fluids.....	130
8.5.1. Fluid trapping conditions	130
8.5.2. Source and nature of hydrothermal fluids.....	131
8.5.3. Fluid evolution and paragenetic model of hydrothermal veining	135
Chapter 9: Concluding Remarks.....	141
References	144
Appendix A – Geological maps and sample locations.....	156
Appendix B – Host rocks	171
Appendix C – Hydrothermal veins	184
Appendix D – Geochemistry	190
Appendix E – Stable isotope calculations	195
Appendix F – Fractional crystallisation modelling	199

List of Figures

Figure 1.1: The location of the Yzerfontein Pluton.....	16
Figure 2.1: The position of the Saldania Belt at the south-westernmost edge of the Kalahari Craton.....	18
Figure 2.2: The western and southern branches of the Malmesbury Group.....	19
Figure 2.3: The most recent subdivision of the Saldania Belt.....	21
Figure 4.1: Outcrops of the leucocratic gabbro.....	33
Figure 4.2: Thin section photomicrographs of the leucocratic gabbro.....	34
Figure 4.3: Outcrops of melanocratic gabbro occurring at Gabbro Point.....	36
Figure 4.4: Thin section photomicrographs of the melanocratic gabbro in XPL.....	37
Figure 4.5: Outcrops of the poikilitic monzogabbro.....	38
Figure 4.6: Felsic dykes cross-cutting the poikilitic monzogabbro.....	39
Figure 4.7: Thin section photomicrographs of the poikilitic monzogabbro.....	40
Figure 4.8: Melanocratic enclaves hosted in the monzonite and syenodiorite.....	42
Figure 4.9: Monzogranite and quartz-microsyenite cross-cutting the syenodiorite and monzonite.....	43
Figure 4.10: Thin section photomicrographs of the weakly altered syenodiorite.....	45
Figure 4.11: Thin section photomicrographs of the moderately altered syenodiorite.....	46
Figure 4.12: Thin section photomicrographs of the monzonite.....	47
Figure 4.13: Hand specimen of the syenite obtained from Hoëbank.....	48
Figure 4.14: Thin section photomicrographs of the syenite.....	49
Figure 4.15: Thin section photomicrographs of the quartz-microsyenite.....	51
Figure 4.16: Thin section photomicrographs of the monzogranite.....	52
Figure 5.1: Quartz-dominated veins at different localities across the study area.....	56
Figure 5.2: Thin section photomicrographs displaying primary growth textures.....	57
Figure 5.3: Thin section photomicrographs displaying textures in quartz and tourmaline.....	60
Figure 5.4: Tourmaline-dominated vein.....	61
Figure 5.5: Breccias and brecciated veins occurring in the study area.....	63

Figure 5.6: Thin section photomicrographs of brecciated tourmaline veins.....	64
Figure 5.7: Jasper-dominated veins crosscutting the monzonite and syenodiorite at various localities.....	65
Figure 5.8: Jasper-dominated veins crosscutting the monzonite at various localities.....	66
Figure 5.9: Thin section photomicrographs displaying primary growth- and recrystallisation textures in quartz.....	67
Figure 5.10: Quartz-epidote veins occurring in the study area.....	68
Figure 5.11: Thin section photomicrographs displaying vermicular-textured tourmaline.....	69
Figure 5.12: WNW-ESE-trending calcite vein cross-cutting the syenodiorite.....	70
Figure 5.13: ENE-WSW-trending barren quartz veins traversing the monzonite.....	71
Figure 5.14: Thin section photomicrograph displaying a bimodal grain size distribution of silica in a barren quartz vein.....	71
Figure 5.15: Thin section photomicrographs demonstrating the change in composition in a quartz-pyrite-tourmaline vein.....	73
Figure 5.16: Thin section photomicrograph of a quartz-calcite-tourmaline-epidote vein.....	75
Figure 5.17: WNW-ESE-trending quartz-pyrite.....	76
Figure 5.18: Thin section photomicrographs illustrating the minerals overgrowing each other in the paragenetic sequence during stages 1 and 2.....	77
Figure 5.19: Thin section photomicrographs illustrating the minerals overgrowing each other in the paragenetic sequence during stage 3.....	78
Figure 5.20: Hydrothermal veins showing cross-cutting relationships in the study area.....	81
Figure 6.1: Rock classification diagrams for the intermediate and mafic rocks.....	83
Figure 6.2: Classification and chemical discrimination diagrams for the felsic rocks.....	89
Figure 6.3: Chemical discrimination diagrams for the felsic rocks.....	90
Figure 6.4: Harker plots of selected major elements for the rocks of the Yzerfontein Pluton....	91
Figure 6.5: Harker plots of selected trace elements for the rocks of the Yzerfontein Pluton.....	92
Figure 6.6: Primitive mantle-normalised REE and spider diagrams for the mafic, intermediate, and felsic rocks of the Yzerfontein Pluton.....	94
Figure 7.1: Photomicrographs and CL images of two selected areas along a quartz-pyrite-tourmaline vein.....	98

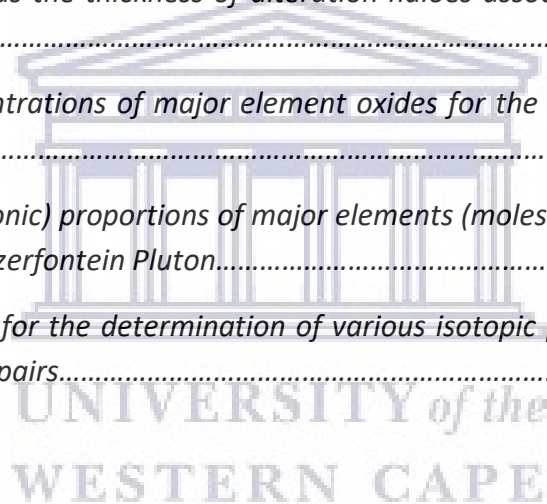
Figure 7.2: Photomicrographs of primary aqueous inclusions.....	100
Figure 7.3: Bivariate plot of $T_h(\text{total})$ vs. salinity	103
Figure 7.4: Histograms showing the distribution of (a) $T_m(\text{ice})$, (b) $T_h(\text{total})$, (c) salinities, (d) densities and (e) homogenization temperature for all type I inclusions.....	104
Figure 7.5: Histograms showing the distribution of (a) $T_m(\text{halite})$, (b) $T_h(\text{total})$, (c) salinities, (d) densities and (e) homogenization pressure for all type II inclusions.....	105
Figure 7.6: $\delta^{18}\text{O}$ isotopic values of quartz, tourmaline, calcite and H_2O	111
Figure 7.7: δD isotopic values of tourmaline and H_2O	111
Figure 7.8: $\delta^{13}\text{C}$ isotopic values of calcite and H_2O	112
Figure 7.9: δD vs. $\delta^{18}\text{O}$ plot of H_2O for samples YZN61a and YZN62.....	113
Figure 8.1: Intrusive contact between two phases of the leucocratic gabbro.....	115
Figure 8.2: Biplots of PC1 vs. PC2 of selected major elements.....	119
Figure 8.3: Binary log-log diagram illustrating the effects of fractional crystallisation.....	123
Figure 8.4: Isotopic diagrams for the rocks of the Yzerfontein Pluton.....	125
Figure 8.5: TiO_2/Yb vs. Nb/Yb basalt classification diagram.....	126
Figure 8.6: Proposed tectonic and emplacement setting and simplified general petrogenetic model for the rocks of the Yzerfontein Pluton.....	127
Figure 8.7: $\text{Y}/15\text{-La}/10\text{-Nb}/8$ tectonic discrimination diagram and T_h vs. Co diagram.....	129
Figure 8.8: Isochore plot showing the possible trapping conditions for type I fluid inclusions.....	131
Figure 8.9: Bivariate plot of salinity vs. $T_{h(\text{total})}$ for type I inclusions.....	133
Figure 8.10: Bivariate plot of salinity vs. $T_{h(\text{total})}$ for type II inclusions.....	135
Figure 8.11: Plot of salinity vs. homogenization temperature.....	138
Figure 8.12: Simplified paragenetic model for hydrothermal fluid flow.....	140
Figure A1: Geological map of the major rock types occurring at Gabbro Point.....	157
Figure A2: Geological map of the major rock types occurring NE of the Visitors Center.....	158
Figure A3: Geological map of the major rock types north, west and SW of the Visitors Center.....	159
Figure A4: Geological map of the major rock types occurring at the Yzerfontein Harbour and Hoëbank.....	160

Figure A5: Geological map of the major rock types occurring at Starck, Duiwenes, Deurspring and Yzerfontein Point.....	161
Figure A6: Geological map of the major rock types occurring at Grasbank and Kollege.....	162
Figure A7: Geological map of the major rock types occurring at Draaibank.....	163
Figure A8: Geological map of the major rock types occurring at Kreefgat and Duckitt se Klip.....	164
Figure A9: Geological map of the major rock types occurring at Schaap Eiland.....	165
Figure A10: Geological map of the major rock types occurring at Freddie se Klip.....	166
Figure B1: Outcrop of melanocratic gabbro hosting a mafic enclave at Gabbro Point.....	172
Figure B2: Monzogranite dyke cross-cutting the poikilitic monzogabbro.....	172
Figure B3: Presence of various compositional phases in the poikilitic monzogabbro.....	173
Figure B4: Large zone of micromonzogabbro enclaves in the syenodiorite.....	173
Figure B5: Portion of a monzogranite dyke cross-cutting the syenodiorite.....	174
Figure B6: Thin section photomicrographs of the leucocratic gabbro.....	175
Figure B7: Thin section photomicrographs of the melanocratic gabbro.....	175
Figure B8: Thin section photomicrograph of the syenodiorite.....	176
Figure B9: Thin section photomicrographs of the syenodiorite	176
Figure B10: Thin section photomicrographs of the monzonite.....	177
Figure B11: Thin section photomicrographs of the monzonite.....	178
Figure C1: Thick quartz-pyrite-tourmaline vein occurring at Schaap Eiland.....	185
Figure C2: NW-SE-trending quartz-tourmaline-jasper vein cross-cutting the syenodiorite....	185
Figure C3: Thin section photomicrographs displaying a globular-like texture in a quartz-pyrite-tourmaline-jasper vein.....	189
Figure C4: Thin section photomicrographs displaying primary and recrystallisation textures in quartz.....	189
Figure F1: Correlation diagrams for the mafic rocks of the Yzerfontein Pluton.....	204
Figure F2: Correlation diagrams for the intermediate rocks of the Yzerfontein Pluton.....	205
Figure F3: Correlation diagrams for the felsic rocks of the Yzerfontein Pluton.....	206

List of Tables

Table 5.1: Hydrothermal veins identified and described in the field and in thin section, and the vein assemblages into which they were grouped.....	55
Table 5.2: Summary of the mineralogy and grain sizes of minerals present along hydrothermal veins and their alteration haloes in thin section, as well as the rock types which they traverse (occurrence).....	58
Table 5.3: Summary of the mineralogy and width of hydrothermal veins and their alteration haloes in thin section.....	59
Table 5.4: Paragenetic scheme displaying the genetic sequence in which minerals precipitated from hydrothermal solutions along conduits and in alteration haloes.....	82
Table 6.1: Whole-rock major (wt.%) and trace element (ppm) compositions for the rocks of the Yzerfontein Pluton.....	84
Table 6.2: Whole-rock rare earth element (REE) concentrations (ppm) for the rocks of the Yzerfontein Pluton. Ratios with subscript PM were normalised to the primitive mantle using the values of McDonough and Sun (1995).....	87
Table 6.3: Whole-rock Rb-Sr isotopic data for the rocks of the Yzerfontein Pluton.....	96
Table 6.4: Whole-rock Sm-Nd isotopic data for the rocks of the Yzerfontein Pluton.....	96
Table 7.1: Microthermometry data for type I and type II aqueous fluid inclusions.....	101
Table 7.2: Composition of hydrothermal veins from which samples were analysed, the rock types which they traverse and the locality from which the samples were collected.....	103
Table 7.3: Measured oxygen, hydrogen and carbon isotopic data for different quartz, tourmaline and calcite samples from hydrothermal veins.....	106
Table 7.4: Composition of hydrothermal veins from which samples were analysed, the rock types which they traverse and the locality from which the samples were collected.....	107
Table 7.5: Calculated oxygen and hydrogen isotopic data for tourmaline and water.....	109
Table 8.1: Partition coefficients of Ba and Sr for various minerals in mafic, intermediate and felsic magmas.....	122
Table A1: GPS location of samples (rock and vein types) collected in the study area and the type of analyses performed on selected samples.....	167
Table B1: Summary of petrographic observations for the samples of leucocratic gabbro....	179
Table B2: Summary of petrographic observations for the samples of melanocratic gabbro...	179

Table B3: Summary of petrographic observations for the samples of poikilitic monzogabbro.....	180
Table B4: Summary of petrographic observations for the samples of weakly altered syenodiorite.....	180
Table B5: Summary of petrographic observations for the samples of moderately altered syenodiorite.....	181
Table B6: Summary of petrographic observations for the samples of monzonite.....	181
Table B7: Summary of petrographic observations for the samples of syenite.....	182
Table B8: Summary of petrographic observations for the samples of quartz-microsyenite...	182
Table B9: Summary of petrographic observations for the samples of monzogranite.....	183
Table C1: Thickness and orientation of hydrothermal veins encountered in different localities across the study, as well as the thickness of alteration haloes associated with each type of vein.....	186
Table D1: Element concentrations of major element oxides for the rocks of the Yzerfontein Pluton.....	191
Table D2: Molecular (cationic) proportions of major elements (moles of elements per 100g of rock) for the rocks of the Yzerfontein Pluton.....	192
Table E1: Equations used for the determination of various isotopic parameters for mineral-mineral and mineral-fluid pairs.....	195



Chapter 1: Introduction

1.1. Background and Locality

The significance of mafic and intermediate rocks occurring in dominantly granitic suites has not received much attention in the last few decades. Most recent investigations have been done by Nandedkar et al. (2014), Keller et al. (2015) and Clemens et al. (2016). There is a growing perception that granitic magmas and mantle-derived mafic magmas are chemically related to each other, and that extensive mafic magmatism may be relevant during the evolution of granitic magmas (Frost and Mahood, 1987; Bateman, 1992; Coleman et al., 1995; Nandedkar et al., 2014). In spite of the fact that much of the exposed continental crust has a granodioritic to granitic composition, the significance of mafic magmas in the origin of intermediate to felsic magmas is often inferred (Coleman et al., 1995). It has also been inferred that mafic magmas, whether they are exposed or not, commonly drive compositional variation. Additionally, mafic magmas are also inferred to represent the heat source for the genesis and differentiation of magma systems that have a high-silica composition (Coleman et al., 1995).

The Yzerfontein Pluton represents a typical example of a group of mafic, intermediate and felsic rocks occurring within a dominantly granitic suite, known as the Cape Granite Suite (CGS). The Yzerfontein Pluton is exposed along the coastline of Yzerfontein, Western Cape, South Africa. It forms part of the CGS of the Pan-African Neoproterozoic Saldania Belt, which is located along the southern and southwestern portions of the Kalahari Craton and is related to other Pan-African belts that resulted in the construction of southwest Gondwana (Fig. 1.1) (Jordaan et al., 1995; Rozendaal et al., 1999; Kisters and Belcher, 2018). The rocks of the Yzerfontein Pluton are traversed by hydrothermal veins of various compositions, some of which host Cu-Au mineralisation, particularly at Schaap Eiland (Figs. A8 to A10) (Rozendaal and Scheepers, 1995). This enrichment of Cu and Au has been known for many years, however, the deposit has a low economic potential due to the low grades reported (Jordaan, 1990). Au grades range between 0.4 and 12 ppm, and Cu up to 0.2%, with the highest Cu-Au grades measured in areas that have experienced pervasive hydrothermal alteration (Scholtz, 1946; Jordaan, 1990; Rozendaal and Scheepers, 1995). In spite of the overall low Cu-Au grades, the high grades reported in selected areas may be indicative of potential ore-forming processes within and associated with the CGS. Jordaan (1990) concluded that the outcrops studied along the West Coast have certain features that reflect a porphyry style Cu deposit, the most significant features being propylitic alteration and mineralisation.

The bulk of the mafic, intermediate and felsic outcrops occur along the coast, extending over a distance of ~8 km, with a few outcrops occurring as offshore islands, and a single outcrop located inland. The CGS makes up the bulk of the intrusions that were emplaced into the metasedimentary rocks of the late-Neoproterozoic to Cambrian Malmesbury Group, particularly towards the southern- and westernmost parts of the West Coast of the Western Cape Province (Kisters and Belcher, 2018). Traditionally, the various magmatic phases of the

CGS have received a considerable amount of attention, particularly in terms of their geochemistry, geochronology, petrogenesis, geochemical affinities, magmatic evolution and their genetic interpretation (e.g. Schoch and Burger, 1976; Scheepers, 1982; Scheepers and Schoch, 1988; Gresse and Scheepers, 1993; Scheepers, 1995; Rozendaal et al., 1999). The S-type granites are the best-studied rocks of the CGS and have been the focus of several publications (e.g. Schoch, 1972; Villaros et al., 2009; Farina et al., 2012; Villaros et al., 2012; Browning and Macey, 2015).

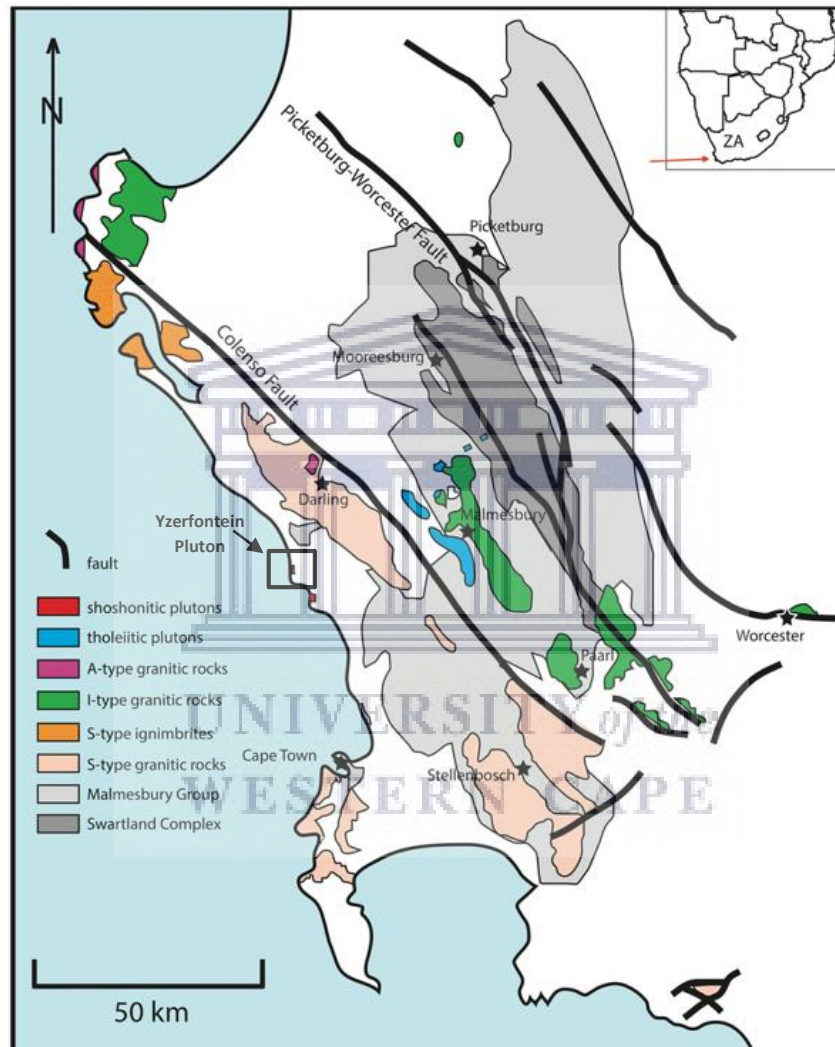


Figure 1.1: Sketch map highlighting the location of the Yzerfontein Pluton and the geographic distribution of associated rocks in the western part of the Saldania Belt (after Clemens et al., 2017a).

Despite the low volumetric extent of the rocks of the Yzerfontein Pluton in comparison to the other plutons of the CGS, these mafic, intermediate and felsic components have not received a significant amount of attention in the past, especially in terms of their intrusive environment with respect to plate tectonics, as well as their petrogenesis (Jordaan, 1990; Jordaan et al., 1995; Clemens et al., 2017a). Several publications have focussed on the dating of the rocks (e.g. Rogers, 1896; Scholtz, 1946; Holmes and Cahen, 1957; Maske, 1957; Allsopp and Kolbe, 1965; Schoch et al., 1975; Jordaan et al., 1995, Clemens et al., 2017a), as well as their

petrology (e.g. Maske, 1957; Jordaan, 1990; Clemens et al., 2017a). The age of the rocks was previously investigated by Jordaan et al. (1995). However, the results were discordant and only yielded an upper concordia intercept age of 519 ± 7 Ma, with assumed recent Pb loss for the lower intercept. The emplacement age of the rocks therefore still remained poorly constrained, until recently when the newly determined U-Pb age of 535 ± 3 Ma placed the average crystallisation age of the rocks into context (Clemens et al., 2017a). Clemens et al. (2017a) also assessed the magmatic affinities of the rocks in order to draw conclusions on their petrogenesis. According to Clemens et al. (2017a), even though the rocks have some crustal signatures, they were derived from an enriched mantle source.

This study will be partly focussed on examining the petrogenesis of these rocks, not only to determine the characteristics of the source from which the rocks were derived, but also to investigate the petrogenetic processes that may have been at play. The intrusive environment with respect to plate tectonics will also be assessed, particularly in the context of the CGS and the overall tectonic evolution of the Saldania Belt.

The hydrothermal veins that cross-cut the rocks of the Yzerfontein Pluton have received the least attention. Clemens et al. (2017a) briefly indicates the presence of these veins, and Maske (1957), Jordaan (1990), Jordaan et al. (1995) briefly account for their compositions. However, none of these included a detailed study of the hydrothermal veins, their internal textures, their variety of compositions and associated alteration haloes, or their paragenetic sequence. This study will therefore also be largely focussed on accounting for these different aspects of the hydrothermal veins, and, most importantly, constructing a paragenetic sequence.

The economic potential of the Yzerfontein Pluton has been investigated previously (e.g. Rozendaal and Scheepers, 1994; Jordaan et al., 1995; Rozendaal and Scheepers, 1995). Jordaan (1990) performed microthermometry on three quartz-bearing samples in order to investigate the composition of the fluid inclusions, the inclusion populations, and the crystallisation conditions. The minimum trapping conditions of the fluids were, however, not well constrained. Given the small number of quartz-bearing samples previously analysed, fluid inclusion petrography and microthermometry will be undertaken in order to investigate and reconstruct the properties of the fluids, their origin(s), as well as their minimum trapping conditions.

Chapter 2: Regional Geology

2.1. Regional Geological Setting

The Saldania Belt is a late Neoproterozoic to early Cambrian fold belt that forms part of a larger system of belts which are related to the events of the Pan African Orogeny (Scheepers and Armstrong, 2002; Chemale et al., 2011; Frimmel et al., 2013). It is typically exposed as inliers in the southern and westernmost parts of the Permo-Triassic Cape Fold Belt and is located towards the south-westernmost parts of the Kalahari Craton, typically along the southern and south-westernmost parts of the Western Cape Province, South Africa (Fig. 2.1) (Chemale et al., 2011).

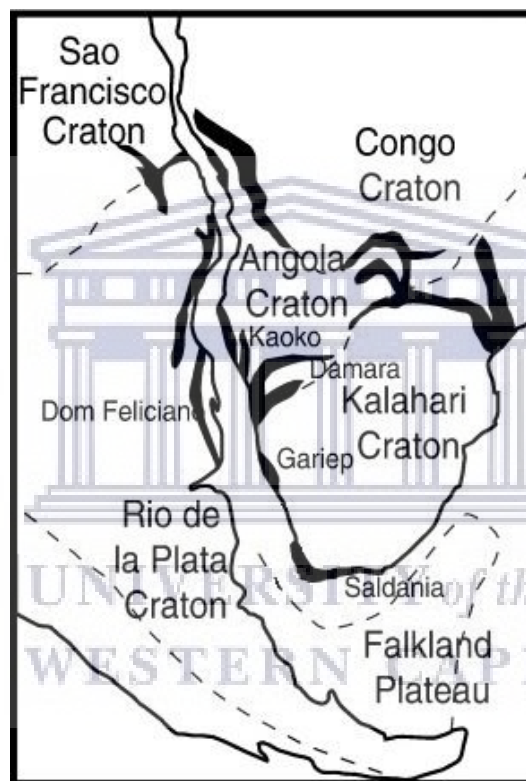


Figure 2.1: Schematic diagram showing the position of the Saldania Belt at the south-westernmost edge of the Kalahari Craton (after Villaros et al., 2009). Also shown is the location of other Pan-African belts in southern Africa and South America in a western Gondwana reconstruction.

Along with various other orogenic belts, such as the Gariiep Belt, the Kaoko Belt and the Damara Belt (Fig. 2.1), the formation of the Saldania Belt was contemporaneous with the construction of the south-westernmost part of the supercontinent Gondwana during the closure of the Adamastor Ocean (Rozendaal et al., 1999; Rowe et al., 2010; Villaros, 2010). Mostly unassociated with mineralisation, the belt is generally related to the occurrence of sedimentary rocks and granite plutons (Rozendaal and Scheepers, 1994). It remains poorly understood due to its complex structural history, limited exposure and intensely weathered surfaces in some localities, as well as its burial and compaction below siliciclastic rocks of the Cape Supergroup (Kisters et al., 2002; Frimmel et al., 2013). The belt is comprised mainly of

volcano-sedimentary sequences that have regionally experienced low-grade metamorphism and were intruded by the S-, I- and A-type granitoids of the CGS. Among the most common sequences are greywacke, shale, conglomerate, limestone, dolomite, phyllite, quartzite, sandstone, calc-silicates, schists and other metavolcanic rocks including quartz-chlorite-muscovite and chlorite schists (Rozendaal et al., 1999).

Two structural trends can be distinguished across the belt, dividing it into two major domains. The first is the southern branch, comprising the E-W-trending Cango, Kaaimans and Gamtoos Groups, which was generated by oblique thrusting (Fig. 2.2) (Belcher, 2003; Chemale et al., 2011; Frimmel et al., 2013; Kisters et al., 2015). The main lithologies include quartzites, schists, granites, phyllites, marble, calc-silicate and meta-basic intrusions (Chemale et al., 2011). The second is the western branch, which is also referred to as a low-grade metamorphic fold belt, and comprises the Malmesbury Group, the Klipheuwel Group, and the granitoids of the CGS (Belcher, 2003; Chemale et al., 2011; Frimmel et al., 2013; Kisters et al., 2015). The main lithologies of the western branch include quartzites, shales, siltstones, metaconglomerates, marble, metagreywacke and metavolcanics intermediate to basic rocks, and it has a NW-SE trend which was generated by transpressive sinistral movement (Chemale et al., 2011; Kisters and Belcher, 2018).

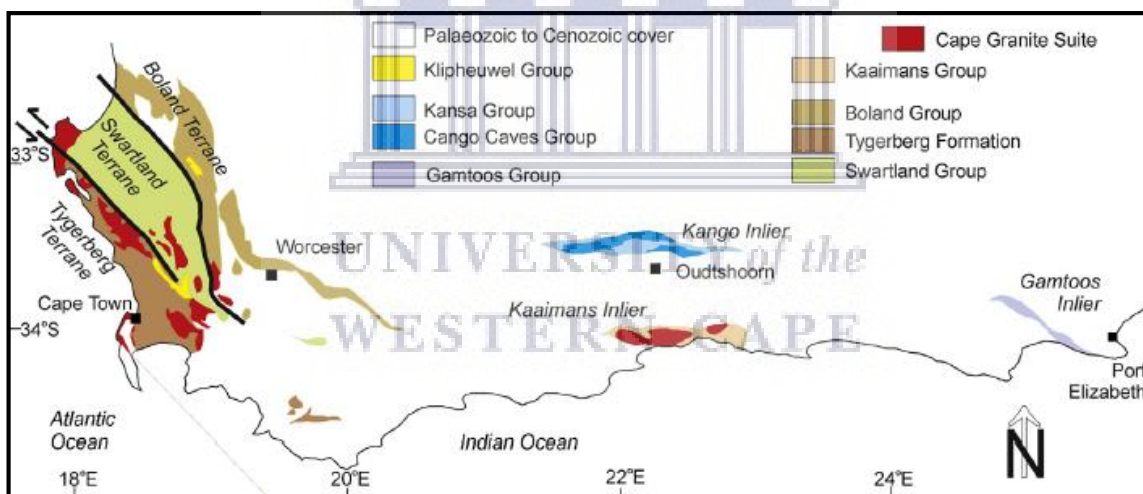


Figure 2.2: Geological map showing the western and southern branches of the Malmesbury Group, as well as its major tectonostratigraphic terranes (after Frimmel et al., 2013).

2.1.1. The western branch of the Saldania Belt

The repetitive nature of supracrustal sequences, poor outcrop conditions and the low grades of metamorphism recorded for the Saldania Belt have led to the proposal of a number of contrasting geodynamic models for the belt. The various geodynamic models attempt to account for the tectonostratigraphic make-up of the belt, as well as the general geodynamic setting of the belt (e.g. Hartnady et al., 1974; Von Veh, 1982; Rozendaal et al., 1999; Belcher and Kisters, 2003; Gresse et al., 2006; Frimmel, 2009; Buggisch et al., 2010; Rowe et al., 2010; Frimmel et al., 2011, 2013; Kisters and Belcher, 2018).

The model proposed by Hartnady et al. (1974) suggests that the Malmesbury Group is comprised of three terranes from SW to NE, namely the Tygerberg, Swartland and Boland terranes, and that they are separated by NW-SE-trending strike-slip faults. The Colenso Fault is inferred to separate the Tygerberg and Swartland terranes, and the Piketberg-Wellington Fault is inferred to separate the Swartland and Boland terranes. Belcher and Kisters (2003) suggested that the western branch of the Saldania Belt is comprised of three unconformably stacked groups known as the Swartland, Malmesbury and Klipheuwel Groups (from oldest to youngest). In a more recent model, Frimmel et al. (2013) suggested the presence of two distinct terranes, namely the Malmesbury Terrane and the Boland Zone, separated by the Piketberg-Wellington Fault. In this model, the Colenso Fault is reinterpreted as a reactivated old structure that once formed part of the basement of the Malmesbury Terrane, rather than a terrane boundary. The most recent geodynamic model for the western branch of the Saldania Belt was proposed by Kisters and Belcher (2018), suggesting the presence of two distinct lithological packages. According to Kisters and Belcher (2018), the structurally lower parts of the belt, known as the Swartland complex, is unconformably overlain by the metasediments and minor metavolcanic rocks of the Malmesbury Group. The geodynamic model by Kisters and Belcher (2018) is followed in this section, as the model is less focussed on providing a new subdivision, and more on how the various lithological packages are correlated, and on sedimentary facies and the structures present across the purported terrane boundaries.

A fore-arc basin is exposed along a section of the western branch of the Saldania Belt which records deformation, sedimentation and plutonism along the obliquely convergent continental margin of the Kalahari Craton during the late Neoproterozoic to Cambrian (Kisters and Belcher, 2018). The fore-arc basin represents relics of deformed yet reasonably coherent rocks collectively known as the Malmesbury Group, which overlies the upper parts of an accretionary prism named the Swartland complex (Fig. 2.3) (Kisters and Belcher, 2018). From the study done by Frimmel et al. (2013), U-Pb isotopic ratios obtained from the isotopic analyses of zircon grains from rocks of the western Saldania Belt revealed, within error, that the Malmesbury Group and the Swartland complex share identical late-Neoproterozoic ages (Kisters and Belcher, 2018).

The Swartland complex is comprised of a variety of lithologies that make up a heterogeneous assemblage. It includes quartz-sericite and chlorite-muscovite schists and phyllites, chlorite- and talc-carbonate schists, graphitic schists and limestones, grey, massive- to well-bedded limestones, quartzites and muscovite quartzites, and highly sheared chert horizons (Rabie, 1948, 1974; Hartnady et al., 1974; SACS, 1980; Theron et al., 1992; Belcher 2003; Belcher and Kisters., 2003; Gresse et al., 2006). In addition to the lithological heterogeneity and structural complexity of the tectonostratigraphic sequences of the Swartland complex, the highly sheared and transposed nature of the rocks characterises it as a *mélange*-like sequence (Kisters and Belcher, 2018). The characteristics that distinguish outcrops of different lithologies in the Swartland complex is a pervasively developed bedding-parallel phyllitic

foliation, S_1 , as well as the presence of quartz and quartz-carbonate veins which are parallel to S_1 and commonly transposed (Kisters and Belcher, 2018).

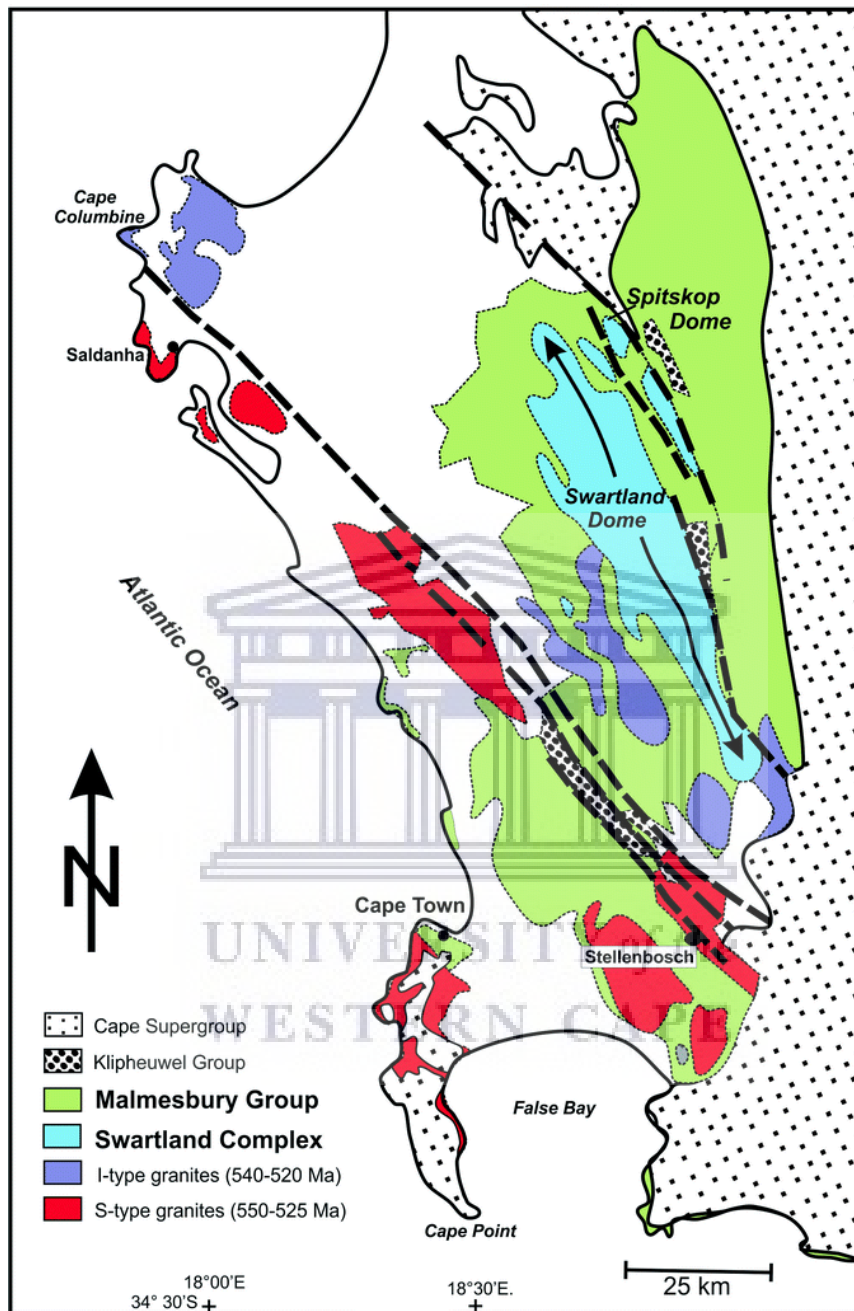


Figure 2.3: Geological map of the western branch of the Saldania Belt depicting the most recent subdivision of the Saldania Belt after Kisters and Belcher (2018). The map highlights the two major structurally bounded packages across purported terrane boundaries, known as the lower Swartland complex and the overlying Malmesbury Group. Also shown is the position of the S- and I-type granites of the CGS.

The Malmesbury Group, regardless of its poorly defined stratigraphic units and structural complexity, remains the most extensive and well-studied group of the Saldania Belt (e.g. Scheepers, 1995; Rozendaal et al., 1999; Belcher, 2003; Belcher and Kisters, 2003; Buggisch et al., 2010; Frimmel et al., 2013; Kisters and Belcher, 2018). The westernmost parts of the

Saldania Belt are comprised of mainly metasedimentary and minor metavolcanic rocks of the Malmesbury Group, with only one stratigraphic unit overlying these parts of the belt, known as the Tygerberg Formation (SACS, 1980; Gresse et al., 2006; Kisters and Belcher, 2018). The Tygerberg Formation is predominantly comprised of a greywacke-dominated succession with siltstone/mudstone alternations, and minor, well-exposed and preserved amygdaloidal mafic- to intermediate lavas, agglomerates and tuffs of the Bloubergstrand Member (Hartnady et al., 1974; Rowe et al., 2010; Frimmel et al., 2013; Kisters et al., 2015; Kisters and Belcher, 2018). The rocks of the Malmesbury Group lack the bedding-parallel foliation, S_1 , and primary bedding features.

The largest structural features of the Saldania Belt are the prominent NW-SE-trending Colenso Fault and the less prominent Piketberg-Wellington Fault (Hartnady et al., 1974; Theron et al., 1992; Belcher, 2003; Frimmel et al., 2013; Kisters and Belcher, 2018). The Colenso Fault is a well-exposed, NW-SE-trending sub-vertical anastomosing fault that records sinistral strike-slip kinematics (Kisters et al., 2002; Kisters and Belcher, 2018). Structurally, at depth, an oblique-slip, east-side up component was inferred, particularly towards the eastern parts of the fault (e.g. Hartnady et al., 1974; Rozendaal et al., 1999; Gresse et al., 2006). Kisters et al. (2002) investigated the timing and kinematics of the Colenso Fault and found that the fault experienced a switch in kinematics from transpressional to transtensional tectonics around 540 Ma, and that a significant part of the intrusions forming part of the CGS were emplaced in this transtensional environment. The fault is therefore best exposed in the granites of the CGS, in particular the central Darling Batholith, and forms a prominent divide between the S- and I-type granites towards the western parts of the Saldania Belt (Scheepers, 1995; Scheepers and Schoch, 2006; Stevens et al., 2007; Villaros et al., 2009; Kisters and Belcher, 2018).

The Piketberg-Wellington Fault is poorly exposed and neither has its location and actual extent, nor its timing and kinematics been ascertained (Rabie, 1948, 1974; Theron et al., 1992; Slabber, 1995; Belcher, 2003; Kisters and Belcher, 2018). It has been established with certainty that displacement of rocks of the Cape Supergroup along the Piketberg-Wellington Fault display a downthrow to the east, with a mainly normal sense of movement (Belcher, 2003; Kisters and Belcher, 2018). However, the actual trace of the Piketberg-Wellington Fault can only be “inferred” along its southern extent, and therefore remains controversial (e.g. Theron et al., 1992).

2.1.2. The Cape Granite Suite

The syn-, late- and post-tectonic granites of the CGS intruded the metasediments of the Malmesbury Group around 550 – 510 Ma (Kisters et al., 2015; Kisters and Belcher, 2018). The rocks of the CGS crop out over a distance exceeding 500 km along the Southern and Western Cape coastline. The CGS represents a group of granitoid plutons and batholiths that formed during the Late Neoproterozoic to Cambrian and have been subdivided into three types based on their textural characteristics, field relationships and geochemistry, as well as their

individual modelled age; they are referred to as the S-, I-, and A-type granites respectively (Rozendaal and Scheepers, 1995; Scheepers, 1995; Scheepers, 2000). The CGS comprises mainly S-type granites (Fig. 2.3), which, according to U-Pb zircon data from Scheepers (1995), Da Silva et al. (2000), Scheepers and Armstrong (2002), Chemale et al. (2011) and Villaros et al. (2012), were emplaced around 550 – 530 Ma. The I-type granites are present in smaller volumes (Fig. 2.3), with ages between 540 – 530 Ma. The ages of the S- and I-type granites suggest that magmatism was largely contemporaneous, considering the overlap of ages between the two granite types (Kisters and Belcher, 2018). The A-type granites, which are only present as a few small plutons, are the youngest and have U-Pb zircon ages between 525 – 510 Ma (Scheepers, 1995; Da Silva et al., 2000; Scheepers and Armstrong, 2002; Chemale et al., 2011; Villaros et al., 2012).

The peraluminous to metaluminous S-type granites are collision-related syn- to post-tectonic granites (Scheepers, 1995; Scheepers and Poujol, 2002). The S-type granites display a similar compositional variation from leucogranite to granodiorite, containing no magmatic or solid-state fabrics (Farina et al., 2012; Kisters and Belcher, 2018). The S-type granites commonly contain several xenoliths of the Malmesbury Group (Scheepers, 1995). The protolith of the S-type granites is inferred to be either a higher grade equivalent of the Malmesbury Group (e.g. Harris et al., 1997), or the Malmesbury Group itself, at depth (e.g. Harris and Vogeli, 2010; Villaros, 2010; Villaros et al., 2012). This is suggested by the $\delta^{18}\text{O}$ values of the rocks of the Malmesbury Group, which indicate that they are suitable source materials to enhance the production of the S-type granites (Harris and Vogeli, 2010). Additionally, the ages of the youngest concordant detrital zircons from the Malmesbury Group/Swartland complex are coeval with the oldest emplacement ages of the S-type granites (e.g. Scheepers and Armstrong, 2002), further suggesting the Malmesbury Group as a protolith for the S-type granites (Clemens et al., 2017b).

In addition to the S-type granites, this phase of granitic magmatism was also accompanied by the extrusion of the intracaldera, S-type, rhyolite ignimbrites of the Saldanha Bay Volcanic Complex (Clemens et al., 2017b). According to Clemens et al. (2017b), these rocks formed around 542 Ma, which is coeval with the formation of the S-type Seeberg and Trekoskraal granites that formed around 540 ± 4 Ma and 539 ± 4 Ma respectively (Scheepers and Armstrong, 2002). These volcanic rocks are mostly strongly peraluminous and are classified as ignimbrite flows, quartz-porphyritic granites and tuffisites (Scheepers and Armstrong, 2002; Clemens et al., 2017b).

The metaluminous to slightly peraluminous I-type granites are post-tectonic and comprise mainly monzogranites, granites, and alkali feldspar granites (Rozendaal and Scheepers, 1995; Scheepers, 1995; Scheepers and Poujol, 2002). They are present as elongate, NW-SE-trending plutons that occur east of the Colenso Fault (Kisters and Belcher, 2018). In the I-type granites, igneous and meta-igneous xenoliths occur more commonly than sedimentary xenoliths (Scheepers and Poujol, 2002).

The A-type granites are anorogenic and comprise high-K calc-alkaline intermediate and mafic plutonic bodies (Scheepers, 1995; Scheepers and Poujol, 2002). The A-type associations comprise alkali granites, alkali feldspar granites, amphibole quartz syenite to biotite quartz syenite, gabbros and diorites (Jordaan et al., 1995; Scheepers, 1995; Scheepers and Poujol, 2002). The intrusive relationships, where present, suggest that emplacement of the gabbroic rocks preceded the emplacement of the other phases (Scheepers, 1995).

2.2. Local geological setting

2.2.1. The Yzerfontein Pluton

The Yzerfontein Pluton is a composite pluton that forms part of the shoshonitic series (Fig. 2.1) (Clemens et al., 2017a). According to Jordaan et al. (1995), the composition of the outcrops along the Yzerfontein Pluton ranges from olivine gabbros (mostly at the northernmost end) to quartz-monzonites, with monzonitic outcrops being the most abundant (central to southernmost portions). Clemens et al. (2017a) reviewed the classification of these rocks by integrating the results of three classification schemes, including the TAS classification schemes of Le Bas and Streckeisen (1991), Le Maitre et al. (2002) and Middlemost (1994). According to Clemens et al. (2017a), the pluton mainly comprises quartz-monzonites, along with monzonites, quartz-monzodiorites, quartz diorites, and smaller volumes of syenites, gabbros, monzodiorites and diorites.

The mafic outcrops commonly display prominent or subtle magmatic layering, whereas the intermediate rocks locally display subtle layering as well as exquisite intrusive contacts and medium-scale mingling features between different intrusive phases (Maske, 1957; Jordaan et al. 1995; Clemens et al., 2017a). Metasedimentary xenoliths are absent in these rocks, whereas melanocratic enclaves occur abundantly in outcrops. These enclaves were interpreted by Clemens et al. (2017a) as autoliths, which represent quenched, aphyric portions of the magma of the main pluton. Cross-cutting the main shoshonitic part of the pluton are fine-grained “sugary-textured” felsic dykes that have a quartz-syenite composition.

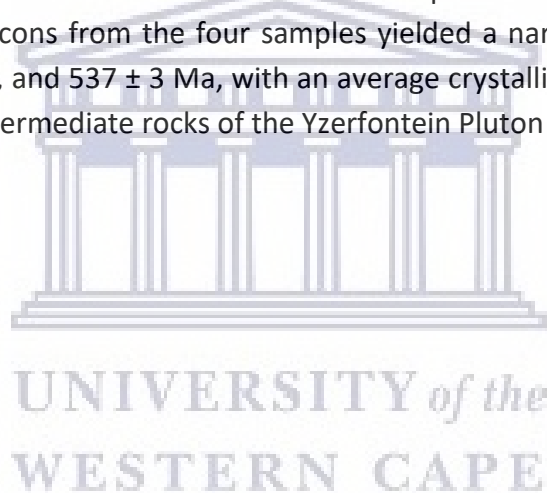
The U-Pb age of the rocks of the Yzerfontein Pluton was previously determined by Jordaan et al. (1995) by ID-TIMS U-Pb analysis of a composite zircon separate, which yielded an upper intercept age of 519 ± 7 Ma. Clemens et al. (2017a) reviewed the age of the rocks of the Yzerfontein Pluton, and the new average U-Pb crystallisation age of the rocks is 535 Ma (roughly coeval with the age of the I-type granites), which is significantly older than the age reported by Jordaan et al. (1995).

2.2.2. Timing of magmatic emplacement

Zircon geochronology work has not been undertaken in the present study for the age determination of the rocks of the Yzerfontein Pluton. However, this section is presented merely to provide an overall summary of the age of emplacement for the mafic and intermediate rocks of the Yzerfontein Pluton. The age of five rocks from the Yzerfontein Pluton, varying in composition from monzonite to monzogabbro, was previously determined

by Jordaan et al. (1995). The method involved isotope dilution-thermal ionisation mass spectrometry (ID-TIMS) U-Pb analysis of five composite zircon samples. The results were discordant, yielding an upper concordia intercept age of 519 ± 7 Ma, with assumed recent Pb loss for the lower intercept. Jordaan et al. (1995) therefore suggested that the upper intercept age of 519 ± 7 Ma represents the minimum age for the emplacement of the rocks. In light of this minimum age, it suggests that the rocks of the Yzerfontein Pluton are much younger relative to the I- and S-type granites of the CGS but relatively contemporaneous with the A-type granites and S-type ignimbrites of the CGS (Clemens et al., 2017a).

New U-Pb ages for the rocks of the Yzerfontein Pluton were determined by Clemens et al. (2017a). These new ages firmly link the emplacement age for the rocks of the Yzerfontein Pluton with that of the late syn-tectonic I- and S-type granites of the CGS, which are aged between 550 – 530 Ma, as opposed to the A-type granites with emplacement ages between 525 – 510 Ma (Scheepers, 1995; Da Silva et al., 2000; Scheepers and Armstrong, 2002; Chemale et al., 2011; Villaros et al., 2012). In the research of Clemens et al. (2017a), U-Pb isotope analysis was performed on subhedral to euhedral prismatic zircon grains from four different samples. The zircons from the four samples yielded a narrow range of concordia ages between 533 ± 3 Ma, and 537 ± 3 Ma, with an average crystallisation age coeval at 535 ± 3 Ma for the mafic to intermediate rocks of the Yzerfontein Pluton (Clemens et al., 2017a).



Chapter 3: Research Methodology and Analytical Techniques

3.1. Field work

Field work was carried out in order to generate a lithological description of the rocks by recording field observations and relationships. This included measuring the extent or size of outcrops, identifying the mineralogy of each rock type as well as determining the grain size, describing the textures, types of alteration (and extent), identifying structures and features, as well as describing the contact relationships between the different rock types. The hydrothermal veins were analysed in terms of their mineralogical composition, thickness, change in mineralogy and proportions of constituent minerals in any particular direction, as well as the composition of associated alteration haloes and their thicknesses. The orientation of the hydrothermal veins, in terms of dip direction/dip angle, were measured in order to determine the dominant directions in which they cross-cut the host rocks. Extensive mapping of the area did not take place due to time constraint. However, the geological maps of Jordaan (1990) were re-digitised using a software package called *Surfer*TM. The geological maps were also updated in terms of the rock types as they were classified in this study by means of integrated petrography and geochemistry.

3.2. Geochemical Sampling

A total of 97 samples were collected across the study area for geochemical analysis, and the GPS location of each sample was recorded (Table A1). From each sample, clean and unweathered portions of rocks were selected for crushing and milling which took place at the University of the Western Cape. The rock samples were crushed using a jaw crusher that produced rock chips which were subsequently milled into a fine pulp using a tungsten carbide mill. Between each crushing and milling run, the equipment was cleaned using quartz and sterilised using acetone in order to avoid cross contamination.

3.3. Analytical Methods

There were several analytical methods involved in studying the geochemical samples. These included transmitted light microscopy, Laser-Ablation Inductively Coupled Plasma Mass Spectrometry (LA-ICP-MS) and X-Ray Fluorescence (XRF). Petrographic analysis of thin sections was done at the University of the Western Cape (UWC) and the geochemical analyses of the unmineralised samples at the Central Analytical Facility (CAF) at the University of Stellenbosch. Stable isotope analyses of the samples were done at the Department of Geological Sciences at the University of Cape Town (UCT).

3.3.1. Optical Petrography

Polished thin sections of all the rock types and hydrothermal veins were prepared at the University of the Western Cape. The samples were analysed using a Leica optical transmitted light microscope in order to identify the different minerals present in the host rocks and the hydrothermal veins, their modal abundance in each rock type, and the textural characteristics

of minerals in the host rocks and the veins. The detailed study and analysis of the samples in thin section was undertaken for the purpose of classifying the rocks more accurately, thereby improving the understanding of their origin and the conditions under which they formed.

3.3.2. X-Ray Fluorescence (XRF)

Fused glass disks were prepared for the geochemical analysis of 49 samples by XRF. This required the preparation of a mixture of 1 g of rock with 10 g of trace element and rare earth element (REE) free flux (Li₂B₄O₇ = 66.67%; LiBO₂ = 32.83%; LiI = 0.50%) (Taylor et al., 2014). The compositions of whole-rock major elements were determined by means of XRF spectrometry on a PANalytical Axios Wavelength Dispersive spectrometer (Taylor et al., 2014). The spectrometer was covered with a rhodium tube and analysing crystals, including LIF200, LIF220, LIF420, PE and PX1 (Taylor et al., 2014). The instrument was also fitted with a gas-flow proportional counter, which makes use of a gas mixture of argon (90%) and methane (10%), and a scintillation detector (Taylor et al., 2014). The major elements on the fused glass disk were exposed to tube operating conditions at 50 Kv and 50 mA (Taylor et al., 2014). Theoretical alpha factors and measured line overlap factors were applied to the raw intensities measured with the SuperQ PANalytical software in order to correct matrix effects in the samples (Taylor et al., 2014). The following control standards were used in the calibration process for major element analyses: BE-N (Basalt Reference values), JB-1 (Basalt (depleted) Reference values), SY-3 (Syenite Reference values), NIM-S (Syenite Reference values), BHVO-1 (Basalt Reference values), ARF D34 (Reference values), JG-1 (Granodiorite Reference values), NIM-G (Granite Reference values), WITS-G (Granite Reference values), WITS-B (Basalt Reference values), DISKO-1 (Basalt Reference values).

3.3.3. Laser-Ablation Inductively Coupled Plasma Mass Spectrometry (LA-ICP-MS)

Fused glass discs were prepared for the geochemical analysis of 49 samples by LA-ICP-MS by making use of an automatic Claisse M4 Gas Fusion instrument using an ultrapure Claisse Flux (Li₂B₄O₇ = 66.67%; LiBO₂ = 32.83%; LiI = 0.50%) and a sample to flux ratio of 1:10 (Taylor et al., 2014). Trace element concentrations of the samples were determined using a Resonetics 193 nm Excimer laser either connected to an Agilent 7500ce ICP-MS or an Agilent 7700 ICP-MS (Taylor et al., 2014). The analytical conditions of the analyses are dependent on the type of ICP-MS used. The analyses either used a 173 µm (Agilent 7500ce) or 100 µm (Agilent 7700) spot size, and a frequency of 10 Hz. Laser ablation analyses was executed in He gas at a flow rate of either 0.30 L/min (Agilent 7500ce) or 0.35 L/min (Agilent 7700), and the He stream was mixed with argon before it was introduced into the ICP plasma (Taylor et al., 2014). For the samples analysed with the Agilent 7500ce ICP-MS it took 10 seconds for the laser to warm-up and 30 seconds for each spot analysis, whereas for the samples analysed with the Agilent 7700, it took 15 seconds for the laser to warm-up and 35 seconds for each spot analysis. After every 12 samples, the calibration standard was run, with a quality control standard run both at the beginning of the sequence and with the calibration standards throughout (Matsumura, 2014). The following certified reference standards were used in the quality control runs: BCR

or BHVO (both basaltic glass certified reference standards). A fusion control standard from certified basaltic reference material (BCR) was analysed at the start of each sequence in order to verify the effective ablation of fused material (Taylor et al., 2014). Finally, the data was processed by making use of the software package called *lolite v 3.34*. Limits of detection for the trace elements were recorded in Tables D3 to D5.

3.3.4. Radiogenic Sr- and Nd-isotope analysis

Four whole rock samples were selected for radiogenic Sr- and Nd-isotope analysis which took place in the Department of Geological Sciences at UCT. A Nu Instruments NuPlasma HR mass spectrometer was used to obtain the Sr- and Nd-isotopic data, which followed the chemical separation procedure described by Miková and Denková (2007) for each of the analyses. Sr isotopes in the four samples were analysed as 200 ppb 0.2% HNO₃ solutions using NIST SRM987 as a reference standard. ⁸⁷Sr/⁸⁶Sr data for each of the samples were normalised using a value of 0.710225. Finally, Rb interference and instrumental mass fractionation in the Sr-isotope data were corrected by making use of the exponential law and an ⁸⁷Sr/⁸⁶Sr value of 0.1194 (Fourie, 2010).

Nd isotopes were analysed as 50 ppb 2% HNO₃ solutions using a Nu Instruments DSN-100 desolvating nebuliser. The Nd-isotopic values for each of the samples were normalised using a value of 0.512115 (JNdi-1) after Tanaka et al. (2000). Finally, Sm and Ce interference and instrumental mass fractionation in the Nd-isotope data were corrected by making use of the exponential law and a ¹⁴⁶Nd/¹⁴⁴Nd value of 0.7219 (Fourie, 2010).

3.4. Stable isotopes

Oxygen and hydrogen isotope analyses were performed on pure quartz, tourmaline and calcite samples extracted from 8 different hydrothermal veins. The samples were prepared at UWC, where portions of hydrothermal veins were crushed in a jaw crusher. 5 g of crushed quartz (± pyrite), tourmaline (± pyrite) and calcite fragments, respectively, were hand-picked. The crushed samples were cleaned using deionised water and placed in a beaker. The sample were then mixed with 100 ml of 27.5% concentrated HNO₃ individually and placed in a shaker for 3 hours in order to dissolve the pyrite. Following this, each sample was washed with deionised water and placed in an oven to dry.

The samples were analysed at the Stable Isotope Lab at UCT in order to measure their oxygen, hydrogen and carbon isotopic ratios. Of the 8 samples submitted for stable isotope analyses, 5 samples were analysed for their O isotope ratio. The samples were prepared into a gaseous form and analysed using a Delta XP dual inlet Gas Source Mass Spectrometer in order to measure the δ¹⁸O, δD and δ¹³C isotopic ratios. By making use of a conventional silicate line, the samples of vein quartz were prepared for the analysis of oxygen. Approximately 10 mg of the sample of vein quartz was measured out and reacted with ClF₃. The O₂ that was liberated during the reaction was converted to CO₂ by making use of a hot platinized carbon rod. Following this, the oxygen isotope ratios were measured offline by making use of a Finnigan

Delta XP mass spectrometer in dual-inlet mode on CO₂ (conventional), and the results given in delta notation (δ), where $\delta^{18}\text{O} = (R_{\text{sample}}/R_{\text{standard}} - 1) \times 1000$, and R = the measured ¹⁸O/¹⁶O ratio. Along with each batch of samples, duplicate splits of the quartz standard (NBS28) were also run for the whole-rock data (whole-rock mill of quartz vein), which were then used to convert the raw data to the Standard Mean Ocean Water (SMOW) scale by making use of the $\delta^{18}\text{O}$ value of 9.64‰ for NBS28, as recommended by Coplen et al. (1983). A 2 σ error of 0.16‰ is inferred from the long-term variability of NBS28 (Harris et al., 2015).

Of the 8 samples submitted for stable isotope analyses, 2 samples were analysed for their C isotope ratio, both of which contained calcite. For the analysis of carbon from the samples, the samples were prepared by making use of a carbonate line for the extraction of CO₂ in carbonate-bearing samples using phosphoric acid. The carbonate samples were reacted with '103%' phosphoric acid overnight at a temperature of 50°C. Hence, the data is representative of the total carbonate (calcite + dolomite) present. In order to normalise the carbonate data to Pee Dee Belemnite (PDB) and SMOW, an internal standard was calibrated against NBS-19 ($\delta^{18}\text{O} = 28.64\text{‰}$, $\delta^{13}\text{C} = 1.95\text{‰}$). Following this, the carbon isotope ratios were measured offline by once again making use of a Finnigan Delta XP mass spectrometer in dual-inlet mode, and the results given in δ notation, where $\delta = (R_{\text{sample}}/R_{\text{standard}} - 1) \times 1000$, and R = the measured ¹³C/¹²C ratio.

Two of the 8 samples submitted for stable isotope analyses were analysed for their H isotope ratio. Approximately 1-2 g of the quartz vein samples were heated at temperatures exceeding 800°C, whereby H₂O and CO₂ were liberated through the decrepitation of the fluid inclusions. The quartz fragments were degassed at a temperature of 200°C for 2 hours, and subsequently at a temperature of 200°C in a vacuum for 30 minutes. The H₂O produced was trapped cryogenically and was then analysed for its hydrogen isotopes following the Zn reduction method, as recommended by Vennemann and O'Neil (1993). The D/H ratios were measured by making use of a Finnigan Delta XP mass spectrometer, and the results given in δ notation, normalized to the SMOW scale. Standardisation was done relative to two in-house water standards of largely different δD values (-7.4 and -131.4‰). Finally, these values were used to correct for scale compression.

3.5. Fluid Inclusion Studies

Fluid inclusions represent bubbles or pockets of fluids that have become trapped within a host crystal either during or after crystal growth from its parent hydrothermal fluid (Greyling, 2009). By analysing the relationship between individual fluid inclusions, it is possible to determine the relative timing of entrapment of the fluids. The primary purpose of studying fluid inclusions in the present study is to determine the minimum trapping conditions and the origin of the fluids by adopting several analytical procedures, such as fluid inclusion petrography, microthermometry and Raman microspectroscopy, amongst other techniques. The two former techniques were used in the analysis of fluid inclusions for this study.

3.5.1. Fluid Inclusion Petrography

Nine ~100 μm doubly-polished thick sections of quartz- and calcite-bearing hydrothermal veins were prepared at UWC for optical transmitted light microscopy. The fluid inclusions were studied petrographically in order to determine whether they are primary (isolated inclusions or inclusions found in trails) or secondary (inclusions found in trails or planes) or pseudosecondary (inclusions found along poorly defined planes) (Greyling, 2009). A low-magnification lens ($\times 6.4$) was used to identify suitable fluid inclusions, mostly those which were large enough to be analysed by microthermometry, as well as to determine the type of fluid inclusions and their distribution along the veins. Images of areas with suitable fluid inclusions were captured.

3.5.2. Microthermometry

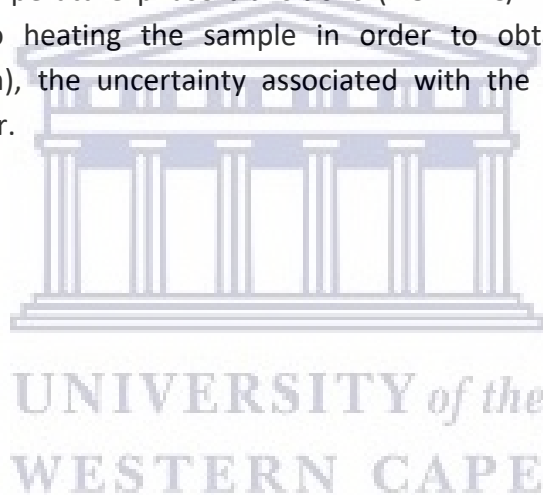
From the 9 doubly-polished thick sections, only 7 were analysed during microthermometry. These doubly-polished thick sections were prepared for microthermometry by breaking them into smaller samples that were able to fit into the circular chamber of the microscope. Fluid inclusion microthermometry was conducted at the University of Stellenbosch. A Linkam 600 heating-freezing stage attached to an Olympus BX50 transmitted light microscope was used. The cooling agent used for freezing runs is liquid nitrogen, which is capable of freezing runs to a temperature of -196°C . The smaller samples were viewed with a $\times 50$ high-powered magnification objective in order to achieve a magnified view of the fluid inclusions.

Analysis of the fluid inclusions involved classification based on their final homogenization temperature ($T_{\text{h(total)}}$) into either “L” (final homogenization to the liquid phase), or “V” (final homogenization to the vapour phase). The fluid inclusions analysed are aqueous, and therefore did not contain carbonic material. The conditions of the entrapment of the fluids were determined by interpreting the phase changes during microthermometry. The first step involved freezing the samples to -100°C at a rate of 15°C per minute, followed by the heating of the samples from -100°C to -35°C at a rate of 15°C per minute. The samples were then heated from -35°C to -28°C at a rate of 4°C per minute, and then further heated from -28°C to 1°C at a rate of 2°C per minute. The temperature of ice melting ($T_{\text{m(ice)}}$) of H_2O -rich fluid inclusions was recorded, and the temperature of the stage warmed to room temperature. The nitrogen gas tube was then removed, and the sample heated once again at a rate of 15°C per minute until the fluid inclusions homogenized. This temperature, referred to as the temperature of homogenization ($T_{\text{h(total)}}$), was recorded. For the H_2O -rich fluid inclusions, the salinities, densities and isochores were calculated using the Hokieflincs_H₂O-NaCl software package (Steele-MacInnis et al., 2012) using the measured $T_{\text{m(ice)}}$ and $T_{\text{h(total)}}$, according to the equations of state recommended by Bodnar (1993), Bodnar and Vitkyk (1994), Lecumberri-Sanchez et al. (2012) and Sterner et al. (1988).

Halite-bearing fluid inclusions (H_2O -NaCl-rich) homogenized by the disappearance of the halite phase (i.e. final homogenization to the liquid phase). When aqueous fluid inclusions had no halite crystals present within them, its salinity was determined by measuring $T_{\text{m(ice)}}$,

and the resulting temperature was always $<0^{\circ}\text{C}$. When aqueous fluid inclusions had halite crystals present within them, their salinity was determined by measuring the temperature at which halite dissolves ($T_{m(\text{halite})}$), and the resulting temperature was always high. Therefore, $T_{m(\text{halite})}$ was measured in order to determine the salinity of the hypersaline (halite-bearing) aqueous fluid inclusions. For all the aqueous fluid inclusions, the salinities, densities and pressures were calculated using the *AqSo_NaCl*[®] software package of Bakker (2018), and the isochores using the *Hokieflincs_H2O-NaCl* software package of Steele-MacInnis et al. (2012). These variables were determined using the measured $T_{m(\text{ice})}$ or $T_{m(\text{halite})}$, as well as $T_{h(\text{total})}$ values, according to the equations of state recommended by Bodnar (1993), Bodnar and Vitkyk (1994), Lecumberri-Sanchez et al. (2012) and Sterner et al. (1988).

The heating-freezing stage was calibrated by making use of synthetic inclusions. The uncertainties associated with the microthermometric measurements are $\pm 0.2^{\circ}\text{C}$ for low-temperature phase transitions, i.e. below 10°C , and $\pm 4^{\circ}\text{C}$ for homogenisation measurements when heating the sample at higher temperatures. Since a smaller incremental heating profile was used for the low-temperature phase transitions ($1.5 - 2^{\circ}\text{C}/\text{min}$ near expected phase transitions) compared to heating the sample in order to obtain its homogenisation temperature ($\sim 10^{\circ}\text{C}/\text{min}$), the uncertainty associated with the low-temperature phase transitions are also smaller.



Chapter 4: Lithological and Petrographic Relationships

4.1. Introduction

The rocks of the Yzerfontein Pluton form an ~2.50 – 2.60 x 0.05 – 0.28 km outcrop area along the shore at Yzerfontein. Eight different rock types were identified in the area, which includes a number of texturally and compositionally distinct mafic, intermediate and felsic rocks. These rock types include melanocratic gabbro, leucocratic gabbro, poikilitic monzogabbro, syenodiorite, monzonite, syenite, quartz-microsyenite, and monzogranite. The mafic rocks occur at Gabbro Point towards the northernmost end of the study area, and these rocks, as the name of the area implies, are gabbroic in composition (Fig. A1). At this location, the gabbroic outcrops are scattered and extend over a distance of ~107 m (from north to south). The remainder of the rock types are seen outcropping from the first sand beach NE of the Visitors Center and extends through the Yzerfontein Harbour area and further south along the shore through Starck, Grasbank and Draaibank as well as Kreefgat, Schaap Eiland and Freddie se Klip (Fig. A2 to A10).

4.2. Classification of host rock

The intermediate to mafic rocks studied have been classified primarily using the multicationic rock classification diagram of De La Roche et al. (1980) together with the total alkalis vs. silica (TAS) diagram proposed by Cox et al. (1979) for plutonic rocks. The nomenclature used to name the various rock types was based on their mineralogy in petrographic thin section. The felsic rocks of the Yzerfontein Pluton were plotted on the QAPF diagram of Streckeisen (1974) based on the petrographic volume percentages of minerals in the thin sections analysed. A total of 43 samples were selected for petrographic examination with the purpose of determining the major rock types, their mineralogical composition, textural characteristics and the nature and extent of alteration; this was done at an outcrop to mesoscale, and finally at a microscale.

4.3. Alteration of host rocks

There are at least five major types of alteration that were identified in the various rock types which will be described in detail. These include: uralitization, chloritization, sericitization, saussuritization and propylitic alteration. **Uralitization** is the process by which a pyroxene is replaced by an amphibole mineral; the pseudomorphing amphibole can form either a rim around the pyroxene, a single altered crystal, or an aggregate of fibrous amphibole minerals (Winter, 2010). **Chloritization** occurs when mafic or ferromagnesian minerals (pyroxenes, amphiboles or micas) undergo alteration to form chlorite (Winter, 2010; Pandit, 2014). **Sericitization** occurs due to the hydration and breakdown of feldspars to form a fine-grained white mica known as sericite; associated with the replacement of feldspar by sericite may be minor amounts of chlorite, quartz, and pyrite (Robb, 2005; Winter 2010). Plagioclase can also be altered to a fine-grained aggregate of minerals from the epidote group, with minor associated calcite and sericite; this process is called **Saussuritization**. **Propylitic alteration** is

defined as the process by which ferromagnesian minerals and feldspar become replaced by chlorite and epidote, with minor amounts of clinozoisite, zoisite, calcite and albite (Robb, 2005; Djouka-Fonkwé et al., 2012).

It is, however, difficult to constrain whether the formation of secondary minerals is a result of late magmatic reactions, such as deuteric alteration, or, alternatively, as a result of fluid-rock interaction (Hekinian, 1982). **Deuteric alteration** is a low to moderate temperature alteration whereby hydration of molten rock during the final stages of crystallisation causes the primary minerals to experience textural and mineralogical changes (Winter, 2010; Hekinian, 1982).

4.4. Mafic Rocks

The gabbroic rocks occur at Gabbro Point towards the northernmost part of the study area (Fig. A1), with smaller outcrops occurring in contact with rocks from the intermediate part of the Yzerfontein Pluton (Fig. A3). Texturally, the gabbroic rocks are medium- to coarse-grained and compositionally they are present as leucocratic gabbros, melanocratic gabbros and monzogabbros at different localities.

4.4.1. Leucocratic Gabbro

Outcrop to mesoscopic scale: Outcrops of leucocratic gabbro are located at the central to northernmost parts of Gabbro Point (Fig. A1). Outcrops vary in size from ~1.0 – 5.5 m (outcrops measured from north to south). They vary in grain size from medium- to coarse-grained. The leucocratic appearance of these outcrops is imparted by the high plagioclase feldspar content within the rock, which ranges from ~55 – 65 vol.% (Figs. 4.1a,b).

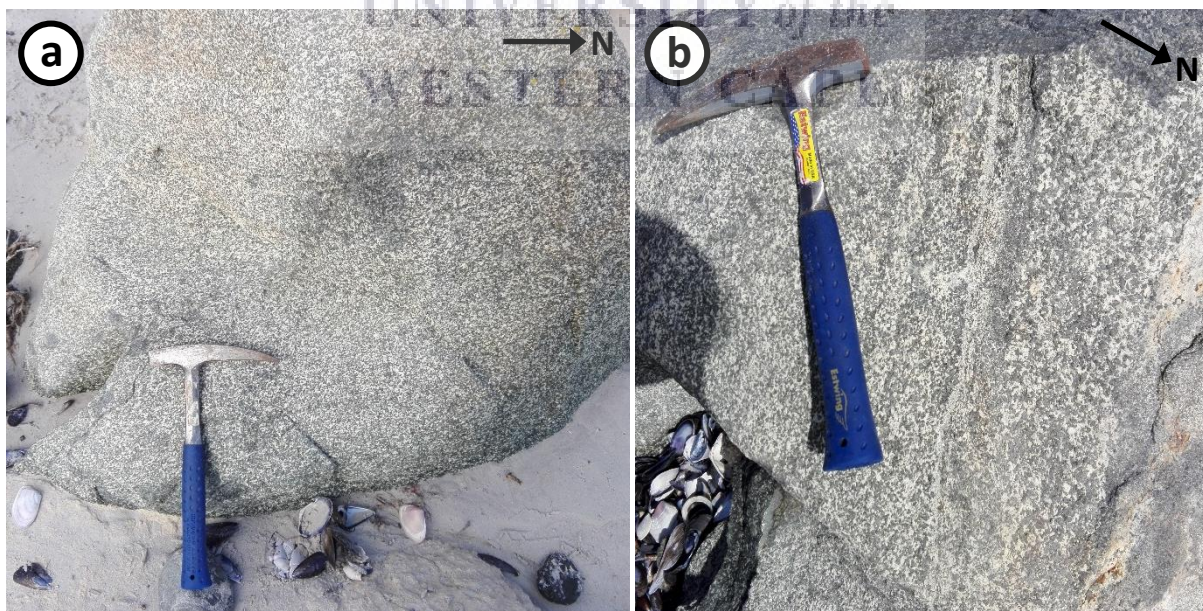


Figure 4.1: Outcrops of the leucocratic gabbro towards the northernmost part of Gabbro Point. In (b), the sub-vertical magmatic layering in the leucocratic gabbro is apparent. Scale: Hammer with length = 33 cm.

Minerals visible in hand specimen mainly include elongated plagioclase feldspar and dark green amphiboles, with smaller amounts of biotite flakes and minor preserved augite. Sericite is weakly visible in hand specimen. Sub-vertical magmatic layering is well developed in some localities and strikes approximately NE-SW (Fig. 4.1b). These layers vary between lighter and darker layers owing to the varying abundances of plagioclase, augite and amphiboles. Lighter bands are rich in plagioclase, and vary in different localities from ~55 – 80 vol.% plagioclase. Darker bands have a higher content of mafic minerals, such as augite and hornblende, and can be classified as bands or layers of melanocratic gabbro. The actual thickness of the bands varies in different localities, ranging from 3 – 24 cm. Contacts between these bands are commonly sharp and can be traced along certain outcrops due to the abrupt change from a lighter, more felsic-dominated band to a darker, more mafic band, and vice versa. In some cases, such as in Fig. 4.1b, the contacts between bands (ranging from 0.5 – 1.0 cm in thickness) are defined by long, narrow accumulations of either felsic or mafic minerals.

Petrography: In terms of the primary minerals, the leucocratic gabbro comprises mainly plagioclase feldspar (~24%), biotite (~7%), augite (~2%), magnetite (~2%), ilmenite (~1%), and minor amounts of apatite (<1%) (Table B1). Secondary minerals formed due to alteration include sericite (~36%), tremolite-actinolite (~20%), hornblende (~6%), calcite (~1%), and minor amounts of chlorite (<1%). Plagioclase has become altered to very fine-grained micaceous aggregates of sericite. The sericitization has locally partly obliterated the original lamellar twinning displayed by plagioclase (Fig. 4.2a). Aside from lamellar twinning, unaltered plagioclase locally displays Carlsbad twinning or a complex twinning pattern.

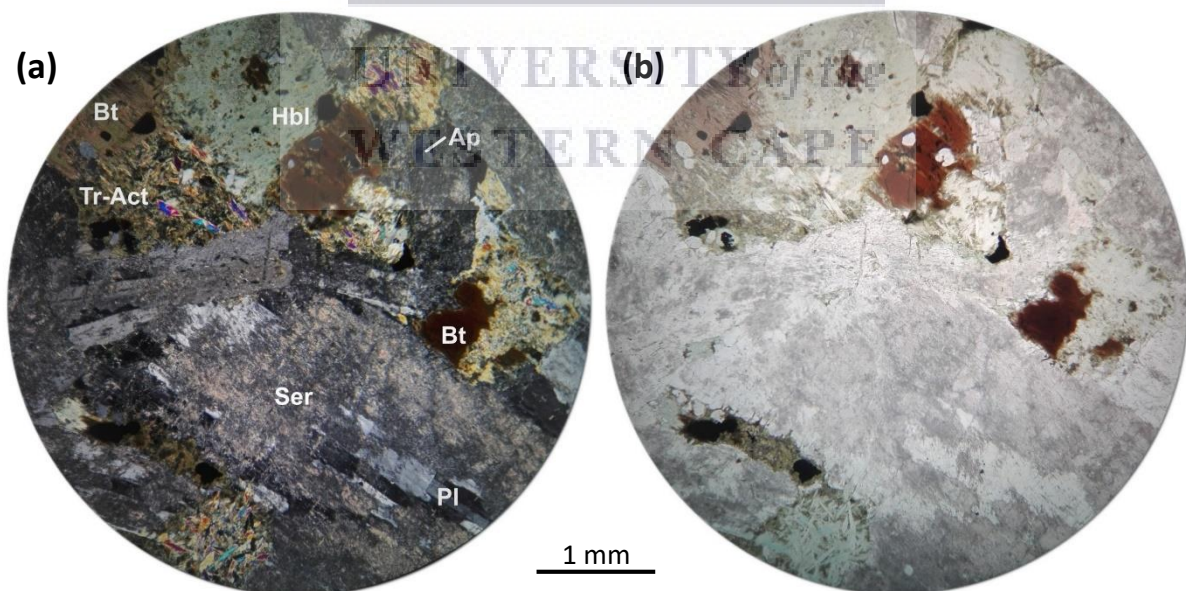


Figure 4.2: Thin section photomicrographs of the leucocratic gabbro at YZN21 displaying the major minerals present in the rock under (a) cross polarized light (XPL) and (b) plane polarized light (PPL). Ap = Apatite, Bt = Biotite, Hbl = Hornblende, Pl = Plagioclase, Ser = Sericite, Tr-Act = Tremolite-Actinolite.

Augite has become almost completely pseudomorphed by hornblende (Figs. 4.2a, b) and minor amounts of calcite (Figs. B6a, b). Hornblende, has in turn, become replaced by

tremolite-actinolite. Tremolite-actinolite has a pale yellow to pale green pleochroism, whereas hornblende has a stronger green to greenish-blue pleochroism. Secondary tremolite-actinolite grains commonly overgrow biotite flakes (Figs. 4.2a, b) and, locally, where it has replaced hornblende, the needles have grown sub-parallel to the growth direction of the augite grains. Anhedral biotite has become weakly pseudomorphed by chlorite. Magnetite and ilmenite is commonly seen forming along the cleavage planes of biotite and altered pyroxene grains, which is due to their breakdown and the release of iron and titanium from their mineral lattice. Closely spaced magnetite octahedra are commonly associated with the precipitation of very fine-grained and fibrous hornblende, which has a dark brownish-green pleochroism and forms a halo-like feature around the magnetite. Apatite prisms are relatively abundant and occur poikilitically in biotite. Overall, the degree of alteration is fairly extensive. However, most of the grain boundaries of the altered pyroxenes are more or less visible showing that, despite the extensive alteration, the original minerals and grain structures are preserved.

4.4.2. Melanocratic Gabbro

Outcrop to mesoscopic scale: Outcrops of melanocratic gabbro are scattered along Gabbro Point (Fig. A1), some of which are obscured by large boulders. Some outcrops of melanocratic gabbro also occur NW of the Visitors Center (Fig. A3). Overall, outcrops vary in size from ~0.5 – 25.0 m (measured from north to south) and are medium- to coarse-grained. The melanocratic appearance of the gabbro is due to the large vol. % of mafic minerals, most notably pyroxenes, amphiboles and biotite. The major minerals that can be identified in hand specimen include augite, orthopyroxene, tremolite-actinolite and hornblende. As a result of the large grain sizes of the minerals in certain places, it is easy to see certain features in individual minerals. Upon close inspection of certain outcrops, hornblende can be seen to form dark green pseudomorphic rims around augite and orthopyroxene. Other minerals visible in hand specimen include plagioclase feldspar, and smaller amounts of biotite, chlorite, epidote, and magnetite.

Magmatic layering in the melanocratic gabbro is sub-vertical and strikes NE-SW (Fig. 4.3a). It comprises alternating or rhythmic bands of leucocratic and melanocratic gabbro. As a result of abrupt changes between leucocratic and melanocratic bands, the bands form sharp contacts with each other. Mafic enclaves comprising pyroxenes and amphiboles, and infrequently, felsic enclaves comprising mainly of plagioclase are enclosed within the melanocratic gabbro (Figs. 4.3a, b, B1). In some cases, the mafic enclaves are elongated in the direction of magmatic layering (Fig. 4.3a), and, in some cases, cross-cuts the melanocratic gabbro (Fig. B1). The plagioclase-rich patches commonly cross-cut the melanocratic gabbro forming sharp contacts, and in some parts are either partly or completely epidotized, particularly those cross-cutting the melanocratic gabbro at the southernmost outcrops. These

mafic and felsic enclaves have varying sizes, with lengths varying from 8 – 50 cm, and widths from 1.2 – 15.0 cm.

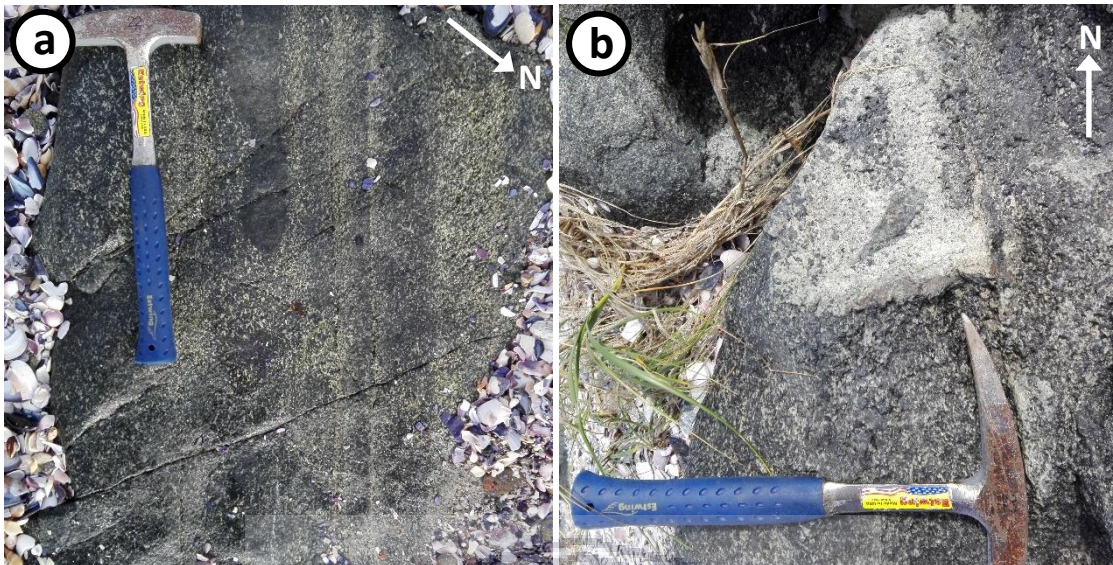


Figure 4.3: Outcrops of melanocratic gabbro occurring at Gabbro Point displaying (a) E-W oriented magmatic layering, as well as a mafic enclave elongate in the direction of magmatic layering, and (b) felsic enclave cross-cutting the melanocratic gabbro. Scale: Hammer with length = 33 cm.

Petrography: The melanocratic gabbro shows varying degrees of alteration at different localities, and therefore the modal abundances of some minerals have been given as a range. Primary minerals in this rock include plagioclase feldspar (~10 – 16%), biotite (~6%), magnetite (~2%), and minor amounts of ilmenite (<1%) and apatite (<1%) (Table B2). Some samples, such as YZN20, also contain additional primary augite (~15%) and orthopyroxene (~9%), and therefore have a lower abundance of other minerals, particularly some of the secondary minerals. Secondary minerals include tremolite-actinolite (~20 – 27%), sericite (~18 – 24%), hornblende (~15 – 20%), chlorite (~3%), calcite (~1%), and minor amounts of epidote (<1%). Two samples of the melanocratic gabbro are shown in Fig. 4.4a and b in order to demonstrate the differences in the extent of alteration in these outcrops. It is important to note that even though YZN20 plots as an ultramafic rock on the R_1 - R_2 multicationic discrimination diagram of De La Roche et al. (1980) (Fig. 6.1b), the petrography and field observations suggest that this rock is a melanocratic gabbro.

Alteration of pyroxenes to hornblende and hornblende to tremolite-actinolite vary in melanocratic gabbro at different locations as shown by their varying modal abundances. On the one hand, YZN20 shows moderate alteration of augite and orthopyroxene to hornblende, and from hornblende to tremolite-actinolite (Fig. 4.4a). YZN95, on the other hand, shows complete alteration from augite and orthopyroxene to hornblende, and moderate alteration of hornblende to tremolite-actinolite (Fig. 4.4b). Hornblende is locally associated with minor secondary calcite and trace amounts of epidote. It commonly has subhedral to euhedral grains and preserves the original simple twinning of the primary augite grains. In YZN20,

hornblende commonly forms pseudomorphic rims around the pyroxenes and replaces the grains from the margins inward, exploiting cleavage planes (Fig. 4.4a). Tremolite-actinolite is present as aggregates of needle-like grains which commonly have sharp terminations. Locally, in YZN20, magnetite and ilmenite are seen forming along the cleavage planes of pyriboles (pyroxenes and amphiboles).

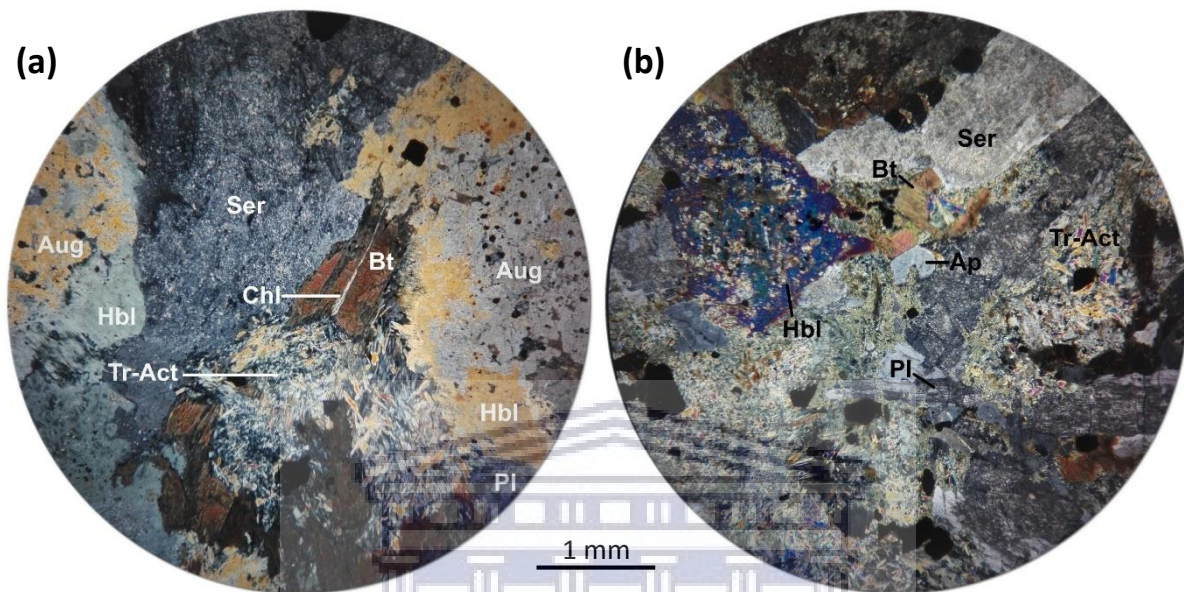


Figure 4.4: Thin section photomicrographs of the melanocratic gabbro in XPL displaying the major primary and secondary minerals present in the rock at (a) YZN20 and (b) YZN95. Ap = Apatite, Aug = Augite, Bt = Biotite, Chl = Chlorite, Hbl = Hornblende, Pl = Plagioclase, Ser = Sericite, Tr-Act = Tremolite-Actinolite.

More than half of the vol. % of plagioclase has become replaced by sericite in YZN20 and YZN95. This type of alteration is a very fine-grained and micaceous type of alteration which gives the minerals a cloudy appearance in thin section. Plagioclase commonly displays lamellar twinning, and also locally shows complex twinning patterns. Biotite flakes are commonly embayed and overgrown by fine-grained aggregates of acicular tremolite-actinolite (Figs. B7a, b). Chloritization of biotite is weak and inhomogeneous and has locally resulted in the precipitation of shapeless ilmenite, as the titanium in biotite cannot be accommodated by chlorite, and therefore precipitates as ilmenite (Whalen and Chappell, 1988). Tiny euhedral apatite prisms are abundant and locally have relatively large sizes of ~1.0 mm.

4.4.3. Poikilitic Monzogabbro

Outcrop to mesoscopic scale: Outcrops of the poikilitic monzogabbro are located north of the Visitors Center (Fig. A3). The outcrops extend ~30 – 35 m across (measured in a NE-SW direction). It is a medium- to coarse-grained variety of gabbro that has a higher plagioclase content, and additionally contains orthoclase which occurs as large poikilitic insets, giving the poikilitic monzogabbro a mottled appearance. The poikilitic monzogabbro forms a gradational contact with the adjacent syenodiorite. The major minerals visible in the poikilitic

monzogabbro include plagioclase, orthoclase, pyroxene and smaller quantities of amphiboles including hornblende and tremolite-actinolite, with minor amounts of epidote and chlorite. Large poikilitic orthoclase crystals have sizes ranging from 1.0 – 4.0 cm. They have various shapes ranging from rounded to elongate to irregular, and are riddled with inclusions of plagioclase, pyroxene, and smaller amounts of biotite and magnetite.

The monzogabbro encloses fine-grained melanocratic enclaves which are predominantly comprised of pyroxenes and amphiboles, with smaller amounts of plagioclase. Based on their mineralogy and grain size, these are micromonzogabbro enclaves. The micromonzogabbro enclaves form sharp contacts with the host monzogabbro, and have various sizes from 6.5 – 15.7 cm x 1.6 – 3.5 cm (Fig. 4.5a). They also occur as large patches of multiple, irregularly shaped enclaves intermixed with the host monzogabbro, and in some places show segregation of felsic material from more mafic material (Fig. 4.5b). These patches have sizes from 0.65 – 0.74 m x 0.28 – 0.58 m.

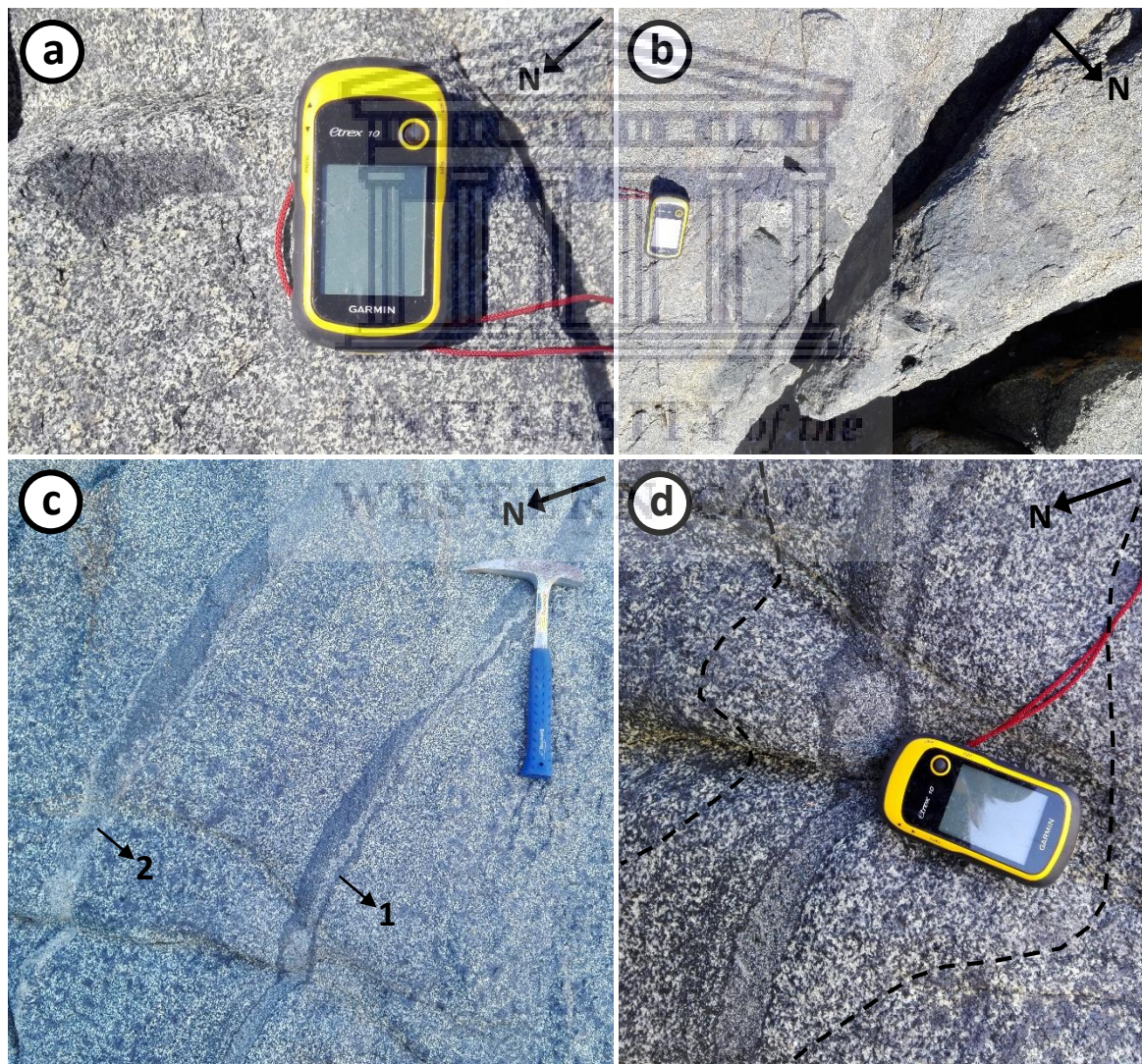


Figure 4.5: Outcrops of the poikilitic monzogabbro displaying various features. (a) & (b) Micromonzogabbro enclaves with irregular shapes. (c) Alternating mafic and felsic band types traversing across the poikilitic monzogabbro, and (d) enlargement of band type 1 in (c) showing gradation from monzogabbro to mottled monzogabbro on either side of band type 1. Scale: GPS with length = 10 cm and width = 5.2 cm; Hammer with length = 33 cm.

Magmatic layering is well-developed in certain localities and strikes approximately NW-SE. Long, linear bands of alternating felsic and mafic minerals also occur in the monzogabbro (Figs. 4.5c, d). However, the lengths of these bands were not measured as they either extend into the inaccessible wave-cut platform or they are obscured by large boulders. These bands either have margins defined by mafic minerals and a central band defined by felsic minerals (band type 1), or vice versa (band type 2). Both band types form sharp contacts with the adjacent monzogabbro. However, in the case of band type 1, a gradational contact occurs as the monzogabbro directly on either side of the mafic layers has no large orthoclase insets (Figs. 4.5c, d). This occurrence is traced for 5.5 – 9.5 cm on either side of the mafic layers in band type 1 before the monzogabbro grades into a poikilitic monzogabbro.

The poikilitic monzogabbro is cross-cut by fine-grained leucocratic dykes which have various compositions ranging from quartz-microsyenite (Fig. 4.6a) to monzogranite (Figs. 4.6b, B2a, b), depending on the quartz and feldspar content. The dykes trend in a NNW-SSE to NW-SE direction, have a low mafic mineral content and form sharp contacts with the poikilitic monzogabbro, commonly enclosing patches thereof (Fig. 4.6b). However, the poikilitic monzogabbro adjacent to the dykes infrequently displays an increase in grain size with increasing distance away from the dyke (Figs. B2a, b). The dykes have various sizes, ranging in width from a few millimetres up to 0.87 m in thickness in certain localities, with lengths ranging from 1 m to >15 m. The dykes are commonly associated with epidote, tourmaline and locally chlorite (Figs. 4.6a, B2a). In some localities in the poikilitic monzogabbro, a compositional variation is seen between different phases of the Yzerfontein Pluton marked by variations in grain size, mineralogy and texture. The contact between the various phases are sharp, with some portions being felsic and rich in plagioclase, others being more mafic and rich in amphiboles, pyroxenes and chlorite, and lastly, some phases being more intermediate between felsic and mafic (Fig. B3).

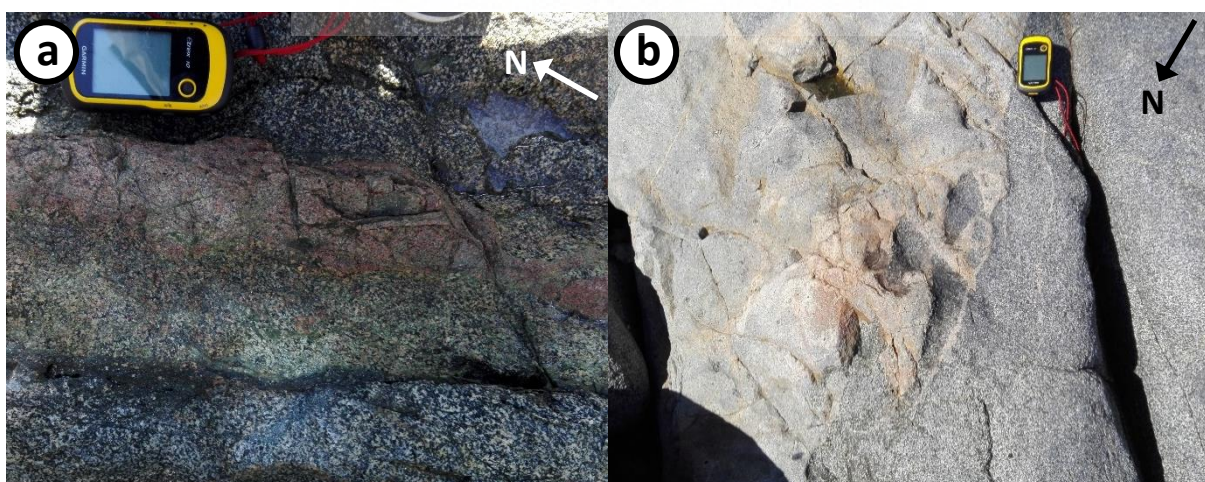


Figure 4.6: Felsic dykes cross-cutting the poikilitic monzogabbro. (a) Quartz-syenite dyke associated with epidote alteration; size of dyke: length = 15 – 16 m and width = 7.5 – 12.0 cm (b) Monzogranite dyke enclosing portions of the surrounding monzogabbro; size of dyke: length = 37.4 – 37.5 m and width 0.40 – 0.87 m. Scale: GPS with length = 10 cm and width = 5.2 cm.

Petrography: The primary minerals in the poikilitic monzogabbro include mainly plagioclase (~25%), orthoclase (~16%), orthopyroxene (~13%), augite (~8%) and biotite (~6%), with smaller amounts of magnetite (~3%), and minor amounts of ilmenite (<1%), interstitial quartz (<1%) and apatite (<1%) (Table B3). Secondary minerals include sericite (~15%), tremolite-actinolite (~10%), hornblende (~4%) and minor amounts of epidote (<1%). Plagioclase occurs as subhedral to anhedral tabular grains which commonly display lamellar twinning, and locally tapered- or multiple twinning. Both plagioclase and orthoclase feldspar have been affected by weak sericitization, which is commonly accompanied by tiny epidote granules (Fig. 4.7a). Orthoclase is subhedral to anhedral. Large orthoclase grains commonly poikilitically include twinned plagioclase laths, and locally also twinned and untwinned orthopyroxene, biotite flakes, magnetite and aggregates of tremolite-actinolite. Locally, orthoclase-microperthite is well developed.

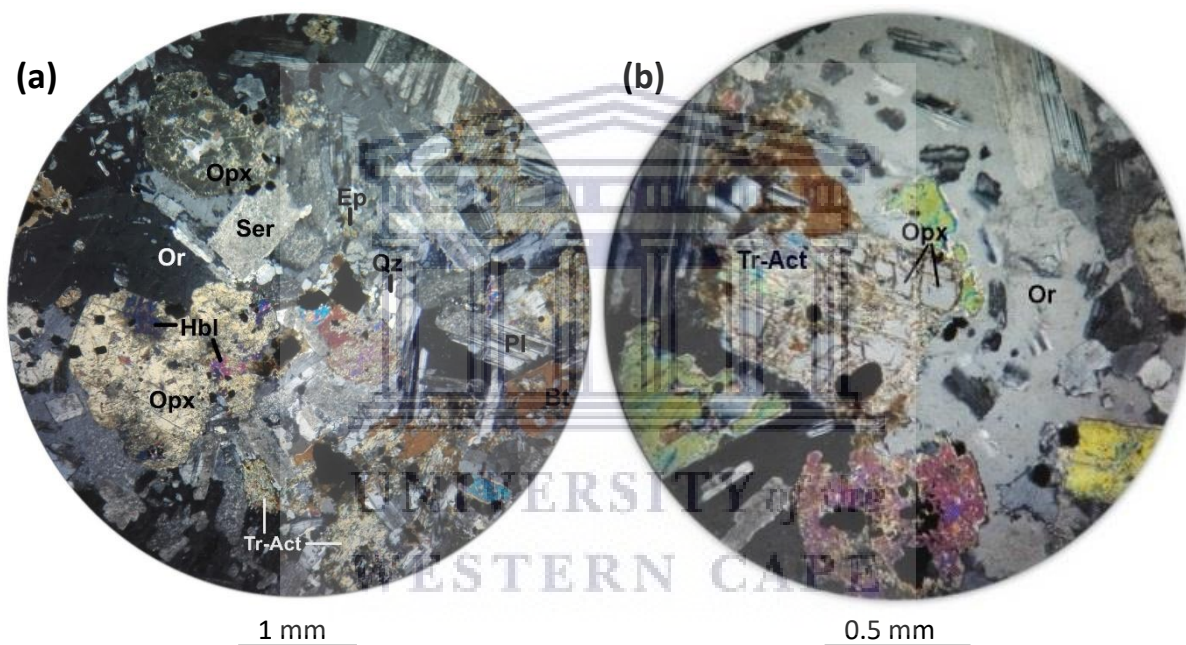


Figure 4.7: Thin section photomicrographs of the poikilitic monzogabbro at YZN75a displaying the major primary and secondary minerals present in the rock under XPL. In (b), the replacement of orthopyroxene by tremolite-actinolite occurs most notably along the cleavages of orthopyroxene. Bt = Biotite, Ep = Epidote, Hbl = Hornblende, Opx = Orthopyroxene, Or = Orthoclase, Pl = Plagioclase, Qz = Quartz, Ser = Sericite, Tr-Act = Tremolite-Actinolite.

Orthopyroxene is subhedral to anhedral and locally encloses small inclusions of quartz. Magnetite octahedra and platy ilmenite is commonly seen forming along the cleavage planes of orthopyroxene and augite due to the breakdown of the host pyroxene grains. Uralitization of pyroxenes is relatively weak, inhomogeneous and patchy, and involves the alteration of pyroxenes to hornblende, and hornblende to tremolite-actinolite. However, in YZN75a, orthopyroxene also uncommonly displays alteration directly to tremolite-actinolite (Fig. 4.7b). In this case, tremolite-actinolite displays a mesh-like texture and it most notably exploits orthopyroxene along the cleavage planes, forming very fine-grained fibrous needles (<0.1 mm). Augite is subhedral to anhedral and commonly displays simple twinning. It

commonly contains inclusions of biotite flakes, apatite prisms, and, locally, plagioclase. Biotite is anhedral and commonly contains inclusions of plagioclase. In some places, it is embayed and overgrown by adjacent augite or plagioclase grains.

4.5. Intermediate Rocks

The intermediate rocks of the Yzerfontein Pluton include syenodiorite, monzonite and syenite, with these rocks occurring at Yzerfontein Harbour, Yzerfontein Point and Schaap Eiland (Figs. A2 to A10). The intermediate rocks are fine- to medium-grained and show varying degrees of alteration, most notably in thin section. The intermediate rocks show very similar features both in outcrops and in thin section, with the syenodiorite and monzonite being nearly indistinguishable on an outcrop to mesoscopic scale. For this reason, field descriptions for the syenodiorite and monzonite are grouped together and discussed concurrently.

4.5.1. Syenodiorite and Monzonite

Outcrop to mesoscopic scale: The syenodiorite and monzonite are the most abundant rock types in the area, covering a large extent of the intermediate part of the Yzerfontein Pluton. The largest outcrop of syenodiorite is found NE of the Visitors Center, extending over a distance of ~160 – 175 m (measured in a NE to SW direction) (Figs. A2 to A3). The largest outcrop of monzonite occurs at Schaap Eiland, extending over an area of ~350 x 330 m (Figs. A8 to A10). Alteration is prevalent in these rocks as they were affected by all the main hydrothermal veining and alteration events. Although prevalent, alteration varies in different localities. It is incipient to patchy in certain localities, particularly in outcrops directly north, west and south of the Visitors Center. The extent of alteration changes towards the Harbour area, and around Yzerfontein Point to Schaap Eiland, with the degree of alteration becoming relatively moderate to strong in certain outcrops.

The mineralogy of the syenodiorite and monzonite is quite variable across the study area owing to mineralogical changes caused by alteration. Where hydrothermal veining is less prevalent (outcrops close to the Visitors Center), mineralogically the outcrops reflect compositions that are weakly altered by deuteric alteration, and have compositions closest to the original composition of the rocks. These outcrops have a high abundance of primary minerals such as orthoclase, plagioclase, augite and orthopyroxene. In localities where hydrothermal veining is more pronounced, such as in the Yzerfontein Harbour, and at various localities along Yzerfontein Point, the primary minerals have become weakly to moderately altered not only due to deuteric alteration, but also as a result of alteration related to hydrothermal veining. Secondary minerals identified in the syenodiorite and monzonite include hornblende, chlorite, minor amounts of epidote, and locally minor amounts of calcite. On an outcrop scale, mineralogical differences between the syenodiorite and monzonite are sometimes difficult to distinguish, and it is only in some localities where this difference becomes apparent, particularly in the Harbour area (Figs. A3, A4) and at Duiwenes, Deurspring and Grasbank (Figs. A5, A6). In these weakly altered outcrops, the syenodiorite shows a slightly higher abundance of orthoclase, pyroxenes and chlorite than the monzonite.

The syenodiorite and monzonite are host to micromonzogabbro, micromonzodiorite and micromonzonite enclaves, with variable lengths ranging from 0.4 cm – 0.76 m and widths ranging from 0.6 cm – 0.65 m. These melanocratic enclaves either occur abundantly within a small distance to form zones of enclaves (Figs. 4.8a, b, B4), or individually within the outcrop (Fig. 4.8c), and usually form sharp contacts with the adjacent syenodiorite or monzonite. The enclaves are predominantly comprised of amphiboles and pyroxenes, as well as minor amounts chlorite, orthoclase, quartz and magnetite. The enclaves have various shapes, including rounded-, sub-rounded-, ellipsoidal-, elongate- and irregular shapes.

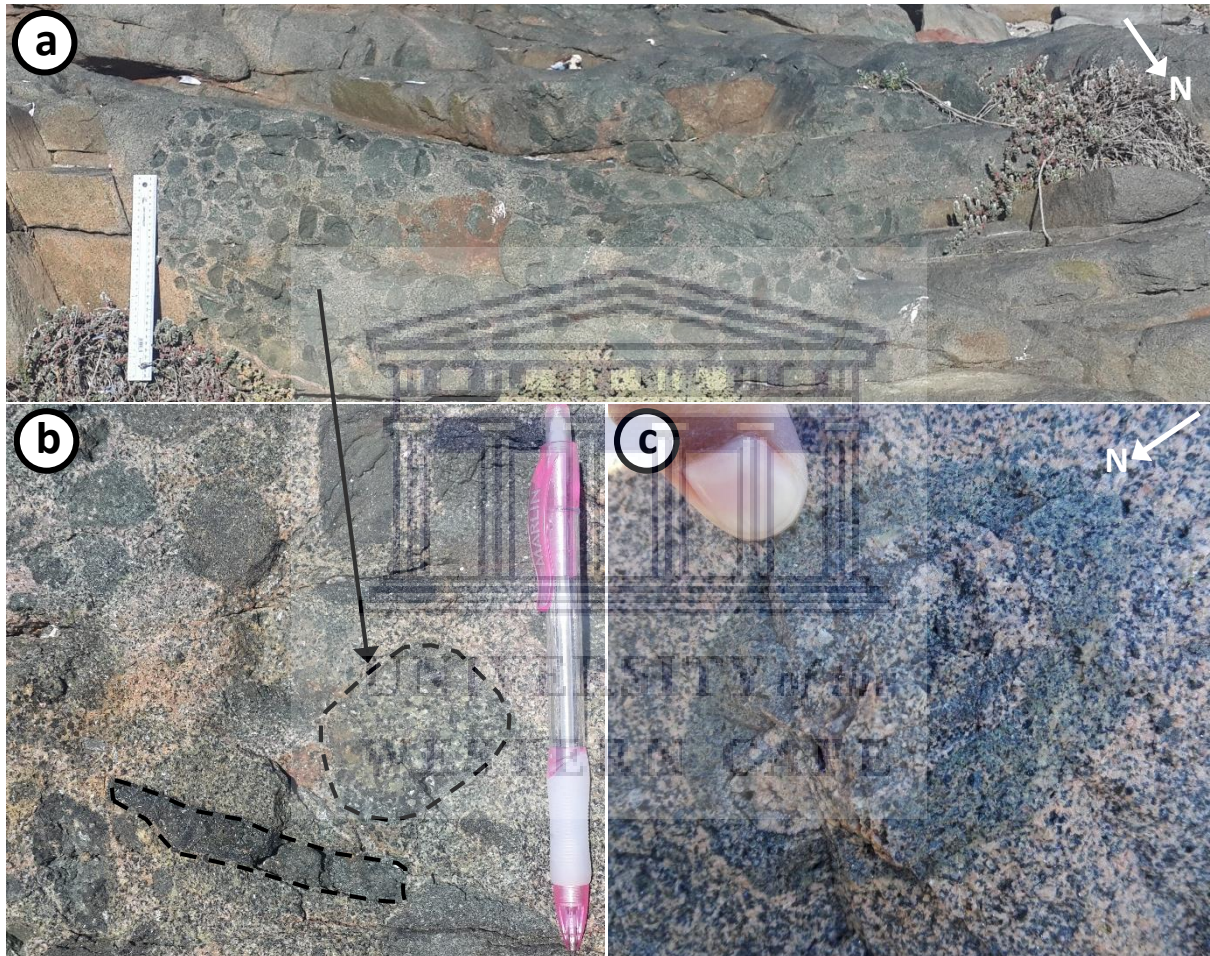


Figure 4.8: Melanocratic enclaves hosted in the monzonite and syenodiorite in the study area. (a) Zone of enclaves hosted by the monzonite at Schaap Eiland. (b) Enlargement of an area in (a) showing the different textures, shapes and compositions of the enclaves; fine-grained, elongate shaped enclave has a monzogabbroic composition, and coarser grained, sub-rounded enclave has a monzonitic composition. (c) Micromonzodiorite enclave hosted by the syenodiorite at Hoëbank, enclosing a portion of the host rock. Scale: Pencil with length = 14.5 cm; Ruler with length = 30 cm; Thumb with width = 1.5 cm.

Fine-grained quartz-microsyenite and monzogranite dykes form sharp contacts with the syenodiorite and monzonite across the study area (Figs. 4.9a to c, B5). They are predominantly comprised of K-feldspar, plagioclase and quartz, with minor amounts of mafic minerals. The dykes are commonly associated with tourmaline, locally chlorite and epidote, and uncommonly minor jasper (Fig. B5). They have varying sizes, with lengths ranging from 6.0 – 46.0 m and widths ranging from 0.02 – 27.0 m. Intermittently, the dykes enclose portions of

fine- to medium-grained monzonite and very fine-grained melanocratic enclaves that have rounded, ellipsoidal and irregular shapes, and share both sharp and diffuse boundaries, particularly with the quartz-microsyenite (Fig. 4.9c). These enclosed portions of rock have various sizes, with lengths ranging from 1.0 – 38.5 cm and widths ranging from 0.8 – 24.5 cm. Uncommonly, the syenodiorite also contain irregular “pockets” of fine- to coarse-grained monzogranite (Fig. 4.9b).

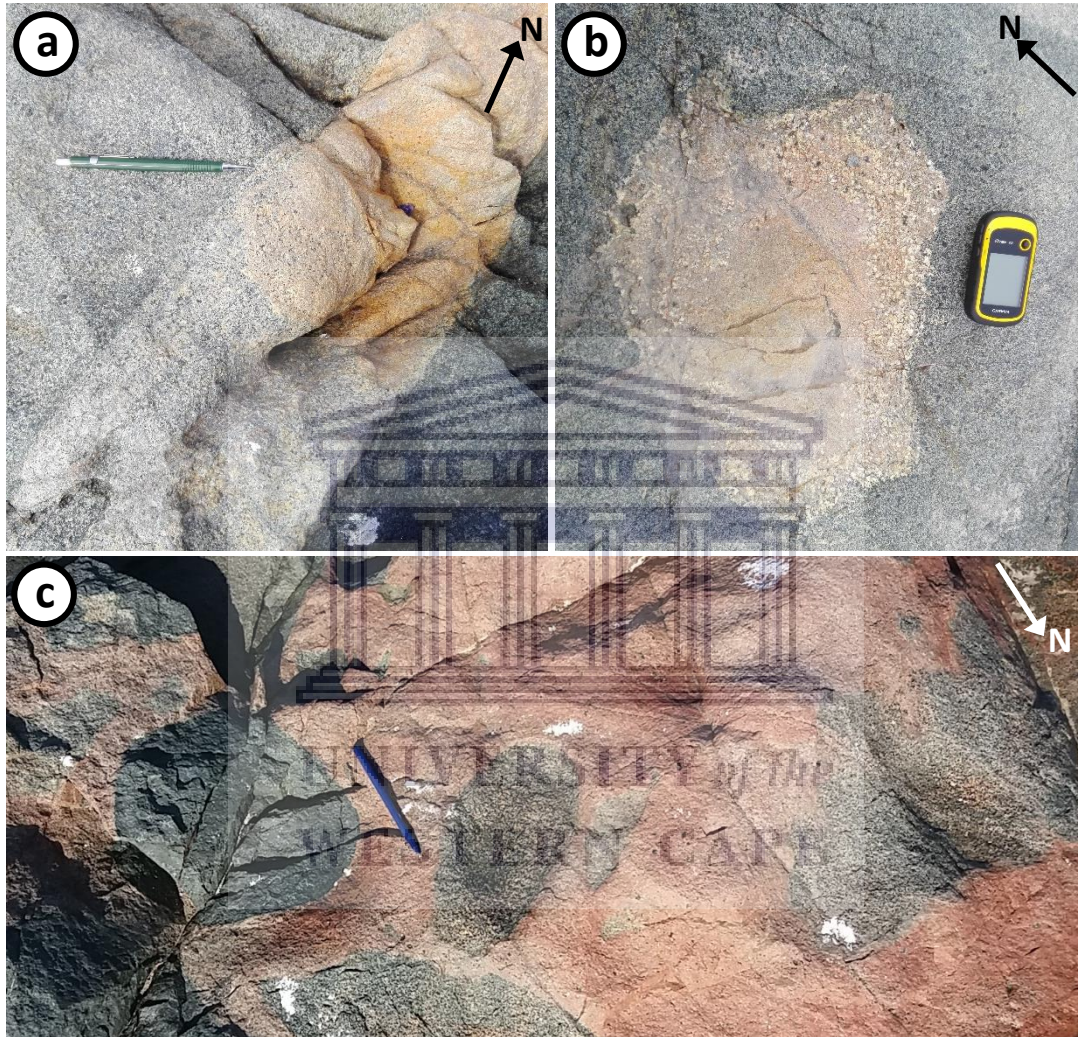


Figure 4.9: Monzogranite and quartz-microsyenite cross-cutting the syenodiorite and monzonite in different localities. (a) Monzogranite dyke showing compositional variation from north to south; size of dyke: length = 22.5 – 22.6 m and width = 0.2 – 0.24 m. (b) Monzogranite “pocket” comprising a fine-grained core of K-feldspar, plagioclase and quartz enclosed by a thick, irregular rim of large K-feldspar phenocrysts; size of monzogranite: length = 0.34 – 0.35 m and width = 0.18 – 0.28 m. (c) Cropped portion of a large, irregular body of quartz-microsyenite at Schaap Eiland enclosing portions of the monzonite and fine-grained melanocratic enclaves; size of dyke: length = 8.5 – 9.0 m and width = 5.5 – 6.2 m. Scale: GPS with length = 10 cm and width = 5.2 cm; Pen with length = 14.5 cm; Pencil with length = 14.4 cm.

Quartz-microsyenite and monzogranite dykes are oriented in various directions between E-W and NNE-SSW in the syenodiorite NE of the Visitors Center and along the Yzerfontein Harbour frontage. Dykes cross-cutting the syenodiorite south of Yzerfontein Point are not as abundant, and are oriented roughly WNW-ESE. The orientation of quartz-microsyenite and

monzogranite dykes in the monzonite across the study area varies significantly. In the monzonitic outcrops in the Yzerfontein Harbour and along Yzerfontein Point, the dykes are oriented roughly NNW-SSE to NW-SE. At Schaap Eiland, dykes are oriented in various directions between E-W and N-S (western parts of Schaap Eiland), to WNW-ESE and NW-SE (Freddie se Klip).

Finally, magmatic layering is only locally apparent in certain outcrops of syenodiorite and monzonite. The orientation of magmatic layering was measured and recorded in the syenodiorite NE and north of the Visitors Center and at Hoëbank, as well as in the monzonite at Schaap Eiland. In outcrops of syenodiorite NE of the Visitors Center, magmatic layering is dominantly striking in a NE-SW to ENE-WSW direction. At Hoëbank, the orientation of magmatic layering in the syenodiorite changes, striking in a NW-SE direction. The orientation of magmatic layering changes in the monzonite at Schaap Eiland, where it strikes in different directions between NNE-SSW and ENE-WSW.

Petrography of the Syenodiorite

As a result of significantly varying degrees of alteration, the syenodiorite displays slightly varying mineral constituents and abundances in thin sections from different localities. Petrographic analysis of the syenodiorite shows that it has been weakly to moderately altered. The primary minerals in the weakly altered syenodiorite include orthoclase (~32%), plagioclase (~28%), augite (~10 – 12%) and orthopyroxene (~4%), with smaller amounts of magnetite (~2%), biotite (~0 – 2%), and quartz (~1%), and minor amounts of ilmenite (<1%) and apatite (<1%) (Table B4). Secondary minerals include chlorite (~7 – 9%), sericite (~5%) and tremolite-actinolite (~5%), with smaller amounts of hornblende (~2%) and epidote (~1%).

Orthoclase is anhedral and commonly displays a microperthitic texture showing exsolution of albite. In some parts it displays Carlsbad twinning and commonly has a poikilitic texture, containing tiny grains of plagioclase, chloritized grains, as well as opaque minerals (Figs. 4.10a, b). In some parts, orthoclase displays a microgranophyric texture (Fig. B8), however, these intergrowths with quartz are irregular across thin sections, with most grains displaying sections that are relatively quartz-free. Orthoclase and plagioclase have become weakly altered to sericite. Plagioclase has subhedral to euhedral elongate shapes, and, aside from lamellar twinning, also locally displays tapered twinning and less commonly complex twinning. In some sections, such as YZN23 and YZN52, epidote is found weakly pseudomorphing plagioclase. Augite and orthopyroxene have become weakly altered to hornblende, which, in turn, is being replaced by tremolite-actinolite. Locally, augite grains have embayments containing tiny plagioclase grains, and commonly poikilitically include tiny sub-rounded quartz grains. Augite displays simple twinning and is commonly seen broken down to form Fe-oxides such as magnetite and ilmenite (Figs. 4.10a, b). Biotite has become almost completely altered by chlorite, and, in some thin sections, it is completely absent. In the latter case, either the augite or chlorite content is slightly higher, such as in YZN52 and YZN40 respectively. Locally, biotite forms at the boundary between pyroxene and hornblende

grains as a result of the reaction of these two minerals. In some places, biotite displays a poikilitic texture, containing inclusions of tiny euhedral apatite, plagioclase and ilmenite.

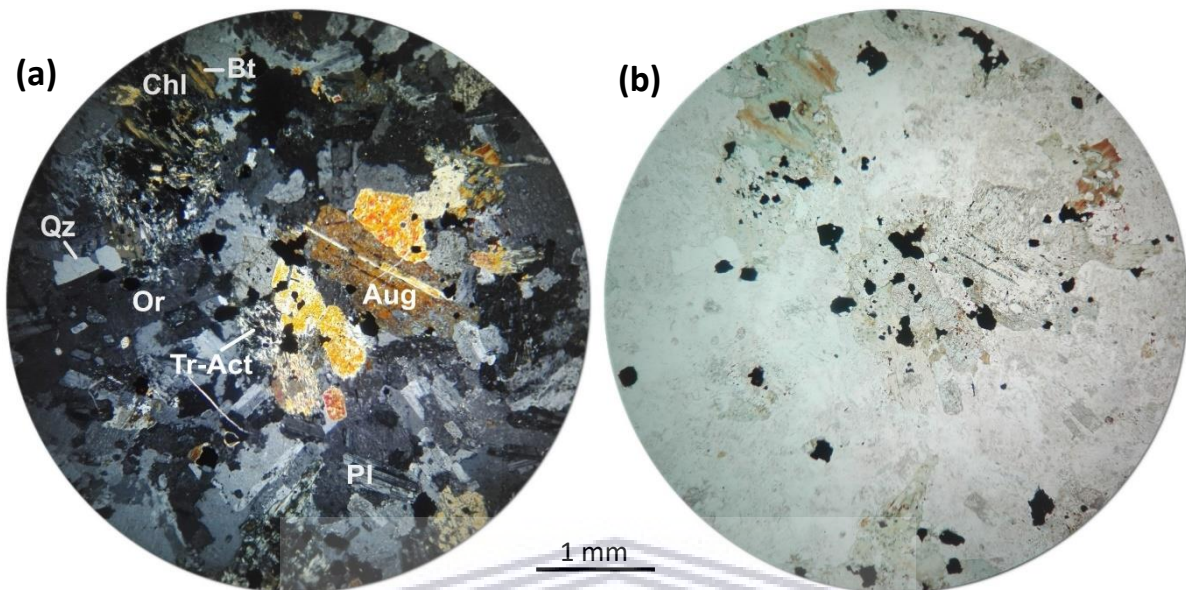


Figure 4.10: Thin section photomicrographs of the weakly altered syenodiorite at YZN23 showing the major primary and secondary minerals present in the rock under (a) XPL and (b) PPL. Aug = Augite, Bt = Biotite, Chl = Chlorite, Or = Orthoclase, Pl = Plagioclase, Qz = Quartz, Tr-Act = Tremolite-Actinolite.

The moderately altered syenodiorite comprises primary orthoclase (~35%), plagioclase (~17%), quartz (~3%) and magnetite (~2%), and minor amounts of ilmenite (<1%) and apatite (<1%) (Table B5). Secondary minerals include hornblende (~15%), epidote (~9%), sericite (~6%), chlorite (~5%), calcite (~4%), tremolite-actinolite (~3%), and minor amounts of zoisite (<1%). Most of the minerals display similar textures and features to those occurring within the weakly altered syenodiorite. Locally, microperthite is well developed in orthoclase. Orthoclase and plagioclase are weakly altered to sericite. Locally, plagioclase is also weakly to moderately pseudomorphed by an assemblage of minerals called saussurite, which comprises the minerals epidote, calcite, and, locally, rare zoisite. Tiny zoisite grains are colourless and have an anomalous blue interference colour. Alteration of plagioclase to epidote is so pervasive in some grains that the original twins of the plagioclase grains are hardly visible. In YZN30, YZN52, and YZN66, saussuritization is characterised by the formation of patches of epidote, calcite and zoisite at the centre of orthoclase grains (Figs. B9a, b).

Pyroxenes have become completely pseudomorphed by hornblende, which, in turn, has become weakly replaced by tremolite-actinolite (Fig. 4.11a). Tremolite-actinolite is mostly present as aggregates growing sub-parallel to the growth direction of the secondary hornblende it replaces. Alteration to amphiboles is uncommonly associated with minor calcite and epidote granules. Biotite is completely altered to scaly aggregates of chlorite which is locally associated with the formation of minor secondary epidote (Fig. 4.11b) and,

uncommonly, actinolite along the cleavage of the chlorite grains. Quartz and apatite occur either interstitially between- or poikilitically within other primary minerals.

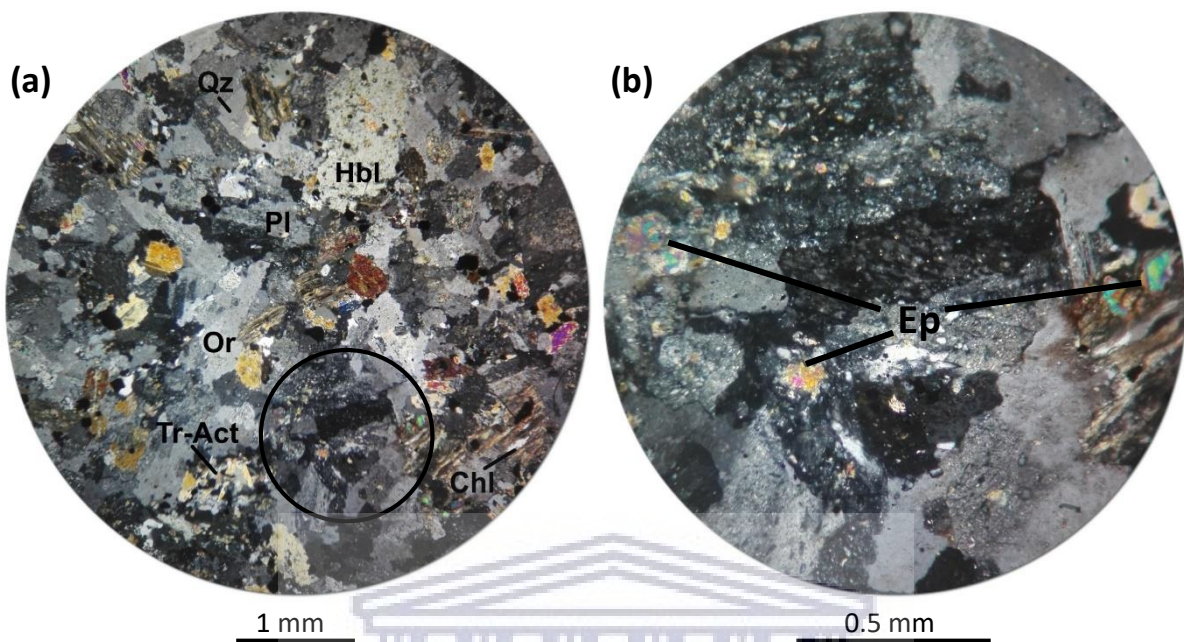


Figure 4.11: Thin section photomicrographs of the moderately altered syenodiorite at YZN30 under XPL. The black circle in (a) represents the enlarged section displayed in (b) showing a closer view of the formation of secondary epidote in chloritized grains (towards the right of figure), as well as in plagioclase. Chl = Chlorite, Ep = Epidote, Hbl = Hornblende, Or = Orthoclase, Pl = Plagioclase, Qz = Quartz, Tr-Act = Tremolite-Actinolite.

Petrography of the Monzonite

Not much variation is seen in terms of alteration of the monzonite in thin sections of samples from different localities. Moreover, the textures and features displayed by the minerals in the monzonite are similar to those of the syenodiorite. The only difference between these two rock types is seen in the relative mineralogy observed in thin section. The monzonite is predominantly comprised of plagioclase (~30%), orthoclase (~28%), augite (~6%), quartz (~4%), orthopyroxene (~3%), and minor amounts of magnetite (~1%), ilmenite (<1%) and apatite (<1%) (Table B6). Secondary minerals in the monzonite include sericite (~9%), hornblende (~7%), chlorite (~5%), tremolite-actinolite (~3%) and epidote (~3%), with minor amounts of tourmaline (<1%) and calcite (<1%).

In the monzonite, the amount of plagioclase observed in thin section is slightly higher than that of orthoclase. Overall, sericitization of feldspars is relatively weak and inhomogeneous (patchy) as feldspar grains in different parts display significantly varying degrees of alteration, particularly in YZN34. Locally, plagioclase is also seen being weakly replaced by clusters of epidote granules, which usually replaces plagioclase from the centre outward. Uncommonly, calcite is also found weakly replacing plagioclase. Orthoclase is poikilitic in some places, containing inclusions of sericitized plagioclase. Carlsbad twins are abundant in some places, particularly in YZN10. Augite is mostly present as elongate grains, and less commonly as irregular grains with anhedral shapes (Figs. 4.12a, b), whereas orthopyroxene is present as

subhedral grains. Alteration of pyroxenes to hornblende is patchy, and, locally, hornblende has replaced the pyroxenes from the margins inward, forming irregular pseudomorph rims (Fig. 4.12b). Moreover, hornblende is replaced by tremolite-actinolite. Both hornblende and tremolite-actinolite are also locally found to be further partially to completely replaced by chlorite. Chlorite has a scaly habit, a strong greenish brown pleochroism and displays first order brown and berlin blue interference colours, reflecting its high Fe content (Figs. 4.12a, b, B10c, d). It is commonly associated with actinolite and epidote along its cleavage planes, particularly in YZN34 and YZN93.

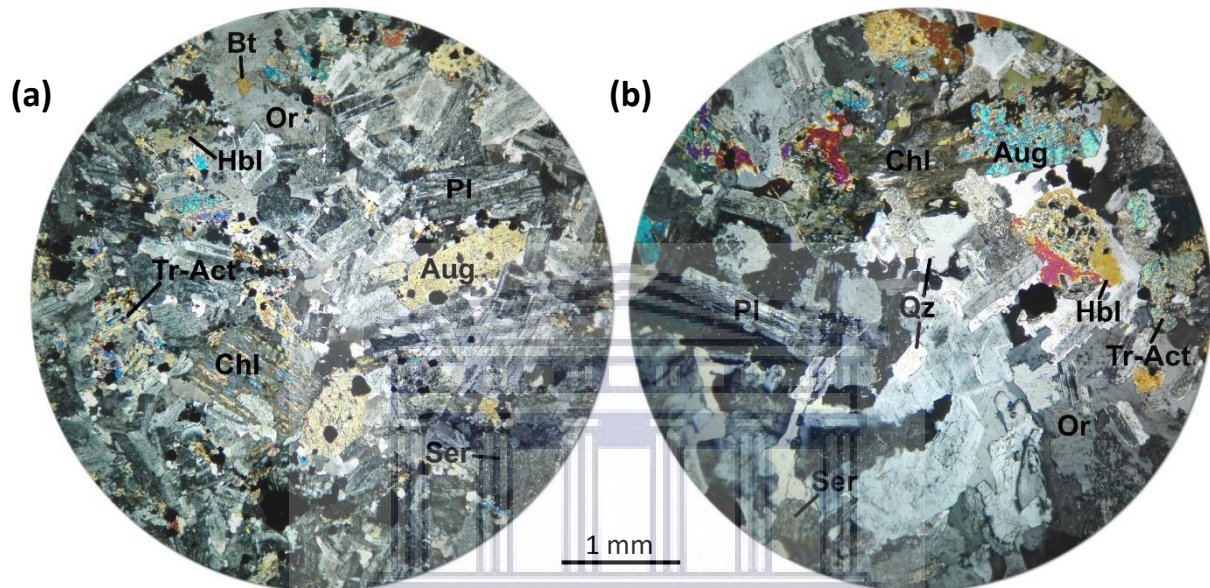


Figure 4.12: Thin section photomicrographs of the monzonite in XPL displaying the major primary and secondary minerals present in the rock at (a) YZN34 and (b) YZN94. Aug = Augite, Bt = Biotite, Chl = Chlorite, Hbl = Hornblende, Or = Orthoclase, Pl = Plagioclase, Qz = Quartz, Ser = Sericite, Tr-Act = Tremolite-Actinolite.

Some partially altered augite grains, particularly in YZN93 and YZN94, show an accumulation of opaque magnetite mimicking the shape of the augite grains at the boundary between the reaction rim and the unaltered core (Figs. B11a, b). In some parts, these opaque minerals also accumulate in clusters toward the centre of grains (Figs. B10a to d). These occurrences are as a result of the breakdown of ferromagnesian minerals. Apatite is scarce to absent and is found as tiny euhedral grains poikilitically included in pyroxenes and amphiboles. Rare interstitial tourmaline grains are locally found in the groundmass.

4.5.2. Syenite

Outcrop to mesoscopic scale: The syenite occurs west of the Visitors Center, at Hoëbank, as well as towards the south of Yzerfontein Point. At the former location, it forms a gradational contact with the adjacent monzonite, and at Hoëbank and south of Yzerfontein Point, it forms a gradational contact with the adjacent syenodiorite. The contact between the syenite and these other two intermediate rocks is fairly indiscernible, making it difficult to trace the extent of these outcrops. It is for this reason that these outcrops have not been indicated on Figs. A3

to A5. The syenite varies in grain size between fine- and medium-grained, and comprises mainly orthoclase, with smaller amounts of plagioclase, pyroxene and amphiboles, most notably hornblende (Fig. 4.13).



Figure 4.13: Hand specimen of the syenite obtained from Hoëbank (YZN42). Scale: R2 coin with diameter = 2.3 cm.

Petrography: Once again, as a result of varying degrees of alteration, the syenite displays slightly varying mineral constituents and abundances in different samples. Overall, petrographic analysis shows that the syenite close to the Visitors Center (such as YZN09) is slightly less altered and, therefore, also has a different mineralogy compared to the syenite at Hoëbank and Yzerfontein Point (YZN42 and YZN46). The syenite close to the Visitors Center comprises predominantly orthoclase (~55%), with smaller quantities of augite (~9%), plagioclase (~8%), orthopyroxene (~4%), quartz (~3%), magnetite (~2%), and minor amounts of ilmenite (<1%) (Fig. 4.14a; Table B7). Secondary minerals in the weakly altered syenite include sericite (~10%), chlorite (~5%), hornblende (~2%), tremolite-actinolite (~1%), and minor amounts of epidote (<1%).

The syenite at Hoëbank and Yzerfontein Point mainly comprises orthoclase (~60%) and plagioclase (~16%), with smaller amounts of magnetite (~2%) and quartz (~1%), and minor amounts of ilmenite (<1%). Secondary minerals formed due to alteration include hornblende (~9%), tremolite-actinolite (~4%), sericite (~3%), chlorite (~2%) and epidote (~2%), with minor amounts of tourmaline (<1%) and calcite (<1%) (Fig. 4.14b; Table B7). Despite the slight discrepancies in the mineralogy of the syenite at various localities, the textures of the minerals are similar.

Orthoclase occupies a large vol. % of the rock. It is anhedral, and large grains are poikilitic, containing tiny sericitized grains of plagioclase. Carlsbad twins are common in the orthoclase (Fig. 4.14a), and, uncommonly, it displays lamellar twinning, but on a much finer scale than plagioclase, showing alteration along the twinning planes. Frequently, pyroxene and large

plagioclase grains are found irregularly overgrowing orthoclase (Fig. 4.14a). Orthoclase is very weakly sericitized compared to plagioclase, which has become moderately altered, commonly to the extent that the original lamellar twinning is no longer visible. Locally, epidote granules are found pseudomorphing plagioclase, but grains are usually small. Plagioclase is tabular and elongate, and shows lamellar twinning (Figs. 4.14a, b).

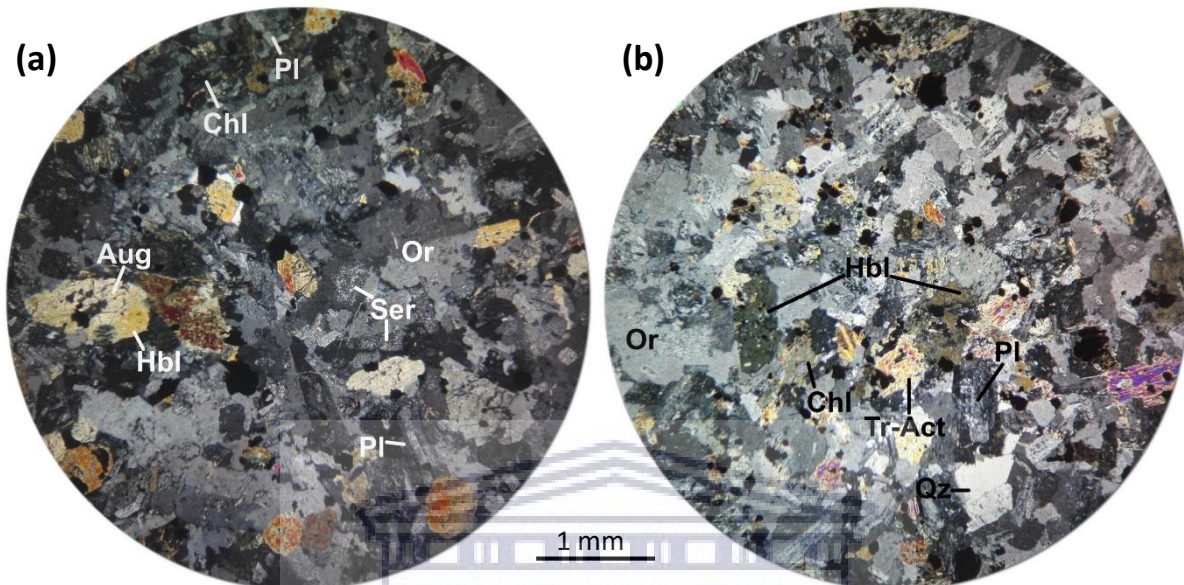


Figure 4.14: Thin section photomicrographs of the syenite in XPL displaying the major primary and secondary minerals present in the rock at (a) YZN09 and (b) YZN42. Aug = Augite, Chl = Chlorite, Hbl = Hornblende, Or = Orthoclase, Pl = Plagioclase, Ser = Sericite, Tr-Act = Tremolite-Actinolite.

Pyroxenes are more weakly altered in YZN09, compared to YZN42 and YZN46 where they have been completely altered. Orthopyroxene locally displays stubby subhedral to euhedral grain shapes and uncommonly displays simple twinning. Augite, in particular, displays rims that have been irregularly pseudomorphed by hornblende. Alteration of the pyroxenes to hornblende is locally associated with minor interstitial calcite. Chlorite is present as anhedral scaly flakes. Magnetite, in particular, is locally associated with fibrous tremolite-actinolite in YZN42 and YZN46. Tourmaline occurs locally in the groundmass in YZN42 and YZN46 and has varying shapes including radiating acicular shapes or anhedral shapes.

4.6. Felsic Rocks

The quartz-microsyenite and monzogranite were classified using the QAPF diagram of Streckeisen (1974) based on the estimated volume percentage of quartz, orthoclase and plagioclase in petrographic thin section, normalised to 100%. It was done this way since the rocks display a mineral composition in thin section that is not always consistent with the rock classification of De La Roche et al. (1980), particularly in the case of YZN38, YZN39 and YZN73. Based on the petrographic examination of the felsic rocks of the Yzerfontein Pluton, they are classified as quartz-microsyenites and monzogranites. These rocks are not only present as dykes that cross-cut the intermediate to mafic rocks across the study area, but are also found as irregularly shaped outcrops that are either isolated (Fig. A3), or in contact with the

intermediate rocks (Figs. A5 to A7). They are aphanitic hypabyssal rocks with minerals so fine-grained that most are difficult to identify in hand specimen.

4.6.1. Quartz Microsyenite

Outcrop to mesoscopic scale: Two large outcrops of quartz-microsyenite occurs at Kollege and Draaibank, forming sharp contacts with the adjacent syenodiorite and monzonite. The quartz-microsyenite at Kollege forms an ~95 – 105 m x 25 – 50 m outcrop in sharp contact with the adjacent syenodiorite and monzonite, and at Draaibank it forms an ~140 – 150 m x 10 – 35 m outcrop in sharp contact with the adjacent monzonite. These leucocratic quartz-microsyenite outcrops are characterised by a pink colour due to the abundance of very fine-grained pink orthoclase. Due to the fine-grain size of this rock, most minerals are only visible with the aid of a hand lens. Major minerals present include orthoclase, plagioclase and quartz, with minor amounts of amphiboles, epidote, chlorite and tourmaline. Quartz-microsyenite dykes were previously discussed in detail in sections 4.4.3 and 4.5.1, and they commonly cross-cut the monzogabbro, syenodiorite and monzonite (Figs. 4.6a; 4.9c). Quartz-microsyenite dykes and outcrops are commonly seen enclosing rounded to irregular shaped portions of the intermediate and mafic rocks (Fig. 4.9c). Locally, quartz-microsyenite dykes and outcrops are cross-cut by quartz-epidote veining and are intimately associated with epidotization. In some cases, epidotization has affected the adjacent rock, which is indicated by the green staining of the feldspars directly adjacent to the dyke or outcrop (Fig. 4.6a).

Petrography: The quartz-microsyenite comprises mainly primary orthoclase (~38%) and plagioclase (~18%), with smaller amounts of quartz (~11%), and minor quantities of magnetite (<1%) and ilmenite (<1%) (Table B8). Secondary minerals include sericite (~24%), tremolite-actinolite (~5%), hornblende (~2%), and minor amounts of epidote (~1%), chlorite (<1%) tourmaline (<1%), and zoisite (<1%). The feldspars are masked by sericitic alteration, imparting a cloudy appearance to these minerals in thin section (Figs. 4.15a, b). This is due to hydration by deuteric alteration, and, as a result of this, it becomes very difficult to distinguish between the feldspars. Locally, orthoclase tends to look like plagioclase. However, the twinning in orthoclase is on a much finer scale compared to what is usually seen in plagioclase. Orthoclase commonly shows alteration along the twinning planes. Another observation which assisted in distinguishing orthoclase from plagioclase in these relatively altered rocks is the fact that orthoclase commonly has stubbier shapes as opposed to plagioclase which is more elongate. Uncommonly, plagioclase is saussuritized, which is evident by the presence of multiple small secondary epidote granules forming on the plagioclase. Locally, epidote is accompanied by minor quantities of zoisite, particularly in YZN39 and YZN76.

Some samples, such as YZN38 and YZN39, contain irregular felted masses of amphiboles which are interstitial between feldspars. These consist mainly of tremolite-actinolite, which has a long and fibrous or needle-like habit (Figs. 4.15a, b). Locally, the tremolite-actinolite is slightly chloritized, particularly along its cleavage (Fig. 4.15b). Chlorite has a light to dark grey birefringence and also locally displays an anomalous blue birefringence in XPL, with a stronger

green pleochroism in PPL, indicative of a high Fe content. In some places, very fine-grained tremolite-actinolite aggregates are seen overgrowing the margins of feldspar grains.

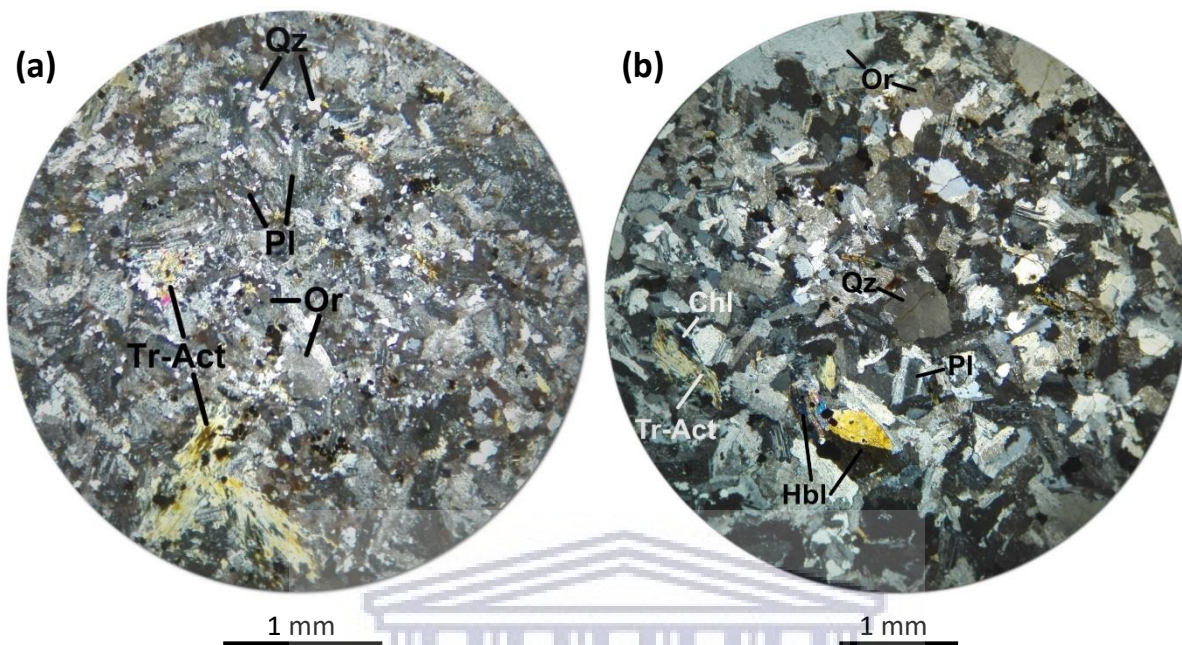


Figure 4.15: Thin section photomicrographs of the quartz-microsyenite in XPL displaying the major primary and secondary minerals present in the rock at (a) YZN39 (b) YZN76. Chl = Chlorite, Hbl = Hornblende, Or = Orthoclase, Pl = Plagioclase, Qz = Quartz, Tr-Act = Tremolite-Actinolite.

Hornblende is less abundant, and locally displays simple twinning (Fig. 4.15b). Quartz, magnetite and ilmenite are interstitial. Magnetite and ilmenite are also locally found as products of the breakdown of ferromagnesian minerals, most notably tremolite-actinolite, which are present as very fine-grained, felted aggregates. Rare tourmaline is also present.

4.6.2. Monzogranite

Outcrop to mesoscopic scale: The monzogranite in the study area is found either as dykes, small “pockets”, or small isolated outcrops with a washed-out pink colour on the surface. Monzogranite dykes and “pockets” and their various sizes were previously discussed in detail in sections 4.4.3 and 4.5.1 (Figs. 4.6b, 4.9a, b, B2a, b, B5). Dykes are commonly seen cross-cutting the monzogabbro, syenodiorite and monzonite across the study area. Small isolated outcrops of monzogranite occur west, north and north-west of the Visitors Center and have sizes of ~8.0 – 9.5 m x 3.0 – 5.0 m (Fig. A3). The monzogranite is a fine-grained, leucocratic rock with a high abundance of felsic minerals, including orthoclase, plagioclase and quartz. Other minerals identified in hand specimen include minor quantities of amphiboles, and, locally, tourmaline, epidote and chlorite.

Petrography: The rock comprises mainly orthoclase (~30%), plagioclase (~29%) and quartz (~20%), with minor amounts of magnetite (<1%) and ilmenite (<1%) (Table B9). Secondary minerals include sericite (~10%), hornblende (~4%), tremolite-actinolite (~3%), epidote

(~2%), chlorite (~1%), and minor amounts of tourmaline (<1%) and zoisite (<1%). Orthoclase also commonly displays a microperthitic texture, and, locally, shows Carlsbad twinning, particularly in YZN73. Orthoclase and plagioclase have become weakly sericitized in this rock, which commonly masks their appearance in thin section. Plagioclase commonly shows lamellar twinning and has locally been replaced by epidote. Hornblende uncommonly displays simple twinning, and has locally been replaced by tremolite-actinolite, usually from the centre outward. Tremolite-actinolite, in turn, has been pseudomorphed by chlorite, which has a scaly texture. In Figs. 4.16a and b, chlorite can be identified by its anomalous blue interference colour. Quartz, magnetite and ilmenite are interstitial.

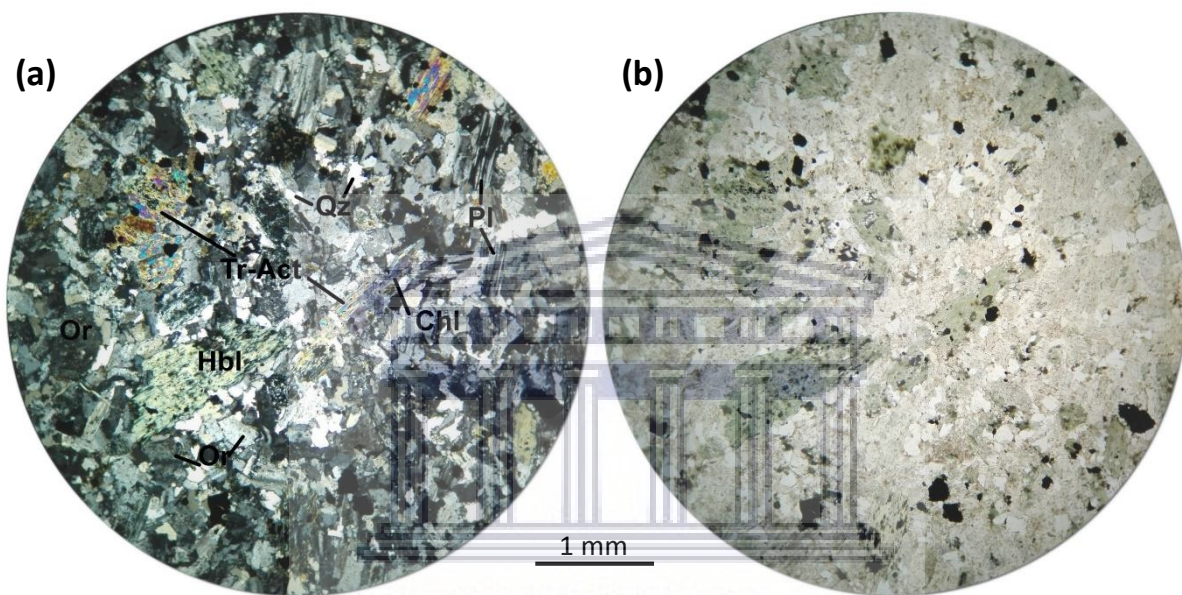


Figure 4.16: Thin section photomicrographs of the monzogranite at YZN50 displaying the major primary and secondary minerals present in the rock under (a) XPL and (b) PPL. Chl = Chlorite, Hbl = Hornblende, Or = Orthoclase, Pl = Plagioclase, Qz = Quartz, Tr-Act = Tremolite-Actinolite.

Chapter 5: Hydrothermal veins and breccias

5.1. Introduction

The rocks of the Yzerfontein Pluton are cross-cut by various generations of hydrothermal veins that attest to the abundant flow of hydrothermal fluids along the pre-existing joints and fractures in the rocks. The dominant direction in which these hydrothermal veins trend is WNW-ESE to NNW-SSE. They have varying mineral assemblages pertaining to the minerals that have precipitated from the hydrothermal fluids at different stages of hydrothermal fluid flow. The minerals that occur within the hydrothermal veins include quartz, pyrite, calcite, tourmaline, jasper and epidote. Accompanying hydrothermal fluid flow was the hydrothermal alteration of primary minerals occurring in the surrounding host rock. Minerals associated with hydrothermal alteration include tourmaline, jasper, epidote, calcite, chlorite and sericite.

Hydrothermal veining cross-cuts all rocks of the Yzerfontein Pluton, except for the rocks that occur at Gabbro Point towards the northern end of the study area. In outcrops around the Visitors Center and the Yzerfontein Harbour (Fig. A3), hydrothermal veins are less prevalent and become more abundant in outcrops toward Yzerfontein Point (Fig. A5) where the distance between veins decrease (distances can decrease to less than half a metre). Ultimately, the frequency in occurrence of hydrothermal veins increases towards Draaibank and Schaap Eiland (Figs. A7 to A10) where large sheeted hydrothermal veins extend over several metres through outcrops. The hydrothermal veins were studied at both outcrop to mesoscale and described in terms of their mineralogical composition, thickness, associated alteration haloes, orientation, and sequence or timing of veins through cross-cutting relationships. A total of 18 samples were selected for the petrographic examination of the hydrothermal veins, and 3 samples were selected for petrographic examination of brecciated tourmaline veins. The petrographic examination of the veins was done to reveal the mineralogical composition of the different types of veins, their textural characteristics and the change in composition along the length of the veins.

5.2. Internal vein textures

There are a number of different types of primary internal vein textures that were petrographically identified in the various minerals occurring in the hydrothermal veins in the study area. These internal vein textures can be classified as either primary growth textures or recrystallisation textures. Primary growth textures identified include colloform banding, crustiform or crustified banding, comb texture and zonal texture (growth zonation). **Colloform banding** is described as the rhythmic banding of minerals that may have spherical, botryoidal, reniform or mammillary forms or surfaces. Each growth period produces a new overgrowth band, and these bands grow concentrically outward from a nucleus or a vug (Rogers, 1918; Ineson, 1989). **Crustiform banding** is a term usually applied to veining that displays successive or rhythmic bands of alternating mineral species that are symmetrically

distributed from both walls of a fracture (Adams, 1920; Dong et al., 1995). **Comb texture** is formed by the growth of large parallel to subparallel euhedral quartz rods perpendicular to the vein walls, projecting into open space (Adams, 1920). **Zonal texture** is commonly displayed by euhedral quartz grains growing perpendicularly to the vein wall, showing growth zoning along their length and thereby recording different growth stages. Growth zones usually contain multiple fluid inclusions that mimic the shape of the grains (Ineson, 1989).

Recrystallisation textures observed in vein quartz include mosaic and plumose texture. Mosaic quartz texture can be displayed by both microcrystalline and crystalline quartz and involves compact masses of quartz grains that have irregular and interpenetrating grain boundaries (Dong et al., 1995). Plumose quartz texture can be either feathery (Adams, 1920) or flamboyant (Dong et al., 1995), and refers to quartz grains that displays variable extinction positions in the same grain, particularly at the edges of the grain. The extinction can be described as feathery, splintery, radial or flamboyant (Adams, 1920; Sander and Black, 1988; Dong et al., 1989). Tourmaline associated with hydrothermal veins also display characteristic textural features in thin section. One of the most common textures displayed by tourmaline is **spherulitic texture**, which refers to the tendency of acicular grains to grow radially from a nucleus into arrays of fibrous aggregates (MacKenzie et al., 1982).

5.3. Hydrothermal vein assemblages

There are at least 21 different types of hydrothermal veins (based on mineralogical composition) and 3 different types of brecciated tourmaline veins which were identified by the integrated study of hydrothermal veins at an outcrop to mesoscopic scale and a petrographic scale. However, not all veins described in thin section were observed and described in the field, and vice versa. In order to simplify the field and petrographic description of the hydrothermal veins, they were grouped into hydrothermal vein assemblages on the basis of common minerals occurring in different types of veins (Table 5.1). The different types of hydrothermal veins were named in a way that more or less reflects the relative timing of the minerals (paragenetic sequence), which is discussed in detail in section 5.5. As a summary, field and petrographic studies of the hydrothermal veins reveal that quartz is one of the earliest minerals to precipitate along fractures and joints during the early stages of hydrothermal fluid flow. Therefore, quartz is the most common mineral present in the hydrothermal veins and accompanies other secondary minerals in nearly all hydrothermal vein types. Precipitation of quartz was followed by the precipitation of pyrite, calcite, tourmaline, jasper, epidote and a final stage involving the formation of barren quartz veins (in order of decreasing age).

Table 5.1: Hydrothermal veins identified and described in the field and in thin section, and the vein assemblages into which they were grouped.

Vein assemblages	Vein Types	
	Field observations	Petrography
Quartz-dominated veins	Qz-Py-Tur Qz-Py Qz-Tur	Qz-Py-Cal-Tur Qz-Py-Tur Qz-Py Qz-Cal-Tur Qz-Tur
Tourmaline-dominated veins	Py-Tur Tur	—
Breccias and brecciated veins	Tourmalinite breccia Qz-Py-Jsp breccia Py-Tur breccia	Tourmalinite breccia Qz-Tur-Jsp breccia
Jasper-dominated veins	Qz-Py-Jsp Qz-Cal-Tur-Jsp Qz-Tur-Jsp Py-Jsp Tur-Jsp	Qz-Py-Tur-Jsp Qz-Py-Jsp
Epidote-dominated veins	Qz-Ep	Qz-Py-Tur-Ep Qz-Cal-Tur-Ep Qz-Tur-Jsp-Ep Qz-Tur-Ep Qz-Ep
Calcite dominated	Cal Cal-Ep	—
Barren quartz veins	Qz	Qz

Abbreviations: Cal = Calcite, Ep = Epidote, Jsp = Jasper, Py = Pyrite, Qz = Quartz, Tur = Tourmaline (after Whitney and Evans, 2010).

5.3.1. Quartz-dominated veins

Outcrop to mesoscopic scale: The quartz-dominated vein assemblage comprises at least five vein types, as shown in Table 5.1. Only three of these vein types were studied in detail in the field. However, geological samples of all five vein types were collected and used to produce thin sections. The three vein types described in the field include: quartz-pyrite, quartz-pyrite-tourmaline and quartz-tourmaline veins. These veins traverse the monzonite, syenodiorite, and, less commonly, the monzogabbro in the study area, and, in some localities, such as in the Yzerfontein Harbour area, they are found to cross-cut the quartz-microsyenite (YZN69). They generally trend in an E-W to NNW-SSE direction, with some quartz-pyrite-tourmaline and quartz-tourmaline veins locally trending in a N-S to NE-SW direction (Table C1).

Quartz-pyrite veins range in thickness between 0.1 and 4 cm, with their associated alteration haloes ranging in thickness between 0.1 and 2.7 cm (Fig. 5.1c, Table C1). Alteration haloes on either side of quartz-pyrite veins usually have a dark green colour due to the chloritic alteration of the host rock minerals. Tourmaline, jasper or epidote uncommonly accompany chlorite in the alteration haloes. Quartz-tourmaline veins range in width between 0.1 and 4 cm, and their alteration haloes usually extend between 0.1 and 5.5 cm (Fig 5.1a, Table C1). They usually have alteration haloes comprising tourmaline or jasper, or both, and locally comprise additional chlorite. Quartz-pyrite-tourmaline veins have widths that range between 0.1 and 2.1 cm, with alteration haloes that extend between 0.1 and 2 cm on either side of the

veins (Fig 5.1b, Table C1). The alteration haloes usually comprise a variety of the different mineral species in different localities and in various abundances. The minerals that are present in most alteration halo assemblages on either side of quartz-pyrite-tourmaline veins are chlorite and tourmaline, and, in some localities, comprise additional jasper or epidote, or both, and uncommonly sericite.

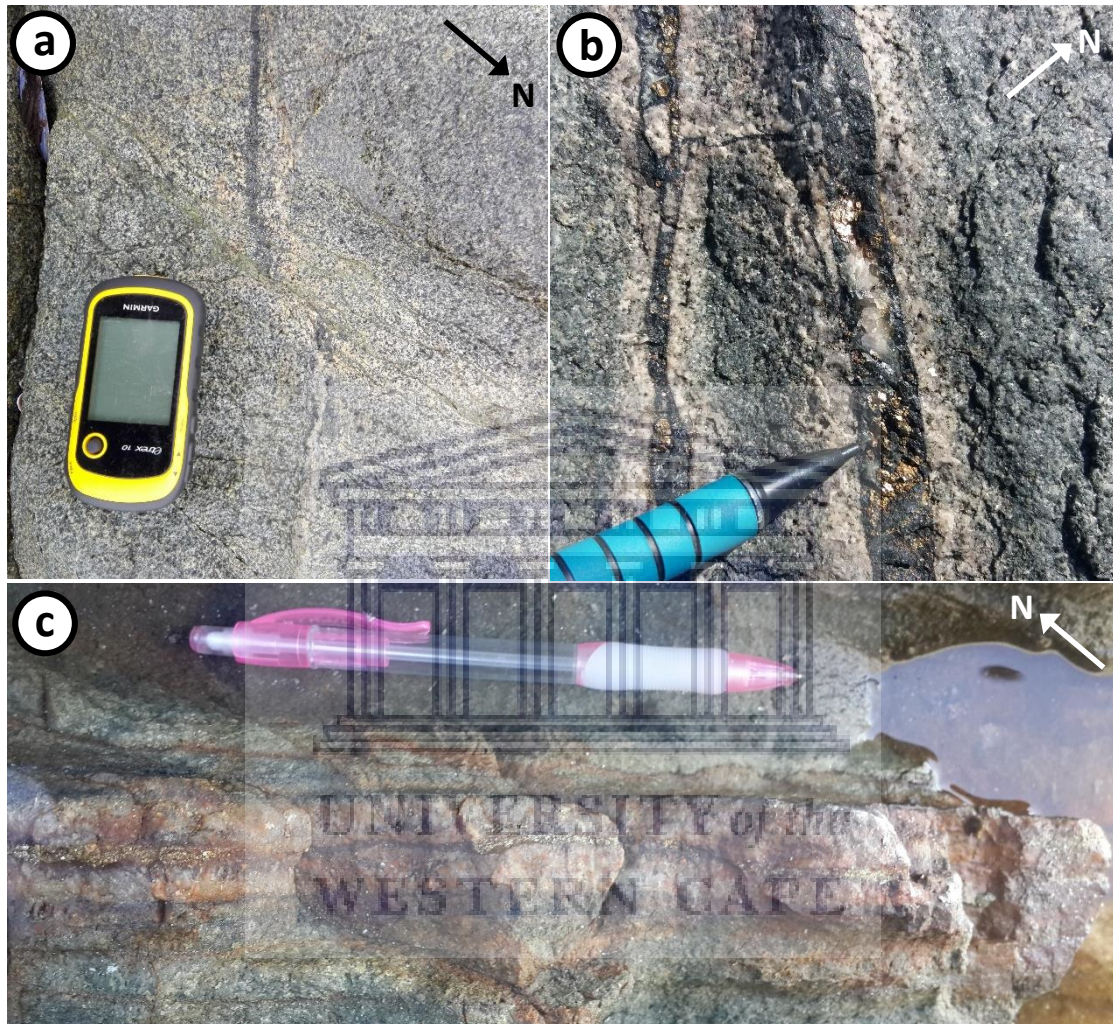


Figure 5.1: Quartz-dominated veins at different localities across the study area. (a) NE-SW-trending quartz-tourmaline vein cross-cut by a N-S-trending quartz-epidote vein in the syenodiorite NE of the Visitors Center. Note the change in composition of the vein from tourmaline-rich (SSW, top in figure) to more quartz-rich (NNE, bottom in figure). Quartz-tourmaline vein offset by later sinistral movement. (b) NW-SE-trending quartz-pyrite-tourmaline veins cross-cutting the syenodiorite in the Yzerfontein Harbour. (c) Thick WNW-ESE-trending quartz-pyrite vein traversing the monzonite at Freddie se Klip with chlorite alteration halo. Scale: GPS with length = 10 cm and width = 5.2 cm; Blue pencil with width = 0.8 cm; Pink pencil with length = 14.5 cm.

At Schaap Eiland, >85 m long and between 0.5 and 0.75 m thick gossanous quartz-pyrite-tourmaline veins cross-cut the monzonite trending in a WNW-ESE direction (Table C1). They comprise alternating veins of quartz, tourmaline, and minor pyrite. Most of the pyrite has become altered to gossanous material which includes mostly limonite which is an Fe-oxyhydroxide formed after the weathering and oxidation of Fe in pyrite (Fig. C1). In some places along the length of the vein, small amounts of pyrite are still visible.

Petrography: Thin sections of all five quartz-dominated vein types were produced and studied. These include: quartz-pyrite (YZN17-2), quartz-pyrite-calcite-tourmaline (YZN34a and b), quartz-pyrite-tourmaline (YZN60a, 1 to 4), quartz-calcite-tourmaline (YZN34b), and quartz-tourmaline veins (YZN27 and YZN61b; Table 5.1). Tables 5.2 and 5.3 display the mineralogy of the different veins and the relative grain sizes of each of the mineral species, as well as that of the secondary minerals occurring in associated alteration haloes. It is important to note that not all hydrothermal veins have uniform alteration haloes. In most cases, they are irregular and therefore have a variable thickness. Additionally, they may also be completely absent in some localities with only traces of secondary minerals found replacing primary minerals in the surrounding host rock.

Quartz-dominated veins range in thickness between 0.2 and 20 mm, with relatively small alteration haloes ranging between <0.1 and 3 mm on either side of the vein. Some veins do not have an alteration halo, which is the case for the veins in YZN27, YZN34a, and YZN60. Tourmaline is the most common mineral in the alteration haloes of quartz-dominated veins. Some veins contain either additional epidote, sericite, chlorite or calcite in their alteration haloes, or a combination of a few of these secondary minerals. Quartz is usually found in the centre along the veins, and, in most cases, shows open space filling which is evident from the increase in grain size of quartz crystals as they grow toward the centre of the vein. In some veins, silica has a bimodal grain size distribution, with grain sizes varying between that of microcrystalline chalcedonic aggregates to crystalline quartz (Figs. 5.2a and b).

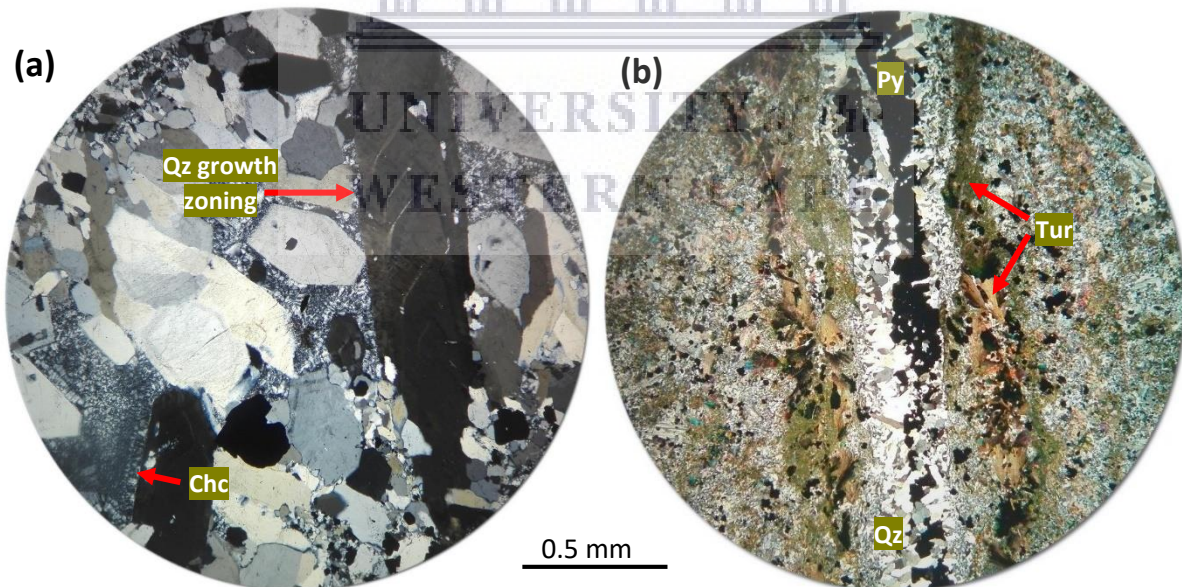


Figure 5.2: Thin section photomicrographs displaying primary growth textures in XPL. (a) Quartz-pyrite-tourmaline vein showing a bimodal grain size distribution of silica and growth zoning in comb quartz (YZN60a). (b) Crustiform banding in a quartz-pyrite-calcite-tourmaline vein (YZN34b). *Chc* = Chalcedony, *Qz* = Quartz, *Py* = Pyrite, *Tur* = Tourmaline.

Table 5.2: Summary of the mineralogy and grain sizes of minerals present along hydrothermal veins and their alteration haloes in thin section, as well as the rock types which they traverse (occurrence).

Vein Composition	Grain size of vein- and alteration minerals (mm)	Sample and occurrence
Quartz-dominated veins		
Qz-Py-Cal-Tur	Qz (<0.1 – 1.5), Py (<0.1 – 3), Cal (<0.1 – 0.5), Tur (<0.1 – 2)	YZN34b, Monzonite
Qz-Py-Cal-Tur	Qz (<0.1 – 0.2), Py (<0.1 – 0.5), Cal (<0.1 – 0.4), Tur (<0.1 – 0.3), Ep (<0.1 – 1.0), Chl (~0.1 – 1)	YZN34a, Monzonite
Qz-Py-Tur	Qz (<0.1 – 6), Py (~0.1 – 2.2), Tur (<0.1 – 0.5)	YZN60a (1 to 4), Monzonite
Qz-Py	Qz (<0.1 – 0.7), Py (<0.1 – 1), Ep (<0.1 – 1), Ser (<1), Chl (~0.1 – 1.2), Tur (~0.1 – 0.)	YZN17-2, Monzonite
Qz-Cal-Tur	Qz (~0.1 – 0.3), Cal (~0.1 – 1.5), Tur (<0.1 – 0.7)	YZN34b, Monzonite
Qz-Tur	Qz (~0.1 – 1.8), Tur (<0.1 – 4.8), Lm (<0.1)	YZN27, Monzonite
Qz-Tur	Qz (<0.1 – 1.4), Tur (<0.1 – 2.2)	YZN61b, Monzonite
Breccias and brecciated veins		
Tourmalinite breccia	Tur (<0.1), Qz (<0.1 – 2.2), Pl (0.1 – 0.8), Lm (<0.1)	YZN62, Monzonite
Brecciated Qz-Tur-Jsp	Qz (<0.1 – 6), Tur (<0.1 – 0.6), Jsp (<0.1 – 0.6), Pl (0.1 – 2), Chl (0.1 – 2.3), Cal (<0.1 – 2)	YZN78, Monzonite
Jasper-dominated veins		
Qz-Py-Tur-Jsp	Qz (<0.1 – 2.6), Py (<0.1 – 1.5), Tur (<0.1 – 0.5), Jsp (<0.1)	YZN59a, Monzonite
Qz-Py-Jsp	Qz (<1 – 2.5), Py (~0.1 – 1), Jsp (<1 – 3.5), Tur (<1 – 0.3), Ser (<1)	YZN17-1, Monzonite
Epidote-dominated veins		
Qz-Py-Tur-Ep	Qz (0.1 – 0.7), Py (<0.1 – 0.4), Tur (<0.1 – 0.1), Ep (<0.1), Ser (<1), Chl (<0.1 – 1.2)	YZN17-2, Monzonite
Qz-Py-Tur-Ep	Qz (<0.1 – 1.1), Py (<0.1 – 1); Tur (0.1 – 2.1), Ep (<0.1 – 0.7)	YZN38, Quartz microsyenite
Qz-Py-Tur-Ep	Qz (<0.1 – 1.5), Py (<0.1 – 4), Tur (<0.1 – 0.5), Ep (<0.1 – 0.2), Chl (0.2 – 1); Cal (<0.1)	YZN69, Syenodiorite
Qz-Py-Tur-Ep	Qz (0.2 – 1.5), Py (<0.1 – 1), Tur (<0.1 – 0.7), Ep (<0.1 – 0.3)	YZN81, Syenodiorite
Qz-Py-Tur-Ep	Qz (0.1 – 1.5), Py (<0.1 – 0.5), Tur (<0.1 – 0.6), Ep (<0.1 – 0.3), Cal (<0.1 – 1.2), Chl (0.2 – 0.5)	YZN83, Syenodiorite
Qz-Cal-Tur-Ep	Qz (0.1 – 0.6), Cal (<0.1 – 0.8), Tur (<0.1 – 0.2), Ep (<0.1 – 0.2)	YZN30, Syenodiorite
Qz-Tur-Jsp-Ep	Qz (0.1 – 0.7), Tur (<0.1 – 0.6), Jsp (<0.1 – 0.6), Ep (<0.1 – 0.1), Ser (<0.1)	YZN25, Syenodiorite
Qz-Tur-Ep	Qz (0.1 – 2.2), Tur (<0.1 – 1), Ep (<0.1 – 0.3); Lm (<0.1)	YZN36, Syenodiorite
Qz-Ep	Qz (<0.1 – 1.5), Ep (<0.1 – 1.0)	YZN50, Monzogranite
Barren quartz veins		
Qz	Quartz (<0.1 – 7 mm)	YZN44, Monzonite

Abbreviations: Cal = Calcite, Chl = Chlorite, Ep = Epidote, Jsp = Jasper, Kfs = K-feldspar, Lm = Limonite, Pl = Plagioclase, Py = Pyrite, Qz = Quartz, Ser = Sericite, Tur = Tourmaline (after Whitney and Evans, 2010).

Table 5.3: Summary of the mineralogy and width of hydrothermal veins and their alteration haloes in thin section.

Vein Composition	Vein width (mm)	Alteration halo composition	Alteration halo width (mm)
Quartz-dominated veins			
Qz-Py-Cal-Tur	9 – 10	Cal + tur	0.7 – 0.9
Qz-Py-Cal-Tur	0.2 – 0.5	Cal + minor Chl + trace Ep	<0.1
Qz-Py-Tur	7 – 19	Minor Tur	<0.1
Qz-Py	1	Ep + Ser + Chl + trace Tur	<0.1 – 2
Qz-Cal-Tur	3 – 20	Tur + minor Cal	0.2 – 1
Qz-Tur	3 – 8	Minor Tur + Lm	<0.1
Qz-Tur	1 – 2	Tur	2 – 3
Brecciated tourmaline veins			
Tourmalinite breccia	150 – 200	None	None
Brecciated Qz-Tur-Jsp	>100	Cal + Jsp + Chl + minor Tur	<0.1
Jasper-dominated veins			
Qz-Py-Tur-Jsp	3 – 15	None	None
Qz-Py-Jsp	5 – 10	Tur + ser	>30
Epidote-dominated veins			
Qz-Py-Tur-Ep	0.5	Chl + Ser + minor Tur	<0.1
Qz-Py-Tur-Ep	1 – 2	Tur + Ep	<0.1
Qz-Py-Tur-Ep	1 – 3	Minor Tur + trace Cal + trace Ep	<0.1
Qz-Py-Tur-Ep	1 – 2.5	Tur	<0.1
Qz-Py-Tur-Ep	0.4 – 0.8	Chl + Ep + minor Cal + trace Tur	<0.1
Qz-Cal-Tur-Ep	0.1 – 0.5	Trace Tur + trace Cal + trace Ep	<0.1
Qz-Tur-Jsp-Ep	1 – 2	Tur + Jsp + Ser	10 – 14
Qz-Tur-Ep	0.3 – 1	Ep + Lm	1 – 3
Qz-Ep	1 – 1.1	Ep	0 – 4
Barren qz			
Qz	>30	None	None

Abbreviations: Cal = Calcite, Chl = Chlorite, Ep = Epidote, Jsp = Jasper, Kfs = K-feldspar, Lm = Limonite, Py = Pyrite, Qz = Quartz, Ser = Sericite, Tur = Tourmaline (after Whitney and Evans, 2010).

Primary growth textures of quartz along quartz-dominated veins include comb texture and less commonly growth zoning and crustiform banding. Comb quartz is especially visible in veins which show open space filling, where long, subparallel quartz rods resemble the teeth of a comb. Growth zoning is seen in long quartz combs in the quartz-pyrite-tourmaline vein in YZN60a, where at least 7 growth stages can be traced across certain grains (Fig. 5.2a). Crustiform banding is only seen in the quartz-pyrite-tourmaline-calcite vein in YZN34b, where a rhythmic succession of minerals is visible (Fig. 5.2b).

There are a variety of recrystallisation textures that are displayed in the quartz-dominated veins. One of the most common recrystallisation textures displayed by quartz is plumose texture, where individual quartz grains display feathery and flamboyant extinction positions (Fig. 5.3a). This texture in quartz is not always apparent and depends on the orientation of the thin section as the stage is rotated. Chalcedony is fibrous, radial, and displays a flamboyant texture. In some veins, tiny recrystallised quartz grains form in larger quartz grains and arrange themselves in a way that mimics the shape of the large grain of quartz (Fig. 5.3a). Quartz also locally displays a mosaic texture having sutured boundaries that are irregularly shaped. In most cases, pyrite is precipitated along the centre of pyrite-bearing veins, typically overgrowing quartz along the centre of the veins, and in some veins it is present as stringers (e.g. YZN17-2, YZN34b – Fig. 5.2b).

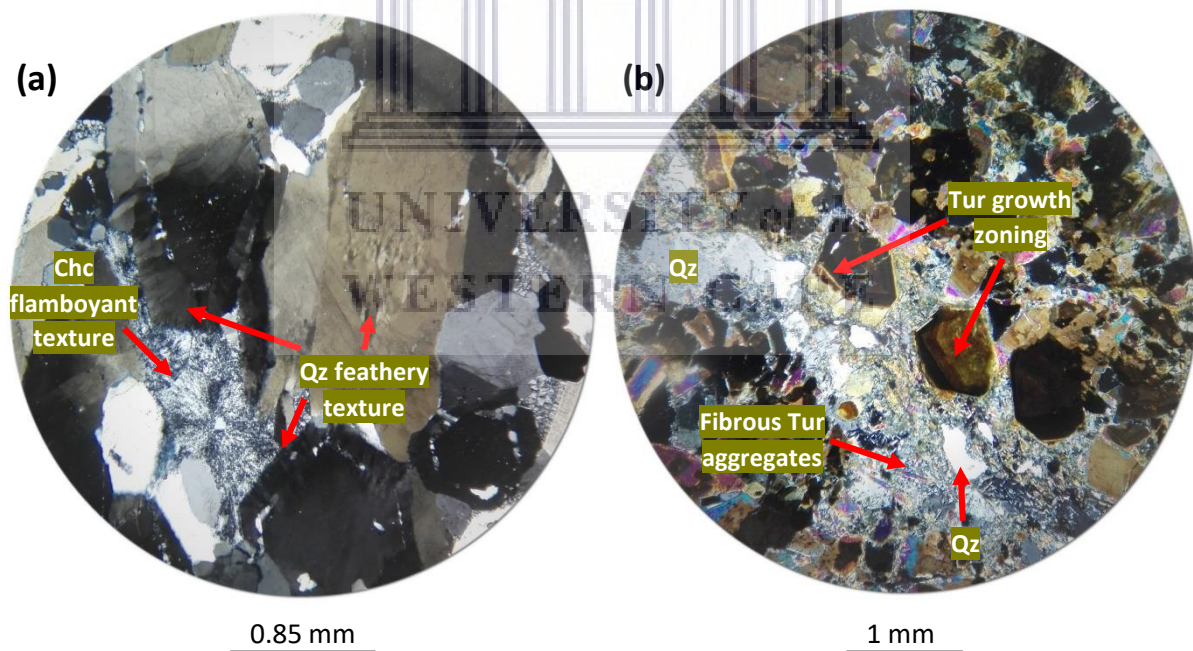


Figure 5.3: Thin section photomicrographs displaying textures in quartz and tourmaline in XPL. (a) Plumose texture in quartz in a quartz-pyrite-tourmaline vein (YZN60a). Quartz displays a plumose texture defined by a feathery texture of quartz at the edges, and locally at the centre of grains; fibrous chalcedony aggregates display a flamboyant texture. Note how tiny quartz grains form within large quartz combs and mimic their shape. (b) Hexagonal-shaped tourmaline grains showing growth zoning in a quartz-tourmaline vein (YZN61b). Chc = Chalcedony, Qz = Quartz, Tur = Tourmaline.

In most tourmaline-bearing veins, tourmaline preferentially grows outward from the vein wall, and, locally, where needles grow toward the centre, they overgrow quartz and pyrite at

the centre of the veins. Uncommonly, tourmaline overgrows quartz to such an extent that most quartz grains in the centre of the vein, as well as their textures, cannot be observed (Fig. 5.3b). Tourmaline is usually present as very fine-grained fibrous aggregates. In some veins, such as in YZN61B, tourmaline grains exhibit hexagonal shapes, some of which show growth zoning (Fig. 5.3b). It also displays a spherulitic texture in some samples, and where needles of tourmaline display incomplete radiation, they form fan-shaped aggregates; this is a common feature in tourmaline that is particularly observed in the coarse-grained variety of tourmaline.

5.3.2. Tourmaline-dominated veins

Outcrop to mesoscopic scale: The tourmaline-dominated veins occurring in the field are either tourmaline-rich, or pyrite-tourmaline-rich (Figs. 5.4a, b). Thin sections for these two vein types were not produced and therefore they will not be described petrographically. Tourmaline-dominated veins are sparsely dispersed in the study area and they mainly traverse the monzogabbro, monzonite and syenodiorite outcrops. From field observations and the measurement of the orientation of tourmaline-dominated veins, they are seen to traverse the host rocks along a NW-SE to NNW-SSE direction, and locally along a N-S to NE-SW direction (Table C1).

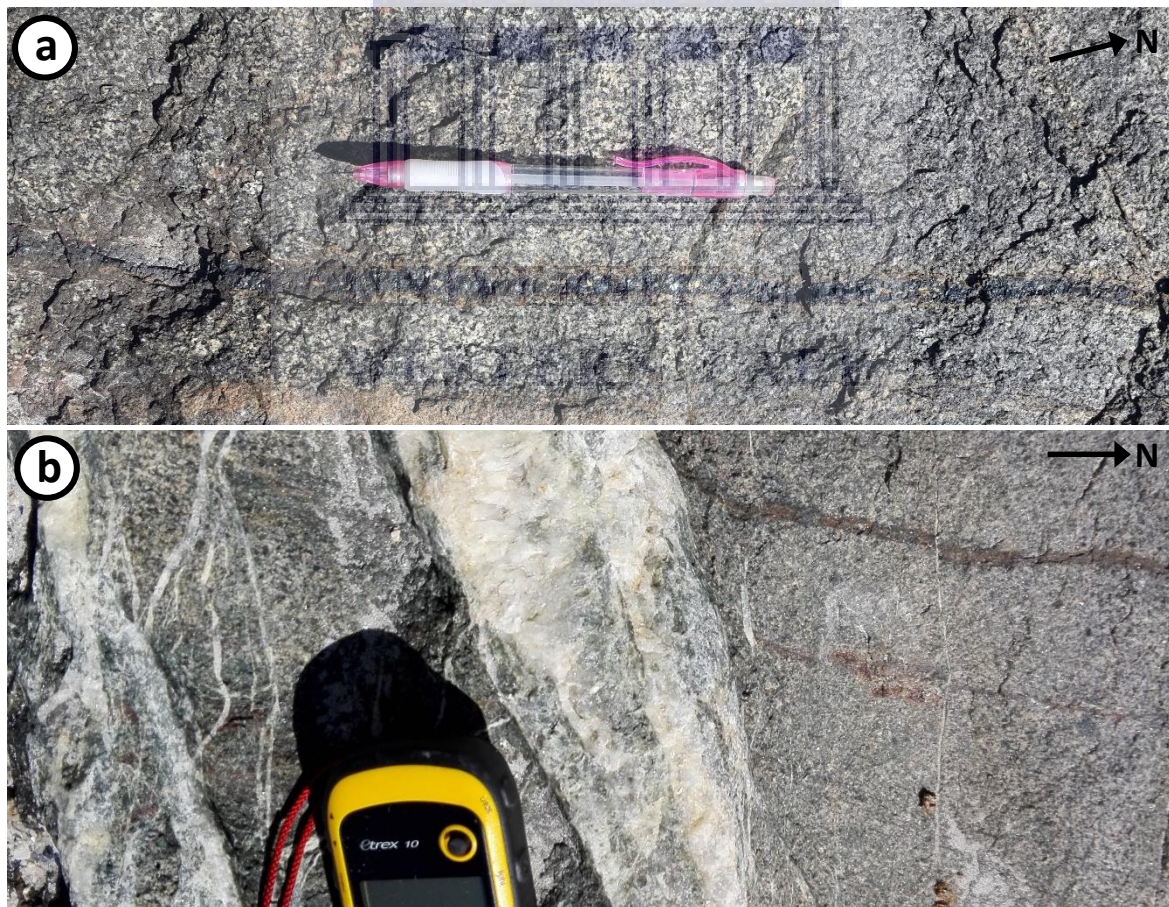


Figure 5.4: Tourmaline-dominated veins. (a) N-S-trending tourmaline-rich vein cross-cutting the monzogabbro N of the Visitors Center. The tourmaline-rich vein has an alteration halo comprising limonite and minor chlorite. (b) N-S-trending pyrite-tourmaline veins cross-cut by later ENE-WSW-trending barren quartz veins in the monzonite W of the Visitors Center. Scale: GPS with width = 5.2 cm; Pencil with length = 14.5 cm.

Tourmaline-rich veins are quite narrow, with widths ranging between 0.05 and 1.2 cm (Fig. 5.4a, Table C1). Alteration haloes associated with tourmaline-rich veins are also relatively narrow, ranging in width between 0.04 and 1.2 cm, and are comprised of either limonite, a combination of limonite and chlorite, or jasper. Pyrite-tourmaline veins have more variable widths ranging between 0.1 and 5.2 cm (Fig. 5.4b, Table C1). Alteration haloes around pyrite-tourmaline veins are either comprised of tourmaline, or a combination of tourmaline and chlorite, and range in width between 0.05 and 2 cm on either side of the vein.

5.3.3. Breccias and brecciated veins

Outcrop to mesoscopic scale: The breccias and brecciated veins occurring in the study area predominantly comprise tourmaline veins and veinlets, which are locally accompanied by other secondary minerals. They traverse monzonitic outcrops in various localities across the study area, as well as the quartz microsyenite outcrop at Grasbank. The different types of breccias and brecciated veins occurring in the field include: tourmalinite breccia, brecciated pyrite-tourmaline veins, and brecciated quartz-tourmaline-jasper veins. These breccias and brecciated veins trend in different directions as they traverse the monzonite and quartz microsyenite outcrops. In the monzonitic outcrops W and SW of the Visitors Center, brecciated tourmaline veins trend WNW-ESE to NNW-SSE, and around the Yzerfontein Harbour trend in a NW-SE to NE-SW direction. Further south, these veins trend roughly N-S around Yzerfontein Point, NW-SE at Kollege, and WNW-ESE at Grasbank and Draaibank. Finally, at Schaap Eiland, brecciated tourmaline veins trend in a N-S and WNW-ESE direction (Figs. A3 to A6 and A8 to A10; Table C1).

Brecciated tourmaline veins occurring in the field are generally quite extensive, ranging in width between 6 and 65 cm (Table C1). In many localities these veins have several tourmaline veinlets that offshoot from the main brecciated tourmaline veins, which, in most cases, trend in the same direction as the brecciated tourmaline veins. The breccias and brecciated veins irregularly and randomly enclose numerous sub-rounded to angular fragments of rock (Figs. 5.5a to d). Fragments of rock enclosed by brecciated tourmaline veins comprise varying abundances of quartz and plagioclase, and are locally either partly weathered to limonite (Figs. 5.5a, b), or have become partly altered to jasper and epidote (Fig. 5.5c). The sizes of these fragments are highly variable with the short axis ranging between 0.05 and 3.5 cm, and long axis ranging between 0.05 and 22.5 cm. Chlorite and jasper are commonly present in alteration haloes on either side of brecciated tourmaline veins, and these alteration haloes range in width between 0.1 and 4.5 cm on either side of the veins where present (Table C1).

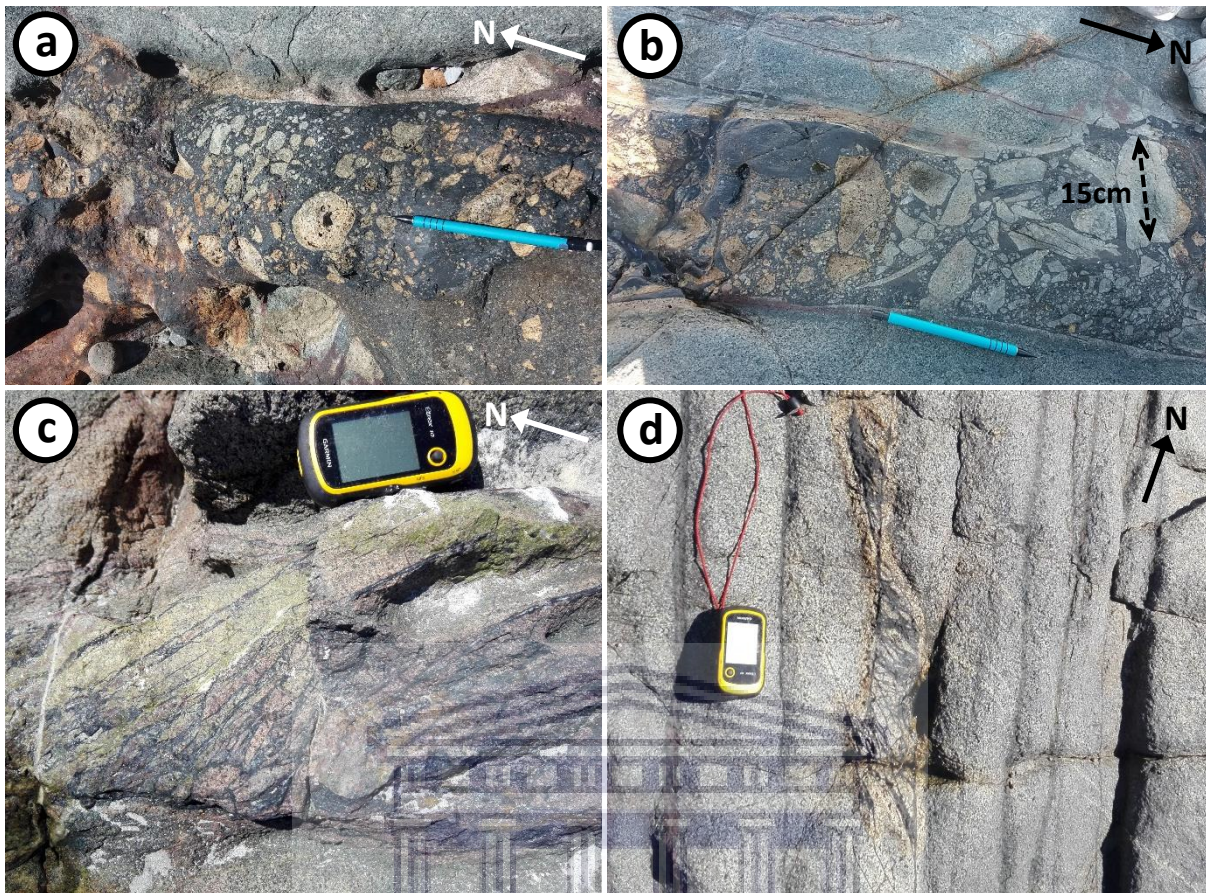


Figure 5.5: Breccias and brecciated veins occurring in the study area. (a) & (b) NNW-SSE-trending tourmalinite breccia veins cross-cutting the monzonite SW of the Visitors Center. Tourmalinite breccias enclose sub-rounded to angular fragments of weathered rock up to 15 cm in size. Alteration haloes have a rusty orange colour due to the presence of limonite. (c) NW-SE-trending brecciated quartz-tourmaline-jasper veins cross-cutting the monzonite W of the Visitors Center. Veins enclose fragments of altered rock which contain a high abundance of secondary jasper and epidote. (d) NNW-SSE-trending brecciated pyrite-tourmaline veins cross-cutting the monzonite W of the Visitors Center with an alteration halo comprising predominantly limonite. Scale: GPS with length 10 cm and width = 5.2 cm; Pencil with length = 15.2 cm.

Petrography: Thin sections of two types of brecciated tourmaline veins were produced and studied. These include: tourmalinite breccia (YZN62) and brecciated quartz-tourmaline-jasper veins (YZN78; Table 5.1.). The mineralogy and grain sizes of the minerals present in the brecciated veins and the fragmented clasts as observed in thin section were recorded in Tables 5.2 and 5.3.

The tourmalinite breccia veins display a cataclastic texture in thin section evident by numerous broken and fragmented clasts of rock enclosed by the tourmaline vein (Fig. 5.6a). It is comprised of fibrous masses of very fine-grained tourmaline. The fragments of rock enclosed by these veins comprise either predominantly quartz, or quartz with minor amounts of plagioclase and limonite. Quartz and plagioclase are coarse-grained, and locally, smaller grains of plagioclase are poikilitically included in quartz. The fragments of rock are commonly overgrown by thin tourmaline needles that grow outward from the vein walls. The brecciated quartz-tourmaline-jasper vein encloses portions of unaltered rock comprising mainly quartz and plagioclase, as well as fragments of altered rock in which the primary minerals have become almost completely altered by secondary jasper, chlorite and calcite. Examples of the

latter are locally seen by the presence of botryoidal chlorite aggregates rimmed by thin jasper bands, imparting a globular-like texture to the minerals (Figs. 5.6b, c). Calcite grains are anhedral and display weak twinning.

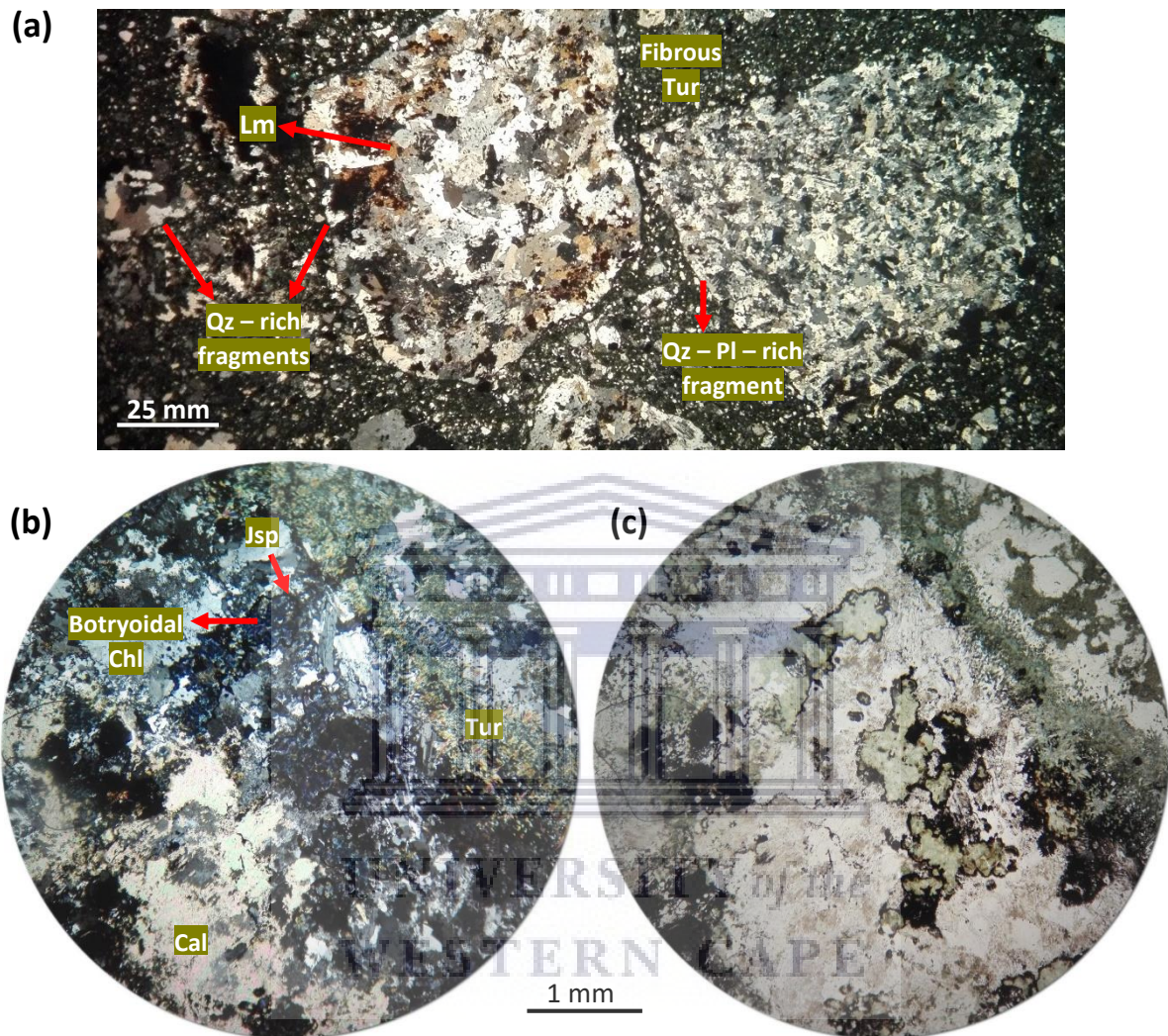


Figure 5.6: Thin section photomicrographs of brecciated tourmaline veins. (a) Tourmalinite breccia vein; rock fragments range in size between <1 – 11 mm (XPL, YZN62). (b) & (c) Brecciated quartz-tourmaline-jasper vein in XPL and PPL respectively; rock fragments range in size between <1 and 8 mm. Botryoidal chlorite aggregates are rimmed by jasper bands, defining a globular-like texture (YZN78). Cal = Calcite, Chl = Chlorite, Jsp = Jasper, Lm = Limonite, Qz = Quartz, Pl = Plagioclase, Tur = tourmaline.

5.3.4. Jasper-dominated veins

Outcrop to mesoscopic scale: There are at least six different vein types that make up the jasper-dominated vein assemblage (Table 5.1). However, only five of these vein types were described in detail during field observations of hydrothermal veins and they include: quartz-pyrite-jasper veins, quartz-calcite-tourmaline-jasper veins, quartz-tourmaline-jasper veins, pyrite-jasper veins, and tourmaline-jasper veins.

Quartz-pyrite-jasper veins traverse the monzonite outcrops at Yzerfontein Point and Draaibank and they trend in a NNW-SSE to NE-SW direction (Fig.). They range in thickness between 0.4 and 1 cm, and locally contain pyrite stringers along the centre of the veins (Fig 5.7a, Table C1). Alteration haloes predominantly comprise chlorite and tourmaline and extend between 0.05 and 3.5 cm on either side of the veins. In some localities, pyrite, which occurs in the adjacent host rock, has become oxidised to form limonite, giving the alteration haloes a rusty orange appearance. Quartz-calcite-tourmaline-jasper veins are unusual and cross-cut the monzonite at Grasbank in a NNE-SSW direction. These veins have widths that ranges between 3 and 3.9 cm, with chlorite and/or epidote alteration haloes that extend between 1.4 and 1.5 cm on either side of the vein (Table C1).

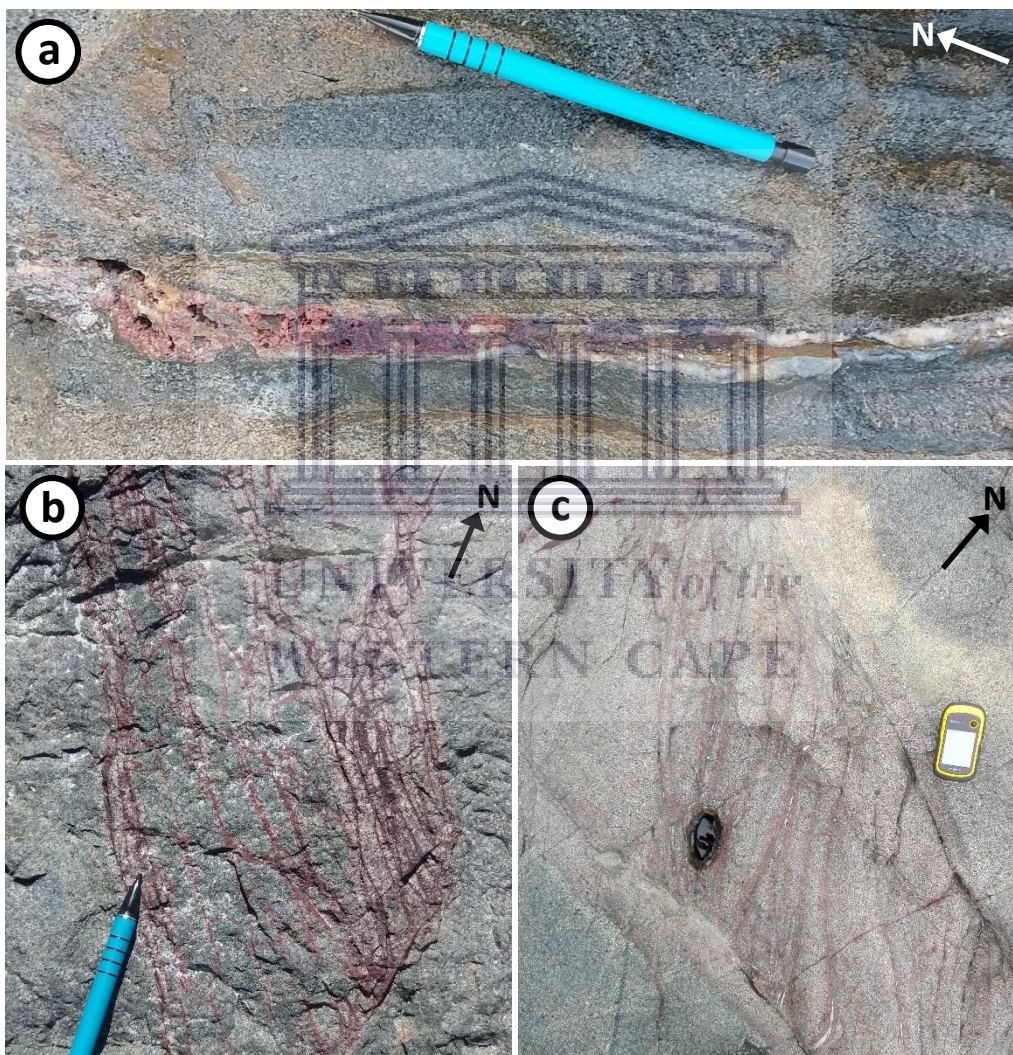


Figure 5.7: (a) NNW-ESE-trending quartz-pyrite-jasper vein cross-cutting the monzonite at Schaap Eiland. Note the change in composition of the vein from quartz-jasper-rich (NNW, left in figure) to more quartz-pyrite-rich (SSE, right in figure). In this case, the alteration halo on either side of the vein is composed of chlorite and limonite. (b) & (c) NW-SE-trending sheeted quartz-tourmaline-jasper veins cross-cutting the monzonite SW of the Visitors Center and the syenodiorite N of the Visitors Center respectively. In (b), note how late-forming jasper has altered the surrounding host rock, forming large alteration haloes that range in width between 0.1 and 20 cm. Scale: GPS with length = 10 cm and width = 5.2 cm; Pencil with length = 15.2 cm.

Quartz-tourmaline-jasper veins traverse the syenodiorite and monzonite at various locations across the study area; these veins mainly trend in a WNW-ESE to NNW-SSE direction, and locally also trend in a NNE-SSW direction. Networks of sub-parallel quartz-tourmaline-jasper veins commonly form sheeted veins, and in some localities they meet and cross-cut each other (Fig. 5.7b, c). Sheeted veins in the study area extend over tens of metres in distance in some localities, such as at Grasbank. Individual veins that make up the sheeted veins are generally thin, ranging in thickness between 0.05 and 1.3 cm (Table C1). Hydrothermal alteration haloes associated with sheeted veins are comprised of jasper and chlorite, and, locally, epidote. The width of alteration haloes varies considerably depending on the extent of alteration, ranging between 0.1 and 20 cm. In some localities, such as at Hoëbank, quartz-tourmaline-jasper veins (1.8 – 2 cm in thickness) are folded within the monzonite, which is a feature that has not been observed in veins towards the north of the study area (Fig. C2).

Both pyrite-jasper and tourmaline jasper-veins are NW-SE-trending veins. On the one hand, pyrite-jasper veins occur in the monzonitic outcrops at Schaap Eiland, range in thickness between 0.6 and 1.7 cm, and have alteration haloes that are comprised of chlorite and limonite (between 0.2 and 1.8 cm in thickness) (Fig. 5.8a; Table C1). Tourmaline-jasper veins, on the other hand, traverse the monzonitic outcrops SW of the Visitors Center and the syenodiorite at Hoëbank (Fig. 5.8b), range in thicknesses between 0.1 and 2.6 cm, and have alteration haloes that are comprised of jasper and chlorite (between 0.2 and 0.8 cm in thickness) (Fig. 5.8b; Table C1).

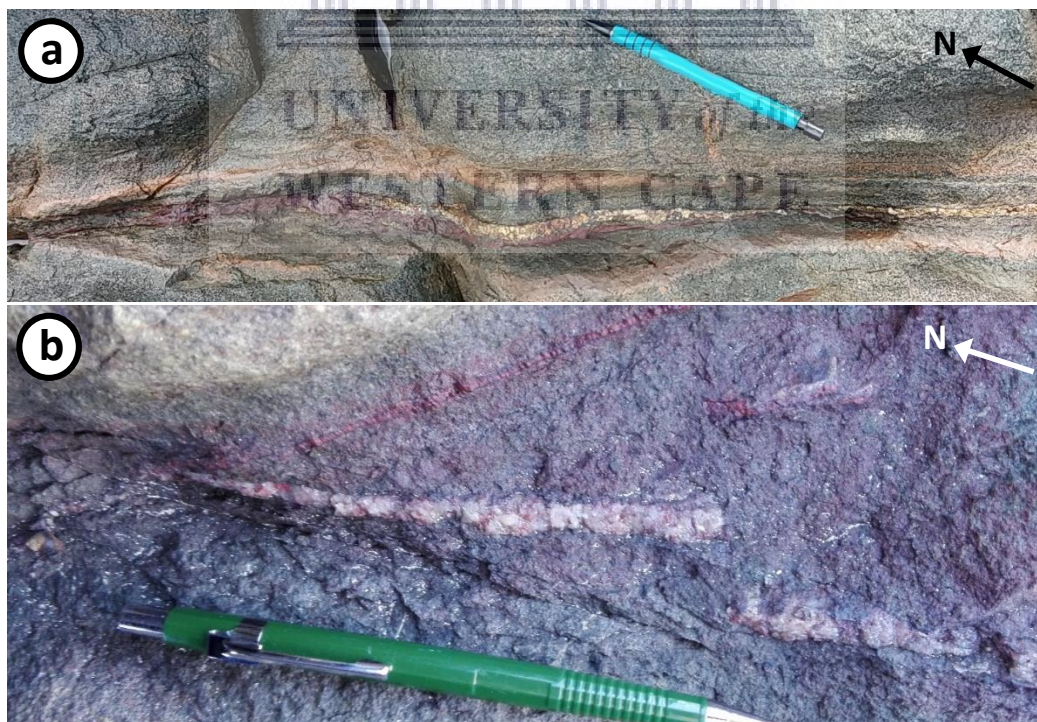


Figure 5.8: (a) NW-SE-trending pyrite-jasper vein cross-cutting the monzonite at Schaap Eiland. Note the change in composition of the vein from jasper-rich (NW, left in figure) to pyrite-jasper-rich (centre of figure), and finally to pyrite-rich (SE, right in figure). (b) NW-SE-trending tourmaline-jasper vein (top in figure) cross-cutting the monzonite at Hoëbank. Veins are offset and show a dextral sense of movement. Scale: Blue pencil with length = 15.2 cm; Green pencil with length = 14.4 cm.

Petrography: Thin sections of two types of jasper-dominated veins were produced, one of which was not studied in detail during field observations of hydrothermal veins. These veins include: quartz-pyrite-jasper veins (e.g. YZN17-1) and quartz-pyrite-tourmaline-jasper veins (e.g. YZN59a; Table 5.1).

The thickness of the quartz-pyrite-jasper veins ranges between 3 and 10 mm, and they have alteration haloes that extend >30 mm on either side of the vein (Tables 5.2, 5.3). Alteration is quite pervasive and comprises fine-grained tourmaline and sericite which replaces quartz and feldspar in the adjacent host rock. The quartz-pyrite-tourmaline-jasper vein has a thickness of >35 mm and occupies the entire thin section. In both veins, silica displays a bimodal grain size distribution, comprising aggregates of fibrous chalcedony as well as coarser crystalline quartz. Colloform banding is well developed in the quartz-pyrite-jasper vein and is defined by thin concentric bands of jasper alternating with fine-grained, fibrous layers of chalcedony aggregates (Fig. 5.9a). The vug around which colloform banding is developed is filled by quartz grains that show an increase in grain size from the walls of the vug towards the centre. In the quartz-pyrite-tourmaline-jasper vein, a globular texture is formed by botryoidal quartz aggregates that are enclosed by thin jasper bands (Fig. C3); microcrystalline quartz grades into a coarser variety of quartz towards the centre of the vug.

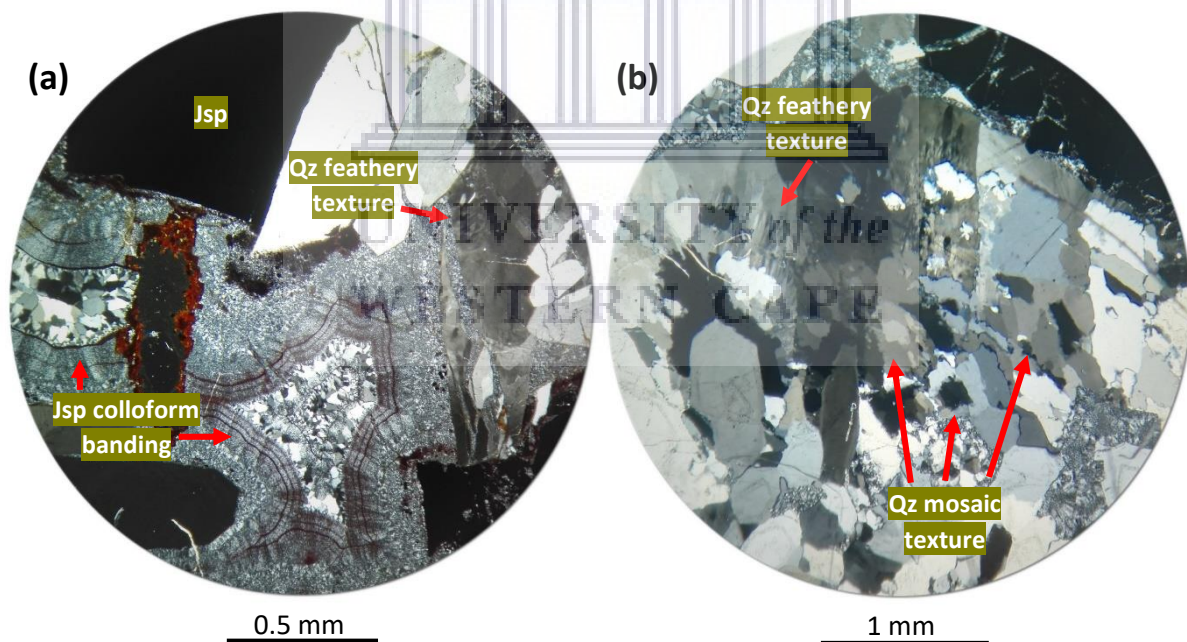


Figure 5.9: Thin section photomicrographs in XPL displaying primary growth- and recrystallisation textures in quartz. (a) Colloform banding around a vug filled with quartz in a quartz-pyrite-jasper vein (YZN17-1). Note the feathery texture at the edge of an adjacent quartz grain. (b) Mosaic texture in quartz displaying interpenetrating grain boundaries in a quartz-pyrite-tourmaline vein (YZN59). Jsp = Jasper, Qz = Quartz.

In some places along the quartz-pyrite-tourmaline-jasper vein, multiple interpenetrating quartz grain boundaries display a mosaic texture (Fig. 5.9b). Comb quartz is present in both vein types and present where long, euhedral quartz grains have grown toward the centre of

open spaces. Locally, quartz also displays either feathery or flamboyant extinction positions, defining a plumose texture (Figs. 5.9a, b). Anhedral pyrite grains form clumps along the centre of the quartz-pyrite-jasper vein, whereas in the quartz-pyrite-tourmaline-jasper vein, pyrite grains are more scattered along the vein. In both veins, tourmaline is present as fibrous and compact aggregates. Uncommonly, tourmaline needles are slightly coarser grained (0.5 mm), and locally display a spherulitic texture.

5.3.5. Epidote-dominated veins

Outcrop to mesoscopic scale: There are at least five different types of epidote-dominated veins (Table 5.1), however, only one of these vein types was studied in detail in the field, namely quartz-epidote veins (Fig. 5.10a, b). Geological samples have, however, been collected of all five vein types which were used to cut thin sections for petrographic examination. Quartz-epidote veins cross-cut nearly all the rock types within the study area and are one of the most common vein types. From field observations of quartz-epidote veins and the measuring of their orientation, it is evident that they cross-cut the host rocks in various directions from E-W to NNE-SSW. Quartz-epidote veins are generally thin with widths ranging between 0.04 and 1.5 cm (Table C1).

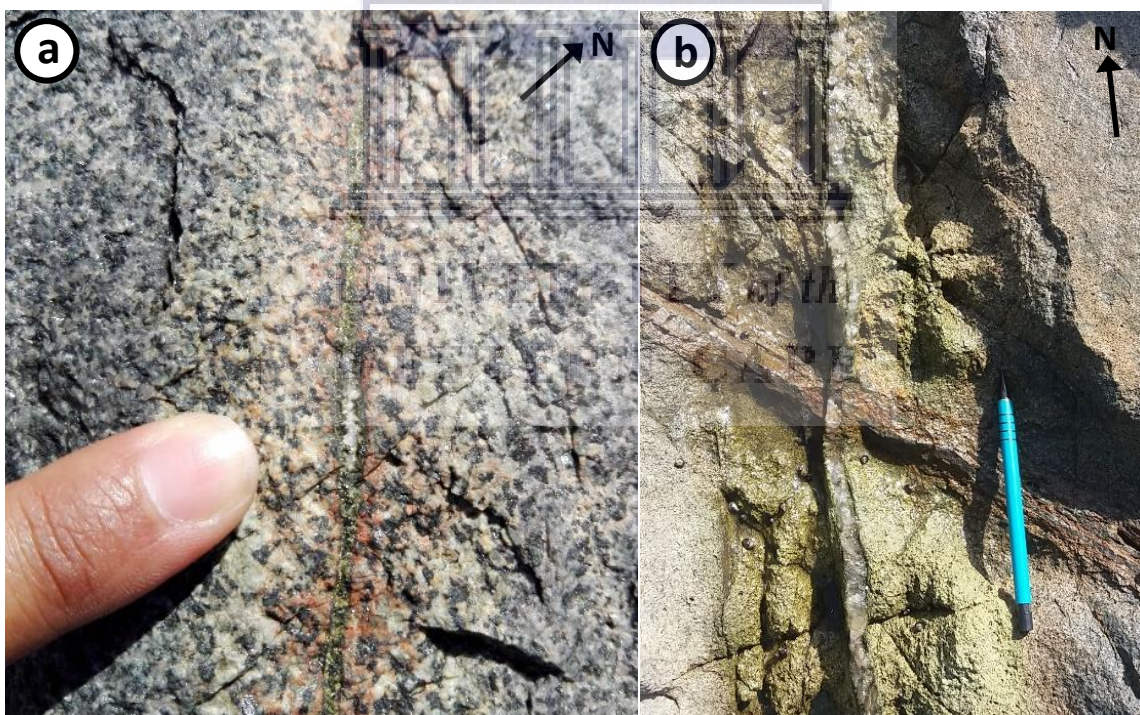


Figure 5.10: Quartz-epidote veins occurring in the study area. (a) NW-SE-trending quartz-epidote vein cross-cutting the syenodiorite N of the Visitors Center. Note the pink discolouration of the rock as a result of alteration, and the change in composition of the vein along its length. It changes from epidote-rich (NW, top in figure) to quartz-rich (centre of figure), and once again becomes epidote-rich (SE, bottom of figure). (b) N-S-trending quartz-epidote vein cross-cutting a gossanous quartz-pyrite vein in the monzonite at Schaap Eiland. The alteration halo comprises epidote and minor chlorite and ranges in width between 6 and 9 cm on either side of the vein. Scale: Finger with width = 1.4 cm; Pencil with length = 15.2 cm.

Quartz-epidote veins have alteration haloes that comprise epidote or chlorite, or a combination of these minerals, which usually stains the rock green on either side of the vein

(Fig. 5.10b). Locally, epidote alteration is accompanied by sericite. Uncommonly, chlorite alteration is associated with jasper, and, locally, sericite. In some localities, the wall rock adjacent to quartz-epidote veins display a pink discolouration, which may be due to the introduction of secondary K-feldspar (Fig. 5.10a). Alteration haloes around quartz-epidote veins have widths that ranges between 0.03 and 5 cm (Table C1).

Petrography: Thin sections of all five epidote-dominated veins were produced and studied. These include: quartz-pyrite-tourmaline-epidote (YZN17-2, YZN38, YZN69, YZN81 and YZN83), quartz-calcite-tourmaline-epidote (YZN30), quartz-tourmaline-jasper-epidote (YZN25), quartz-tourmaline-epidote (YZN36), and quartz-epidote veins (YZN50) (Table 5.1).

Epidote-dominated veins have thicknesses ranging between 0.1 and 3 mm in thin section (Tables 5.2 and 5.3). In most thin sections, secondary minerals do not form well defined alteration haloes around the veins, but instead are disseminated in the surrounding host rock, weakly and randomly replacing primary minerals. Where alteration haloes are present, they range in thickness between <0.1 and 14 mm. Secondary minerals associated with alteration include either one or a combination of minerals including chlorite, sericite, tourmaline, calcite, epidote, jasper and limonite. Uncommonly, tourmaline displays a vermicular or bleb-like texture adjacent to the veins, and is intergrown with tiny blebs of quartz (Fig. 5.11a). These tourmaline grains display zonal compositional and colour variation, reflecting two different compositions of tourmaline, where the core is defined by tourmaline with a brown pleochroism mantled by a strongly blue pleochroic and Fe-rich variety of tourmaline at the rims (Figs. 5.11a, b).

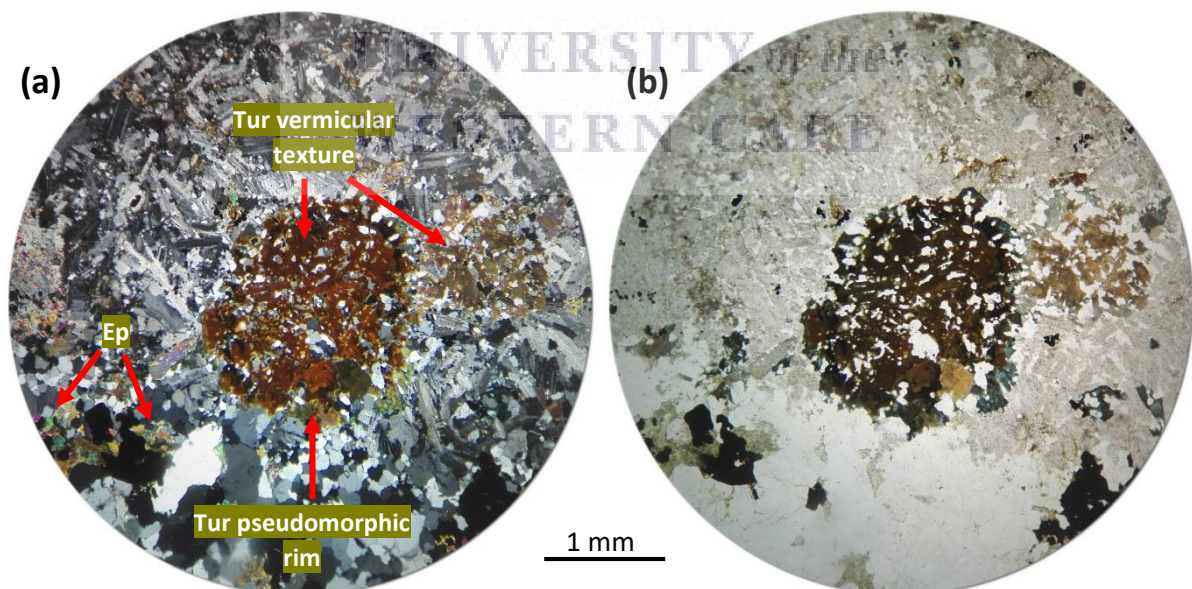


Figure 5.11: Thin section photomicrographs displaying vermicular-textured tourmaline grains intergrown with quartz adjacent to a quartz-pyrite-tourmaline-epidote vein in (a) XPL and (b) PPL (YZN38). Ep = Epidote, Tur = Tourmaline.

In many of the veins, primary growth textures in quartz cannot be readily identified due to later secondary mineral growth overgrowing or replacing quartz, such as pyrite, jasper and

epidote. Primary growth textures in quartz include a feathery texture, where quartz grains display multiple extinction positions (Fig. C4a). In some veins, recrystallisation of quartz in veins has resulted in a mosaic texture where the irregular grain boundaries in quartz interlock (Fig. C4b).

5.3.6. Calcite-dominated veins

Outcrop to mesoscopic scale: Calcite-dominated veins mainly occur in the Yzerfontein Harbour area, traversing the syenodiorite (Fig. A4). There are two types of calcite-dominated veins, including: calcite, and epidote-calcite veins (Table 5.1). Thin sections for calcite-dominated veins were not produced and therefore they will not be described petrographically. Calcite veins cross-cut the syenodiorite in a NW-SE direction and are relatively thin, ranging in thickness between 0.2 and 0.5 cm (Fig. 5.12, Table C1). Based on field observations of calcite veins, they do not have any alteration haloes associated with them. Epidote-calcite veins trend in a WNW-ESE to NW-SE direction and they range in thickness between 0.1 and 0.3 cm. Alteration haloes around epidote-calcite veins range in thickness between 3.2 and 7 cm and are comprised of epidote and minor chlorite.

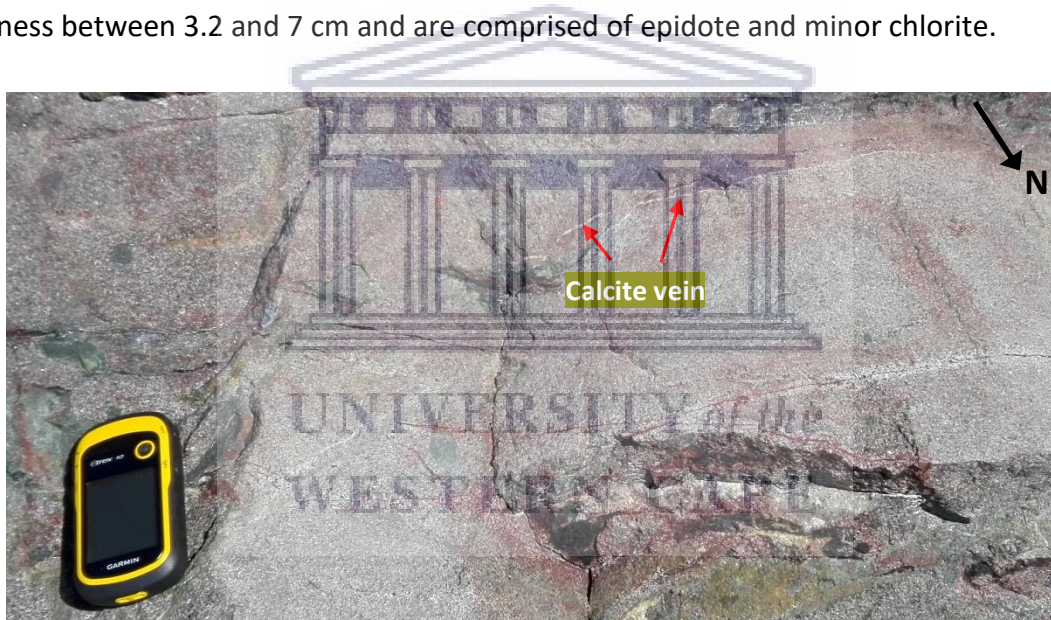


Figure 5.12: WNW-ESE-trending calcite vein cross-cutting the syenodiorite in the Yzerfontein Harbour. Jasperlitic alteration haloes close to calcite vein are associated with very thin tourmaline-jasper veins a few millimetres to centimetres away on either side of the calcite vein. Scale: GPS with length = 10 cm and width = 5.2 cm.

5.3.7. Barren quartz veins

Outcrop to mesoscopic scale: Barren quartz veins cross-cut the syenodiorite and monzonite in the study area and they trend in a ENE-WSW to NW-SE direction. Barren quartz veins range from very thin to massive, with thicknesses ranging between 0.3 and 25 cm, and do not have any alteration haloes associated with them (Fig. 5.13a, b; Table C1). Barren quartz veins cross-cut and locally offset earlier formed veins in the study area, and therefore represent the last and youngest generation of hydrothermal veining in the study area (Fig. 5.4b).



Figure 5.13: ENE-WSW-trending barren quartz veins traversing the monzonite W of the Visitors Center. (a) Quartz vein 2 – 10 cm in thickness and (b) quartz vein 2 – 4 cm in thickness cross-cutting a quartz-pyrite-tourmaline-jasper vein. Scale: GPS with length = 10 cm and width = 5.2 cm.

Petrography: Silica has a bimodal grain size distribution, with both chalcedony and coarser crystalline quartz present (Fig. 5.14). Large quartz combs are abundant, with grains reaching up to 7 mm in length. Locally, quartz display a comb texture resembled by quartz grains preferentially growing inward with sub-parallel c-axes. Plumose texture in quartz is an abundant primary growth texture, and is seen by the feathery appearance of larger quartz grains as the stage is rotated (Fig. 5.14).

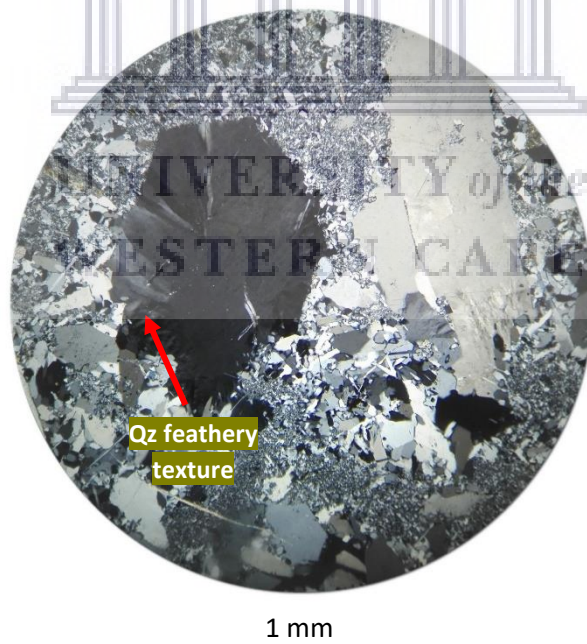


Figure 5.14: Thin section photomicrograph displaying a bimodal grain size distribution of silica in a barren quartz vein (XPL, YZN44). Large crystalline quartz grains frequently display a feathery texture, most commonly at the grain margins. Qz = Quartz.

5.4. Compositional changes in hydrothermal veins

Outcrop to mesoscale: In certain localities in the study area, hydrothermal veins show changes in mineralogical composition in certain directions along their length. One of the most important overall field observations made was the increase in the amount of pyrite in veins towards the south, particularly in veins at Schaap Eiland and Freddie se Klip (Figs. A9, A10). The quartz-pyrite and quartz-pyrite-tourmaline veins in these areas are also conspicuously thicker than at the other locations in the study area, particularly along the hydrothermal zone in the channel area that separates Schaap Eiland from the parking lot (Figs. A8, A9).

There are a number of observations recorded in the field where veins change in composition along their length in a particular direction. The following are just a few examples of hydrothermal veins that show a change in composition along their length:

- A quartz-tourmaline vein N of the Visitors Center shows a change in composition from ENE to WSW from quartz-rich to tourmaline-rich (Fig. 5.1a).
- A quartz-pyrite-tourmaline vein W of the Visitors Center displays a change in composition from N to S from quartz-pyrite-tourmaline-rich to quartz-tourmaline-rich, and finally to pyrite-tourmaline-rich at the southernmost end of the vein.
- N of the Visitors Center, a quartz-epidote vein displays a change in composition from NW to SE from epidote-rich to quartz-rich at the centre, and it once again becomes epidote-rich towards the SE (Fig. 5.10a).
- At Hoëbank, a quartz-tourmaline-jasper vein displays a change in composition from NW to SE from quartz-tourmaline-jasper-rich to tourmaline-jasper-rich.
- A quartz-pyrite-tourmaline vein at Draaibank changes in composition from N to S from quartz-pyrite-rich to tourmaline-rich.
- A quartz-pyrite-jasper vein at Schaap Eiland displays a change in composition from NNW to SSE from quartz-jasper-rich to quartz-pyrite-rich (Fig. 5.7a).
- At Schaap Eiland, a quartz-pyrite vein changes in composition from NW to SE from quartz-rich to pyrite-rich.

An overall, generalised observation from the above examples is that the veins are seemingly more pyrite-rich toward the S and E, and more quartz- and jasper-rich toward the N and W. The above observations may directly reflect the evolution of the hydrothermal fluids in these directions. It could potentially point to a source for the fluids more toward the SE where there is more Fe and S, and becoming more dilute and silica-rich further away from the source toward the NW. However, this requires a more in-depth investigation of the change in composition of veins in different directions.

Petrography: A set of 4 thin sections were cut from a quartz-pyrite-tourmaline vein from Schaap Eiland in order to conduct a more magnified examination of the change in composition along the length of the vein from W (YZN60d) to E (YZN60a) (Fig. 5.15a to d). The thin sections were cut from the central parts of the vein, which is the most representative part of the vein,

and therefore only these portions of the vein were studied. From petrographic observations, a decrease in the abundance of both quartz and pyrite was observed from W to E, as opposed to tourmaline which increases in abundance (Fig. 5.15a to d).

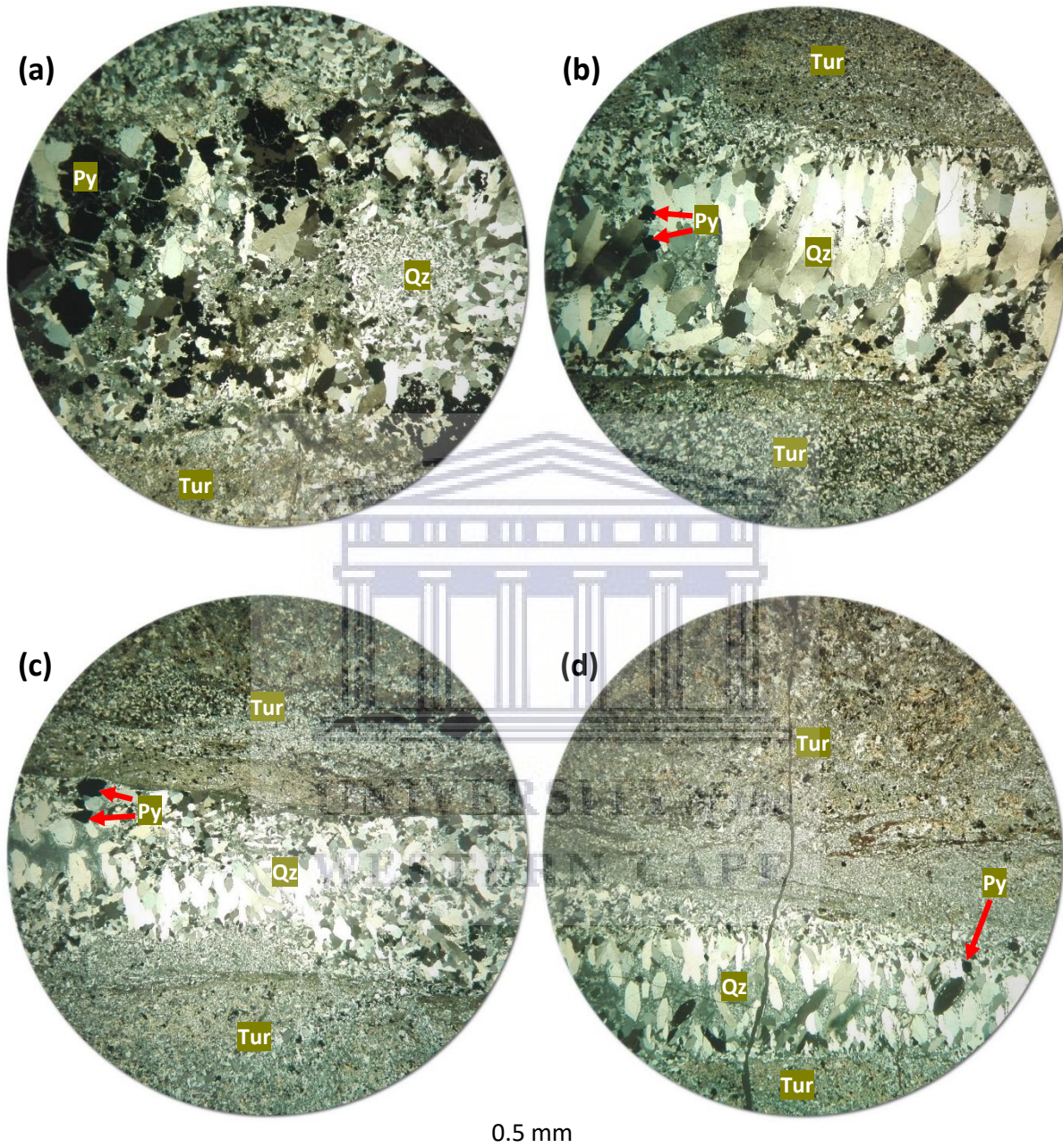


Figure 5.15: Thin section photomicrographs demonstrating the change in composition in a quartz-pyrite-tourmaline vein at Schaap Eiland from W to E (XPL). The most notable observation is that the vein at YZN60d in (a) displays the highest abundance of quartz and pyrite, and the lowest abundance of tourmaline. Moving further E towards YZN60c in (b), the abundance of pyrite has significantly decreased, while the abundance of quartz only slightly decreased. The grain sizes of quartz are also larger in YZN60c. Further E at YZN60b in (c), the abundance and grain size of quartz decrease significantly, fibrous tourmaline becomes more abundant, and pyrite is scarce. These change persist through to (d) at YZN60a where fibrous tourmaline occupies the largest part of the field of view. Py = Pyrite, Qz = Quartz, Tur = Tourmaline.

The width of the vein which is occupied by quartz becomes progressively thinner from W to E, as the width of the vein occupied by fibrous tourmaline aggregates progressively increases.

The largest grain sizes of quartz are observed in YZN60c (i.e. towards the W, Fig. 5.15b), where long, sub-parallel comb-textured quartz that reaches up to 6 mm along their long axis grow towards the centre of the vein as they fill the open space. The grain size of quartz crystals further decreases from W to E and microcrystalline quartz becomes more abundant along the centre of the vein. Growth zonation in crystalline quartz also seemingly becomes more common in comb quartz further E, which, upon magnification, is defined by tiny primary fluid inclusions that mimic the shape of the quartz grains.

5.5. Paragenetic sequence of hydrothermal events

A paragenetic sequence refers to the order or sequence in which minerals have formed, listed in a genetic time succession from earliest to latest (Ineson, 1989; Robb, 2005). There is no single “custom method” for the determination of a paragenetic sequence, but instead it involves a number of different methods and principles which require detailed examination in order to develop a paragenetic model (Ineson, 1989; Craig and Vaughan, 1994). Multiple methods have been used to determine a paragenetic sequence, whether it is by making use of the habit and textures displayed by the minerals (crystal morphology, colloform banding or growth zoning), replacement or pseudomorphic reactions, twinning and exsolution, or cross-cutting relationships, or making use of ancillary techniques (cathodoluminescence and fluorescence). Essentially, all these methods can be used to elucidate a paragenetic sequence. In this study, the paragenetic sequence of the minerals occurring in the hydrothermal veins was determined using two different methods or principles: 1.) overgrowth, replacement and growth zoning relationships, and 2.) cross-cutting relationships. The former method is an integrated one, comprising three different principles that can be used in the petrographic examination of hydrothermal veins in order to decipher the paragenetic sequence. Table 5.4 illustrates the paragenetic sequence of minerals that formed during hydrothermal activity in the Yzerfontein Pluton, which resulted in hydrothermal veining and alteration.

5.5.1. Overgrowth, replacement and growth zoning relationships

The principle of minerals overgrowing and/or replacing one another as a means of determining a paragenetic sequence relies on the notion that a mineral that is being overgrown or replaced (pseudomorphed) is older than the one overgrowing or replacing it (Craig and Vaughan, 1994). Multiple examples of minerals overgrowing and replacing one another were observed in thin section. Growth zonation can be seen both in petrographic thin section, as well as in CL imaging, and the growth bands display a colour and compositional variation suggesting a change in the environment of formation of a particular mineral (section 7.2) (Craig and Vaughan, 1994; Dye, 2015; Frelinger et al., 2015).

i.) Stage 1

During the earliest stage of hydrothermal fluid flow, quartz and chalcedony were the first minerals to precipitate from hydrothermal solutions along pre-existing fractures and joints (Table 5.4). This is indicated by the overgrowing of quartz by all other secondary minerals along hydrothermal veins, including pyrite, calcite, tourmaline, jasper and epidote during

later hydrothermal stages. Quartz usually occupies the central parts of all quartz-bearing hydrothermal veins, growing from the walls of veins towards the centre during open space filling. Locally, quartz at the centre of veins is accompanied by later formed pyrite (Fig. 5.2b) and/or jasper, tourmaline (Fig. C4b) and epidote (Fig. 5.19a). Quartz commonly comprises growth bands, as illustrated in Fig. 5.2a, where quartz shows at least seven distinct growth bands. This suggests that the environment of formation of quartz must have changed several times, and could also indicate that quartz precipitated in more than one stage of hydrothermal flow.

The formation of quartz and chalcedony during stage 1 was accompanied by the deposition of pyrite and calcite (Table 5.4). This paragenesis of minerals is illustrated in Fig. 5.2b where quartz is overgrown by pyrite at the centre of a quartz-pyrite-calcite-tourmaline vein at YZN34b, and in Fig. 5.16, where nearly all quartz at the centre of the vein has been overgrown by calcite (and tourmaline) in a quartz-calcite-tourmaline-epidote vein at YZN30. During this stage, incipient hydrothermal alteration of the surrounding host rock resulted in the replacement of primary pyroxenes and feldspars by chlorite, calcite and sericite in the adjacent host rock (e.g. Figs. 5.6b, c).

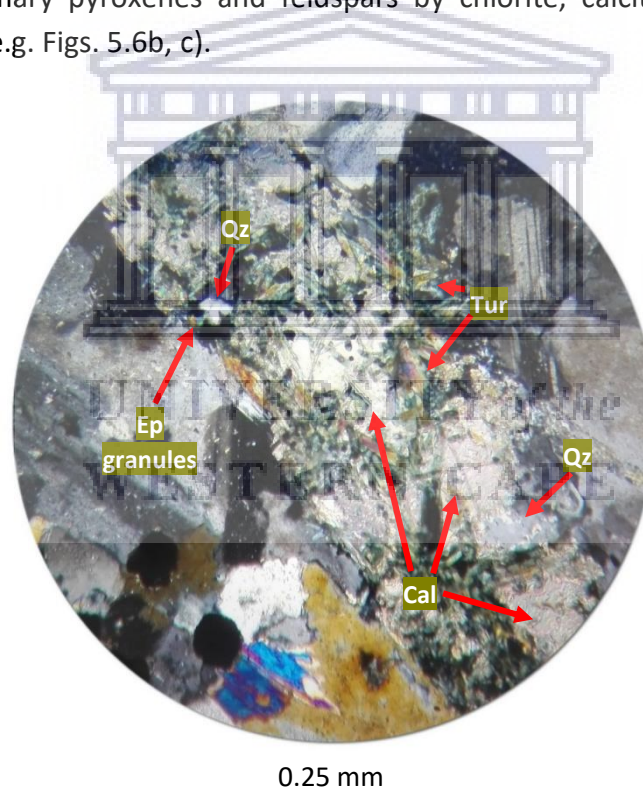


Figure 5.16: Thin section photomicrograph of a quartz-calcite-tourmaline-epidote vein in XPL at YZN30. It illustrates how nearly all quartz along the vein formed during the first hydrothermal event have become replaced by later formed minerals such as calcite and tourmaline. Cal = Calcite, Ep = Epidote, Qz = Quartz, Tur = Tourmaline.

ii.) Stage 2

Precipitation of pyrite, quartz and chalcedony from hydrothermal solutions persisted through the second hydrothermal event, accompanied by tourmaline and jasper along pre-existing conduits and veins (Table 5.4). This stage also involved the formation of brecciated tourmaline veins and sheeted quartz-tourmaline-jasper veins. This stage marks the main ore-forming

event marking the precipitation of low-grade pyrite mineralisation from hydrothermal solution, the locus of which is at Schaap Eiland. Schaap Eiland and Freddie se Klip are the only localities where pyrite occurs as thick stringers along quartz-pyrite-bearing veins (Fig. 5.17). Massive gossanous veins at Schaap Eiland, such as the one illustrated in Fig. C1, are remnants of pyrite mineralisation and are another marker for the precipitation of low-grade pyrite ore.



Figure 5.17: WNW-ESE-trending quartz-pyrite vein at Freddie se Klip ranging in thickness between 2.8 and 4 cm. Scale: Pencil with length = 14.5 cm.

This stage of hydrothermal activity was the most complex stage of all, as petrographic examination of hydrothermal veins reveals complex overgrowth relationships. Pyrite is commonly overgrown by tourmaline, however, in some veins tourmaline is overgrown by pyrite (along pre-existing veins and in the adjacent host rock). The pyrite overgrown by tourmaline, as shown in Fig. 5.18a, was precipitated during the first stage of hydrothermal activity. The pyrite overgrowing tourmaline, both in veins and in the adjacent host rock, as shown in Fig. 5.18b, precipitated from solution during the second stage of hydrothermal activity. This indicates that the precipitation of tourmaline was subsequently followed by the precipitation of stage 2 pyrite. This clearly testifies to the continued precipitation of pyrite during the second stage of hydrothermal activity. Other than tourmaline overgrowing stage one pyrite, evidence for the precipitation of tourmaline during the second stage is petrographically illustrated where tourmaline overgrows quartz and calcite (Figs. 5.16, 5.18a). Commonly, tourmaline is present at the vein walls where it grew outward into the surrounding host rock, and locally towards the vein centre. However, tourmaline aggregates also locally form randomly at the centre of some veins, as illustrated in Figs. 5.3b, C3a, b, C4a, b, and 5.16.

In jasper-bearing veins, jasper is rarely overgrown by any of the earlier formed minerals occurring in the hydrothermal veins, including tourmaline. One thin section in particular, YZN17-1, shows how pyrite overgrows jasper (Fig. 5.18c). This indicates that as jasper precipitated from solution early during stage 2, it was subsequently followed by the precipitation of pyrite. In botryoidal aggregates comprising quartz and chlorite rimmed by jasper bands, the growth of adjacent tourmaline needles and aggregates sharply terminates at the contact of jasper, which is an indication that jasper must have formed after tourmaline. The second hydrothermal event was also accompanied by moderate hydrothermal alteration of the surrounding host rock minerals. Hydrothermal alteration involved tourmaline and

jasper, which commonly form hydrothermal alteration haloes around veins. These alteration haloes also incorporated or accompanied minerals formed during the first stage of hydrothermal alteration (see Tables 5.3 and C1 for compositions of alteration haloes).

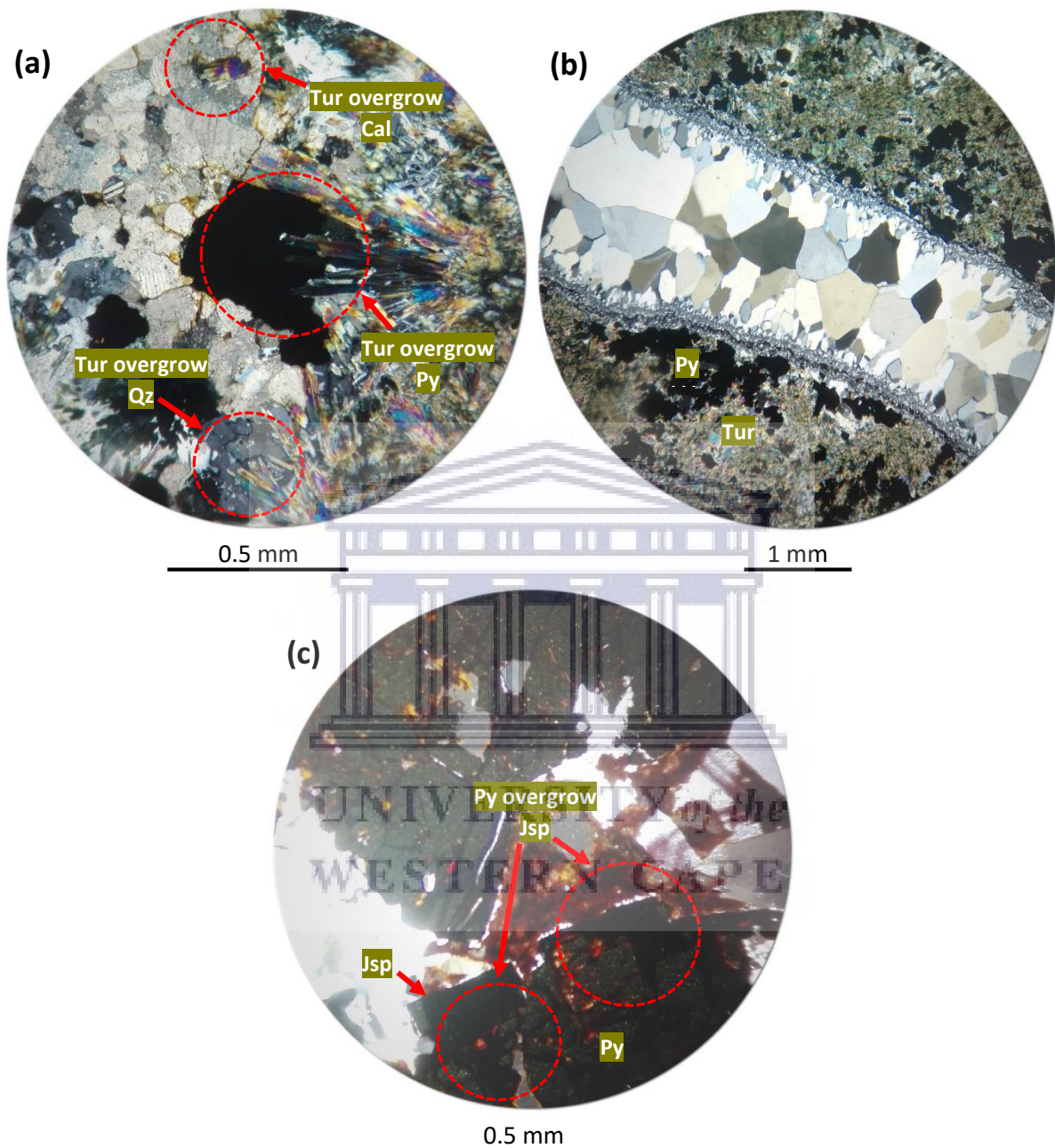


Figure 5.18: Thin section photomicrographs in XPL illustrating (a) tourmaline overgrowing stage 1 quartz, pyrite and calcite in a quartz-pyrite-calcite-tourmaline vein (YZN34b), (b) stage 2 pyrite overgrowing fibrous tourmaline adjacent to a quartz veinlet offshoot from the quartz-pyrite-tourmaline-jasper vein (YZN59a), and (c) stage 2 pyrite overgrowing jasper in a quartz-pyrite-jasper vein (YZN17-1). Cal = Calcite, Ep = Epidote, Jsp = Jasper, Py = Pyrite, Qz = Quartz, Tur = Tourmaline.

iii.) Stage 3

During this stage, quartz, chalcedony and tourmaline continued to precipitate from hydrothermal solutions along pre-existing conduits and veins, along with epidote and pyrite. In thin section, epidote is not frequently seen forming in large quantities or as large grains in

epidote-bearing veins, except for in quartz-epidote veins (Fig. 5.19a). In thin section, epidote is commonly seen overgrowing earlier formed quartz (Fig. 5.19a) and tourmaline (Fig. 5.19c). Epidote is also commonly seen overgrowing pyrite, however, in some veins, epidote is seen to be overgrown by pyrite. This suggests two points: 1.) stage 3 epidote overgrows earlier formed pyrite, most likely that which formed during stage 2 (Fig. 5.19b), and, 2.) pyrite continued to precipitate during the later phases of stage 3, and, in turn, overgrows minerals which formed during the earlier phases of stage 3, including epidote and tourmaline (Fig. 5.19d).

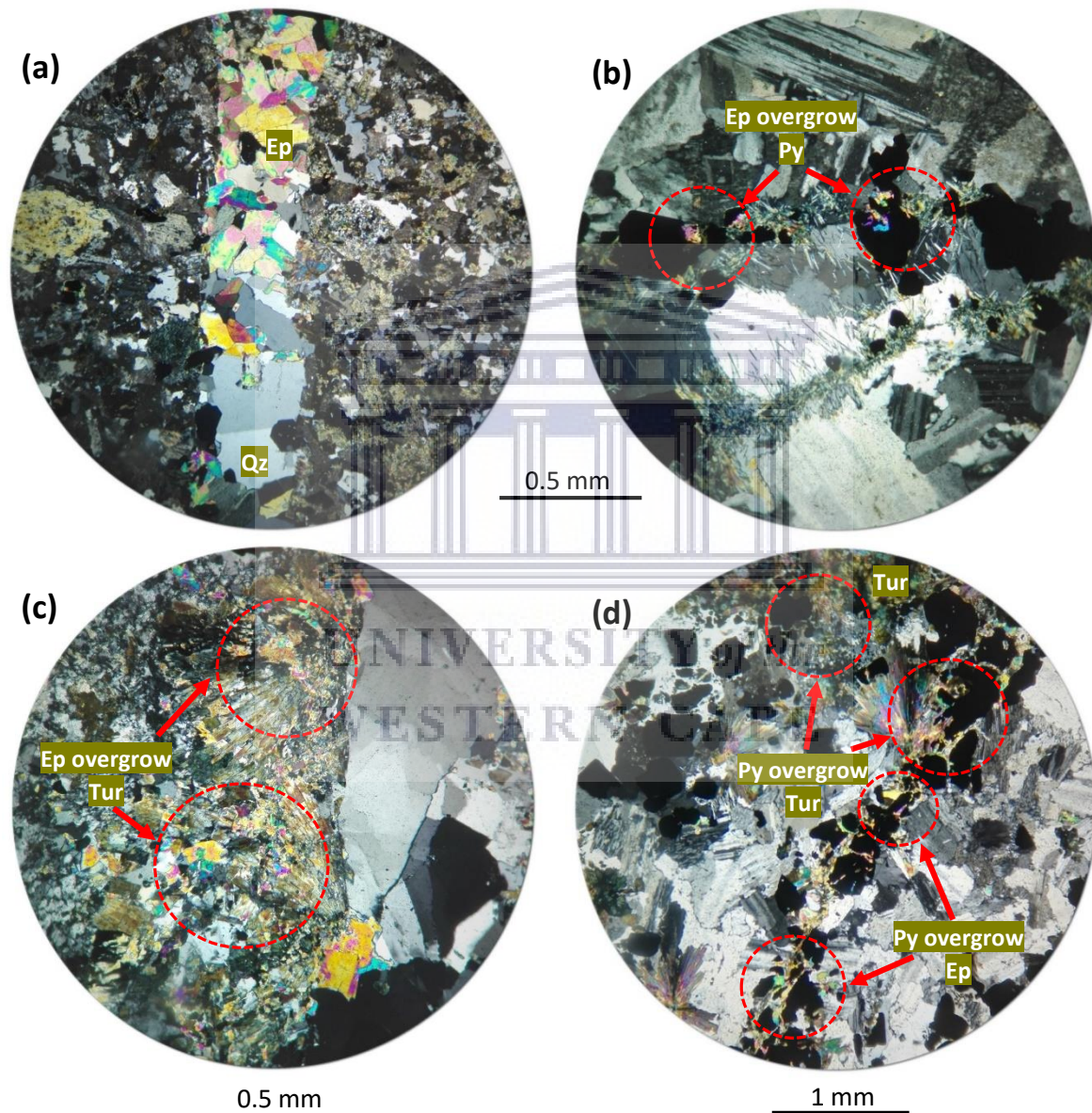


Figure 5.19: Thin section photomicrographs in XPL illustrating (a) epidote granules overgrowing quartz in a quartz-epidote vein (YZN50), (b) multiple epidote granules overgrowing pyrite in a quartz-pyrite-tourmaline-epidote vein (YZN83), (c) epidote overgrowing tourmaline in a quartz-tourmaline-epidote vein (YZN36), and (d) stage 3 pyrite overgrowing tourmaline in a quartz-pyrite-tourmaline-epidote vein and in the surrounding host rock (YZN81); it also displays pyrite overgrowing small epidote granules along the vein. Ep = Epidote, Py = Pyrite, Qz = Quartz, Tur = Tourmaline.

Growth zoning in tourmaline grains, such as those displayed in Fig. 5.3b, record at least two growth periods of tourmaline. The colour and compositional variation displayed by the tourmaline growth bands suggest a change in the environment of formation of tourmaline, which could, in turn, suggest that precipitation of tourmaline persisted after stage 2. This is further demonstrated by tourmaline growth zoning shown in Figs. 5.11a and b, where one compositionally different tourmaline grain is being mantled by another generation of tourmaline that is more Fe-rich; this is particularly evident by the variation in the birefringence (Fig. 5.11a) and pleochroism (Fig. 5.11b) of tourmaline at the margin compared to the core. Finally, the third hydrothermal stage was accompanied by hydrothermal alteration of the primary minerals in the surrounding host rock. At least two minerals have been identified to form part of this hydrothermal alteration assemblage, including secondary tourmaline and epidote (see Tables 5.3 and C1 for compositions of alteration haloes).

iv.) Stage 4

The fourth stage of hydrothermal fluid flow involved the precipitation of quartz and chalcedony from hydrothermal solutions, giving rise to long, and locally thick, barren quartz veins across the study area (Table 5.4). Evidence for precipitation of barren quartz is seen at outcrop scale where it commonly cross-cuts earlier formed veins (discussed later in section 5.5.2). In the barren quartz veins, silica displays a bimodal grain size distribution, with crystalline quartz having fairly large sizes. The great thickness of these veins (up to 25 cm in some localities), suggests that hydrothermal veining during this stage must have occurred in an extensional environment. These barren quartz veins are the last generation of hydrothermal veining to have occurred, having no associated sulphide mineralisation, and thereby indicating that quartz was the last mineral to precipitate out from hydrothermal solution after all the other solvents that formed the pyrite, calcite, tourmaline, jasper and epidote veins had precipitated out.

v.) Supergene alteration

The supergene enrichment stage is the final event to occur and it involves surface and near surface enrichment that accompanies processes such as weathering, oxidation and leaching (Robb, 2005). It takes place when descending acidic solutions react with the sulfides in a rock, or, in this case in hydrothermal veins, resulting in the formation of sulfuric acid and ferrous sulfate. These chemical compounds further break down other sulfides and eventually leaching occurs, forming Cu-hydroxides and/or oxidation takes place, forming gossanous Fe-oxy-hydroxides (Craig and Vaughan, 1994; Robb, 2005). Along the vertical section at the Yzerfontein Harbour, carbonated water that formed through the mixing of the overlying calcrite with meteoric water, reacted with the copper in the pyrite-bearing hydrothermal veins. This resulted in the formation of malachite due to leaching of copper from the pyrite-bearing hydrothermal veins (Table 5.4). In many localities in the study area, gossanous veins have formed through the oxidation of copper and iron in the pyrite-bearing hydrothermal veins, as well as in brecciated tourmaline veins, resulting in the formation of limonite (Figs.

C1, 5.10b; Table 5.4). This type of alteration in pyrite-bearing veins is also commonly seen in thin section (Fig. 5.6a), and locally in alteration haloes (Tables 5.2, 5.3).

5.5.2. Cross-cutting relationships

One of the most important and relatively straightforward principles in constructing a paragenetic model is the study of cross-cutting relationships (Craig and Vaughan, 1994; Plumlee and Whitehouse-Veaux, 1994; Legros et al., 2016). This principle of hydrothermal veins cross-cutting one another as a means of determining a paragenetic sequence relies on the notion that a vein cross-cutting (or intersecting) another vein is younger than the vein which it cuts across, and is therefore later in the paragenetic sequence (Craig and Vaughan, 1994). Multiple examples of hydrothermal veins cross-cutting one another were observed in the field.

Quartz-pyrite veins were the first hydrothermal veins to form, which is not only suggested by overgrowing relationships previously discussed, but is also demonstrated by later cross-cutting generations of hydrothermal veins. Locally, quartz-pyrite veins are cross-cut by tourmaline veins at outcrop scale (e.g. in the monzogabbro NE of the Visitors Center), suggesting that the quartz and pyrite were most likely precipitated during the first hydrothermal stage before tourmaline was introduced into the hydrothermal system. Quartz-pyrite veins are cross-cut by quartz-tourmaline veins in some localities (e.g. at Hoëbank), suggesting that the quartz and tourmaline in the cross-cutting vein was precipitated during a later stage of hydrothermal fluid flow (most likely during stage 2 or early during stage 3). Fig. 5.10b displays a quartz-pyrite vein that, in this case, is cross-cut by a quartz-epidote vein, suggesting that the quartz and epidote in the cross-cutting vein was formed later in the paragenetic sequence (most likely during stage 3). Finally, Fig. 5.20b illustrates another example of how a quartz-epidote vein cross-cuts three different sets of veins in the monzonite at Schaap Eiland, two of which are quartz-tourmaline veins and a central vein comprising quartz and pyrite. The quartz-epidote vein is traced across the intersection of the veins, while the other three veins terminate at the intersection. This further corroborates what was previously suggested, that quartz-pyrite and quartz-tourmaline veins were formed earlier in the paragenetic sequence compared to quartz-epidote veins.

Locally, quartz-tourmaline veins (e.g. in the syenodiorite NE of the Visitors Center (Fig. 5.1a) and at Hoëbank, as well as the monzonite at Grasbank) and quartz-tourmaline-jasper veins (e.g. in the syenodiorite N of the Visitors Center and at Hoëbank (Fig. 5.20a)) are cross-cut by quartz-epidote veins. This indicates that quartz-tourmaline-jasper veins, along with quartz-tourmaline veins, were formed during the second stage (or early during the third stage), and quartz-epidote veins during the third stage.

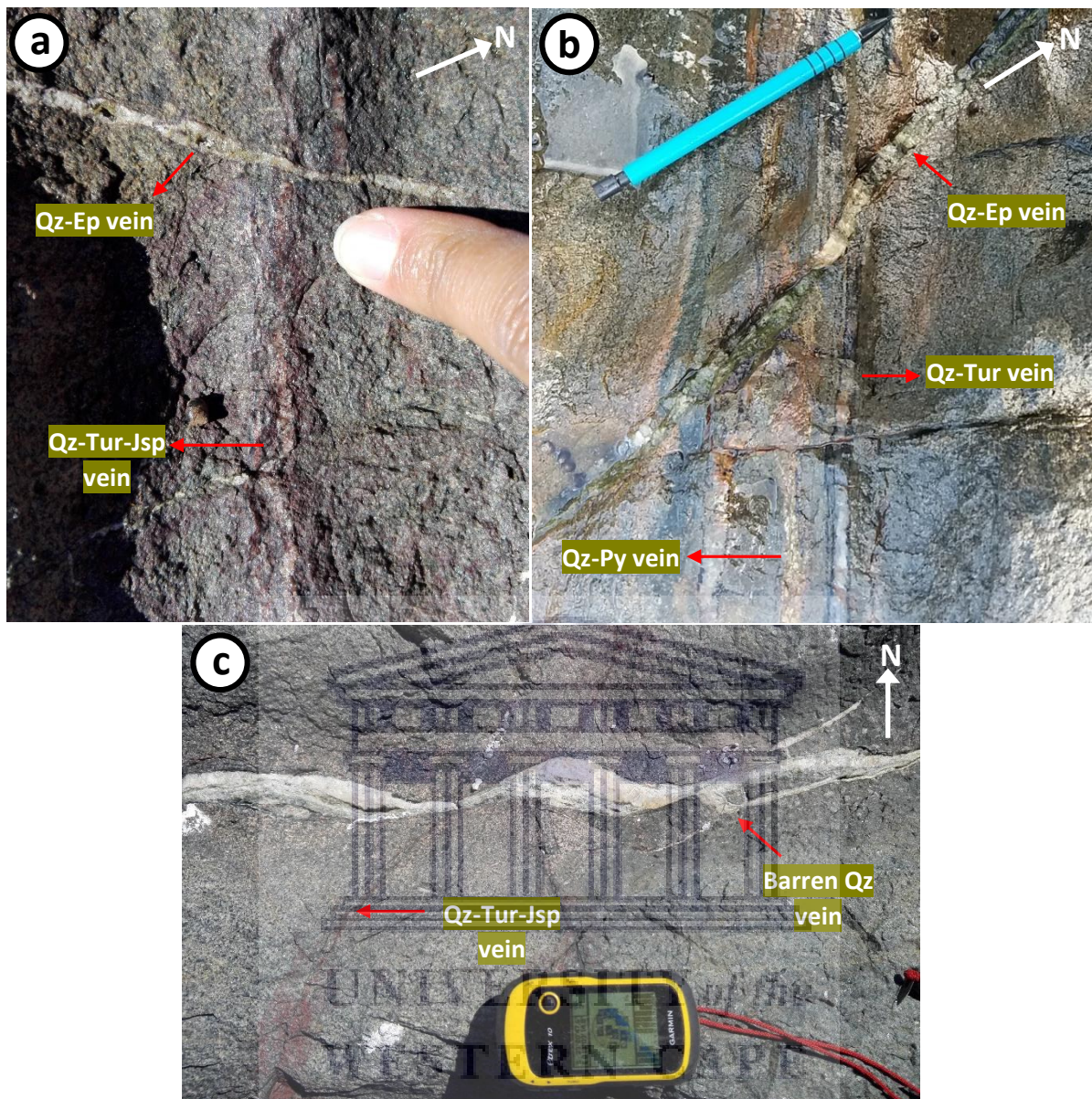


Figure 5.20: Hydrothermal veins showing cross-cutting relationships in the study area. (a) WNW-ESE-trending quartz-tourmaline-jasper vein cross-cut by a NE-SW-trending quartz-epidote vein in the syenodiorite at Hoëbank. The quartz-epidote vein therefore precipitated later in the paragenetic sequence. (b) A set of three NW-SE-trending veins, two being quartz-tourmaline veins and one quartz-pyrite vein, cross-cut by a N-S-trending quartz-epidote vein in the monzonite at Schaap Eiland. This once again suggests that the quartz-epidote vein precipitated later in the paragenetic sequence. (c) E-W-trending barren quartz vein cross-cutting a NE-SW-trending quartz-tourmaline-jasper vein in the monzonite W of the Visitors Center. The barren quartz vein is therefore later in the paragenetic sequence. Jsp = Jasper, Qz = Quartz, Tur = Tourmaline. Scale: Finger with width = 1.4 cm; GPS with length = 10 cm and width = 5.2 cm; Pencil with length = 15.2 cm.

Barren quartz veins were the last veins to have precipitated out from solution and are therefore last in the paragenetic sequence, which is evident from the fact that they cross-cut all other hydrothermal veins across the study area. Two examples of barren quartz veins cross-cutting earlier generations of veins have already been illustrated in Figs. 5.4b and 5.13b. In these figures, barren quartz veins cross-cut a pyrite-tourmaline vein and a quartz-pyrite-tourmaline-jasper vein, respectively, in the monzonite W of the Visitors Center. There are several other examples in the field, including where barren quartz veins cross-cut quartz-tourmaline-jasper veins (e.g. in the monzonite W of the Visitors Center, Fig. 5.20c), as well as

gossanous veins (e.g. in the monzonite at Schaap Eiland). All of these observations confirm that the barren quartz veins were introduced into the hydrothermal system during the final stage of hydrothermal fluid flow.

From the results presented in this subsection, it can be inferred that the first stage of hydrothermal fluid flow involved the precipitation of quartz-pyrite veins. Calcite-bearing veins are uncommon and did not display any cross-cutting relationships with other veins. Nevertheless, from petrographic studies, it was shown that calcite formed during the first stage of hydrothermal fluid flow. During stages 2 and 3 of hydrothermal fluid flow, quartz and pyrite continued to precipitate out from solution, while tourmaline and jasper were introduced during stage 2, and epidote during stage 3. During the last stage, the precipitation of all minerals from hydrothermal solution, except for quartz, ceased. This resulted in the formation of barren quartz veins across the study area. All the observations presented here represent only a few examples of cross-cutting hydrothermal veins noted in the study area. The observations recorded at an outcrop scale in this subsection are consistent with the observations recorded at a microscale discussed in the previous section. These findings were integrated to generate a paragenetic sequence for the minerals occurring in hydrothermal veins (Table 5.4).

Table 5.4: Paragenetic scheme displaying the genetic sequence in which minerals precipitated from hydrothermal solutions along conduits and in alteration haloes.

		Stages				Supergene alteration
Minerals		Stage 1	Stage 2	Stage 3	Stage 4	
Veining	Quartz	████████████████████				
	Chalcedony	████████████████████				
	Pyrite	████████████████████				
	Calcite	████████████████				
	Tourmaline		████████████████	████████████████		
	Jasper		████████████████			
	Epidote			████████████████		
Alteration	Chlorite	████████████████				
	Calcite	████████████████				
	Sericite	████████████████				
	Tourmaline		████████████████	████████████████		
	Jasper		████████████████			
	Epidote			████████████████		
	Limonite					████████████████
	Malachite					████████████████
	Geological time →					

Chapter 6: Whole-rock geochemistry

6.1. Introduction

In the following sections, the whole-rock elemental and isotopic results for each of the rock types of the Yzerfontein Pluton are presented and described. A total of 49 samples were selected for major and trace element analysis, and 4 samples for radiogenic Sr-Nd isotope geochemistry; these results are presented in Tables 6.1 to 6.3. On the Harker plots presented in this chapter, the results of this study are compared to the data published by Clemens et al. (2017a) for the rocks of the Yzerfontein Pluton, as well as the results presented by Adriaans (2018) for I-type granites of the CGS Vredenburg Batholith. This is done in order to investigate and discuss the magmatic relationship of the rocks of the Yzerfontein Pluton with previously published data for this pluton, as well as data for the Vredenburg I-type granites of the CGS. The data used to generate the Harker diagrams are presented in Table D1.

6.2. Major, trace and rare earth element (REE) geochemistry

6.2.1. Rock classification

According to the total alkalis vs. silica (TAS) diagram of Cox et al. (1979), the intermediate rocks of the Yzerfontein Pluton classify mainly as syenodiorite, with one sample plotting in the gabbro field (Fig. 6.1a). These rocks have SiO_2 contents ranging between 51.11 and 61.70 wt. %. The mafic rocks of the Yzerfontein Pluton plot in the gabbro field on the TAS diagram, with one sample plotting in the syenodiorite field. The mafic rocks have SiO_2 contents ranging between 46.07 and 53.24 wt. %. The R_1 - R_2 diagram of De La Roche et al. (1980) provides a more comprehensive classification of the rocks, making use of the entire major element geochemistry to classify the different rock types. The intermediate and mafic rocks plot in various fields on the R_1 - R_2 diagram (Fig. 6.1b).

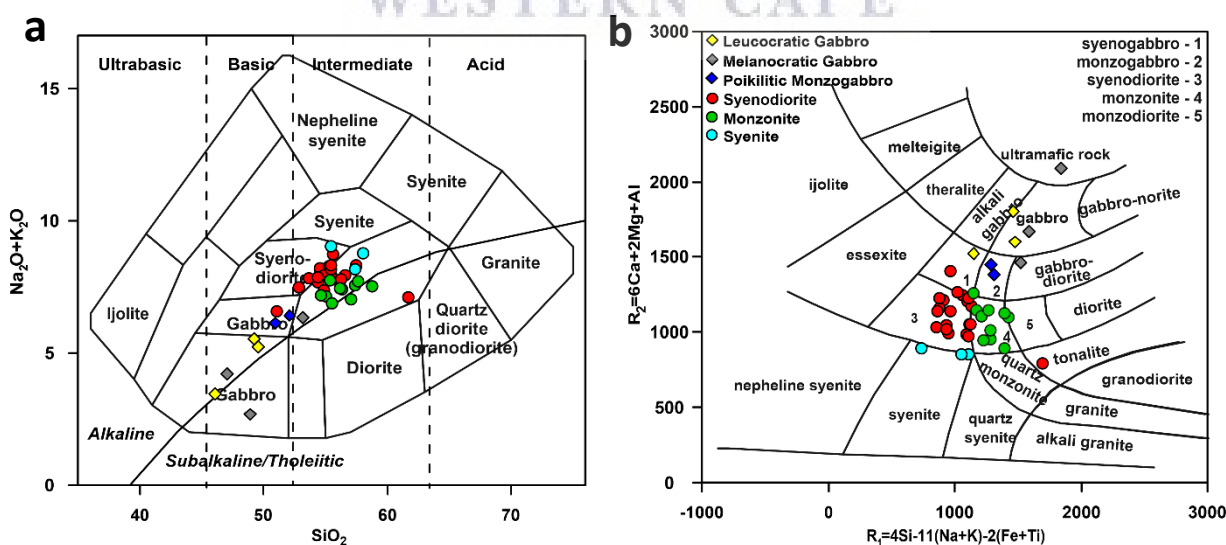


Figure 6.1: Rock classification diagrams for the intermediate and mafic rocks of the Yzerfontein Pluton. (a) Total alkalis vs. silica plot (Cox et al., 1979), and (b) R_1 - R_2 multicationic discrimination diagram (De La Roche et al., 1980). Symbols: red, green and light blue circles represent intermediate rocks, and yellow, grey and dark blue diamonds represent mafic rocks.

Table 6.1: Whole-rock major (wt. %) and trace element (ppm) compositions for the rocks of the Yzerfontein Pluton.

Sample	YZN01	YZN02	YZN03	YZN04	YZN05	YZN06	YZN07A	YZN07B	YZN09	YZN10	YZN11	YZN12	YZN13	YZN14	YZN15	YZN16
SiO ₂	54.41	61.70	55.46	54.92	51.11	53.73	54.57	54.60	57.45	56.18	55.08	57.44	57.64	54.92	55.66	57.48
Cr ₂ O ₃	0.02	0.02	0.03	0.02	0.02	0.01	0.01	0.01	0.02	0.02	0.02	0.03	0.02	0.03	0.03	0.02
TiO ₂	0.84	0.66	0.76	0.86	0.93	0.85	0.84	0.82	0.77	0.81	0.86	0.89	0.89	0.81	0.72	0.77
Al ₂ O ₃	14.76	15.18	14.58	15.31	14.53	15.44	15.65	15.65	15	14.99	14.87	15.38	15.29	14.17	14.40	15.03
Fe ₂ O ₃	9.06	6.69	8.37	9.28	10.99	9.53	9.02	8.95	8.32	8.85	9.48	8.54	8.19	8.77	7.94	7.93
MnO	0.14	0.11	0.13	0.16	0.19	0.17	0.17	0.17	0.12	0.16	0.16	0.15	0.14	0.15	0.17	0.13
MgO	4.78	3.20	4.72	4.11	5.04	3.91	3.70	3.65	3.61	3.85	3.93	3.41	3.59	5.13	5.06	3.78
CaO	6.60	3.05	6.28	6.13	8.03	6.60	6.14	5.99	3.42	5.72	6.06	4.38	4.26	6.75	6.34	4.61
Na ₂ O	2.79	3.58	2.80	3.03	3.24	3.20	3.48	3.62	3.44	3.13	3.15	3.02	3.45	3.05	3.34	3.49
K ₂ O	4.86	3.50	5.13	4.31	3.29	4.58	4.64	4.54	4.68	4.27	3.97	4.51	4.24	4.85	4.40	4.77
P ₂ O ₅	0.53	0.32	0.44	0.53	0.67	0.57	0.53	0.54	0.42	0.42	0.51	0.43	0.45	0.45	0.42	0.40
L.O.I.	0.81	2.19	0.90	0.75	1.32	0.45	0.99	0.98	2.02	1.39	1.62	1.51	1.47	0.65	1.15	1.48
Total	99.60	100.20	99.60	99.41	99.36	99.04	99.74	99.52	99.27	99.79	99.71	99.69	99.63	99.73	99.63	99.89
Sc	25.7	21.4	25.0	25.0	28.4	24.7	23.8	23.9	24.2	25.0	26.2	24.0	22.7	27.0	24.9	23.6
Ti	5036	3957	4556	5156	5575	5096	5036	4916	4616	4856	5156	5336	5336	4856	4316	4616
V	260	165	231	266	324	273	262	256	227	248	274	212	204	248	220	223
Cr	136	155	167	99.0	110	95.3	82.4	94.6	127	119	126	155	125	214	193	142
Co	28.5	16.4	26.6	26.2	32.4	27.5	25.7	26.6	31.7	26.1	27.6	21.9	19.7	28.5	25.4	20.9
Ni	34.3	34.6	45.3	32.3	32.6	30.6	23.5	22.7	29.6	24.1	24.9	37.4	29.6	50.2	43.7	29.3
Cu	125	112	94.9	125	184	104	77.2	117	146	107	233	278	248	88.6	113	98.5
Zn	111	103	104	123	127	127	116	117	83.9	123	126	141	125	116	104	86.0
Rb	155	166	180	166	113	144	133	132	191	155	151	188	213	227	188	207
Sr	888	892	810	921	1257	1076	1029	1015	888	931	890	647	662	814	865	804
Y	25.3	28.1	23.2	27.3	28.0	26.9	25.8	26.4	26.1	26.3	28.6	32.3	32.7	26.8	27.0	26.9
Zr	143	237	161	200	130	119	138	151	178	202	177	342	391	237	304	258
Nb	9.02	14.5	12.6	8.82	6.77	7.03	7.17	7.57	10.6	10.8	10.1	19.6	22.2	13.4	14.1	12.5
Mo	4.51	5.87	5.73	4.76	5.02	5.25	3.85	4.41	6.56	6.55	7.70	7.74	5.52	6.89	6.54	8.71
Cs	14.7	11.6	19.2	24.2	11.1	16.7	7.67	9.08	11.1	11.6	10.4	15.9	13.7	29.2	13.1	15.4
Ba	872	586	687	919	966	987	998	893	866	778	804	661	604	708	651	832
Hf	3.88	6.79	4.88	5.32	3.70	3.29	3.72	4.21	5.02	5.76	5.23	8.45	10.4	6.62	7.84	6.90
Ta	0.59	1.19	0.94	0.62	0.45	0.48	0.47	0.54	0.80	0.79	0.77	1.35	1.57	1.01	1.10	0.89
Pb	41.5	37.5	44.1	41.4	32.4	39.2	42.0	39.3	67.2	45.0	40.9	60.0	51.5	47.3	45.4	35.5
Th	23.6	40.0	44.8	22.1	16.4	16.7	17.9	21.0	27.4	29.9	27.4	50.3	59.1	44.4	47.7	33.2
U	4.29	6.23	7.95	6.59	4.95	4.42	4.21	4.75	7.82	5.17	7.49	11.4	10.8	9.04	16.4	7.42

Table 6.1 (continued)

Sample	YZN17	YZN18	YZN20	YZN21	YZN22	YZN23	YZN24	YZN29	YZN30	YZN31	YZN32	YZN34	YZN38	YZN39	YZN40	YZN42
SiO ₂	55.31	56.37	48.91	49.23	46.07	54.40	52.89	58.82	55.49	56.63	56.29	55.54	65.23	64.11	55.66	55.45
Cr ₂ O ₃	0.02	0.03	0.08	0.04	0.08	0.01	0.01	0.02	0	0.01	0.01	0.01	0.01	0.01	0.01	0
TiO ₂	0.80	0.83	0.92	0.67	0.62	0.86	0.92	0.87	0.82	0.82	0.86	0.87	0.55	0.55	0.80	0.82
Al ₂ O ₃	14.90	14.75	8.21	17.47	13.06	15.09	15.07	15.09	14.94	14.90	14.96	14.75	15.51	15.59	15.38	15.21
Fe ₂ O ₃	8.84	8.50	11.92	9.04	11.57	9	9.98	7.86	8.89	7.91	8.44	9	3.41	4.06	8.23	8.65
MnO	0.15	0.13	0.23	0.16	0.19	0.15	0.17	0.13	0.17	0.12	0.14	0.16	0.04	0.05	0.15	0.16
MgO	3.99	4.05	12.59	6.92	12.12	4	4.13	3.34	3.93	3.84	3.93	4.35	1.66	1.51	3.44	3.91
CaO	5.08	5.65	12.15	7.77	8.79	5.93	6.68	3.93	4.63	5.22	5.15	5.88	1.66	2.30	5.10	3.65
Na ₂ O	3.29	3.35	1.98	3.42	2.25	3.27	3.46	3.18	3.36	3.47	3.30	3.26	4.27	4.30	3.45	3.52
K ₂ O	4.95	4.02	0.68	2.09	1.18	4.58	4.01	4.32	4.79	4.45	4.47	3.60	5.13	5.40	5.24	5.50
P ₂ O ₅	0.48	0.43	0.36	0.55	0.64	0.53	0.60	0.40	0.49	0.41	0.44	0.43	0.17	0.17	0.47	0.48
L.O.I.	1.66	1.33	1	2.12	3.25	2.98	1.96	2.11	1.62	1.37	1.26	1.39	1.82	1.46	1.12	1.65
Total	99.47	99.44	99.03	99.48	99.82	100.80	99.88	100.07	99.13	99.15	99.25	99.24	99.46	99.51	99.05	99
Sc	24.6	24.5	48.4	19.7	22.5	22.6	23.1	20.5	22.7	21.1	21.4	23.5	11.8	11.6	20.7	20.7
Ti	4796	4976	5515	4017	3717	5156	5515	5216	4916	4916	5156	5216	3297	3297	4796	4916
V	248	239	309	255	217	225	252	179	222	197	204	226	92.2	99.5	208	210
Cr	113	163	505	236	491	99.6	80.4	139	72.8	96.9	109	109	130	92.2	79.7	61.5
Co	24.1	22.9	44.1	38.2	52.1	21.2	27.0	20.8	26.7	21.6	20.9	24.0	6.41	7.29	18.9	19.4
Ni	27.6	34.8	159	99.8	222	24.8	23.0	26.9	23.0	27.9	27.4	30.5	19.6	15.9	19.9	20.1
Cu	85.5	191	59.5	217	97.4	138	116	75.7	147	120	160	143	13.7	223	100	174
Zn	91.4	88.4	97.0	80.6	105	96.8	92.6	64.7	101	57.3	74.4	74.2	34.2	35.0	79.3	62.0
Rb	193	174	27.7	76.9	43.9	133	115	164	165	182	184	146	202	194	173	194
Sr	850	770	531	1533	1194	851	1040	572	704	636	644	735	426	525	777	640
Y	28.2	29.2	23.0	13.3	13.9	24.8	25.5	29.5	25.0	26.3	26.2	26.8	24.2	23.2	24.7	26.6
Zr	231	228	113	87.6	75.7	163	125	311	173	233	226	181	293	288	159	227
Nb	12.0	12.8	6.93	4.28	4.23	7.60	6.74	17.3	10.1	12.6	12.5	11.0	17.9	15.7	8.12	11.9
Mo	7.66	9.83	2.43	2.00	1.90	4.61	4.51	5.95	6.64	7.64	7.02	5.42	5.99	5.60	5.14	3.53
Cs	11.2	11.8	2.26	5.11	3.15	7.78	7.51	11.0	8.95	9.04	10.4	12.4	10.0	8.16	11.0	7.66
Ba	904	728	151	423	324	836	920	668	853	679	652	755	683	740	822	880
Hf	6.64	6.60	3.66	2.53	2.17	4.28	3.30	8.41	4.73	6.16	5.83	4.78	8.11	7.78	4.47	6.02
Ta	0.90	0.91	0.41	0.28	0.26	0.49	0.48	1.20	0.70	0.84	0.84	0.68	1.48	1.21	0.58	0.77
Pb	35.7	40.8	8.88	15.7	16.1	40.2	33.4	25.0	96.0	29.8	34.1	23.7	12.7	15.1	32.8	25.8
Th	35.7	35.5	11.4	11.8	9.38	17.5	18.2	44.6	26.9	34.1	33.4	22.0	57.1	47.4	24.4	33.5
U	10.1	11.6	2.69	3.14	2.51	4.86	4.55	7.05	8.05	11.4	10.8	6.24	9.44	9.25	6.64	6.17

Table 6.1 (continued)

Sample	YZN43	YZN46	YZN48	YZN50	YZN51	YZN52	YZN70	YZN71	YZN73	YZN75a	YZN75b	YZN76	YZN79	YZN92	YZN93	YZN95	YZN96
SiO ₂	55.49	58.07	57.12	68.64	54.71	57.49	64.06	62.93	67.68	52.12	50.96	64.10	53.24	55.44	56.21	47.06	49.56
Cr ₂ O ₃	0	0.01	0.01	0.01	0.02	0.01	0.02	0.02	0.02	0.02	0.01	0.01	0.04	0.02	0.03	0.08	0.06
TiO ₂	0.80	0.74	0.83	0.40	0.83	0.72	0.52	0.55	0.33	0.92	0.97	0.44	0.77	0.79	0.78	0.63	0.70
Al ₂ O ₃	15.26	15.84	14.40	13.52	14.09	15.39	16.07	16.27	15.33	14.72	14.32	15.70	13.37	15.18	14.91	13.65	14.88
Fe ₂ O ₃	8.48	7.27	8.18	3.99	9.16	7.41	4.44	4.24	3.46	10.41	11.65	4.58	9.33	9.11	8.39	11.33	9.59
MnO	0.16	0.12	0.15	0.06	0.17	0.14	0.03	0.08	0.04	0.18	0.20	0.07	0.16	0.21	0.14	0.19	0.15
MgO	3.70	3.04	4.18	1.27	4.76	3.11	1.10	1.88	0.84	5.42	5.30	1.39	6.82	3.37	4.51	11.60	8.64
CaO	4.88	3.54	5.57	0.88	6.89	4.72	1.53	2.57	0.92	7.63	8.39	1.58	7.96	5.02	5.59	7.65	8.16
Na ₂ O	3.46	3.43	2.85	3.04	3.14	3.52	5.43	4.60	4.32	3.22	3.09	5.08	2.55	3.03	3.24	2.30	2.96
K ₂ O	4.81	5.31	4.15	6.09	4.01	4.75	4.39	5.38	5.51	3.19	3.02	5.03	3.75	4.67	4.18	1.89	2.26
P ₂ O ₅	0.48	0.42	0.37	0.16	0.43	0.40	0.18	0.19	0.13	0.64	0.69	0.18	0.49	0.47	0.45	0.61	0.61
L.O.I.	1.84	1.41	1.61	1.67	1.08	1.38	2.20	1.56	1.67	1.17	1.17	1.58	1.52	2.36	1.43	2.69	2.46
Total	99.36	99.20	99.42	99.73	99.29	99.04	99.97	100.27	100.25	99.64	99.77	99.74	100	99.67	99.86	99.68	100.03
Sc	20.4	18.3	23.5	10.6	25.5	18.3	14.3	14.4	11.8	28.1	32.0	13.2	30.9	23.1	24.0	20.8	23.0
Ti	4796	4436	4976	2398	4976	4316	3117	3297	1978	5515	5815	2638	4616	4736	4676	3777	4197
V	208	172	208	82.8	229	179	117	105	70.7	265	317	93.8	241	218	209	206	211
Cr	65.6	74.1	110	122	126	79.1	161	172	198	168	123	145	323	155	224	586	433
Co	21.3	15.8	22.0	10.1	25.7	18.7	11.5	13.1	2.83	32.5	35.0	8.90	34.8	21.0	21.9	50.1	43.1
Ni	20.3	20.3	25.6	14.6	29.3	26.5	19.4	18.0	13.5	41.3	31.8	12.9	77.5	24.8	37.1	236	138
Cu	135	85.9	120	80.8	121	150	81.1	223	112	151	254	167	124	324	129	41.2	85.5
Zn	84.3	57.5	92.2	58.7	92.7	71.7	37.3	50.5	56.9	148	132	71.1	105	116	90.7	122	90.5
Rb	165	208	145	254	147	176	178	213	207	141	105	174	108	171	161	73.1	93.5
Sr	877	671	706	261	762	822	342	591	424	1062	1268	533	864	814	764	1283	1089
Y	24.8	28.3	25.0	20.8	22.6	24.6	20.3	20.0	16.9	28.3	30.1	15.4	24.5	26.5	24.4	13.8	17.2
Zr	202	273	217	213	175	224	275	302	185	165	114	187	118	205	235	80.5	98.3
Nb	10.3	14.6	15.1	21.4	11.0	11.8	15.4	15.9	13.5	10.8	5.86	11.9	5.19	10.5	11.8	3.48	5.13
Mo	3.94	4.28	4.53	8.61	5.51	3.96	9.83	20.3	10.4	6.36	4.68	8.16	5.81	8.43	9.04	3.62	4.74
Cs	5.47	9.78	7.63	6.12	7.66	10.2	7.00	11.6	8.16	22.1	11.0	7.88	11.1	8.64	11.6	7.21	7.26
Ba	823	749	639	473	693	781	535	775	645	881	1050	706	1022	935	686	540	278
Hf	5.49	7.48	5.77	7.87	4.87	5.96	7.26	7.38	5.18	4.65	3.44	4.98	3.42	5.79	6.52	2.42	2.92
Ta	0.79	1.10	0.97	2.18	0.62	0.89	1.15	1.10	1.06	0.76	0.44	0.88	0.39	0.78	0.97	0.27	0.38
Pb	34.0	27.6	42.3	44.6	38.7	36.6	27.1	28.4	64.0	45.1	36.6	45.0	35.1	47.0	56.1	14.8	18.5
Th	31.3	46.9	34.1	109	24.5	36.4	45.2	42.5	35.1	27.4	15.0	31.6	17.4	30.1	36.0	9.65	13.1
U	8.38	9.56	9.57	24.7	7.55	8.44	10.8	13.6	10.2	8.61	4.47	7.24	4.20	8.56	9.89	2.74	3.51

Table 6.2: Whole-rock rare earth element (REE) concentrations (ppm) for the rocks of the Yzerfontein Pluton. Ratios with subscript PM were normalised to the primitive mantle using the values of McDonough and Sun (1995).

Sample	YZN01	YZN02	YZN03	YZN04	YZN05	YZN06	YZN07A	YZN07B	YZN09	YZN10	YZN11	YZN12	YZN13	YZN14	YZN15	YZN16
La	58.7	58.4	64.9	61.1	60.2	63.2	61.7	62.1	52.7	57.2	59.3	74.0	81.3	73.9	75.8	63.2
Ce	122	117	134	127	129	133	128	128	111	120	125	152	165	156	157	126
Pr	15.0	13.6	16.4	15.5	16.1	16.6	15.8	15.7	13.6	14.5	15.3	17.8	19.1	18.8	18.7	15.1
Nd	60.2	51.3	64.4	62.1	68.4	66.5	63.5	64.0	55.4	58.7	60.8	67.3	72.5	74.4	72.9	57.2
Sm	12.0	10.3	12.4	12.6	14.4	13.7	13.2	13.4	11.3	11.8	12.2	12.5	13.8	14.6	14.1	11.8
Eu	2.65	1.84	2.45	2.70	3.25	3.16	3.21	2.94	2.50	2.36	2.64	2.26	2.18	2.59	2.51	2.37
Gd	9.35	7.47	8.78	10.0	11.3	10.7	9.86	10.5	8.60	8.87	10.0	9.74	9.72	10.7	9.92	7.83
Tb	1.12	1.03	1.05	1.20	1.26	1.25	1.20	1.18	1.07	1.10	1.13	1.24	1.26	1.10	1.18	1.06
Dy	5.17	5.15	5.11	5.76	5.98	5.77	5.52	5.72	5.40	5.38	5.59	6.53	6.10	5.65	5.53	5.59
Ho	0.920	1.09	0.850	1.01	1.01	1.06	0.980	0.950	0.980	1.01	1.04	1.14	1.17	0.980	0.980	1.05
Er	2.50	2.84	2.34	2.87	2.48	2.76	2.62	2.47	2.51	2.65	2.90	3.14	3.35	2.46	2.64	2.80
Tm	0.320	0.400	0.330	0.400	0.360	0.330	0.350	0.320	0.360	0.370	0.390	0.450	0.480	0.390	0.380	0.370
Yb	2.20	2.60	1.83	2.64	2.34	2.21	2.14	2.17	2.68	2.53	2.63	3.07	3.29	2.13	2.57	2.55
Lu	0.350	0.330	0.320	0.370	0.310	0.350	0.330	0.360	0.350	0.360	0.380	0.470	0.460	0.370	0.380	0.360
Eu/Eu*	0.76	0.64	0.72	0.73	0.78	0.80	0.86	0.76	0.77	0.70	0.73	0.62	0.57	0.63	0.65	0.75
(Tb/Yb) _{PM}	2.26	1.76	2.56	2.03	2.40	2.53	2.49	2.42	1.79	1.94	1.92	1.80	1.71	2.31	2.06	1.85
(La/Sm) _{PM}	3.06	3.57	3.28	3.03	2.62	2.90	2.94	2.90	2.91	3.03	3.06	3.70	3.69	3.16	3.38	3.36
(Gd/Lu) _{PM}	3.31	2.80	3.47	3.40	4.57	3.88	3.74	3.63	3.05	3.07	3.28	2.57	2.63	3.57	3.24	2.70
(La/Yb) _{PM}	18.2	15.3	24.1	15.8	17.5	19.5	19.6	19.5	13.4	15.4	15.4	16.4	16.8	23.7	20.1	16.9
Sample	YZN17	YZN18	YZN20	YZN21	YZN22	YZN23	YZN24	YZN29	YZN30	YZN31	YZN32	YZN34	YZN38	YZN39	YZN40	YZN42
La	67.3	64.4	28.0	41.0	36.1	57.1	57.6	66.4	59.6	58.0	58.3	50.2	53.7	45.9	58.7	66.2
Ce	140	132	68.0	79.0	75.6	117	121	135	124	120	122	106	112	88.9	125	136
Pr	16.9	16.2	9.49	9.34	9.22	14.2	15.2	15.5	15.1	14.3	14.6	12.9	13.1	9.99	15.4	16.0
Nd	68.6	61.5	42.1	35.6	37.2	57.5	61.2	57.8	61.1	55.7	56.4	51.6	47.9	36.0	60.6	65.0
Sm	13.9	12.4	9.21	6.69	6.78	11.9	12.4	11.1	11.9	10.9	11.1	10.9	8.19	6.91	12.4	12.3
Eu	2.79	2.24	1.78	1.77	1.51	2.54	2.59	1.95	2.54	2.09	2.07	2.22	1.33	1.33	2.53	2.55
Gd	10.2	9.52	7.40	4.63	4.95	8.96	9.28	8.42	9.43	8.46	7.98	8.06	6.26	5.72	8.99	9.68
Tb	1.25	1.14	0.99	0.51	0.57	1.08	1.07	1.07	1.00	1.00	0.93	1.04	0.77	0.71	1.03	1.10
Dy	5.80	6.20	4.83	2.71	3.13	5.47	5.34	5.64	5.29	5.40	5.29	5.04	4.50	4.36	5.04	5.79
Ho	0.980	1.10	0.900	0.480	0.490	0.900	0.910	1.01	0.900	0.950	0.950	0.930	0.840	0.870	0.890	0.950
Er	2.71	3.04	2.35	1.31	1.28	2.37	2.37	3.00	2.56	2.64	2.70	2.59	2.48	2.37	2.35	2.63
Tm	0.390	0.410	0.320	0.160	0.190	0.320	0.300	0.420	0.350	0.360	0.390	0.360	0.350	0.360	0.320	0.340
Yb	2.49	2.56	2.08	1.17	1.11	2.16	2.10	2.71	2.14	2.53	2.42	2.38	2.37	2.29	2.20	2.15
Lu	0.350	0.380	0.290	0.160	0.160	0.320	0.300	0.400	0.310	0.360	0.360	0.350	0.340	0.380	0.320	0.350
Eu/Eu*	0.71	0.63	0.66	0.97	0.80	0.75	0.74	0.62	0.73	0.67	0.67	0.72	0.57	0.65	0.73	0.71

Table 6.2 (continued)

Sample	YZN17	YZN18	YZN20	YZN21	YZN22	YZN23	YZN24	YZN29	YZN30	YZN31	YZN32	YZN34	YZN38	YZN39	YZN40	YZN42	
(Tb/Yb) _{PM}	2.24	1.98	1.94	1.95	2.29	2.23	2.26	1.75	2.07	1.76	1.71	1.95	1.44	1.38	2.09	2.28	
(La/Sm) _{PM}	3.03	3.25	1.90	3.84	3.34	3.02	2.92	3.74	3.15	3.35	3.30	2.89	4.11	4.16	2.97	3.38	
(Gd/Lu) _{PM}	3.68	3.14	3.21	3.66	3.89	3.54	3.89	2.64	3.81	2.92	2.74	2.92	2.34	1.89	3.48	3.47	
(La/Yb) _{PM}	18.4	17.2	9.16	24.0	22.2	18.0	18.7	16.7	18.9	15.6	16.4	14.3	15.4	13.7	18.2	21.0	
Sample	YZN43	YZN46	YZN48	YZN50	YZN51	YZN52	YZN70	YZN71	YZN73	YZN75a	YZN75b	YZN76	YZN79	YZN92	YZN93	YZN95	YZN96
La	60.5	68.8	52.5	68.0	49.3	61.1	42.1	41.8	43.9	66.3	58.1	41.5	53.3	60.8	59.6	36.7	47.5
Ce	125	138	107	133	103	125	86.8	86.8	84.3	140	123	80.5	110	123	122	73.1	94.4
Pr	15.0	16.6	12.9	14.3	12.7	14.8	9.26	9.92	8.62	17.3	15.4	8.60	13.9	14.3	14.6	8.72	11.1
Nd	60.1	63.3	48.8	49.5	49.4	57.6	32.6	37.8	30.7	67.1	66.9	31.5	60.6	58.8	58.8	36.0	44.8
Sm	12.2	12.2	10.4	8.41	10.1	11.1	6.21	7.19	5.52	14.3	14.0	5.71	12.9	11.8	11.3	6.62	8.23
Eu	2.32	2.26	1.99	1.22	2.19	2.13	1.25	1.53	1.05	2.73	3.09	1.27	2.52	2.60	2.23	1.61	1.82
Gd	8.88	9.59	7.61	5.85	8.23	8.62	5.00	5.48	4.35	10.5	11.5	4.22	9.38	9.11	8.35	4.80	5.91
Tb	1.08	1.10	0.90	0.72	0.96	0.97	0.63	0.67	0.53	1.16	1.29	0.50	1.07	1.08	0.96	0.56	0.68
Dy	5.21	5.71	5.01	3.58	4.75	4.90	3.87	3.81	2.86	5.88	6.41	2.87	5.06	5.21	4.92	2.73	3.45
Ho	0.950	1.00	0.860	0.670	0.850	0.920	0.710	0.740	0.630	1.01	1.12	0.510	0.820	0.910	0.840	0.490	0.620
Er	2.49	2.78	2.38	2.03	2.15	2.25	2.06	2.07	1.84	2.67	2.96	1.50	2.48	2.63	2.46	1.32	1.81
Tm	0.350	0.360	0.360	0.300	0.260	0.330	0.300	0.300	0.250	0.360	0.410	0.210	0.290	0.330	0.330	0.180	0.220
Yb	2.49	2.52	2.26	1.74	1.95	2.32	1.98	2.14	1.80	2.37	2.45	1.48	1.97	2.35	2.14	1.09	1.43
Lu	0.310	0.360	0.310	0.290	0.280	0.320	0.290	0.320	0.300	0.350	0.360	0.240	0.310	0.350	0.310	0.180	0.200
Eu/Eu*	0.68	0.64	0.68	0.53	0.73	0.67	0.69	0.74	0.65	0.68	0.74	0.79	0.70	0.77	0.70	0.87	0.79
(Tb/Yb) _{PM}	1.94	1.94	1.78	1.85	2.19	1.86	1.42	1.39	1.31	2.18	2.35	1.51	2.42	2.05	2.01	2.28	2.11
(La/Sm) _{PM}	3.11	3.53	3.17	5.07	3.05	3.45	4.25	3.64	4.98	2.90	2.59	4.55	2.59	3.24	3.32	3.48	3.62
(Gd/Lu) _{PM}	3.60	3.33	3.08	2.49	3.72	3.38	2.15	2.14	1.81	3.73	4.05	2.20	3.74	3.25	3.35	3.38	3.65
(La/Yb) _{PM}	16.5	18.6	15.9	26.6	17.3	17.9	14.5	13.3	16.6	19.0	16.2	19.1	18.5	17.6	19.0	22.9	22.6

The intermediate rocks classify mainly as syenodiorite and monzonite, while three samples plot as syenite, and another three samples as tonalite, monzodiorite and syenogabbro, respectively (Fig. 6.1b). The sample plotting as tonalite (YZN02) has a higher SiO₂ content (61.70 wt. %) compared to the other intermediate rocks. The mafic rocks plot as a variety of compositionally different gabbros, including syenogabbro, monzogabbro, gabbro-diorite, alkali gabbro, gabbro, and one sample plotting as an ultramafic rock. The sample plotting as an ultramafic rock (YZN20) has a higher MgO and CaO content (12.59 wt. % and 12.15 wt. % respectively) compared to the other mafic rocks.

The felsic rocks of the Yzerfontein Pluton were classified using the QAPF diagram of Streckeisen (1974) based on the estimated volume percentage of quartz, orthoclase and plagioclase in petrographic thin section, normalised to 100%. Based on the normalised values, they are classified as quartz-microsyenites and monzogranites on the QAPF diagram (Fig. 6.2a), with SiO₂ contents ranging between 62.93 and 68.64 wt. %. The felsic rocks plot in the granite field on the An-Ab-Or diagram, and have an alkalic character on the Na₂O + K₂O – CaO vs. SiO₂ classification diagram (Figs. 6.2b, c).

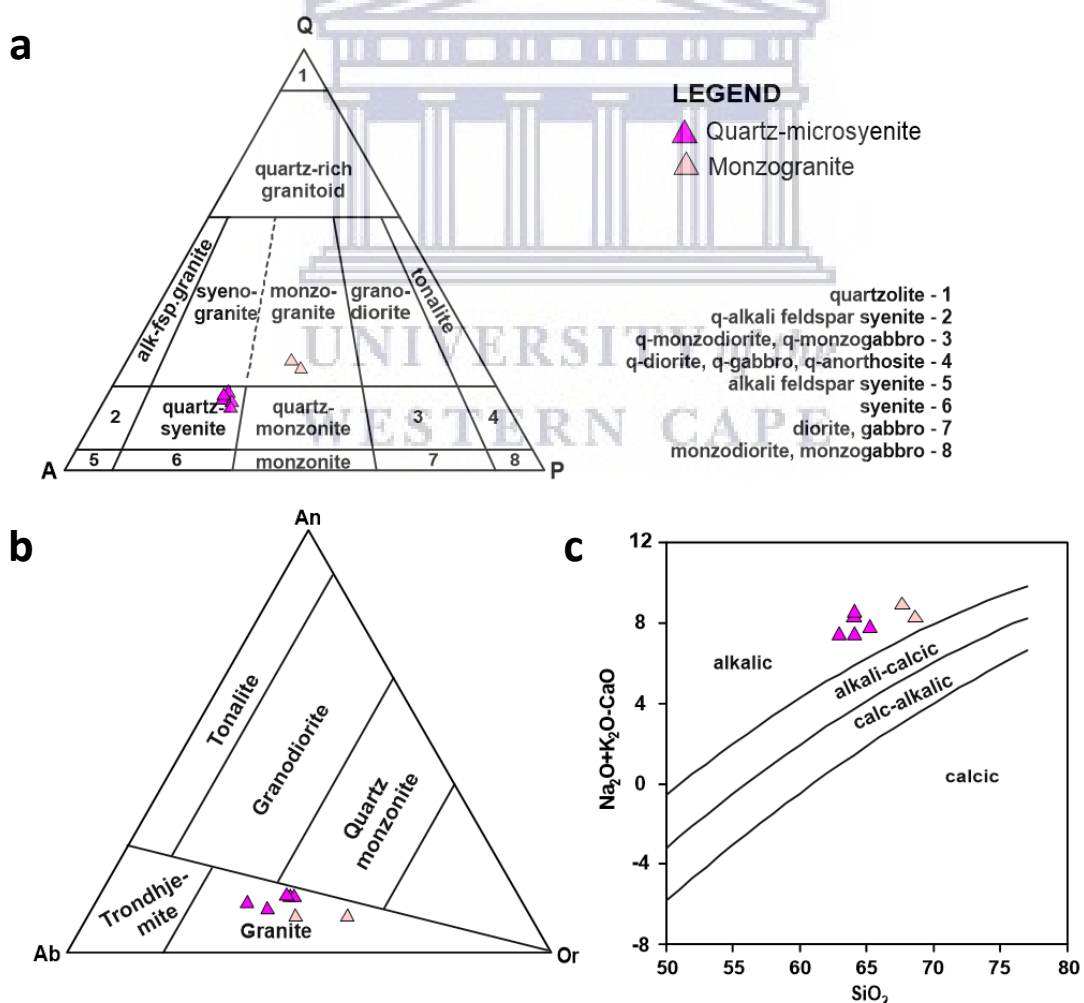


Figure 6.2: Classification and chemical discrimination diagrams for the felsic rocks of the Yzerfontein Pluton. (a) QAPF ternary classification diagram (after Streckeisen, 1976), (b) normative An-Ab-Or ternary plot showing the composition of the felsic rocks (after O'Connor, 1965), and (c) Na₂O + K₂O – CaO vs. SiO₂ classification diagram (after Frost et al., 2001).

The felsic rocks predominantly plot in the magnesian field on the $\text{FeOt}/(\text{FeOt} + \text{MgO})$ vs. SiO_2 discrimination diagram, with one quartz-microsyenite sample (YZN70) plotting in the ferroan field (Fig. 6.3a). Two samples, YZN70 (quartz-microsyenite) and YZN73 (monzogranite), plot close to the Fe-index boundary, with $\text{FeOt}/\text{FeOt} + \text{MgO}$ values of ~ 0.80 . On the A/NK vs. ASI diagram, four of the quartz-microsyenite samples are metaluminous, with one quartz-microsyenite plotting together with the monzogranites as weakly peraluminous (Fig. 6.3b).

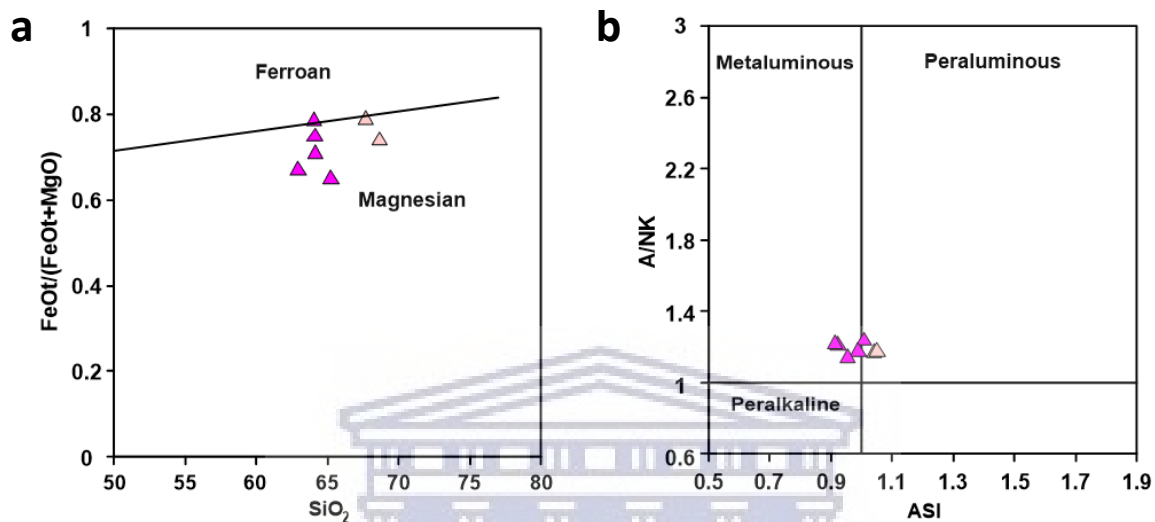


Figure 6.3: Chemical discrimination diagrams for the felsic rocks of the Yzerfontein Pluton. (a) $\text{FeOt}/(\text{FeOt} + \text{MgO})$ vs. SiO_2 discrimination diagram (after Frost et al., 2001), (b) A/NK ($\text{Al}_2\text{O}_3/(\text{Na}_2\text{O} + \text{K}_2\text{O})$) vs. ASI (molecular $\text{Al}/(\text{Ca} - 1 \cdot 67\text{P} + \text{Na} + \text{K})$) discrimination diagram (after Frost et al., 2001). Symbols: same as in Fig. 6.2.

6.2.2. Major element variation

The elemental concentrations of all the major element oxides were calculated and plotted against Si on Harker diagrams (Fig. 6.4, Table D1). Overall, most of the samples display a continuous evolutionary trend on the Harker diagrams: Ti, Fe, Mg, Ca and P show negatively correlated trends with Si, while Na and K show positively correlated trends with Si. Al defines a relatively flat trend with the exception of YZN20 (melanocratic gabbro) which has a much lower Al content compared to the rest of the samples (Fig. 6.4b).

In terms of the felsic rocks, a negatively correlated trend is seen in nearly all the plots, except for in the plot of K vs. Si. The intermediate rocks usually plot in a middle position between the mafic and felsic rocks on the Harker diagrams and define negative trends for Ti, Fe, Mg, Ca, and P vs. Si, and positive trends for Al, Na and K vs. Si. The mafic rocks define positively correlated trends in the Ti, Al, Na, and K vs. Si plots, negatively correlated trends in the Fe and Mg vs. Si plots, and relatively scattered trends in the Ca and P vs. Si plots. On the Harker plots, most of the intermediate and felsic samples from this study plot within the field of published Yzerfontein data of Clemens et al. (2017a). However, most of the gabbroic samples plot outside of this field on all Harker plots. In terms of the intermediate and felsic rocks, only a selective number of samples of syenodiorite, syenite, quartz-microsyenite and monzogranite

are outliers on the Harker plots. Most of the rocks do not plot within the field of the I-type granite data of Adriaans (2018), except for the monzogranite (Figs. 6.4a, c, d, f, g, h).

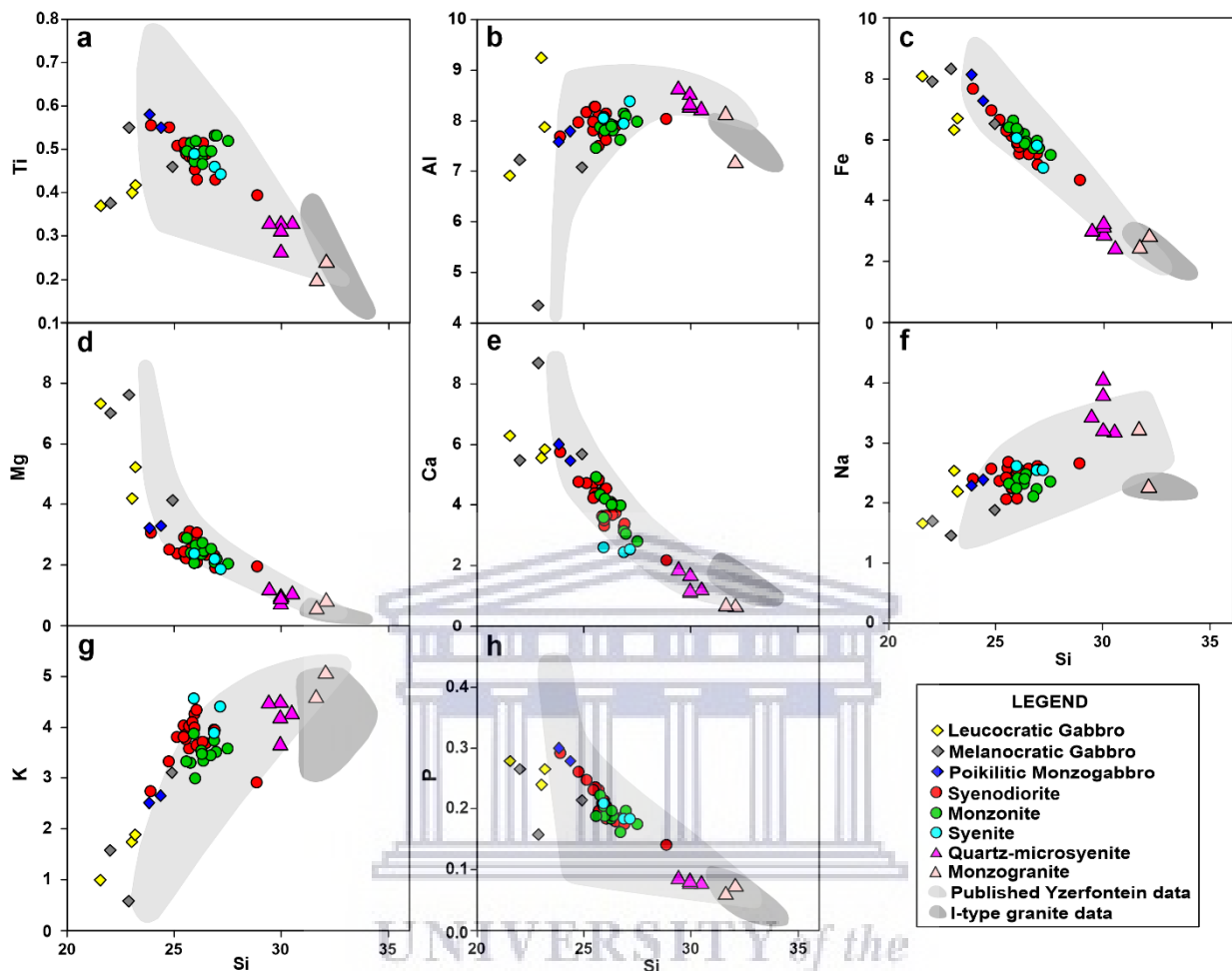


Figure 6.4: Harker plots displaying geochemical trends in elemental composition of selected major elements for the rocks of the Yzerfontein Pluton. Published Yzerfontein data is from Clemens et al. (2017a), and I-type granite data is from Adriaans (2018).

6.2.3. Trace element variation

In order to assess the geochemical trends between selected trace elements and Si, they were plotted on Harker diagrams (Fig. 6.5, Tables 6.1, 6.2, D1). Large ion lithophile elements (LILE) such as Rb, Sr, Ba and Eu show variable relationships with Si. For all rock types, Rb displays a positive correlation with Si, and Sr a negative correlation with Si, which is logical given the incompatible nature of Rb, and the compatible nature of Sr (Figs. 6.5a, b). In the Ba vs. Si and Eu vs. Si plots, a negative correlation is defined with regards to both the felsic and intermediate rocks, while a positive correlation is apparent in the mafic rocks (Figs. 6.5c, l). High field strength elements (HFSE) such as Th, Zr and Nb, show similar trends with increasing Si. In terms of the mafic rocks, Th, Zr and Nb are positively correlated with Si, whereas intermediate rocks, Th, Zr and Nb define positive to steeply positive linear correlations with increasing Si. The felsic rocks show variable trends with increasing Si, defining positively

correlated trends in the Th vs. Si and Nb vs. Si plots, and a negatively correlated trend in the Zr vs. Si plot (Figs. 6.5d, f, h).

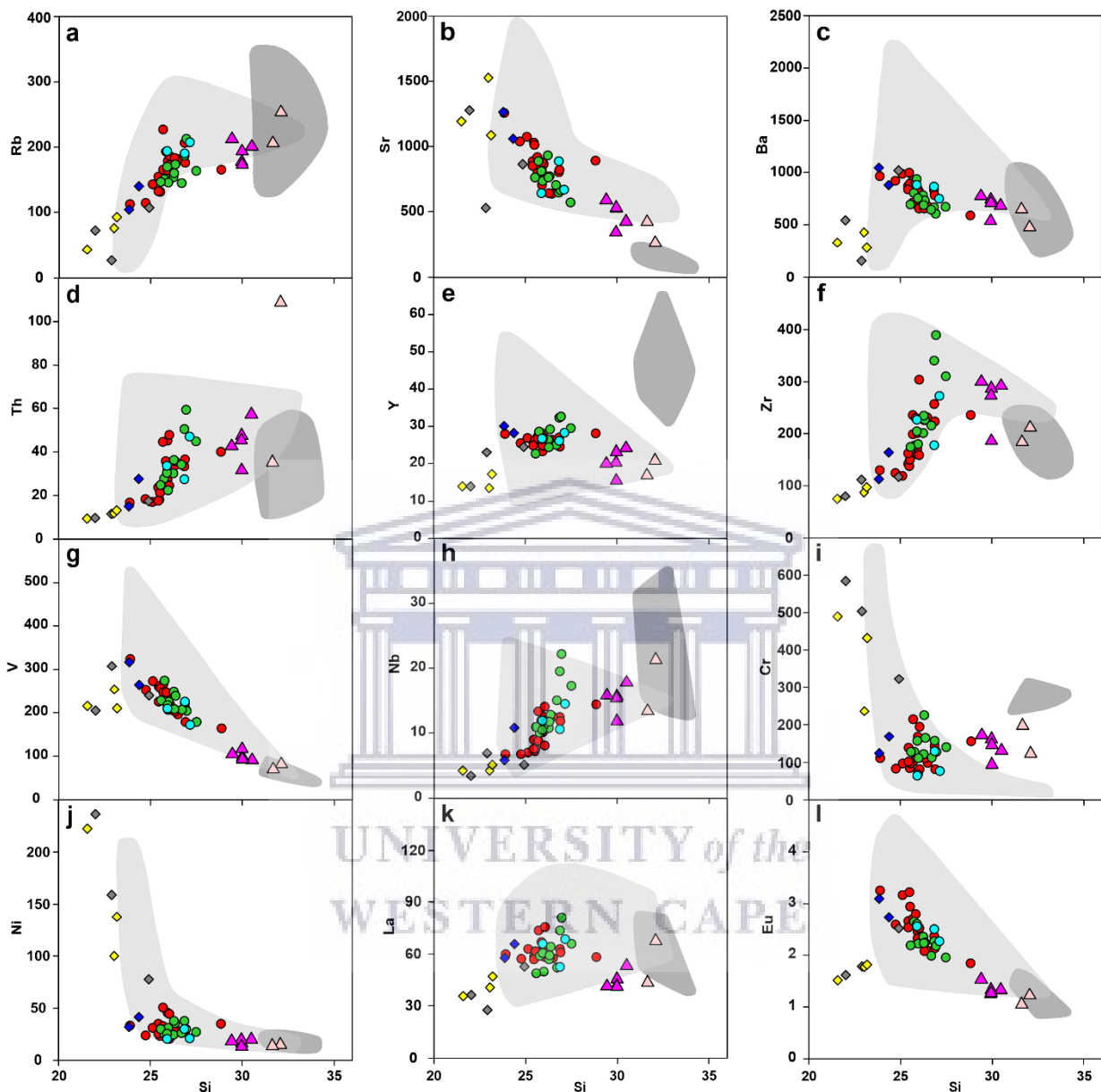


Figure 6.5: Harker plots displaying geochemical trends of selected trace elements for the rocks of the Yzerfontein Pluton. Symbols: same as in Fig. 6.4.

Overall, the compatible trace elements such as V, Cr and Ni, generally display negatively correlated trends with increasing Si (Figs. 6.5g, i, j). In terms of the felsic rocks, a negative correlation is apparent between V and Si, a scattered trend between Cr and Si, and a flat linear correlation between Ni and Si. With the intermediate rocks, a negative correlation is defined between V and Si, a scattered trend between Cr and Si and a relatively flat trend between Ni and Si. Finally, the mafic rocks define a scattered trend in the plot of V vs. Si, and steep negatively correlated trends in the plots of Cr and Ni vs. Si. Variation is seen in the trends between the incompatible elements, such as Y and La, and Si (Figs. 6.5e, k). In terms of the

felsic rocks, Y defines a relatively scattered trend with increasing Si, and La a positively correlated trend with increasing Si. The intermediate rocks display a weakly positive trend in the Y vs. Si plot, and a scattered trend in the La vs. Si plot. Lastly, the mafic rocks display positive trends in both the Y vs. Si and La vs. Si plots.

Overall, most of the samples plot well within the boundaries of the field of published Yzerfontein data on the Harker diagrams, except for selected mafic rocks. In terms of the mafic rocks, selective samples of leucocratic and melanocratic gabbro plot as outliers on all Harker plots. With regards to the intermediate rocks, most of the samples plot well within the boundaries of the field of published Yzerfontein data, with the exception of a few sample outliers (mostly syenodiorite and/or monzonite). Figs. 6.5a, b, c, f, k and l indicate a few sample outliers of quartz-microsyenite and/or monzogranite, whereas in Fig. 6.5i, all the felsic rocks plot outside the field of published Yzerfontein data. Lastly, samples of the monzogranite commonly plot within the field of the I-type granite data.

6.2.4. Rare earth elements (REE)

The REE were normalised to the primitive mantle-normalising values of McDonough and Sun (1995). On the primitive mantle-normalised REE diagrams, the various rock types of the Yzerfontein Pluton display consistent REE patterns which, overall, display gentle negative gradients ($(La/Lu)_{PM} = 10.20 - 27.24$, where the subscript PM denotes primitive mantle normalisation) (Figs. 6.6a, c, e). The light rare earth elements (LREE) define a gently sloping negative pattern with $(La/Sm)_{PM}$ values between 1.90 and 5.07, relative to the heavy rare earth elements (HREE) which define a flat to slightly concave-upward pattern, with $(Gd/Lu)_{PM}$ values between 1.81 and 4.57.

Eu displays moderate to strong negative anomalies, with Eu/Eu^* between 0.53 and 0.97. For the primitive mantle-normalised multi-element spider diagrams, the elements were also normalised to the primitive mantle-normalising values of McDonough and Sun (1995) (Figs. 6.6b, d, f). The rocks display consistent saw-tooth trace element patterns that are gradually negatively sloping. They show enrichments in the LILE, such as Cs, K and Sr, as well as some HFSE, such as Th, U, Pb, La, Nd and Sm, relative to negative anomalies, as shown by some of the LILE including Rb, Ba and Eu, and HFSE, such as Nb, P, Zr and Ti.

In the primitive mantle-normalised REE diagrams, all the samples from this study show similar REE patterns to the published Yzerfontein data (Fig. 6.6a, c, e). They also show similar REE patterns to the I-type granite data, particularly in terms of La, Ce, Pr, Nd and Sm, as opposed to Gd, Tb, Dy, Ho, Er, Tm, Yb and Lu, which show slightly higher concentrations in terms of the I-type granite data. Overall, in the primitive mantle-normalised multi-element spider diagrams, the samples from this study show relatively consistent patterns with the published Yzerfontein data, with few deviations (Fig. 6.6b, d, f). However, the concentration of P from this study appears to be more depleted in the rocks from this study compared to the published Yzerfontein and I-type granite data.

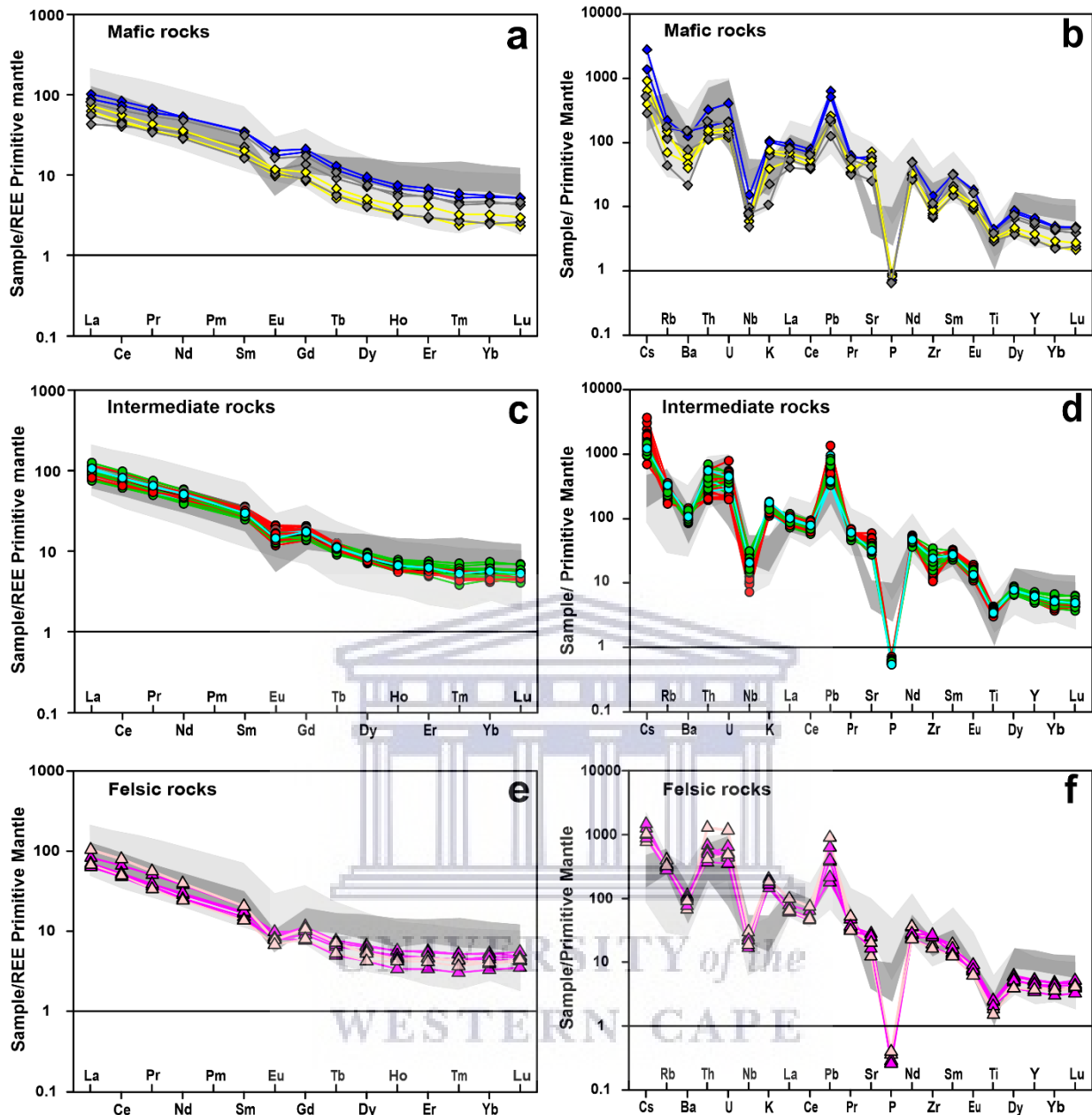


Figure 6.6: Primitive mantle-normalized REE and spider diagrams for the mafic, intermediate, and felsic rocks of the Yzerfontein Pluton (after McDonough and Sun, 1995). Symbols: same as in Fig. 6.4.

6.3. Radiogenic isotope geochemistry

The radiogenic Rb-Sr and Sm-Nd isotope data were obtained for 4 samples, which include a sample of quartz-microsyenite, poikilitic monzogabbro, monzonite and melanocratic gabbro (Tables 6.3 and 6.4). The $\epsilon_{\text{Nd}(t)}$ values were calculated using a reference crystallisation age of 535 Ma for the rocks of the Yzerfontein Pluton, as inferred by Clemens et al. (2017a) from U-Pb zircon data. The gabbroic rocks have Rb/Sr ratios that range between 0.06 and 0.13, with a slightly higher ratio calculated for the monzonite (0.21), and a much higher ratio for the quartz-microsyenite (0.52). The present day $^{87}\text{Sr}/^{86}\text{Sr}_0$ values vary between 0.705388 and 0.714788, relative to initial Sr (Sr I, or alternatively written as initial $^{87}\text{Sr}/^{86}\text{Sr}$) values which range between 0.704225 and 0.705825. These $^{87}\text{Sr}/^{86}\text{Sr}_0$ and Sr I values correspond to a large

range in $^{87}\text{Rb}/^{86}\text{Sr}$ ratios for the various rock types; the gabbroic rocks have $^{87}\text{Rb}/^{86}\text{Sr}$ ratios that range between 0.1512 and 0.3518, with the monzonite having a slightly higher ratio of 0.5569, and the quartz-microsyenite having a much higher ratio of 1.3852.

The four rocks show fairly consistent isotopic ratios, with Sm/Nd ratios (0.18 – 0.21), corresponding to present day $^{143}\text{Nd}/^{144}\text{Nd}_0$ ratios between 0.512237 and 0.512307, and $^{147}\text{Sm}/^{144}\text{Nd}$ ratios between 0.1112 and 0.1290. Additionally, the rocks have consistent initial Nd (Nd I, or alternatively written as initial $^{143}\text{Nd}/^{144}\text{Nd}$) values which range between 0.5118 and 0.5119, with whole-rock Sm-Nd model ages (T_{DM}) of ~1.60 – 1.25 Ga. Lastly, initial epsilon Nd ($\epsilon\text{Nd}_{(t)}$) values are slightly negative, ranging between -2.75 and -0.62, compared to present day epsilon Nd ($\epsilon\text{Nd}_{(0)}$) values which have fairly higher negative values ranging between -7.86 and -5.54. Overall, according to Tables 6.3 and 6.4, the Rb-Sr and Sm-Nd isotopic data presented here are consistent with the published Yzerfontein data of Clemens et al. (2017a).



UNIVERSITY *of the*
WESTERN CAPE

Table 6.3: Whole-rock Rb-Sr isotopic data for the rocks of the Yzerfontein Pluton.

Sample	Rock Type	Rb (ppm)	±2σ	Sr (ppm)	±2σ	⁸⁷ Sr/ ⁸⁶ Sr ₀	±2σ	⁸⁷ Rb/ ⁸⁶ Sr	Sr I	Data source
YZN70	Quartz-microsyenite	178	6.58	342	12.73	0.714788	17	1.3852	0.704225	Present study
YZN75a	Poikilitic Monzogabbro	141	4.53	1062	3.54	0.708086	10	0.3518	0.705403	Present study
YZN92	Monzonite	171	5.30	814	15.56	0.710071	16	0.5569	0.705825	Present study
YZN95	Melanocratic Gabbro	73	3.04	1283	2.83	0.705388	14	0.1512	0.704234	Present study
H10	Monzonite	183	0.60	815	3.70	0.710567	12	0.648	0.70570	Publ. Yzerfontein data
H11	Quartz monzonite	211	1.70	734	6.50	0.712006	10	0.831	0.70577	Publ. Yzerfontein data
H12	Syenogranite dyke	213	0.40	441	1.10	0.715740	13	1.397	0.70526	Publ. Yzerfontein data
H13	Quartz diorite	53	0.20	1278	1.50	0.705268	14	0.120	0.70437	Publ. Yzerfontein data
H24	Monzonite enclave	188	1.50	948	12.60	0.709445	14	0.575	0.70531	Publ. Yzerfontein data
H25	Monzodiorite	88	1.00	1378	30.80	0.710235	11	0.185	0.70885	Publ. Yzerfontein data
H26	Monzodiorite	111	1.60	1458	9.10	0.706850	11	0.219	0.70521	Publ. Yzerfontein data
822B	Hornblendite cumulate	16	0.30	820	19.10	0.704730	9	0.057	0.70430	Publ. Yzerfontein data

Note: Publ. (Published) Yzerfontein data obtained from Clemens et al. (2017a). ⁸⁷Sr/⁸⁶Sr₀ refers to the ⁸⁷Sr/⁸⁶Sr ratio measured at the present day. Sr I refers to the initial ⁸⁷Sr/⁸⁶Sr ratio at the time of emplacement of the rocks, and was determined using the reference age (535 ± 3 Ma) inferred from the U–Pb zircon data in Clemens et al. (2017a). The decay constant used to determine Sr I is 1.42 x 10⁻¹¹ (Steiger & Jäger, 1977).

Table 6.4: Whole-rock Sm-Nd isotopic data for the rocks of the Yzerfontein Pluton.

Sample	Rock Type	Sm (ppm)	±2σ	Nd (ppm)	±2σ	¹⁴³ Nd/ ¹⁴⁴ Nd ₀	±2σ	¹⁴⁷ Sm/ ¹⁴⁴ Nd	Nd I	εNd(t)	εNd(0)	Age (Ma) ^a	T _{DM} (Ga)	Data source
YZN70	Quartz-microsyenite	6.21	0.03	32.60	0.99	0.512237	10	0.1152	0.511833	-2.26	-7.83	535	1.41	Present study
YZN75a	Poikilitic Monzogabbro	14.30	0.92	67.05	0.92	0.512260	12	0.1290	0.511808	-2.75	-7.37	535	1.60	Present study
YZN92	Monzonite	11.78	0.16	58.75	1.34	0.512283	10	0.1212	0.511858	-1.77	-6.93	535	1.43	Present study
YZN95	Melanocratic Gabbro	6.62	0.52	36.00	0.14	0.512307	11	0.1112	0.511917	-0.62	-6.46	535	1.25	Present study
H10	Monzonite	13.60	0.10	69.30	0.80	0.512268	10	0.1186	0.511852	-1.88	-7.22	535	1.41	Publ. Yzerfontein data
H11	Quartz monzonite	12.70	0.20	66.60	0.20	0.512268	9	0.1153	0.511864	-1.65	-7.22	535	1.37	Publ. Yzerfontein data
H12	Syenogranite dyke	6.73	0.10	38.80	0.40	0.512235	11	0.1049	0.511867	-1.59	-7.86	535	1.28	Publ. Yzerfontein data
H13	Quartz diorite	4.40	0.08	24.20	0.20	0.512312	13	0.1099	0.511927	-0.43	-6.36	535	1.23	Publ. Yzerfontein data
H24	Monzonite enclave	11.24	0.09	57.10	0.80	0.512292	15	0.1190	0.511875	-1.44	-6.75	535	1.38	Publ. Yzerfontein data
H25	Monzodiorite	13.78	0.14	68.30	1.50	0.512301	12	0.1220	0.511873	-1.47	-6.57	535	1.41	Publ. Yzerfontein data
H26	Monzodiorite	12.54	0.28	61.40	0.10	0.512320	13	0.1235	0.511887	-1.20	-6.20	535	1.40	Publ. Yzerfontein data
822B	Hornblendite cumulate	12.43	0.06	62.30	0.20	0.512354	9	0.1206	0.511931	-0.34	-5.54	535	1.30	Publ. Yzerfontein data

Note: Publ. (Published) Yzerfontein data obtained from Clemens et al. (2017a), and ^a is the reference age (535 ± 3 Ma) inferred from the U–Pb zircon data in Clemens et al. (2017a). Time t is the time of emplacement of the rocks. ¹⁴³Nd/¹⁴⁴Nd₀ refers to the ¹⁴³Nd/¹⁴⁴Nd ratio measured at the present day. Nd I refers to the initial ¹⁴³Nd/¹⁴⁴Nd ratio at the time of emplacement of the rocks, and was determined using the reference age (^a). The decay constant used to determine Nd I is 6.54 x 10⁻¹² (Lugmair and Marti, 1978).

Chapter 7: Fluid Inclusion Analysis and Stable Isotope Geochemistry

7.1. Fluid Inclusion Analysis: Introduction

A total of 9 samples were prepared for fluid inclusion petrography, 7 of which were further analysed during microthermometry. The microthermometry data of the 7 samples are recorded in Table 7.1, and the compositions of the hydrothermal veins from which the samples were analysed for fluid inclusions are recorded in Table 7.2. During fluid inclusion petrography of the doubly-polished thick sections, the fluid inclusions were classified into fluid inclusion assemblages (FIAs) as either primary, secondary or pseudosecondary fluid inclusions. **Primary fluid inclusions** are formed during the precipitation of the enclosing crystal, and are trapped along the growth zones or the crystal faces of the growing crystal (Randive et al., 2014). These are inferred to be good indicators of the crystallisation conditions of the host crystals. **Secondary fluid inclusions** are formed after the precipitation of the enclosing crystal, and are trapped along healed fractures of the host crystal as they grow. They generally occur as trails or clusters of inclusions that traverse the grain boundaries. **Pseudosecondary fluid inclusions** are formed when a crystal fractures during its growth, and usually occur as trails of inclusions that terminate at the grain boundaries or growth zones (Samson et al., 2003; Randive et al., 2014).

During microthermometry, fluid inclusions were grouped into different types according to their final homogenization ($T_{h(\text{total})}$) phase or behaviour as: 1.) "L", if the final homogenization is characterised by a liquid phase, 2.) "V", if the final homogenization is characterised by a vapour phase, or 3.) "H", if the final homogenisation is characterised by a solid halite phase (Greyling, 2009; Hunt et al., 2011). Generally, fluid inclusions contain more than one of these phases. Fluid inclusions can also be characterised further based on whether they contain a dominant aqueous or carbonic species, however, only aqueous inclusions were identified in this study.

7.2. Fluid Inclusion Petrography

CL imaging was used during fluid inclusion petrography, as it significantly aids in determining the presence of growth zones and classification of fluid inclusion assemblages (Boiron et al., 1992; Greyling, 2009). The growth bands or zones displayed in CL imaging not only record different growth periods (section 5.2), but they also display a colour and compositional variation suggesting a change in the environment of formation of a particular mineral (Craig and Vaughan, 1994; Dye, 2015; Frelinger et al., 2015). The latter is particularly evident by the variation in the lighter and darker coloured bands, as seen in CL imaging. CL imaging was obtained for YZN60a, which is 1 of the 9 samples prepared for fluid inclusion petrography. It displays growth zonation in quartz very well, and it also shows fluid inclusion trails, predominantly along the growth zones. From this observation, most of the fluid inclusions were identified as primary FIAs, with only a small number of inclusions being secondary and pseudosecondary FIAs. This is particularly seen in Fig. 7.1a to f, where the preponderance of fluid inclusions trapped along the growth bands of the quartz grains are illustrated.

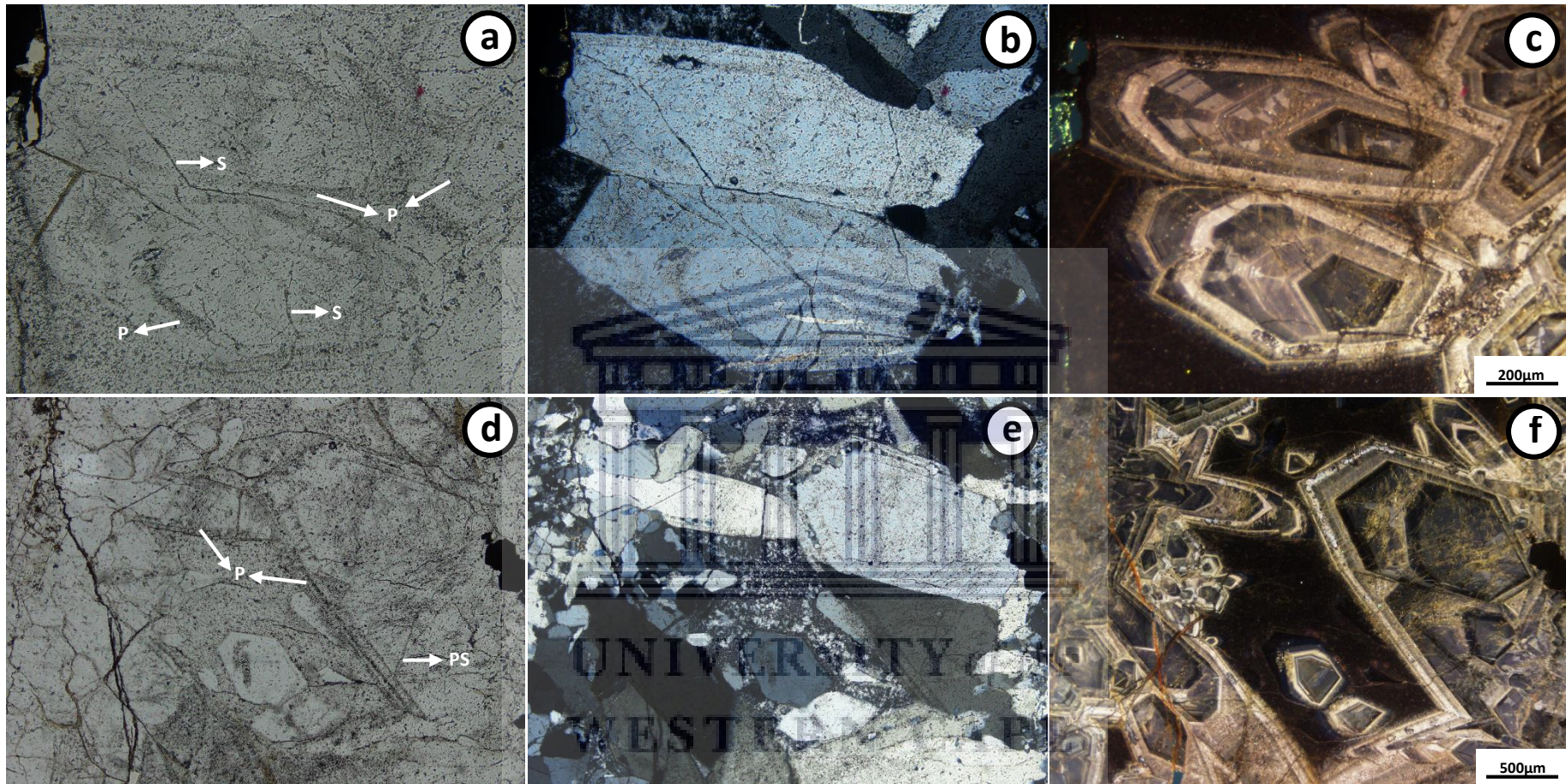


Figure 7.1: Photomicrographs and CL images of two selected areas along a quartz-pyrite-tourmaline vein (YZN60a). (a) and (d) were taken under PPL, and (b) and (e) under XPL in transmitted light. Note the preponderance of primary (P) FIAs along the growth zones of individual crystals. The presence of secondary (S) and pseudosecondary (PS) FIAs are also shown. (c) and (f) are CL images and highlights growth zoning in the quartz crystal; the dark portions of the CL images, as seen in the centre of Fig. 7.1f, are due to the presence of chalcidony which generally gives a dark CL response.

7.3. Microthermometry

7.3.1. Terminology

There is a general consensus amongst researchers on the usage of the correct terminology in microthermometry (Randive et al., 2014). There are several terminologies that are commonly used in fluid inclusion studies, however, only the parameters that were measured during microthermometry in this study are listed below and the terminology was obtained from Diamond (2003):

- i.) $T_{m(\text{ice})}$ – the final temperature at which the solid H_2O phase is completely melted (or dissolved or dissociated) through the progressive heating of a fluid inclusion.
- ii.) $T_{m(\text{halite})}$ – the final temperature at which the solid halite crystal in a fluid inclusion was completely dissolved or dissociated by progressive heating of the fluid inclusion.
- iii.) $T_{h(\text{total})}$ – the total homogenization temperature at which a fluid inclusion was completely transformed (melted/dissolved) from a heterogeneous (two-phase) state to a homogeneous (single-phase) state. Several different phase transitions are possible, and the reactants and products must be recorded together with the temperature: (a) homogenization to the liquid phase via a bubble-point transition, $T_h(\text{LV} \rightarrow \text{L})$; (b) homogenization to the vapour phase via a dew-point transition, $T_h(\text{LV} \rightarrow \text{V})$ or $T_h(\text{critical})$; (c) homogenization to a supercritical fluid via a critical transition, $T_h(\text{LV} \rightarrow \text{SCF})$; (d) homogenization to the liquid phase via a liquidus (melting or dissolution) transition, $T_h(\text{SL} \rightarrow \text{L})$, and homogenization to the vapour phase via a vapourus (sublimation) transition, $T_h(\text{SV} \rightarrow \text{V})$.

The term bubble-point refers to the phase transition when the boundary between the stability field of LV and L is intersected in a phase diagram for multi-phase fluid inclusions (Diamond, 2003a). The term dew-point refers to the phase transition when the boundary between the stability field of LV and V is intersected in a phase diagram for multi-phase fluid inclusions (Diamond, 2003a). These temperatures were, in turn, used to determine the salinity, density and pressure at homogenization by using the software package *AqSo_NaCl*[®] of Bakker (2018).

7.3.2. Fluid Inclusion Types

Jordaan (1990) studied the properties of the fluid inclusions occurring in quartz from two samples of hydrothermal veins at Yzerfontein. The first sample was taken from veins of the main hydrothermal stage, which, according to Jordaan (1990), involved the formation of quartz, pyrite, epidote, jasper, calcite and magnetite veins, whereas the second sample was taken from the later, cross-cutting milky quartz veins. Raman spectroscopic analyses using a microprobe revealed the presence of H_2O -rich liquid and vapour phases, as well as solid NaCl-rich inclusions. However, no CO_2 -rich fluid inclusions were found, even though the presence of CO_2 was indicated by clathrate melting temperatures.

From the results of the present study, the fluid inclusions that were analysed are aqueous, therefore containing no carbonic material, which further corroborates the findings of Jordaan (1990). Two types of fluid inclusions were identified during microthermometry (Table 7.1): (a) Type I: L + V, and (b) Type II: L + V + H. Type I fluid inclusions are characterised by two phases which comprise an aqueous liquid phase and a small vapour phase (H₂O-rich) (Fig. 7.2a, b); they range in size from 4 – 25 μm (Table 7.1). Locally, some fluid inclusions contain a trapped solid which was identified as an opaque phase. The vapour phase in type I fluid inclusions have a vapour volume percentage ranging from 4 – 25%.

Type II fluid inclusions are characterised by an aqueous liquid phase, a solid halite phase and a small vapour phase (H₂O-NaCl-rich) (Figs. 7.2c, d), and they range in size from 5 – 20 μm (Table 7.1). Locally, some fluid inclusions have more than one trapped halite crystal, and others contain an additional trapped opaque phase (Fig. 7.2d). The vapour phase in type II inclusions has a vapour volume percentage ranging from 4 to 12%. Considering the small sizes of these fluid inclusions, it made them difficult to analyse or, at times, to verify the presence of certain phases. Nevertheless, only the largest fluid inclusions were selected where all phases could be identified confidently. It is only in YZN82 where type II fluid inclusions occur together with type I fluid inclusions within the same sample chips.

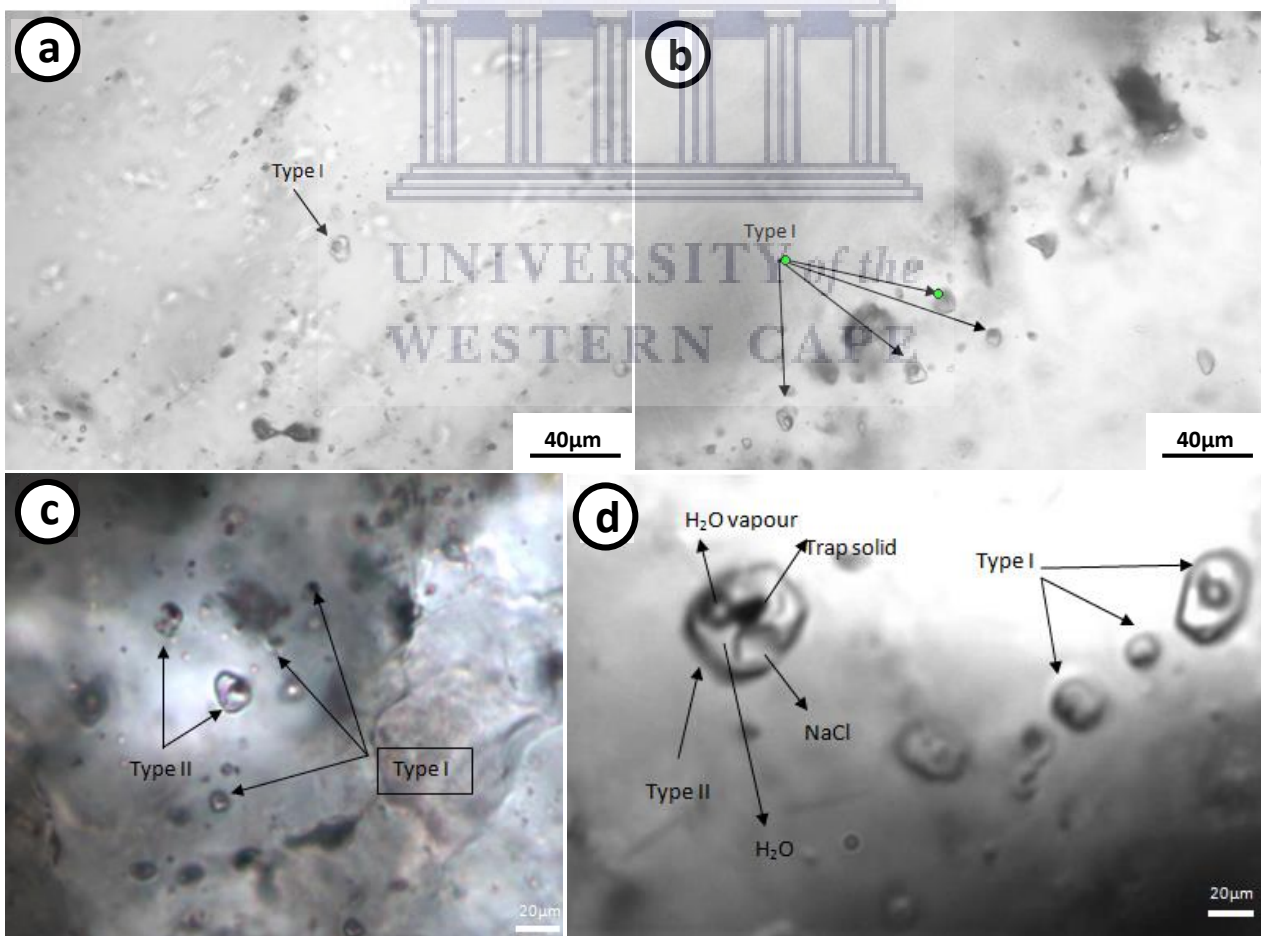


Figure 7.2: Photomicrographs of primary aqueous inclusions. (a) and (b) type I fluid inclusions containing a liquid phase and a small vapour phase (YZN90). (c) and (d) type II fluid inclusions containing a liquid phase, a halite crystal and a small vapour phase (YZN82).

Table 7.1: Microthermometry data for type I and type II aqueous fluid inclusions.

Sample	Chip	FI #	Inclusion Type	Fluid inclusion type	Size (μm)	Vapour volume (%)	$T_{\text{m(ice)}}$	$T_{\text{m(halite)}}$	$T_{\text{h(total)}}$ ($^{\circ}\text{C}$)	$T_{\text{h(total)}}$ phase	Salinity (wt. % NaCl _{equiv.})	Density (g/cm^3)	Pressure at homogenization (MPa)
YZN44	1	1	1	P	10	16	-2.2		225	L	3.71	0.87	3
		2	1	P	5	16	-2.4		228	L	4.03	0.86	3
YZN54	1	1	1	P	5	10	-6.0		175	L	9.21	0.96	1
YZN60a	1	1	1	P	6	15	-4.5				7.17		
		2	1	P	5	15	-2.1		223	L	3.55	0.87	2
YZN60b	1	1	1	P	8	27	-6.5		320	L	9.86	0.79	11
		2	1	P	5	10	-2.2		155	L	3.71	0.94	1
	3	2	1	P	5	5	-6.0				9.21		
		3	1	P	10	10			125	L			
		1	1	Ps	15	15	-7.7		236	L	11.34	0.92	3
		2	1	Ps	13	15							
		3	1	Ps	4	10	-5.5				8.55		
		4	1	Ps					188	L			
5	1	Ps					175	L					
YZN82	1	1	2	P	6	10		310	175	L	38.86	1.21	278
		2	2	P	8	9		302	163	L	38.29	1.21	294
	2	1	2	P	7	4		290	210	L	37.27	1.17	145
		2	1	P					288	L			
	3	1	1	Ps	10	11	-5.6		190	L	8.68	0.94	1
	4	1	2	P	10	6		330	170	L	40.29	1.22	350
		2	2	P	10	5		372	166	L	43.50	1.25	554
	5	1	1	P	20	15	-5.6		222	L	8.68	0.91	2
	6	1	2	P	7	10		350	186	L	41.94	1.22	357
	7	1	1	P	8	10	-3.8		170	L	6.16	0.94	1
	8	1	2	P	15	12		379	203	L	44.48	1.24	395
	9	1	2	P	12	8		332	198	L	40.43	1.20	262
	10	1	2	P	20	10		316	188	L	39.30	1.20	255
		2	2	P	14	10		320	195	L	39.60	1.20	245
11	1	2	P	7	8		314	162	L	39.18	1.22	332	
12	1	2	P	5	7		317	158	L	39.41	1.22	355	
13	1	2	P	10	12		260	167	L	35.37	1.18	182	
14	1	2	P	14	12		294	177	L	37.67	1.19	233	

Abbreviations: FI # = fluid inclusion number; P = primary fluid inclusion; S = Secondary fluid inclusions; Ps = Pseudosecondary fluid inclusion; L = liquid phase. Note: The last three parameters on the right side of the table (salinity, density and pressure) have been calculated, and the other parameters on the left side of the table ($T_{\text{m(ice)}}$, $T_{\text{m(halite)}}$ and $T_{\text{h(total)}}$) have been measured.

Table 7.1 (continued)

Sample	Chip	FI #	Inclusion Type	Fluid inclusion type	Size (μm)	Vapour volume (%)	$T_{\text{m(ice)}}$	$T_{\text{m(halite)}}$	$T_{\text{h(total)}}$ ($^{\circ}\text{C}$)	$T_{\text{h(total)}}$ phase	Salinity (wt. % NaCl _{equiv.})	Density (g/cm^3)	Pressure at homogenization (MPa)
YZN82	15	1	2	P	10	10		270	197	L	36.04	1.17	139
	16	1	1	P	8	12	-4.1		189	L	6.59	0.93	1
	17	1	2	P	11	8		323	172	L	39.82	1.22	321
YZN86	1	1	1	P	10	10	-2.5				4.18		
YZN90	1	1	1	P	15	22	-2.1		273	L	3.55	0.80	6
	2	1	1	P	8	20	-2.1		170	L	3.55	0.92	1
		2	1	P	14	20	-1.9		154	L	3.22	0.94	1
		3	1	P	15	25	-1.9		210	L	3.22	0.88	2
		4	1	P	10	15	-1.9				3.22		
		5	1	P	10	15	-1.8				3.06		
	3	1	1	P	18	18	-3.9		243	L	6.30	0.87	3
		2	1	P	18	18	-3.9		243	L	6.30	0.87	3
	4	1	1	P	10	15			279	L			
	5	1	1	S	25	10	-4.7		174	L	7.45	0.95	1
		2	1	S	25	15	-2.0		196	L	3.39	0.90	1
	6	1	1	P	25	15	-2.2		206	L	3.71	0.89	2
	7	1	1	P	15	12	-2.0		172	L	3.39	0.92	1
		2	1	P	13	11	-2.1		176	L	3.55	0.92	1
		3	1	P	15	11	-2.0		179	L	3.39	0.91	1
	4	1	P	14	12	-2.0		168	L	3.39	0.92	1	
	5	1	P	12	10	-2.1		175	L	3.55	0.92	1	

Abbreviations: FI # = fluid inclusion number; P = primary fluid inclusion; S = Secondary fluid inclusions; Ps = Pseudosecondary fluid inclusion; L = liquid phase. Note: The last three parameters on the right side of the table (salinity, density and pressure) have been calculated, and the other parameters on the left side of the table ($T_{\text{m(ice)}}$, $T_{\text{m(halite)}}$ and $T_{\text{h(total)}}$) have been measured.

Table 7.2: Composition of hydrothermal veins from which samples were analysed, the rock types which they traverse and the locality from which the samples were collected.

Sample	Vein Composition	Rock Type	Area
YZN44	barren Qz	Monzonite	Yzerfontein Point
YZN54	Qz-Tur	Monzonite	Freddie se Klip
YZN60a	Qz-Py-Tur	Monzonite	Schaap Eiland
YZN60b	Qz-Py-Tur	Monzonite	Schaap Eiland
YZN82	Cal-Ep	Syenodiorite	Yzerfontein Harbour
YZN86	Qz-Tur-Jsp	Syenodiorite	Grasbank
YZN90	Qz-Tur	Monzonite	Yzerfontein Point

Abbreviations: Cal = Calcite, Ep = Epidote, Jsp = Jasper, Py = Pyrite, Qz = Quartz, Tur = Tourmaline (after Whitney and Evans, 2010).

Type I fluid inclusions have ice melting temperatures ($T_{m(\text{ice})}$) that range from -7.7 to -1.8°C , with densities ranging from $0.79 - 0.96 \text{ g/cm}^3$ (Table 7.1). They have fairly low to high homogenization temperatures ($T_{h(\text{total})}$) ranging from $125 - 320^\circ\text{C}$, with low associated salinities and homogenization pressures ranging from $3.06 - 11.34 \text{ wt. \% NaCl}_{\text{equiv.}}$ and $1 - 11 \text{ MPa}$, respectively (Fig. 7.3 and Table 7.1). The solid halite phases contained in type II inclusions cannot be interpreted as daughter minerals since the halite melting temperatures are higher than the temperatures associated with vapour homogenization to the liquid phase (Greyling, 2009). Type II inclusions have halite melting temperatures ($T_{m(\text{halite})}$) that range from $260 - 379^\circ\text{C}$, with densities ranging from $1.17 - 1.25 \text{ g/cm}^3$ (Table 7.1). The $T_{h(\text{total})}$ of type II inclusions is fairly moderate, ranging from $158 - 210^\circ\text{C}$, with high associated salinities and homogenization pressures ranging from $35.37 - 44.48 \text{ wt. \% NaCl}_{\text{equiv.}}$ and $139 - 554 \text{ MPa}$, respectively (Fig. 7.3 and Table 7.1). From these observations, it is evident that type II inclusions have lower $T_{h(\text{total})}$ and higher salinities, as well as higher homogenization pressures than type I inclusions (Fig. 7.3).

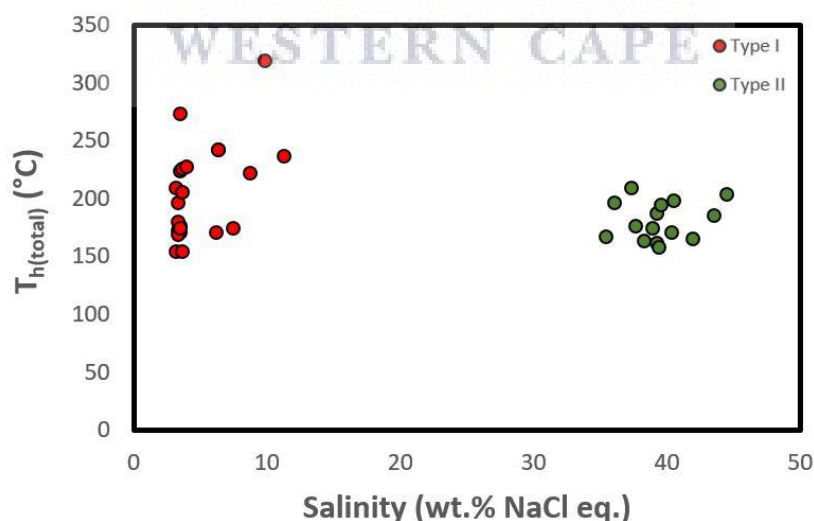


Figure 7.3: Bivariate plot of $T_{h(\text{total})}$ vs. salinity differentiating between Type I and Type II fluid inclusions.

Figs. 7.4 and 7.5 display histograms that illustrate the distribution of the various microthermometry results for type I and type II fluid inclusions, respectively.

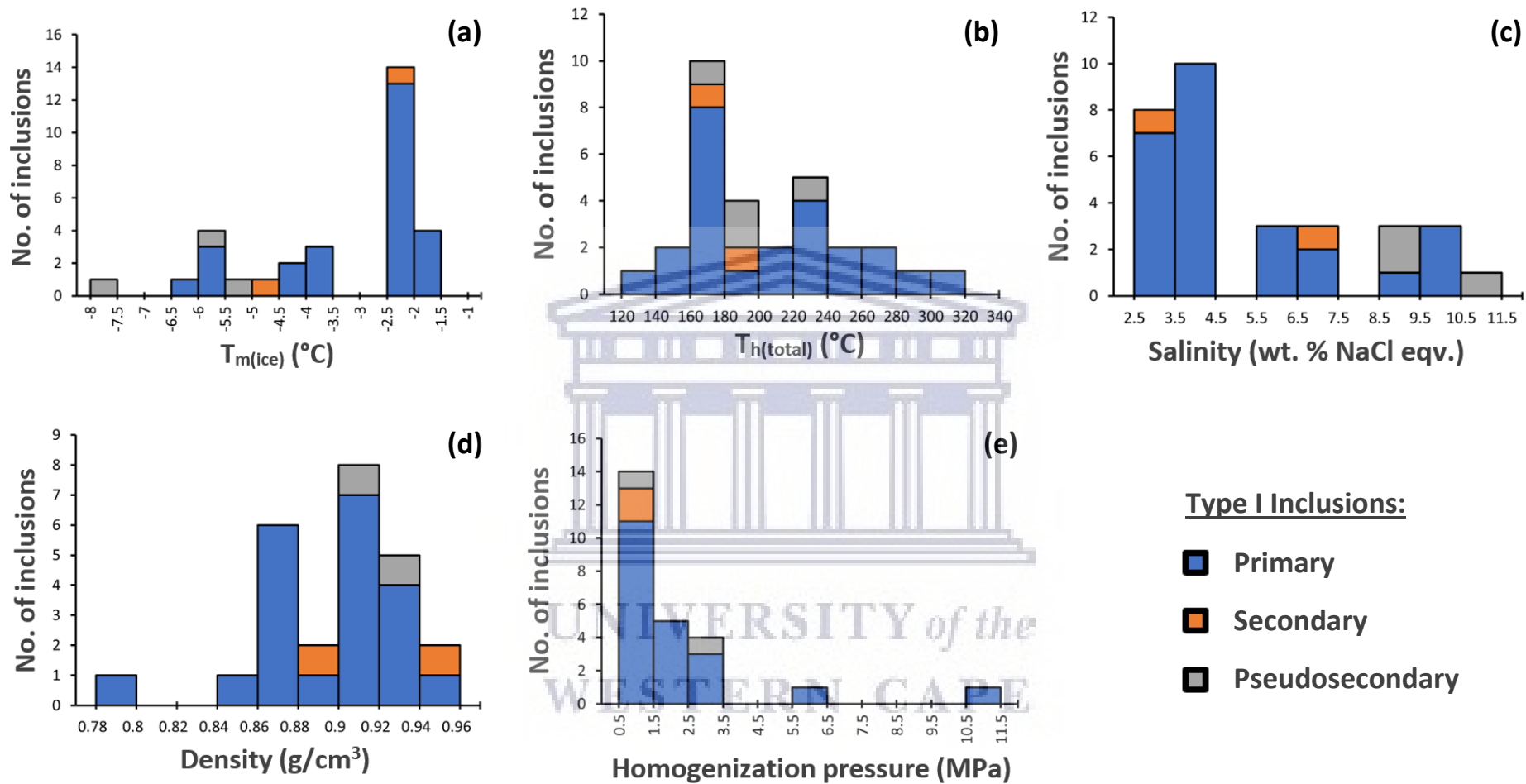


Figure 7.4: Histograms showing the distribution of (a) $T_{m(ice)}$, (b) $T_{h(total)}$, (c) salinities, (d) densities and (e) homogenization temperature for all type I inclusions. The histograms also distinguish between primary, secondary and pseudosecondary fluid inclusions. Homogenization for all type I fluid inclusions are to the liquid phase (see Table 7.1).

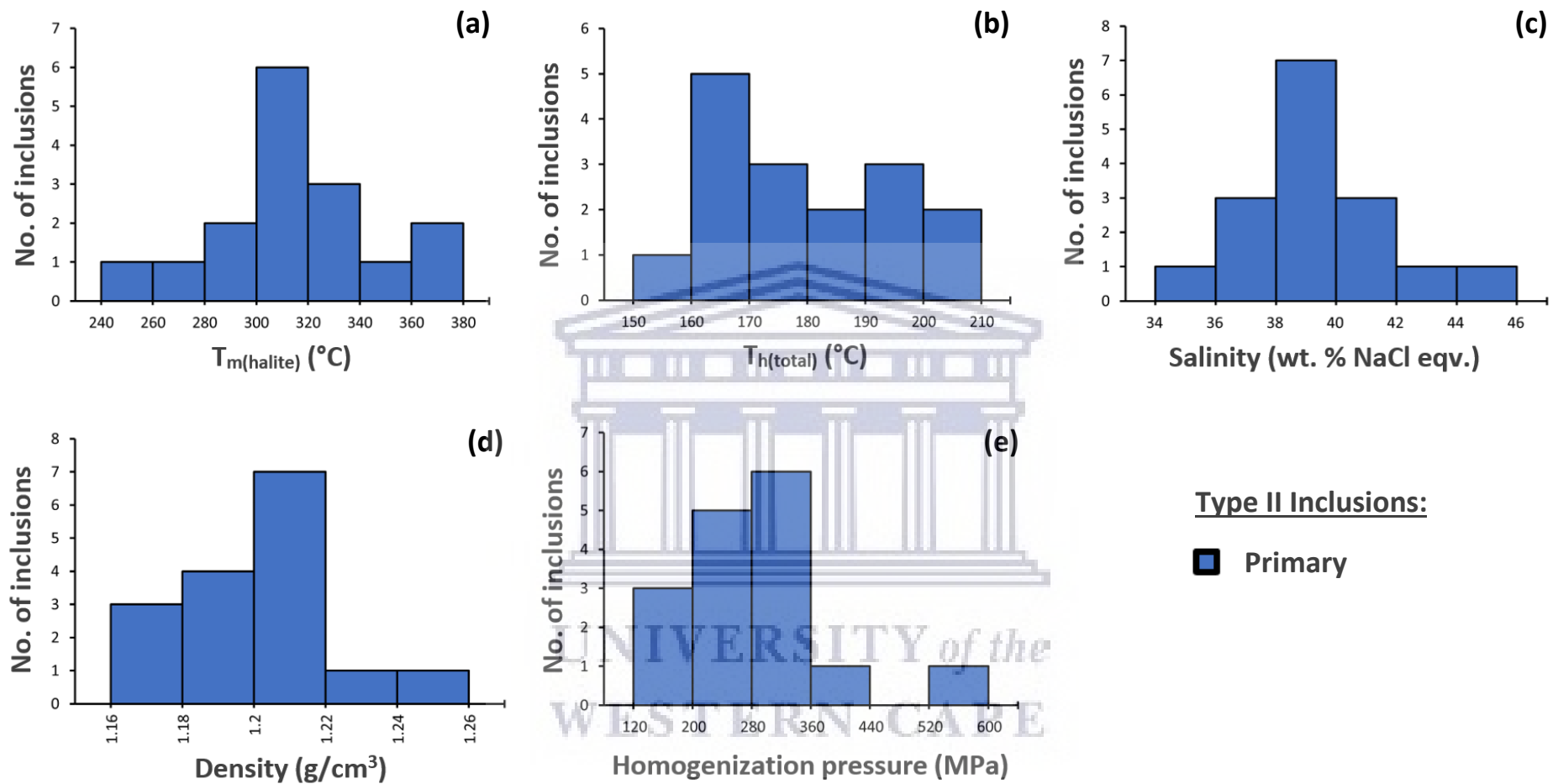


Figure 7.5: Histograms showing the distribution of (a) $T_{m(\text{halite})}$, (b) $T_{h(\text{total})}$, (c) salinities, (d) densities and (e) homogenization pressure for all type II inclusions. Only primary fluid inclusions were identified. Homogenization for all Type II fluid inclusions are to the liquid phase (see Table 7.1).

Most of the type I fluid inclusions melt between -2.5 and -2.0 °C, with most inclusions homogenizing to the liquid phase between 160 and 180 °C (Fig. 7.4a, b). The inclusions mostly have salinities in the range of 2.5 – 4.5 wt. % NaCl_{equiv.}, with the majority of the inclusions having densities in the range of 0.86 – 0.94 g/cm³ (Fig. 7.4c, d). Finally, the bulk of the type I fluid inclusions have homogenization pressures in the range of 0.5 – 1.5 MPa, with two primary inclusions plotting away from the sample distribution and having much higher homogenization pressures of 6 MPa (or in the range of 5.5 – 6.5 MPa) and 11 MPa (or in the range of 10.5 – 11.5 MPa), respectively (Table 7.1 and Fig. 7.4e).

In type II inclusions halite melts mostly at temperatures between 300 and 320 °C. Type II fluid inclusions define a narrower range of homogenization temperatures (150 – 210 °C, as was mentioned before) compared to type I fluid inclusions, with most of the type II inclusions homogenizing to the liquid phase between 160 and 180 °C (Fig. 7.5a, b). The majority of the type II inclusions have salinities in the range of 38 – 40 wt. % NaCl_{equiv.}, with most of the inclusions having densities in the range of 1.20 – 1.22 g/cm³ (Fig. 7.5c, d). Lastly, type II inclusions define a broad range of homogenization pressures (139 – 554 MPa, as was mentioned before), most of which plot in the range of 200 – 360 MPa (Fig. 7.5e). One sample in particular plots away from the sample distribution with a very high homogenization pressure of 554 MPa (or in the range of 520 – 600 MPa) (Table 7.1).

7.4. Stable Isotope Geochemistry

7.4.1. Introduction

A total of 8 samples from various hydrothermal veins were selected for stable isotope geochemistry. Oxygen isotope ($\delta^{18}\text{O}$) compositions are recorded for quartz, tourmaline, H₂O and calcite, deuterium isotope (δD) compositions for tourmaline and H₂O, and carbon isotope ($\delta^{13}\text{C}$) compositions for calcite (Table 7.3). The compositions of the hydrothermal veins from which the samples were extracted and analysed for stable isotopes are recorded in Table 7.4.

Table 7.3: Measured oxygen, hydrogen and carbon isotopic data for different quartz, tourmaline and calcite samples from hydrothermal veins.

Sample	$\delta^{18}\text{O}$ qz	Sample	$\delta^{18}\text{O}$ tur	Sample	$\delta^{18}\text{O}$ cal	Sample	δD tur	Sample	$\delta^{13}\text{C}$ cal
YZN44	11.17	YZN61a	8.94	YZN82	15.06	YZN61a	-34.50	YZN82	-2.33
YZN45	14.38	YZN62	10.87	YZN98	16.12	YZN62	-43.70	YZN98	-1.93
YZN60a	13.74								
YZN61a	14.70								
YZN63	10.78								

Abbreviations: Cal = Calcite, Qz = Quartz, Tur = Tourmaline (after Whitney and Evans, 2010).

Table 7.4: Composition of hydrothermal veins from which samples were analysed, the rock types which they traverse and the locality from which the samples were collected.

Sample	Vein Composition	Rock Type	Area
YZN44	barren Qz	Monzonite	Yzerontein Point
YZN45	Qz-Py-Tur-Jsp	Monzonite	Starck
YZN60a	Qz-Py-Tur	Monzonite	Schaap Eiland
YZN61a	Qz-Py-Tur	Monzonite	SW of Visitor's Center
YZN62	tourmalinite breccia	Monzonite	W of Visitor's Center
YZN63	Qz-Tur	Monzonite	W of Visitor's Center
YZN82	Cal-Ep	Syenodiorite	Yzerfontein Harbour
YZN98	Cal	Syenodiorite	Yzerfontein Harbour

Abbreviations: Cal = Calcite, Ep = Epidote, Jsp = Jasper, Py = Pyrite, Qz = Quartz, Tur = Tourmaline (after Whitney and Evans, 2010).

In order to use the oxygen and hydrogen fractionation equations, a temperature factor must be established. The $T_{h(\text{total})}$ of type I and type II fluid inclusions can only be used to determine minimum trapping temperatures, and this does not provide the exact temperature of entrapment of the fluids, which, in turn, records the crystallisation temperature of the fluids, as is needed to determine the isotopic values. Since no such temperature was determined in the present study, and due to the lack of any other constraints, independent geothermometers can be useful to determine unknown isotopic values using fractionation equations. If the crystallisation temperature of a mineral was determined by chemical analysis, it can serve as a mineral geothermometer. Therefore, if the crystallisation temperature of at least one mineral (either associated with the hydrothermal veins and/or the alteration haloes) in the paragenetic sequence was determined, it is possible to calculate the unknown isotopic values using fractionation equations. Alternatively, a stable isotope geothermometer can also be determined by means of oxygen isotope fractionation between silicates, provided that the $\delta^{18}\text{O}$ isotopic values of two co-existing minerals are known.

The importance of calculating the isotopic values for H_2O , particularly the $\delta^{18}\text{O}$ and δD values, is to determine the origin and nature of the fluids that gave rise to the hydrothermal veins (Taylor, 1997; Robb, 2005). Therefore, it is important to note that there are several sources of hydrothermal fluids, the principal types including: (i) seawater, (ii) meteoric water and (iii) juvenile water (Hoefs, 2018). Juvenile water is defined by Hoefs (2018) as water that was derived from the degassing of the mantle and has never formed part of the surficial hydrological cycle. Nevertheless, the principal sources of hydrothermal fluids have strictly defined isotopic compositions. The other possible reservoirs by which ore fluids may be generated include formation water, metamorphic water and magmatic water, and these are considered to be recycled reservoirs that have, to some extent, been derived from the mixing of one or more of the three principal reference waters (Figs. 7.6 to 7.8) (Hoefs, 2018).

7.4.2. Isotope geothermometer

Only one sample (YZN63), that contained co-existing quartz and tourmaline (both silicates), was analysed for its $\delta^{18}\text{O}$ isotope values (Table 7.3). The $\delta^{18}\text{O}$ isotope values of these co-existing minerals can be used to calculate a stable isotope geothermometer that serves as a temperature estimate for further $\delta^{18}\text{O}$ isotope value determinations. The empirical quartz-tourmaline oxygen isotope fractionation equation of Kotzer et al. (1993) is useful as an oxygen isotope geothermometer. It helps to constrain the temperature of oxygen isotope fractionation between quartz and tourmaline if the fractionation factor, $\alpha_{(qz-tur)}$, is known. The equation is as follows:

$$1000 \ln \alpha_{(qz-tur)} = 1.0 \left(\frac{10^6}{T^2} \right) + 0.39 \quad \text{Equation 7.1}$$

The constants present in the above equation were experimentally determined. Given the quartz and tourmaline $\delta^{18}\text{O}$ isotopic values, the temperature of oxygen isotope fractionation between these two minerals was determined and a temperature of ~ 162 °C was obtained (Appendix E). The error on this temperature, assuming reasonable errors on the $\delta^{18}\text{O}$ isotope values (0.2 per mil each), is ± 1.62 °C, which is approximately a 100th of the calculated temperature. According to Hoefs (2018), one disadvantage of stable isotope geothermometers, particularly in slowly cooled metamorphic and magmatic rocks, is that they yield temperature estimates that are significantly lower than those from other geothermometers. A temperature of ~ 162 °C is certainly very low, especially considering that most fractionation equations are reliable at a more elevated temperature (i.e. higher than ~ 162 °C). Using a temperature that does not fall within the reliable temperature range of a particular fractionation equation can yield spurious and incorrect results. Moreover, there is no way of knowing exactly how far off the temperature estimate is from the actual temperature of oxygen isotope fractionation between quartz and tourmaline, except by means of chemical analysis.

It is for the above reasons that the isotope geothermometer of ~ 162 °C will not be used. As mentioned previously, if the crystallisation temperature of at least one mineral (either associated with the hydrothermal veins and/or the alteration haloes) in the paragenetic sequence was determined, it can serve as a mineral geothermometer. Jordaan (1990) determined the crystallisation temperature of chlorite by performing microprobe analyses at regular intervals across chlorite layers, and subsequently converted each of the chemical analyses to a temperature by using appropriate formulas. The chlorite layers analysed were taken from a single hydrothermal vein containing chlorite, quartz, jasper and pyrite. Ultimately, the temperature of crystallisation was constrained to around 300 °C. This temperature of crystallisation corresponds with, and falls in the overall range of $T_{h(\text{total})}$ obtained from microthermometric analyses of type I and II fluid inclusions (125 – 320 °C) in this study. This temperature was therefore used to determine the various unknown $\delta^{18}\text{O}$, δD and $\delta^{13}\text{C}$ isotopic values in order to decipher the origin and nature of the fluids.

7.4.3. $\delta^{18}\text{O}$ isotope results

Measured $\delta^{18}\text{O}$ isotopic values

$\delta^{18}\text{O}$ isotopic values were measured from samples comprising various generations of veins, as shown in Table 7.3. The veins which were analysed for quartz $\delta^{18}\text{O}$ isotope values have values ranging between 10.78 and 14.70 ‰, with YZN63 and YZN61a having the lowest and highest values respectively. Only two samples of tourmaline were analysed for their $\delta^{18}\text{O}$ isotopic values. The lowest value was recorded for YZN61a with a $\delta^{18}\text{O}$ isotopic value of 8.94 ‰, and a higher value of 10.87 ‰ measured for YZN62. Two calcite-bearing veins, YZN82 and YZN98, were also analysed for their $\delta^{18}\text{O}$ isotope values and have values of 15.06 ‰ and 16.12 ‰ respectively.

Calculated $\delta^{18}\text{O}$ isotopic values

Where $\delta^{18}\text{O}$ isotopic values for H_2O and tourmaline were not available from stable isotope analyses, they were determined by making use of various oxygen fractionation equations listed in Table E1. The empirical quartz-tourmaline oxygen isotope fractionation equation of Kotzer et al. (1993) (equation 7.1) can be used to constrain the $\delta^{18}\text{O}$ isotopic value of tourmaline for samples which have known quartz $\delta^{18}\text{O}$ isotopic values, but unknown tourmaline $\delta^{18}\text{O}$ isotopic values. Equation 7.1 is reliable particularly for temperatures between 200 and 600 °C. The crystallisation temperature of chlorite (300 °C) will be used as the temperature factor, T , in equation 7.2. The resulting calculated $\delta^{18}\text{O}$ isotopic values for tourmaline ranges between 7.34 and 10.94 ‰ (Table 7.5; Appendix E).

Table 7.5: Calculated oxygen and hydrogen isotopic data for tourmaline and water.

Sample	$\delta^{18}\text{O}$ tur	Sample	$\delta^{18}\text{O}$ $\text{H}_2\text{O}^{(b)}$	Sample	δD H_2O
YZN45	10.94	YZN44	4.28	YZN61a	4.05
YZN60a	10.30	YZN45	7.49	YZN62	-5.15
YZN63	7.34	YZN60a	6.85		
		YZN61a	7.81 (1)		
		YZN61a	6.18 (2)		
		YZN62	8.11		
		YZN63	3.86		

(1) value determined using oxygen isotope fractionation equation for the qz- H_2O pair,

(2) value determined using oxygen isotope fractionation equation for the tur- H_2O pair,

Abbreviations: Tur = Tourmaline (after Whitney and Evans, 2010).

The $\delta^{18}\text{O}$ isotopic value of H_2O can be determined by making use of the equations for oxygen isotope fractionation between quartz and H_2O (Clayton et al., 1972), as well as between tourmaline and H_2O (Zheng, 1993). For the quartz- H_2O pair, the equation is:

$$1000 \ln \alpha_{(qz-H_2O)} = \left(\frac{3.38 \times 10^6}{T^2} \right) - 3.40 \quad \text{Equation 7.2}$$

In the case of the tourmaline- H₂O pair, the equation is:

$$1000 \ln \alpha_{(tur-H_2O)} = \left(\frac{4.21 \times 10^6}{T^2} \right) + \left(\frac{-6.99 \times 10^3}{T} \right) + 2.14 \quad \text{Equation 7.3}$$

Equation 7.2 is reliable for temperatures between 200 and 500 °C, and equation 7.3 for temperatures between 0 and 1200 °C. Using a temperature of 300 °C, the equations yield δ¹⁸O isotopic values for H₂O ranging between 3.86 and 8.11 ‰ (Table 7.5; Appendix E.)

7.4.4. δD isotope results

Measured δD isotopic values

Hydrogen isotopic values were measured from two tourmaline-bearing samples (Table 7.3). YZN61a has a δD isotopic value of -34.50 ‰, with YZN62 having a lower value of -43.70 ‰.

Calculated δD isotopic values

The δD isotopic value of H₂O can be determined by making use of the equation for hydrogen isotope fractionation between tourmaline and H₂O (Jiang, 1998):

$$1000 \ln \alpha_{(tur-H_2O)} = -14.2 \left(\frac{10^6}{T^2} \right) + 4.7 \quad \text{Equation 7.4}$$

Equation 7.4 is reliable particularly for temperatures between 300 and 600 °C. Using a temperature of 300 °C, the resulting calculated δD isotopic values of H₂O for samples YZN61a and YZN62 are 4.05 ‰ and -5.15 ‰, respectively (Table 7.5; Appendix E). These δD isotopic values of H₂O, together with the δ¹⁸O isotopic values of H₂O, are important as they can be used to plot a diagram of δ¹⁸O vs. δD in order to constrain the origin of the fluids, as will be illustrated in Section 7.4.6 (Fig. 7.9).

7.4.5. δ¹³C isotope results

Measured δ¹³C isotopic values

Carbon isotopic values were measured from two calcite samples, with YZN98 having a value of -1.93 ‰, and YZN82 having a slightly lower value of -2.33 ‰ (Table 7.3).

7.4.6. Origin of the fluids

Overall, the δ¹⁸O isotopic values (both measured and calculated) of quartz (10.78 – 14.70 ‰), calcite (15.06 ‰ – 16.12 ‰), H₂O (3.86 – 8.11 ‰) and tourmaline (7.34 – 10.94 ‰), both calculated and obtained from stable isotope analyses, overlap with values from meteoric water, magmatic water and metamorphic water (Fig. 7.6). This provides a mixed signal for the origin of the fluids. Based on these observations, the origin of the fluids cannot be conclusively inferred from Fig. 7.6. The origin of these fluids will be further assessed and discussed in more detail later in this section, as well as in Section 8.5.2 where all the strands (microthermometry, stable isotopes, petrography, etc.) are brought together.

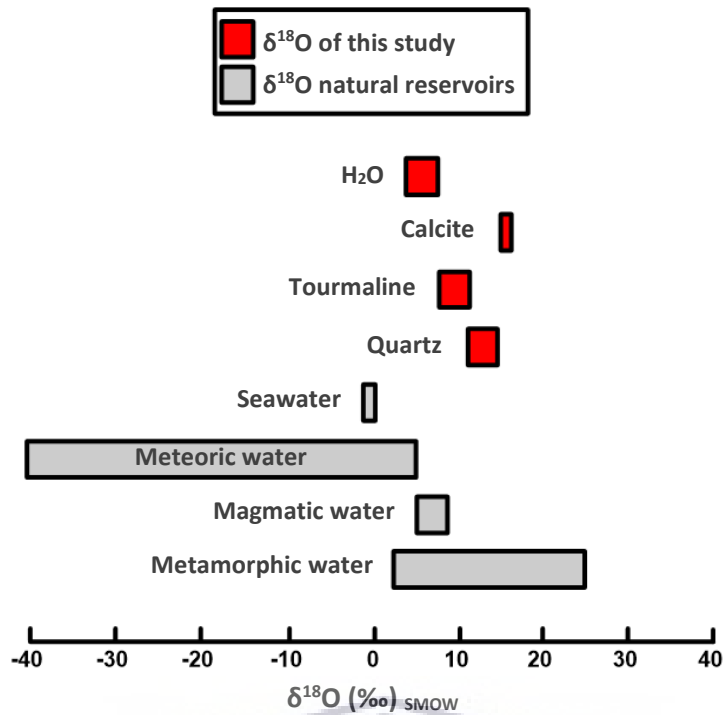


Figure 7.6: $\delta^{18}\text{O}$ isotopic values of quartz, tourmaline, calcite and H_2O from present study, as well as known natural reservoirs according to Taylor (1974) and Hoefs (1987).

The measured δD isotopic values of tourmaline for samples YZN61a and YZN62 (-34.50 – -43.70 ‰) overlap with values from meteoric-, magmatic- and metamorphic water, and the calculated δD isotopic values of H_2O for these two samples (4.05 – -5.15 ‰) overlap with values from seawater, meteoric- and metamorphic water (Fig. 7.7). From these observations, an overall meteoric origin is inferred for the tourmaline-bearing fluids, however, a metamorphic origin could also apply. δD isotopic values of H_2O indicate a mixed signal for the origin of H_2O -bearing fluids with both seawater and meteoric water playing a role.

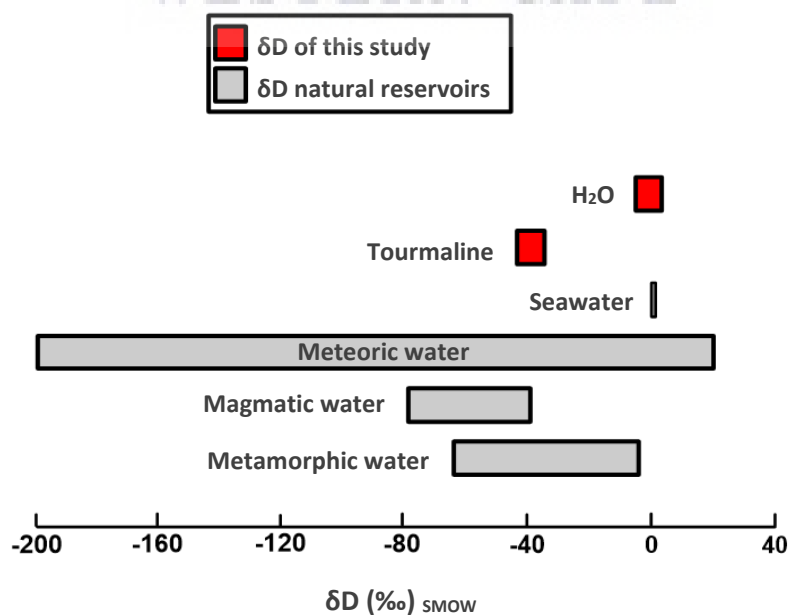


Figure 7.7: δD isotopic values of tourmaline and H_2O from present study, as well as known natural reservoirs according to Taylor (1974) and Hoefs (1987).

The measured $\delta^{13}\text{C}$ isotopic values of calcite for samples YZN82 and YZN98 (-2.33 – -1.93 ‰) overlap with $\delta^{13}\text{C}$ isotopic values of limestone, marine carbonates and the range of mantle $\delta^{13}\text{C}$ isotopic values.

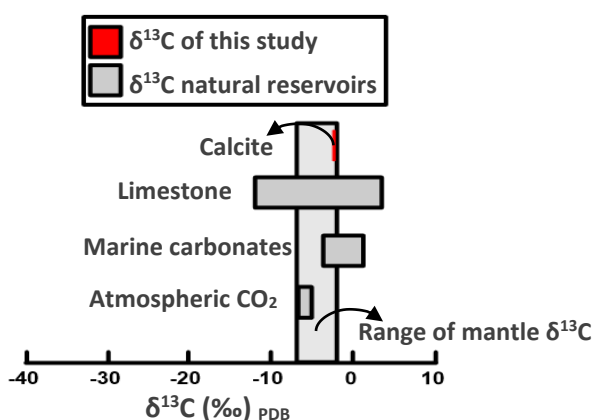


Figure 7.8: $\delta^{13}\text{C}$ isotopic values of calcite and H_2O from present study (for YZN82 and YZN98), as well as known natural reservoirs (after Hoefs, 1987, 2018; Schidlowski, 1987). The arrow pointing to the left is showing the range of $\delta^{13}\text{C}$ values for calcite (thin red line), and the arrow pointing to the right is showing the range of mantle $\delta^{13}\text{C}$ (grey vertical bar in the center).

Even though only a small number of samples were analysed for stable isotope values, these samples are spread over a large extent of the study area, and therefore provides an overall idea of the isotopic values of the veins from W of the Visitors Center through to Schaap Eiland (Figs. A3, A4, A5, A9). From the overall observations made with respect to Figs. 7.6, 7.7 and 7.8, it is apparent that the $\delta^{18}\text{O}$ and δD isotope values of quartz-, tourmaline- and calcite-bearing hydrothermal veins from W of the Visitors Center (YZN62 and YZN63), SW of the Visitors Center (YZN61a), Starck (YZN45), Yzerfontein Point (YZN44) and Schaap Eiland (YZN60a) correspond largely to values of fluids that indicate a substantial meteoric component. The $\delta^{13}\text{C}$ isotopic value of the calcite samples from the Yzerfontein Harbour (YZN82 and YZN98) is more difficult to constrain to a particular origin as it corresponds to $\delta^{13}\text{C}$ isotopic values for limestone, marine carbonates and the mantle. Derivation of calcite from mantle-derived magmatic rocks can possibly be inferred as an origin for the calcite, however, these samples require further considerations with regards to their microthermometry in order to constrain the origin of these fluids.

The $\delta^{18}\text{O}$ vs. δD diagram, as mentioned before, can also be used to constrain the origin of fluids. The measured δD isotopic values of H_2O , together with the calculated $\delta^{18}\text{O}$ isotopic values of H_2O , were plotted on a $\delta^{18}\text{O}$ vs. δD diagram (Fig. 7.9). Both samples plot relatively close to the meteoric water line and are rich in δD , suggesting that their origin is related to a dominantly meteoric water source, and specifically one at low latitudes. This correlates with the observations made from Figs. 7.6, 7.7 and 7.8, however, a much larger dataset is still needed to effectively constrain the origin of the fluids. A much larger dataset would also be useful in describing any variation and distribution of the stable isotope values.

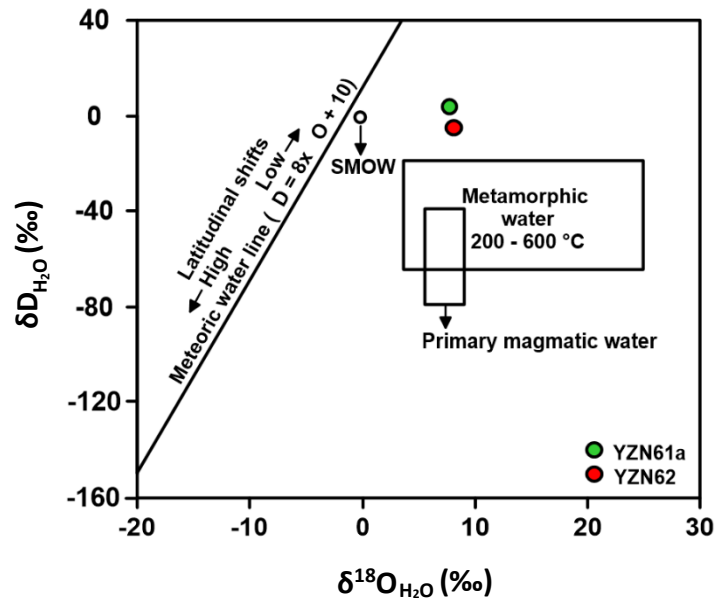


Figure 7.9: δD vs. $\delta^{18}O$ plot of H_2O for samples YZN61a and YZN62. SMOW after Taylor (1997).



Chapter 8: Discussion

8.1. Introduction

In this chapter, the petrogenetic processes that gave rise to this composite pluton is modelled, and the nature of the possible sources and their characteristics are also reviewed. The tectonic setting and the geochemical characteristics of the rocks of the Yzerfontein Pluton are investigated and discussed. The structural setting is also discussed. Additionally, the paragenesis of hydrothermal veining that cross-cut the host rocks is modelled. Conclusions are also made with respect to the origin and evolution of the hydrothermal fluids.

8.2. Petrogenesis

The composite nature of the Yzerfontein Pluton indicates that several intrusive phases exist (Jordaan et al., 1995 and Clemens et al., 2017a). Scheepers (1995) and Jordaan et al. (1995) suggested a high-K calc-alkaline character for the rocks of the Yzerfontein Pluton. According to Clemens et al. (2017a), as well as the present study, the rocks can be classified as having a high-K calc-alkaline and shoshonitic character, as shown on the Th vs. Co diagram (Fig. 8.7b). This shoshonitic character of the rocks of the Yzerfontein Pluton can be interpreted to be the result of the chemical and mineralogical characteristics of the source for the rocks. This source for the rocks, as well as the petrogenetic processes responsible for the compositional variation seen in the rocks are investigated and modelled in this section.

8.2.1. Petrogenetic processes

The petrogenetic processes that played a role in the compositional variation in the mafic to felsic rocks of the Yzerfontein Pluton to form this composite pluton, certainly require modelling. The question is, which petrogenetic process is responsible for the compositional variation seen in these rocks? According to Janoušek et al. (2016), the best approach to constrain a model is to consider at least more than one petrogenetic process, and to select the one that matches the data more effectively. The role of magma mingling in the differentiation of the rocks of the Yzerfontein Pluton is one of the processes that will be discussed, merely based on field relationships (contact relationships and mingling features). The role of magma mixing in the differentiation of the rocks of the Yzerfontein Pluton will also be discussed; this was chemically modelled (Fig. 6.3). The trends on Harker diagrams suggest the crystallisation (or fractionation) of certain minerals during different stages of the chemical evolution of the Yzerfontein magmas, resulting in the compositional variation of the rocks; the role of fractional crystallisation will therefore be modelled in order to determine whether it played a role.

8.2.1.1. Magma mixing and mingling

An interesting observation made by Jordaan et al. (1995) is the small patches of mafic material that form a gradational contact with the host monzonite of the Yzerfontein Pluton. As noted by Clemens et al. (2017a), this may suggest that petrogenetic processes such as magma mixing and mingling may have played a role in the chemical evolution of the Yzerfontein magmas. As

noted in section 4.4.3 (chapter 4), locally, in the poikilitic monzogabbro, a compositional variation is seen between different phases of the Yzerfontein Pluton marked by variations in grain size, mineralogy and texture. The contact between the various phases are sharp, with some portions being felsic and plagioclase-rich, others being more mafic and rich in amphiboles, pyroxenes and chlorite, and lastly, some phases being more intermediate between felsic and mafic (Fig. B3). Clemens et al. (2017a) noted the presence of such “mingling features” and the absence of gradational contacts, similar to what is depicted in Fig. 8.1.



Figure 8.1: (a) and (b) Hand specimen of the leucocratic gabbro from the northernmost end of the study area at Gabbro Point. Two distinct phases of the gabbro are apparent, with one being medium- to coarse grained and containing a higher plagioclase content (central portion in both Figs) compared to the other (at the margins of the sample) which is coarse-grained and plagioclase-poor. Intrusive contact between the two phases are clearly sharp and purely mechanical, suggesting that they may represent two distinct magma pulses. Scale: R5 coin with diameter = 2.6 cm.

The contacts made by these intrusive phases are indeed purely mechanical, at least at an emplacement level, and may reflect multiple magma pulses that have undergone differentiation to produce compositionally heterogeneous batches (Fig. 8.1a, b) (Clemens et al., 2017a). Differentiation of these various magma batches could be attributed to fractional crystallisation in some deep-seated magma chamber, which, from time to time, released a more fractionated magma batch, and ultimately produced the mingling character of the rocks as seen in certain outcrops (at emplacement level).

In order to account for the observations made by Jordaan et al. (1995) (as discussed earlier), Clemens et al. (2017a) tested the role of magma mixing in the differentiation of the Yzerfontein magmas through chemical modelling. By making use of Harker diagrams and isotopic plots, Clemens et al. (2017a) effectively illustrated that magma mixing did not play a role in the chemical differentiation of the rocks of the Yzerfontein Pluton, at least not at an emplacement level. Indeed, this can also be seen from the Harker diagrams in Fig. 6.3, showing the absence of mixing trends between the various rocks of the Yzerfontein Pluton, as well as between the rocks of the Yzerfontein Pluton and the I-type granites of the CGS. Instead, the mafic, intermediate and felsic rocks tend to form separate trends on these

diagrams. The lack of magma mixing trends was also demonstrated by Adriaans (2018) by means of chemical modelling of the major element oxide data of Clemens et al. (2017a) and the Vredenburg I-type granites of the CGS, similar to what was done in Fig. 6.3 in this study. These diagrams do not only indicate the absence of mixing trends between the Yzerfontein Pluton and the Vredenburg I-type granites, but it also suggests that there are no magmatic kinships between these rocks. Nevertheless, it is therefore suggested that if magma mixing had played a role in the differentiation of the Yzerfontein magmas, it may have done so at depths below emplacement levels (Clemens et al., 2017a). Additionally, the lack of gradational contacts between various intrusive phases, especially those seen between the melanocratic enclaves and the intermediate rocks (Figs. 4.8a to c, B4), is evidence for the differentiation of the rocks of the Yzerfontein Pluton unrelated to magma mixing processes.

The separate trends formed by the mafic rocks on the Harker diagrams, and their field occurrence as melanocratic enclaves in sharp contact with the intermediate part of the pluton tend to suggest that they must have been emplaced during an earlier stage of magmatism (Maske, 1957; Clemens et al., 2017a). The zones of mafic enclaves seen within the syenodiorite (Fig. B4), monzonite (Fig. 4.8a, b) and quartz-microsyenite (Fig. 4.9c) in various localities at Schaap Eiland further corroborate their generation by an earlier and separate magma pulse that preceded the intrusion of the intermediate and felsic pulses. These numerous melanocratic enclaves within the intermediate and felsic parts of the pluton, as well as the occurrence of cross-cutting felsic dykes, particularly in the intermediate part of the pluton (Figs. 4.6a, b, 4.9a, B2a, b, B5), attest to the role of fractional crystallisation in the chemical differentiation of the rocks, as opposed to magma mixing, at least at a local scale (Clemens et al., 2017a). The role of magma mixing in the differentiation of these rocks is therefore unlikely.

8.2.1.2. Fractional crystallisation

In order to better understand the mechanisms that played a role in producing the compositional variation and separate trends, as illustrated in chapter 6, fractional crystallisation modelling will be carried out. Fractional crystallisation is a mechanism that can potentially explain the compositional variations seen in these rocks. Therefore, fractional crystallisation modelling was carried out in order to test whether the compositional variation and separate trends represented by the different compositional types signify separate magma pulses generated by, and related to each other by fractional crystallisation. Some general observations of the trends on the Harker diagrams indicate the fractionation of certain mineral species at different stages of magmatism. Firstly, the negative trends between Si and Ti, Fe, Mg and Ca (Fig. 6.3a, c, d, e), may suggest fractionation which was dominated by ferromagnesian minerals (pyroxenes and olivine) and plagioclase. Plagioclase fractionation is further suggested by the negative trends seen in the Harker plots that involve elements which are compatible with plagioclase, including Sr, Ba and Eu (Fig. 6.4b, c, l). The prominent negative Eu anomaly for all the rock types shown in Fig. 6.5a, c and e also testifies to the role of plagioclase in the fractionating sequence (e.g. Rollinson, 1993).

Additionally, a Ti- and Ba-bearing mineral (most likely biotite), if it played a role, must have only done so later within the intermediate and felsic phases, as shown by the negative trends on the Si vs. Ti and Si vs. Ba Harker diagrams for the intermediate and felsic rocks (Figs. 6.3a, 6.4c). The intermediate and felsic rocks not only have higher alkali feldspar contents relative to the mafic rocks (Chapter 4; Tables B1 to B7), but also have higher Rb contents (Table 6.1 and Fig. 6.4a), which is not surprising, as Rb acts incompatibly. Moreover, these high Rb contents for the intermediate and felsic rocks, together with the slightly negatively sloping trends observed in the Si vs. Ba Harker plot (Fig. 6.4c), suggest that alkali feldspar crystallisation, similar to biotite, only played a role later in the fractionating sequence.

Compatible trace elements, such as V, Cr and Ni, generally display negatively correlated trends with increasing Si (Fig. 6.4g, i, j), and have the highest concentrations within the mafic rocks, which could indicate that these elements were more highly partitioned into the mafic rocks. The trend observed in the Cr vs. Si Harker diagram is similar to that in the Ni vs. Si Harker diagram, which is more or less expected as these elements are related by their compatible nature. Lastly, Zr forms an overall convex-upward shape with increasing Si, with the intermediate rocks, in particular, displaying a nearly vertical trend at Si = 25 – 27.5 (Fig. 6.4f). This suggests that Zr was concentrated into the mafic melt during early stages (shown by the positive trend for the mafic rocks in the Zr vs. Si plot), subsequent to which it achieved zircon saturation and crystallisation (shown by the near-vertical trend for the intermediate rocks), and finally levelled off to lower concentrations in the felsic melt as zircon continued to crystallise out (shown by the relatively negatively sloping trend of the felsic rocks) (Watson and Harrison, 1983; Todd et al., 2003; Shao et al., 2019). Th, which is strongly compatible in zircon, shows a similar trend (Fig. 6.4d).

The crystallisation of these minerals, and their role in the chemical differentiation of the rocks will be modelled in the following sections. For each type of modelling, only the major findings are reported, with a more detailed interpretation provided in Appendix F. The role of olivine in the differentiation of the mafic rocks will also be modelled. According to Maske (1957), primary olivine was not observed in any of the thin sections analysed, however, its presence in the darker varieties of gabbro (i.e. the melanocratic gabbro) was presumed and confirmed through the chemical analysis of the gabbro. Jordaan (1995) also did not observe olivine in thin section, however, he acknowledged the presence of olivine based on the work of Maske (1957). Moreover, Clemens et al. (2017a) did not mention the presence of olivine in the petrographic analysis of the rocks, however, major and trace element analyses were performed on two “olivine-bearing gabbros”. In the present study, as is shown by the petrographic examination of the rocks, no primary olivine was observed. However, since its presence was confirmed through the chemical analysis of the gabbroic samples (Maske, 1957), its potential crystallisation in the mafic rocks will be modelled.

Maske (1957) recorded the presence of primary hornblende in the petrology of the mafic rocks of the Yzerfontein Pluton. However, the hornblende observed was said to be mostly

confined to the outer rims of pyroxene, which, in the present study were predominantly identified as pseudomorphic rims formed as a result of uralitization. Nevertheless, Maske (1957) described the hornblende as a primary mineral. Jordaan (1995) also recorded the presence of hornblende in highly altered outcrops of monzonite, its mineral abundance varying with different degrees of alteration. Clemens et al. (2017a) recorded the presence of hornblende in thin section in nearly all the rock samples analysed. It can be assumed that most of the hornblende observed was primary, considering that sampling was done distant to alteration zones. Based on the petrographic examination of the different rock samples in the present study, the amphiboles were only present as secondary minerals which formed as a result of uralitization. Primary hornblende was not observed in any of the samples analysed. This could possibly be due to its replacement by tremolite-actinolite in the samples analysed. Nevertheless, since the presence of primary hornblende was confirmed petrographically (e.g. Maske, 1957; Clemens et al., 2017a), its potential crystallisation in the mafic, intermediate and felsic rocks will be modelled.

i.) Principal component analysis (PCA)

Principal component analysis (PCA) was performed (using the *GCDkit*[®] software) in order to determine which major and trace elements, respectively, are responsible for the most differentiation (Janoušek et al., 2016). For a given geochemical dataset, PCA points out the directions that show the highest variance, which, in turn, could be directly related to the fractionation of particular mineral species (Janoušek et al., 2016). The first component reflects the strongest differentiation within the dataset, with the other component showing a secondary effect (refer to Appendix F for more information on PCA). Fig. 8.2 illustrates the result of performing PCA on the Yzerfontein Pluton dataset. For more details on this process and interpretations, the reader is referred to Appendix F.

In Fig. 8.2a, MgO is responsible for the highest variation in the mafic rocks, with Al₂O₃, SiO₂, and, to some extent, CaO, playing a secondary role. Fe₂O₃ did not play a very big role. These observations suggest that there may have been fractionation of ferromagnesian minerals, such as the pyroxenes, and potentially hornblende and olivine (probably the more Mg-rich end-member) during the early stages of the melt, and they are therefore mainly responsible for the differentiation of the mafic rocks. Furthermore, the observations also suggest that plagioclase, if it played a role, must not have been very significant. Based on the petrography, these observations definitely hold true, at least in terms of the melanocratic gabbro and poikilitic monzogabbro which have a high abundance of pyroxene relative to the felsic minerals (Tables B1 to B3).

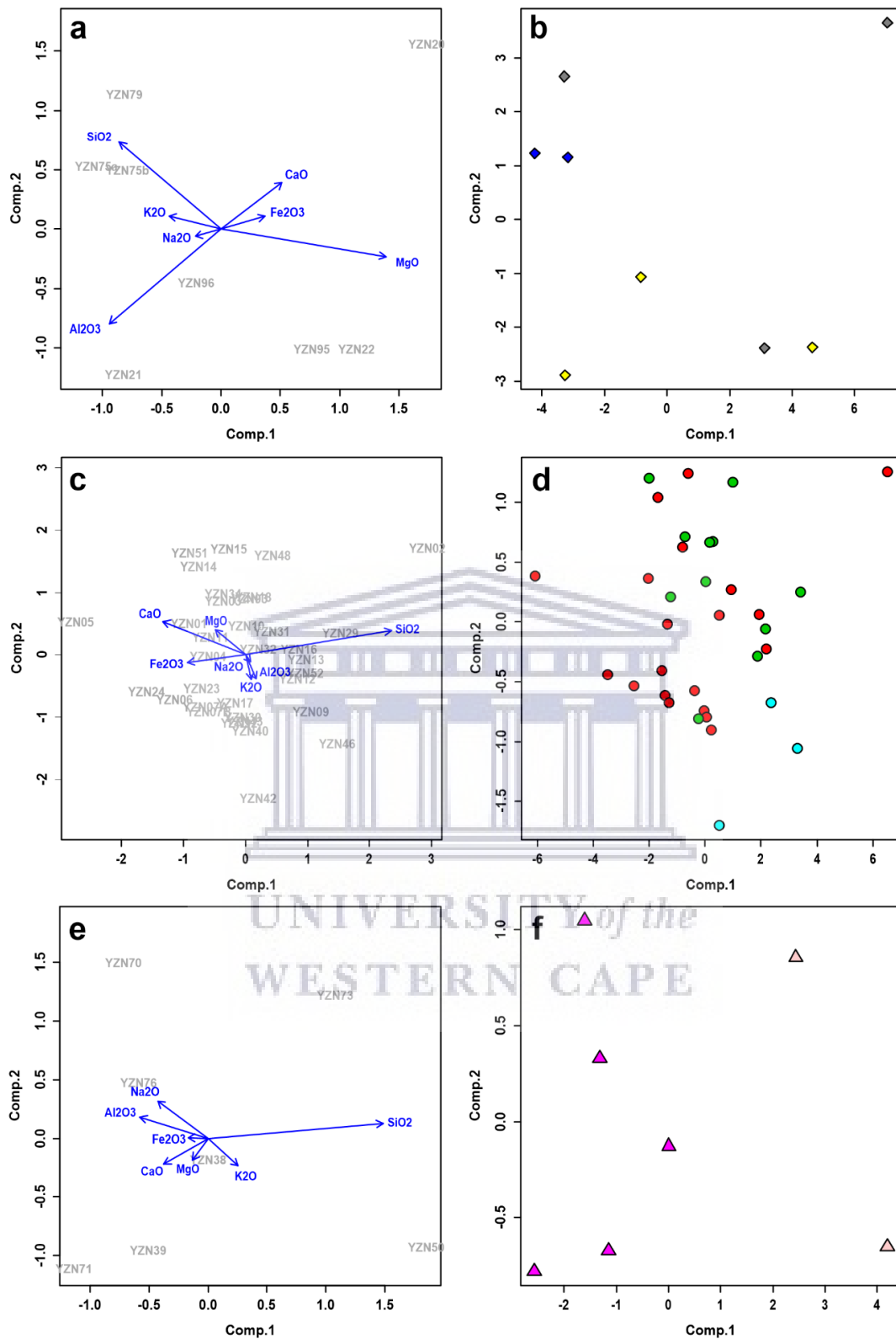


Figure 8.2: Biplots of PC1 vs. PC2 (principal components 1 and 2) of selected major elements for the different rock compositions of the Yzerfontein Pluton. (a) and (b) mafic rocks, (c) and (d) intermediate rocks, and (e) and (f) felsic rocks. Symbols: same as in Fig. 6.4.

In Fig. 8.2c, SiO₂ is responsible for the highest variation in the intermediate rocks, with CaO and Fe₂O₃ playing a secondary role. MgO did not play a very big role in the differentiation of

the intermediate rocks. Overall, it once again suggests that there may have been fractionation of pyroxenes in the intermediate rocks. Additionally, it also suggests fractionation of the more anorthite-rich end-member of plagioclase, which, as opposed to the mafic rocks, may have played a more significant role in the differentiation of the intermediate rocks. Crystallisation of alkali-feldspar appears to have played a small role compared to the other minerals, as seen from the projection of the K_2O vector. These observations are certainly consistent with the petrography of the intermediate rocks (Tables B4 to B7).

Lastly, in Fig. 8.2e, SiO_2 is responsible for the highest variation in the felsic rocks, with Al_2O_3 , Na_2O , and, to a lesser extent CaO and K_2O , playing a secondary role. It appears that MgO and Fe_2O_3 did not play a very big role. These observations suggest that, at this point in the fractionating sequence, most of the pyroxenes and hornblende had crystallised out of the melt to form the mafic and intermediate rocks, producing a remaining melt that is more felsic in composition relative to the primary melt. These observations indicate that fractionation of the feldspars was dominantly responsible for the differentiation within the felsic rocks. Orthoclase is likely the main alkali feldspar that fractionated, as illustrated by the projection of the K_2O vector, indicating that this mineral plays a bigger role in the felsic rocks compared to that in the other compositions. Overall, observations from PCA plots are consistent with the petrographic observations, in that the mafic rocks have a higher mafic mineral content and lower feldspar content (Tables B1 to B3) relative to the intermediate and felsic rocks (Tables B4 to B9), which show a gradual decrease in mafic mineral content as the feldspar content increases (likely fractionation-related).

ii.) Major and trace element correlation

Correlation of major and trace elements was applied to the data as it effectively illustrates which major or trace elements share the greatest correlation, which is an indication as to which minerals could have played a major role in the differentiation of the various rock types (Figs. F1 to F3). For more details on this process and interpretations, the reader is referred to Appendix F. In Fig. F1a, the strong correlations between Al_2O_3 and CaO , and SiO_2 and MgO indicate that pyroxenes played a big role in the differentiation of the mafic rocks (particularly clinopyroxene and to a lesser extent orthopyroxene), as well as Mg-rich olivine. Strong correlations between Al_2O_3 and CaO , MgO and Na_2O , Al_2O_3 and Na_2O , and SiO_2 and MgO suggest that crystallisation of hornblende played a role. Good correlations between Al_2O_3 and CaO , and Al_2O_3 and Na_2O suggest that plagioclase played a smaller role. Lastly, the good correlation between MgO and K_2O , SiO_2 and K_2O , and SiO_2 and MgO could suggest that biotite also crystallised and therefore may have played a smaller role in the differentiation of the mafic rocks. Moving on to the trace elements (Fig. F1b), the strongest correlation exists between Cr and Ni, which is expected as they are highly partitioned into mafic minerals such as orthopyroxene, clinopyroxene and hornblende in basaltic liquids (Rollinson, 1993). The strong correlations between Zr and Nb and Rb and La, as well as Th and Zr may be related to biotite and zircon fractionation, respectively. Ba and Eu also share a good correlation, which,

to some extent, may be related to plagioclase fractionation. These observations are consistent with the petrographic observations of the mafic rocks made in Chapter 4.

In Fig. F2a, the strong correlations between SiO_2 and CaO , MgO and CaO , and Fe_2O_3 and CaO indicate the fractionation of pyroxene in the intermediate rocks, possibly more so of clinopyroxene than orthopyroxene. These correlations are also indicative that hornblende may potentially have played a subordinate role. The strong correlation between SiO_2 and CaO also suggest that the anorthite-rich end-member of plagioclase may have played a significant role during fractionation. In terms of the trace elements (Fig. F2b), the intermediate rocks show some similar correlations to the mafic rocks. The strong correlation between Ba and Eu may suggest plagioclase fractionation, whereas the Cr and Ni correlation implies fractionation of mafic minerals such as the pyroxenes and potentially hornblende. These observations, in terms of both the major and trace element correlations of the intermediate rocks, are mostly consistent with the petrographic observations made in Chapter 4.

In Fig. F3a, the highest correlation is observed between Na_2O and K_2O , followed by Al_2O_3 and Na_2O , SiO_2 and Al_2O_3 , and SiO_2 and CaO , and are all indicative of feldspar fractionation in the felsic rocks. Based on the strongest correlation, the compositional variation is dominated by an alkali feldspar (most likely orthoclase). The strong correlation of Al_2O_3 and Na_2O suggests that the albite-rich end-member of plagioclase played a bigger role in the compositional variation of the felsic rocks. The good correlation between MgO and CaO suggests that clinopyroxene or hornblende have played a role to a lesser extent. In thin section, though the studied samples of felsic composition do not contain primary pyroxenes, secondary amphiboles such as hornblende and tremolite-actinolite formed as a result of uralitization, which is a clear indication that primary pyroxenes were once present (Tables B8, B9). For the trace elements (Fig. F3b), the strong correlation between Sr and Ba is directly associated with plagioclase fractionation, as these two elements are strongly compatible with, and highly partitioned into plagioclase (Rollinson, 1993). Rb is highly partitioned into alkali feldspar (Rollinson, 1993) and its strong correlation with the other trace elements is certainly an indication that the felsic rocks contain high concentrations of alkali feldspar, and that they are more fractionated, reflecting the significant influence of this mineral to the overall compositional variation in the felsic rocks. This suggestion is also supported by the isotopic data, which indicates that the sample of quartz-microsyenite (YZN70) has the highest $^{87}\text{Rb}/^{86}\text{Sr}$ ratio (1.3852) compared to the other rocks, reflecting its high alkali feldspar content, as is also corroborated by petrographic observations of the felsic rocks (Tables 6.3, B8, B9). Overall, then, the major and trace element correlations of the felsic rocks are consistent with their petrographic observations, at least in terms of the pyroxenes and plagioclase. Additionally, for all three rock compositions (mafic, intermediate and felsic) it is largely apparent that the minerals inferred to have fractionated based on the major element trends correlate with those inferred to have fractionated based on trace element trends.

iii.) Rayleigh-type fractionation

Since the mineral species that may have played a role in the compositional variation seen in each of the rock compositions of the Yzerfontein Pluton are known to some extent, they can be modelled for fractional crystallisation via Rayleigh-type fractionation. Using the trace element concentrations of Ba and Sr in Table 6.1, and their partition coefficients in Table 8.1 fractionation vectors were modelled for each of the rock compositions using compatible-compatible binary log-log trace element plots. Modelling fractionation vectors is an effective method for identifying which minerals controlled the compositional variation within a magma (Janoušek et al., 2016). For more details on the process, the reader is referred to Appendix F.

Table 8.1: Partition coefficients of Ba and Sr for various minerals in mafic, intermediate and felsic magmas.

		Mafic magmas					
		Orthopyroxene	Clinopyroxene	Amphibole	Olivine	Plagioclase	Biotite
Ba		0.002	0.0006	0.450	0.0020	0.300	3.480
Sr		0.007	0.0963	0.450	0.0022	2.000	0.183
		Intermediate magmas					
		Orthopyroxene	Clinopyroxene	Amphibole	K-feldspar	Plagioclase	Biotite
Ba		0.010	0.150	0.500	0.500	0.500	6.000
Sr		0.030	0.090	0.600	0.900	2.600	0.150
		Felsic magmas					
		Orthopyroxene	Clinopyroxene	Amphibole	K-feldspar	Plagioclase	Biotite
Ba		0.200	0.400	0.280	7.200	0.363	6.400
Sr		0.100	0.150	0.250	4.500	4.400	0.250

Note: partition coefficients are from various sources, including: Schnetzler and Philpotts (1970), Nagasawa and Schnetzler (1971), Fujimaki et al. (1984), Bacon and Druitt (1988), Stix and Gorton (1990), McKenzie and O'Nions (1991), Ewart and Griffin (1994), Foley et al. (1996).

The main mineral assemblage which crystallised out of the mafic magma is clino- and orthopyroxene, with hornblende and plagioclase playing a more subordinate role (Fig. 8.3a). Olivine, which projects on top of the orthopyroxene vector, potentially played an equally significant role as the pyroxenes in the differentiation of the mafic rocks. K-feldspar, as shown in the principal component analysis and major and trace element correlation, did not play a role in the differentiation of the mafic rocks. Besides, K-feldspar would not ordinarily be expected to crystallise from a mafic magma, and partition coefficients for K-feldspar in mafic melts are also not reported in the literature used to construct Table 8.1. Biotite can be seen to project oblique to the trend of the samples in Fig. 8.3a.

It must, however, be noted that the poikilitic monzogabbro contains alkali feldspar inclusions. Maske (1951) effectively accounted for the presence of these inclusions and their crystallisation. Maske (1957) suggests that as the magma cooled after its emplacement, fractional crystallisation continued apace and the earlier formed olivine, pyroxene and plagioclase crystals settled down to the bottom of the intrusion due to their densities (i.e. under the influence of gravity). Differential crystal settling resulted in the development of a well-defined primary banding (this is clearly seen in the gabbros) and igneous lamination parallel to the

floor of the intrusion. This removal of the earlier, dense minerals by fractional crystallisation left a melt enriched in potassium and aluminium, some of which became trapped within the interstices of the settled crystals of the banded gabbro and ultimately crystallised as orthoclase (this assumes that the original mafic magma had enough K and Al in it to allow for the crystallisation of K-feldspar). Maske (1951) also suggested that the same is the case for biotite, which is also enriched in potassium and aluminium. This could possibly explain why orthoclase and biotite did not play a very big role in the differentiation of the mafic rocks, as was previously suggested by the PCA, and as is also evident from the mineral abundances obtained from the petrographic examination of the mafic rocks.

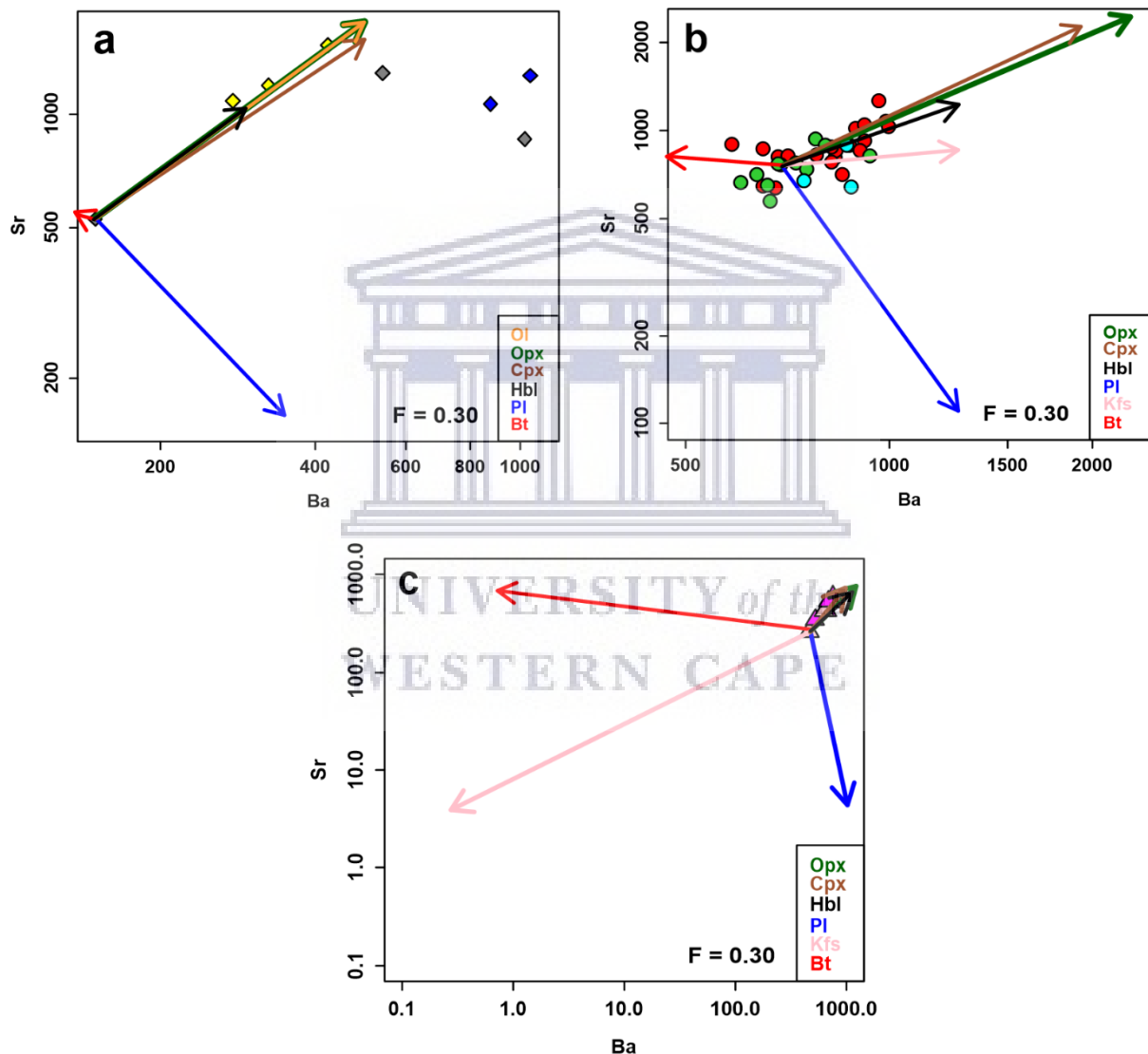


Figure 8.3: Binary log-log diagram illustrating the effects of fractional crystallisation of various mineral assemblages through trace-element modelling of (a) mafic, (b) intermediate, and (c) felsic rocks of the Yzerfontein Pluton (after Janoušek et al., 2016). Symbols: same as in Fig. 6.4.

Maske (1957) goes on to suggest that much of the remaining melt concentrated towards the roof of the magma body where the magma progressively continued to become enriched in K and Al under the influence of crystal fractionation, and this ultimately decreased the fluidity

of the magma (i.e. increasing its viscosity). As the viscosity increased, settling of the early formed crystals ceased. The orthoclase which had crystallised from the K-rich residual melt ultimately enclosed the earlier formed crystals in a poikilitic fashion, thereby forming the poikilitic monzogabbro. This explains why orthoclase can be found in the poikilitic monzogabbro, but not the other types of gabbros.

For the intermediate rocks (Fig. 8.3b), the pyroxenes are responsible for most of the differentiation, more so clinopyroxene than orthopyroxene. This would make sense as most samples tend to reflect lesser amounts of crystallisation of orthopyroxene in order to account for their compositions. This is also consistent with the petrographic observations of the intermediate rocks which tend to reflect a higher abundance of clinopyroxene (augite) than orthopyroxene (Tables B4 to B7). Hornblende potentially played a subordinate role in the differentiation of the intermediate rocks. Plagioclase and K-feldspar have also played a role to some extent. The vector for biotite, however, indicates that it did not play a very big role in the differentiation of the intermediate rocks. Overall, then, most of the differentiation in the intermediate rocks must have been driven by the fractionation of the pyroxenes, and to a lesser extent the feldspars.

In Fig. 8.3c, it appears that K-feldspar is driving most of the differentiation of the felsic rocks, with the pyroxenes and hornblende playing a much smaller role. The vector for plagioclase and biotite projects oblique to the trend of the samples, which indicates that these minerals did not play a very big role in the differentiation of the felsic rocks. Overall, these observations are not entirely consistent with the petrographic observations of the felsic rocks. The mineralogy of the felsic rocks tends to suggest that a higher amount of plagioclase crystallised compared to the pyroxenes (which have been altered to amphiboles), which is not consistent to what is depicted in Fig. 8.3c. Perhaps if more samples of the felsic rocks were geochemically analysed, more accurate and reliable inferences could be made from the Rayleigh fractionation plots, and thus better correlations could be made with the petrographic observations. Nevertheless, the inferences made from Fig. 8.3c certainly hold true and correlate with the petrographic observations made in terms of K-feldspar and biotite, as the mineralogy of the felsic rocks suggests that K-feldspar was the main mineral that crystallised out, and no evidence for the presence of biotite was observed (Tables B8 and B9).

Overall, the modelling suggests that the rocks of the Yzerfontein Pluton are related to the same parental magma that progressively fractionated from mafic to intermediate to felsic. A general petrogenetic model that has been developed to account for the compositional variation seen in the rocks of the Yzerfontein Pluton (Fig. 8.6), and will be discussed in the next section after discussing the source of the rocks.

8.2.2. Source characterisation

The rocks of the Yzerfontein Pluton have high present day $^{87}\text{Sr}/^{86}\text{Sr}_0$ values (0.705388 – 0.714788), with relatively low to intermediate present day $^{143}\text{Nd}/^{144}\text{Nd}_0$ values (0.512237 – 0.512307). They have negative initial $\epsilon\text{Nd}(t)$ values between -2.75 and -0.62, with

Mesoproterozoic T_{DM} model ages between 1.60 and 1.25 Ga. These negative initial $\epsilon Nd(t)$ values are indicative of a source(s) exhibiting a lower Sm/Nd ratio than the chondritic uniform reservoir (CHUR), suggesting a mildly enriched mantle source for the rocks of the Yzerfontein Pluton (Fig. 8.4a) (Rollinson, 1993; Clemens et al., 2017a), which is consistent with the findings of Clemens et al. (2017a). Given the subduction-related history of the study area (Scheepers, 1995; Belcher, 2003; Kisters et al., 2015), the most reliable model would be that subduction was the main source for the enrichment of the mantle wedge along the active continental margin (Fig. 8.6a) (Clemens et al., 2017a). An enriched mantle source for the rocks is further indicated in Fig. 8.4b.

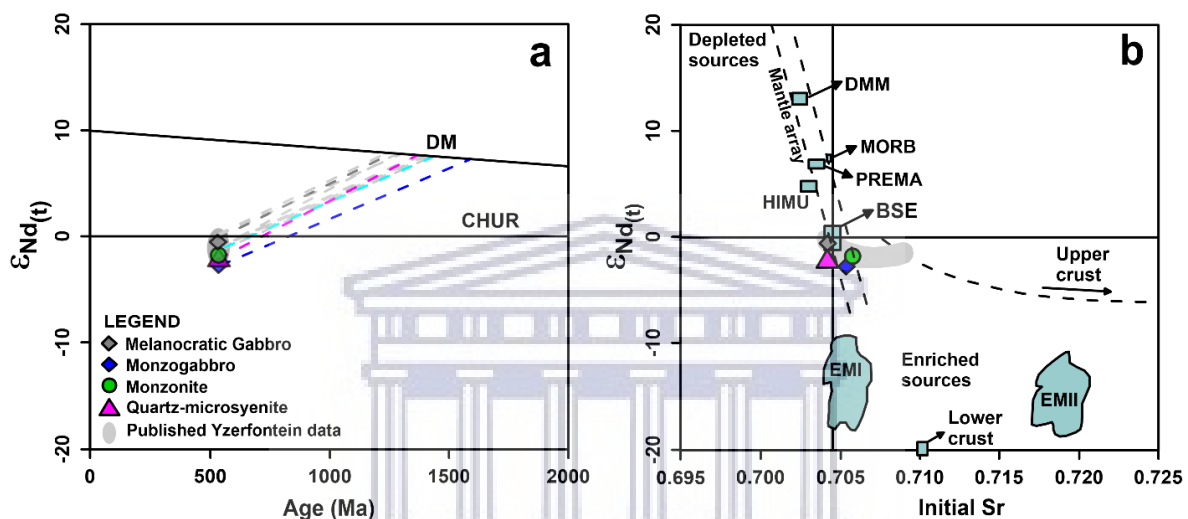


Figure 8.4: Isotopic diagrams for the rocks of the Yzerfontein Pluton. (a) $\epsilon Nd(t)$ vs. age (Ma) diagram with two major reservoir lines shown: CHUR = chondritic uniform reservoir, DM = depleted mantle (after DePaolo, 1981). (b) $\epsilon Nd(t)$ vs. initial Sr diagram displaying the positions of major crustal and mantle reservoirs: BSE = bulk silicate earth, MORB = mid-oceanic ridge basalts, DMM = depleted MORB mantle, PREMA = frequently observed prevalent mantle composition, EMI and EMII = enriched mantle I and II, HIMU = high mantle U/Pb ratio (after Zindler and Hart (1986)). Upper and lower crust reservoirs are from Harris et al. (1986) and Ben Othman et al. (1984) respectively. Published Yzerfontein data is from Clemens et al. (2017a).

The relative enrichment in the LILE, such as Cs, Rb, Sr, Ba, and Pb, as well as the low contents of the HSFE, such as Th, U, Nb and Hf, suggests a subduction-related history with a possible crustal contribution for the rocks of the Yzerfontein Pluton (Fig. 6.5) (Gill, 1981; Wilson, 1989; McCulloch and Gamble, 1991; Gribble et al., 1996; Janoušek et al., 2000). This is also further supported by the depletion of Nb and Ta relative to La, as well as Zr, Hf, Nb/Zr and Nb/La depletions (Gill, 1981; Wilson, 1989; McCulloch and Gamble, 1991; Gribble et al., 1996). Nb depletion, or anomalies, are generally known to suggest the involvement of a crustal component during magma processes (Rollinson, 1993). However, the effects of crustal contamination have not been assessed or modelled, and, therefore, inferences about a crustal component cannot be conclusively made.

Additionally, the enrichment of the LREE compared to the HREE for all rock types reflects a degree of igneous fractionation (Gill, 1981; Wilson, 1989; McCulloch and Gamble, 1991; Gribble et al., 1996). The LREE exhibit more incompatible behaviour, and their degree of

enrichment can be determined by the $(La/Sm)_{PM}$ ratio (where the subscript PM denotes primitive mantle normalisation using the values of McDonough and Sun (1995)). The HREE exhibit more compatible behaviour, and their degree of enrichment can be determined by the $(Gd/Lu)_{PM}$ ratio. $(La/Sm)_{PM}$ and $(Gd/Lu)_{PM}$ ratios between 1 and 2 suggests weak fractionation of the LREE and HREE respectively, whereas a value of 3 and more suggests a greater degree of fractionation. With that being said, in general, felsic rocks (or rocks with a felsic protolith) tend to be enriched in the LREE relative to the HREE, as opposed to mafic rocks, for which the opposite is true. This is certainly the case for the rocks of the Yzerfontein Pluton. The mafic to intermediate rocks have moderate to high $(Gd/Lu)_{PM}$ ratios (2.57 – 4.57) and low to moderately low $(La/Sm)_{PM}$ ratios (1.90 – 3.84), whereas the felsic rocks have higher $(La/Sm)_{PM}$ ratios (3.64 – 5.07) and lower $(Gd/Lu)_{PM}$ ratios (1.81 – 2.49) (Table 6.2). This suggests that the mafic and intermediate rocks are highly fractionated within the HREE relative to the LREE, whereas the felsic rocks are highly fractionated within the LREE relative to the HREE. These inferences are certainly a reflection of the interplay between fractionation and the chemical character of the source (Rollinson, 1993).

For a more petrogenetic-based discrimination of the source characteristics, a ratio plot proposed by Pearce (2008) was generated for the rocks of the Yzerfontein Pluton (Fig. 8.5). The TiO_2/Yb vs. Nb/Yb plot in Fig. 8.5 highlights the melting depth proxy (Pearce, 2008). N-MORB is characterised by Nb/Yb ratios less than 1.45, and E-MORB by Nb/Yb ratios greater than 1.45. With Nb/Yb ratios ranging between 2.39 and 12.28, and most of the rocks plotting within the MORB array, the rocks of the Yzerfontein Pluton are suggested to have been derived from an enriched source which has experienced shallow melting (Pearce, 2008).

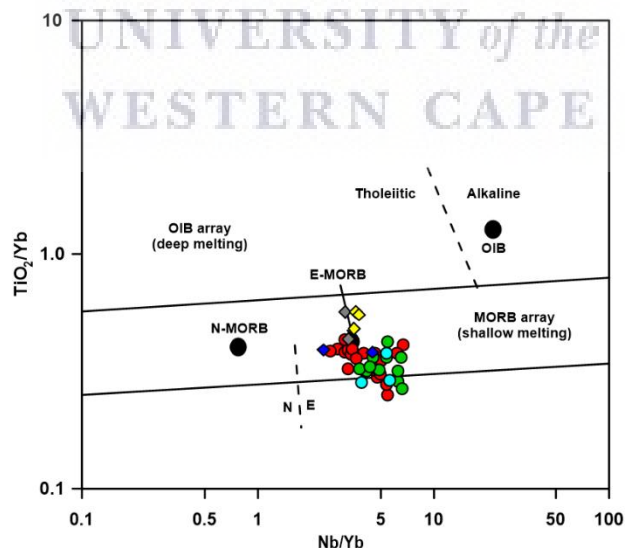


Figure 8.5: TiO_2/Yb vs. Nb/Yb basalt classification diagram highlighting melting depth of source. Symbols: same as in Fig. 6.4.

8.2.3. Petrogenetic model for the rocks of the Yzerfontein Pluton

As have been mentioned in the previous section, considering the subduction-related history of the study area (Scheepers, 1995; Belcher, 2003; Kisters et al., 2015), the most reliable model would be that subduction was the main source for the enrichment of the mantle wedge along the active continental margin, as have also been suggested by Clemens et al. (2017a); this is illustrated in Fig. 8.6a.

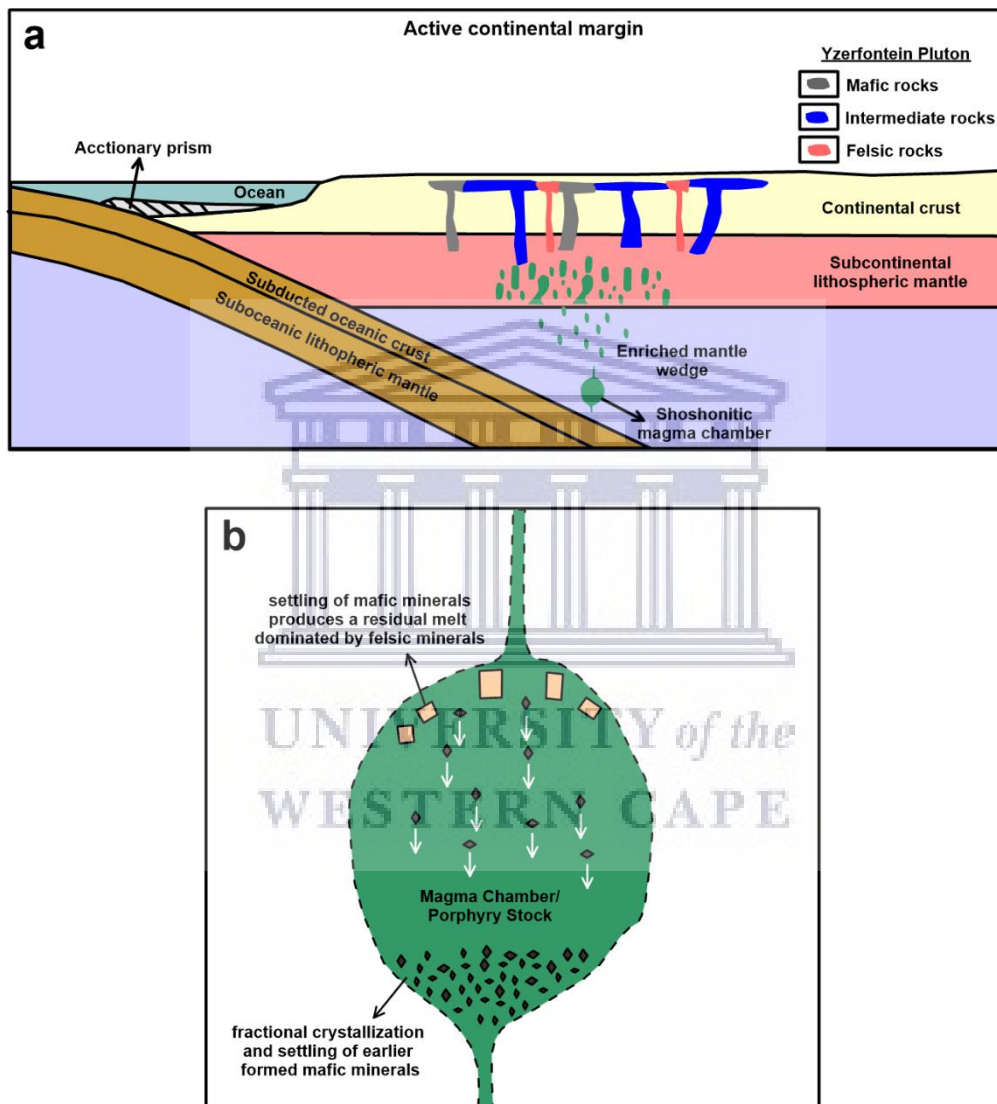


Figure 8.5: Schematic diagram illustrating (a) proposed tectonic and emplacement setting for the rocks of the Yzerfontein Pluton along an active continental margin (adapted and modified after Xia et al., 2015), and (b) simplified general petrogenetic model for the rocks of the Yzerfontein Pluton as explained by fractional crystallisation (adapted from Earle, 2015).

From the various fractional crystallisation plots in Section 8.2.1 (Figs. 8.5, 8.6, F1, F2, F3), as well as the petrographic observations made in Chapter 4 (summarised in Tables B1 to B9), the following is a general fractionation model for the rocks of the Yzerfontein Pluton: the ferromagnesian minerals (pyroxenes, hornblende and olivine) were the first to settle and

crystallise out of the parent magma, along with smaller amounts of biotite and plagioclase. This resulted in the emplacement of the gabbroic rocks with varying compositions as have been illustrated in Chapter 4 and Figs. 8.1a and b. However small the amount of plagioclase that was fractionated from the system, it was likely occurring in varying proportions, i.e. different fractions of these plagioclase crystals were likely being removed periodically over time. The same is true for any other mineral that is undergoing fractional crystallisation in the system. This ultimately gave rise to a variety of gabbroic rocks as seen in outcrop, some being more pyroxene-rich (melanocratic gabbro), and some being more plagioclase-rich (leucocratic gabbro). This is ideally what happens during fractional crystallisation – a single parent magma is being periodically tapped to produce a range of compositionally different but related magma types as varying amounts of crystals are being removed from the magma chamber as they form (Rollinson, 1993; Winter, 2001; Ersoy and Helvacı, 2010).

The same process would hold true for the intermediate rocks which also have different compositions. After the settling out and crystallisation of much of the pyroxenes (and potentially hornblende and olivine) to form the mafic rocks, naturally, the remaining melt would have a more intermediate composition (Fig. 8.6b). As fractional crystallisation continued, the amount of ferromagnesian minerals crystallising from the system would naturally be lower, however, they are still controlling the compositional variation. This is seen both petrographically and geochemically, as the intermediate rocks have lower amounts of ferromagnesian minerals (lower Mg, Fe and Ca) compared to the mafic rocks. Furthermore, K-feldspar may not have played a very significant role in all the intermediate rocks, however, it certainly played a role to some extent particularly in the syenite, and to a lesser extent in the syenodiorite. These rocks have a higher K-feldspar (orthoclase) content than the monzonite, which, in turn, has a higher plagioclase content (Tables B4 to B7). Given that most of the ferromagnesian minerals crystallised out to form the earlier mafic and intermediate phases, eventually the remaining melt must have been rich in potassium and aluminium (Fig. 8.6b). This is further corroborated by petrographic observations which shows that the mineralogy of the felsic rocks is dominated by K-feldspar and to a lesser extent plagioclase (Tables B8 and B9).

8.3. Tectonic Setting

Determining the tectonic setting in which rocks have formed is integral in reconstructing the geologic-tectonic history of a particular area, and in so doing, aids in constructing a model for the tectonic evolution of that area (Verma and Verma, 2013). The tectonic setting of the mafic rocks of the Yzerfontein Pluton was previously studied by Jordaan et al. (1995) by making use of a ternary Ti–Zr–Y diagram, and inferring an ocean floor basalt and calc-alkaline basalt tectonic setting for these rocks. However, Clemens et al. (2017a) argued that, with the Yzerfontein Pluton being late- to post-collisional, it is not advisable to make use of such tectonic discrimination diagrams for inferring the tectonic setting for these rocks. In this study, however, the tectonic setting of the Yzerfontein Pluton will be reviewed briefly in order to place it into context before moving on to the next section which deals with the source

characterisation of the rocks. The tectonic setting and source characterisation of rocks are two interrelated concepts, as the tectonic setting of a particular suite of rocks can provide significant information about their source, and, to some extent, may also provide information on source-dependent petrogenetic pathways (Pearce, 1996).

One very significant event in the history of the Pan-African Saldanian Orogeny, as well as one which may have controlled the emplacement of some of the plutons of the CGS (e.g. Peninsula Pluton), is the reversal of strike-slip movement along the Colenso Fault (Kisters et al., 2002). This re-activation of the Colenso Fault occurred at ~540 Ma (Kisters et al., 2002) when it experienced a shift from sinistral transpressional tectonics to dextral transtensional (extensional) tectonics. Given the newly determined 535 Ma age of the rocks of the Yzerfontein Pluton (Clemens et al., 2017a), it confirms the post-orogenic nature of the Yzerfontein Pluton. Additionally, it also confirms the proposed extensional (rift-related) tectonic setting for the rocks of the Yzerfontein Pluton, as inferred by Scheepers (1995) and Kisters et al. (2002) for the A-type granites.

According to Pearce (1996), a post-collision tectonic setting generally infers mantle sources which have become enriched by subduction-related or intraplate processes, which is also one of the many kinships this tectonic setting shares with volcanic arc tectonic settings. It is more likely that this enrichment of the mantle was subduction-related, as have also been suggested by Clemens et al. (2017a); this is illustrated in the Fig. 8.6a. Additionally, this type of tectonic setting is characterised by significant interaction between the mantle-derived magmas (which, in this case, is the enriched mantle; discussed in section 8.4.1) and the upper continental crust (Pearce, 1996). A rifting environment is also further indicated by the calc-alkaline composition of the rocks, as depicted on the Y/15–La/10–Nb/8 (after Cabanis and Lecolle, 1989) and Th vs. Co diagrams (Hastie et al., 2007) (Figs. 8.7a, b).

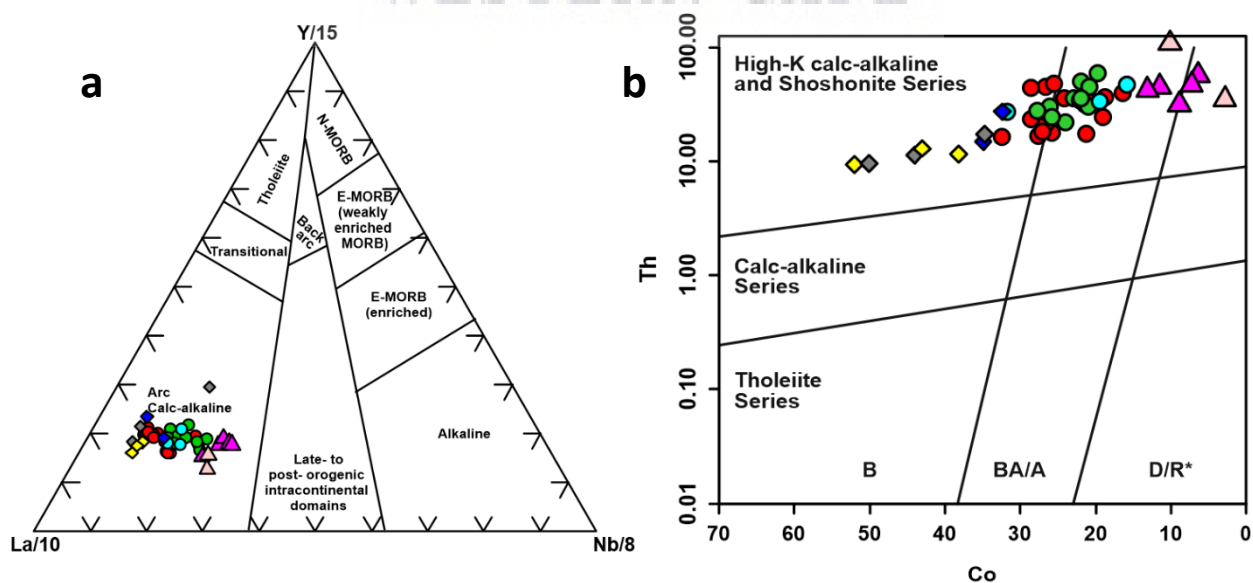


Figure 8.7: (a) Ternary Y/15–La/10–Nb/8 tectonic discrimination diagram (after Cabanis and Lecolle, 1989). (b) Th vs. Co diagram (after Hastie et al., 2007). Abbreviations: B = Basalt, BA/A = Basaltic andesite and andesite, D/R* = Dacite and Rhyolite. Symbols: same as in Fig. 6.4.

8.4. Relationship with the I-type granites of Cape Granite Suite

The intrusive relationship between the Yzerfontein Pluton and the I-type granites of the CGS was suggested (e.g. Jordaan et al., 1995; Clemens et al., 2017a; Adriaans, 2018). On the one hand, Jordaan et al. (1995) suggested that the Yzerfontein Pluton, based on its age and major- and trace-element geochemistry, represents the mafic to intermediate equivalents of a high-K calc-alkaline series, while the I-type granites of the Swartland Terrane represent the felsic end-members. Clemens et al. (2017a) and Adriaans (2018), on the other hand, argued that, based on geochemical trends and isotopic data, there are no kinships between the Yzerfontein Pluton and the I-type granites of the CGS, but rather that there are clear differences between the two. Additionally, as opposed to Jordaan et al. (1995), Clemens et al. (2017a) interpreted the I-type granites to be high-K calc-alkaline, as opposed to the Yzerfontein Pluton which has a dominantly shoshonitic character.

In sections 6.2.2 to 6.2.4 (chapter 6), geochemical data for the Yzerfontein Pluton (present study) were plotted together with that of Clemens et al. (2017a) and the I-type granites of the CGS. On Harker plots, the rocks from the present study almost always plot within the fields established for the data of Clemens et al. (2017a), and rarely overlap with the fields established for the I-type granites; it is only the monzogranite that commonly plots within this field. However, these are only 2 out of a total of 49 samples. These binary major and trace element plots, as well as what has been inferred from the chemical modelling of magma mixing (e.g. Clemens et al., 2017a), do not suggest a magmatic relationship or compositional affinity of the Yzerfontein Pluton with the I-type granites.

8.5. Trapping conditions, origin and paragenesis of hydrothermal fluids

8.5.1. Fluid trapping conditions

The homogenization temperatures and pressures of type I and type II fluid inclusions were used to calculate and construct isochores on a temperature vs. pressure graph (P-T graph). The purpose of plotting isochores on a P-T graph is to constrain the possible temperatures and pressures during trapping of the aqueous fluid inclusions (Roedder, 1984; Goldstein and Reynolds, 1994). Isochores for type I fluid inclusions are shown in Fig. 8.8 and were calculated using Hokieflincs_H₂O-NaCl (Steele-MacInnis et al., 2012). The present day lithostatic gradient of 28 °C/226 bar and hydrostatic gradient of 28 °C/100 bar (Goldstein, 2001) was used to deduce the minimum conditions of formation of the fluid inclusions. It is important to note that these are far assumptions, but may not always necessarily be the case.

The intersection between the hydrostatic gradient and the isochores for type I fluid inclusions indicate a minimum trapping temperature of 186 °C at a pressure of 0.56 kbar, therefore reflecting depths of ~2 km. The intersection between the hydrostatic gradient and the isochores for type II fluid inclusions indicated a range of trapping temperatures between 260 and 379 °C, with corresponding pressures ranging between 1.39 and 5.55 kbar, and therefore reflecting depths between ~5 – 22 km. This does not only cover a large range in trapping P-T conditions, but also indicates a wide range in depth, reflecting the possible depths from which

these associated hydrothermal fluids may have percolated. It is important to note that these temperatures and pressures obtained from the P-T graph merely serve as minimum estimations of the trapping conditions of the aqueous fluid inclusions, and do not actually constrain and reflect the actual mineralisation temperature.

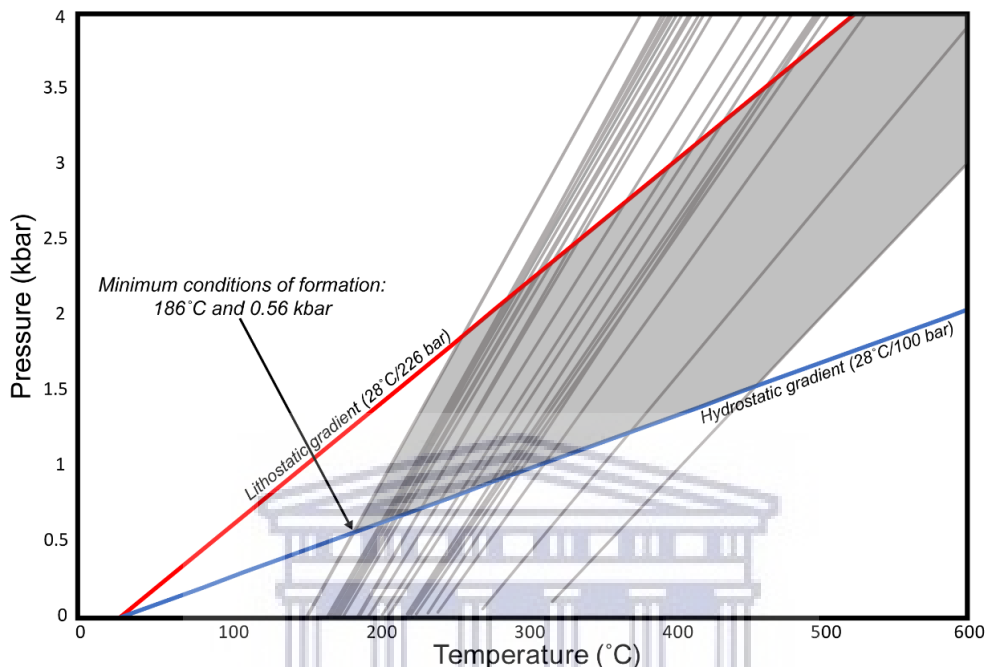


Figure 8.8: Isochore plot showing the possible trapping conditions for type I fluid inclusions, with a present day lithostatic gradient of 28°C/226 bar and hydrostatic gradient of 28°C/100 bar.

8.5.2. Source and nature of hydrothermal fluids

The purpose of doing fluid inclusion studies is to constrain the fluid temperature, pressure and composition, and, most importantly, the minimum trapping or formational conditions for the different types of fluids. With the bulk of the fluid inclusions being primary FIAs, by definition, it suggests that the fluids predominantly became trapped in the host crystals during quartz vein formation (Randive et al., 2014). There are at least two types of aqueous fluid inclusions that were identified during microthermometry:

- i.) **Type I** – two phase (L+V), H₂O-rich fluids characterised by fairly low to high homogenization temperatures (125 – 320 °C), low pressures (0.52 – 10.68 MPa) and low salinities (3.06 – 11.34 wt. % NaCl_{equiv.}).
- ii.) **Type II** – three phase (L+V+H), H₂O-NaCl-rich fluids characterised by moderate temperatures (158 – 210 °C), very high pressures (139.24 – 553.45 MPa) and salinities (35.37 – 44.48 wt. % NaCl_{equiv.}).

8.5.2.1. Type I fluid inclusions

Type I inclusions, being fairly low to high homogenization temperature, low pressure and low salinity fluids tend to suggest a meteoric origin for these fluids. These findings are consistent

with the stable isotope results, which suggest a dominantly meteoric origin for the fluids. Similar to the stable isotope values, even though only a small number of samples were analysed for fluid inclusions, these samples are spread over a large extent of the study area, and, therefore, provide an overall idea of the fluid properties of type I inclusions in veins from the Yzerfontein Harbour through to Schaap Eiland (Figs. A4, A5, A6, A9). The type I inclusions were mainly hosted in quartz from quartz-pyrite-tourmaline (YZN60a and YZN60b), quartz-tourmaline-jasper (YZN86), quartz-tourmaline (YZN90), calcite-epidote (YZN82) and barren quartz veins (YZN44). The microthermometry results suggest that type I fluid inclusions were trapped in the minerals which are first in the paragenetic sequence, such as quartz, calcite, pyrite and tourmaline (Table 5.4), and that they were dominantly precipitated from low to high temperature, low pressure and low salinity fluids during the early stages of hydrothermal activity. Moreover, the same conditions must also have operated during the last stages of hydrothermal activity which involved the formation of epidote-bearing and barren quartz veins.

The barren quartz veins (eg. YZN44) are the last generation of hydrothermal veining to have occurred, and their barren nature is inferred to be the result of the upwelling of predominantly meteoric fluids, that, at depth, had become depleted of metals in solution, resulting in the precipitation of dominantly silica-rich material in the form of quartz (Camprubí and Albinson, 2007). This would suggest that quartz was the last mineral to precipitate out from hydrothermal solution after all the other solvents that formed the pyrite, calcite, tourmaline, jasper and epidote veins had precipitated out.

Boiling is a term used to describe the progressive increase in salinity as the temperature of homogenization and depth decreases, and can be inferred from fluid inclusion microthermometry (Canet et al., 2011; Hammond et al., 2011). This definition, in particular, holds true for aqueous H₂O-rich fluid inclusions that reflect the partitioning of non-volatile (and non-carbonic) solutes into the liquid phase during steam loss (Canet et al., 2011). Boiling, along with fluid mixing, are arguably the most valuable and relevant processes and trigger the precipitation of metals from solution in many mineralizing systems (Wilkinson, 2001; Canet et al., 2011).

The relationship between salinity and homogenization temperature can be illustrated diagrammatically. The distribution of the type I fluid inclusions illustrates a shotgun-type spread (Fig. 8.9). There is no real consistency in the distribution pattern of the inclusions, as seen from most of the salinities being fairly low between 3 and 4 wt. % NaCl_{equiv.}, with only a few higher values. Therefore, boiling cannot be inferred from the distribution of the data and remains unclear. In hydrothermal systems at shallow depths of 2 km, boiling is responsible for controlling the chemical characteristics necessary for mineral precipitation, including the pH, fluid composition and mineral solubility (Canet et al., 2011). that have experienced pervasive hydrothermal alteration (refer to Introduction) (Scholtz, 1946; Jordaan, 1990; Rozendaal and Scheepers, 1995). These depths certainly correspond with type I inclusions which were inferred to have minimum depths of fluid trapping around 2 km. However, the

overall sub-economic to poorly mineralised nature of this deposit further corroborates that boiling, if it had taken place at all, may not have played a very big role in metal precipitation. This is seen from the low near-surface distribution of Cu and Au in hydrothermal veins, and also from the low grades of these metals measured in areas.

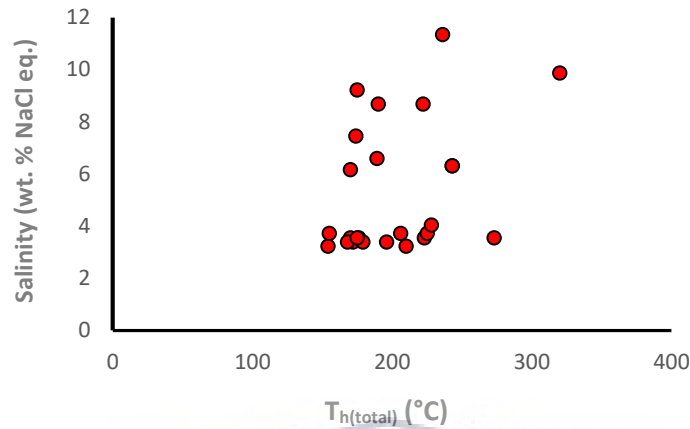


Figure 8.9: Bivariate plot of salinity vs. $T_{h(\text{total})}$ for type I inclusions illustrating that there is no evidence for boiling in these inclusions.

8.5.2.2. Type II fluid inclusions

Type II fluid inclusions, which were only found in one of the seven samples analysed by microthermometry (YZN82 – Yzerfontein Harbour, Fig. A4), are characterised by moderate temperatures and very high pressures and salinities. The origin of these fluids are a bit more obscure, as has also been shown by the stable isotope results. The $\delta^{18}\text{O}$ isotopic value of YZN82 (8.13 – 12.05 ‰) tends to point towards a meteoric origin for the calcite-epidote-bearing fluids (Fig. 7.6), whereas the $\delta^{13}\text{C}$ isotopic value of YZN82 corresponds with $\delta^{13}\text{C}$ isotopic values of limestone, marine carbonates and the mantle. It is possible that these values reflect the mixing of fluids of different origin as they percolated from depths over space and time. Therefore, these fluids could be thought of as evolving fluids over a complex P-T path, especially considering the wide range in corresponding depths as inferred from the trapping P-T conditions (~5 – 22 km).

Using the $\delta^{18}\text{O}$ isotopic value of minerals can be crucial in determining whether mixing of fluids of different origin took place (e.g. Sun and Eadington, 1987). Generally, when samples reflect a variation in $\delta^{18}\text{O}$ isotopic values, it is an indication of fluctuating isotopic composition of hydrothermal solutions which may be attributed to variable degrees of mixing between fluids of different origins (Sun and Eadington, 1987). For the present study, however, only two calcite-bearing samples from hydrothermal veins were analysed, and these two values are not enough to constrain whether mixing of fluids have taken place. However, what is known is that meteoric water generally has low δD and $\delta^{18}\text{O}$ values (Taylor, 1974; Yu et al., 2019). Both samples analysed for their δD and $\delta^{18}\text{O}$ values have relatively low δD and $\delta^{18}\text{O}$ values between -2.33 and -1.93 ‰ (Table 7.3), reflecting that type II inclusions were predominantly

derived from a meteoric water source, which, based on the δD isotopic values, probably mixed with fluids from another source at depth.

The high salinities of type II fluids cannot solely be associated with a meteoric water source, as meteoric waters are generally associated with fluids that have lower salinities (e.g. Greyling, 2009; Yu et al., 2019). This could further indicate that the low salinity meteoric water mixed with a more saline water source at depth to give rise to these high salinity fluids. A magmatic component to the hydrothermal fluids associated with type II fluid inclusions is proposed. This magmatic fluid component likely cannot be related to the mafic and intermediate rocks of the Yzerfontein Pluton, especially since rocks of these compositions do not have large magmatic fluid components associated with them, but, instead, have very low viscosities with high mafic mineral densities, compared to felsic rocks (Robb, 2005). Nevertheless, they do tend to exsolve a magmatic liquid phase, however, the resultant mass fraction of exsolved water is much lower in mafic rocks than in felsic rocks (Robb, 2005). Therefore, felsic rocks, such as the S- or I-type granites of the CGS could explain the magmatic component. I-type granites, in general, are known to be associated with Cu-Au mineralisation (Robb, 2005). The I-type granites, being contemporaneous in age with the Yzerfontein Pluton, could likely account for the origin of these supersaturated type II fluid inclusions. However, this deposit is a very under-developed/poorly developed porphyry Cu-Ag-type deposit, as suggested by Jordaan (1990) and also supported by the absence of zonation of alteration zones (the typical potassic through phyllic to propylitic zonation), as is expected in porphyry Cu-Ag-style deposits (Robb, 2005).

The S-type granites, also contemporaneous in age with the Yzerfontein Pluton, could also possibly explain the magmatic component to type II inclusions. Rozendaal and Bruwer (1995) studied the tourmaline and quartz-tourmaline nodules occurring in the S-type granites of the CGS. These nodules are prominent within the Yzerfontein-Helderberg linear zone (trending sub-parallel to the Colenso Fault), and, according to Rozendaal and Bruwer (1995), are inferred to represent features of post-magmatic replacement related to hydrothermal alteration of the S-type granites with their distribution controlled by fluid movement along fractures. This, of course, suggests major fluid movement related to tectonism and movement along the Colenso Fault.

The presence of ubiquitous tourmaline and tourmaline nodules (particularly associated with the occurrence of the felsic dykes in some localities, Chapter 4, Fig. B5), as well as the presence of tourmalinite and tourmaline-bearing breccias (Chapter 5) tend to suggest a link with the occurrence of these tourmaline nodules, especially since they are related temporally and spatially with respect to the Yzerfontein-Helderberg zone. The NW-SE-oriented Colenso Fault (e.g. Kisters et al., 2002; Kisters and Belcher, 2018) certainly relates to the preferred direction of hydrothermal fluid flow along the fractures of the Yzerfontein Pluton, as suggested by the bulk of the veins being oriented WNW-ESE through NW-SE, to NNW-SSE (Table C1), forming an almost Riedel pair to the Colenso Fault. Nevertheless, considering the high possibility of the link between the tourmaline nodules found within the S-type granites

of the CGS and the tourmaline found within the rocks of the Yzerfontein Pluton, it can be inferred that the presence of the tourmaline relates to a magmatic hydrothermal fluid of dominantly felsic magmatic origin possibly related to the S-type granites.

In terms of boiling for type II fluid inclusions, the inclusions define a more or less flat trend, and do not particularly indicate an increase in salinity with decreasing homogenization temperature, and therefore do not indicate much evidence for boiling or phase separation, if any at all (Fig. 8.10).

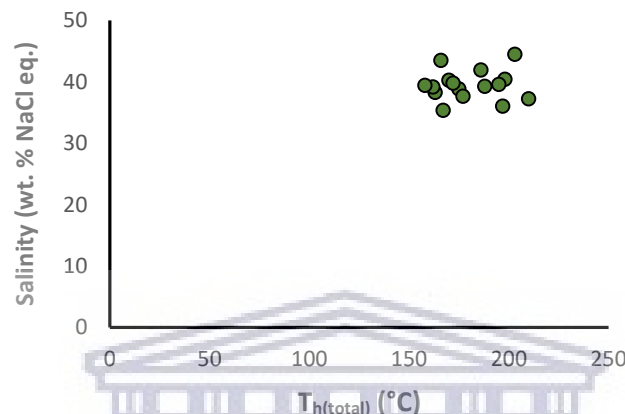


Figure 8.10: Bivariate plot of salinity vs. $T_{h(\text{total})}$ for type II inclusions illustrating that there is no evidence for boiling in these inclusions.

Overall, then, it is proposed that type II fluid inclusions reflect the mixing of a meteoric fluid with a magmatic fluid, where the meteoric fluid likely dominated over the magmatic component. This further explains why the hydrothermal veins are of a sub-economic to very poorly mineralised nature, and that there was no extensive fluid flow and hydrothermal alteration to generate a well-mineralised system. From the inferences made above, it is suggested that the calcite-epidote-bearing hydrothermal vein in the Yzerfontein Harbour (YZN82 - Fig. A4) was most likely dominated by fluids that reflect the mixing of meteoric and magmatic water, containing both type I and type II fluid inclusions in the same vein. In the Yzerfontein Harbour, and moving south towards Yzerfontein Point, Grasbank, and through to Schaap Eiland (Figs. A4, A5, A6, A9), where type I fluid inclusions tend to dominate within quartz-, calcite-, pyrite-, tourmaline-, jasper- and epidote-bearing hydrothermal veins, the fluids are inferred to be related to a meteoric origin.

8.5.3. Fluid evolution and paragenetic model of hydrothermal veining

The Yzerfontein deposit was previously construed as a porphyry Cu-style mineralizing system (e.g. Rozendaal and Scheepers, 1994, 1995; Jordaan et al., 1995). The deposit has, however, been inferred to be an under-developed porphyry Cu-Ag mineralising system (e.g. Jordaan, 1990), characterised by a generally poor economic potential. Evidence for this is suggested by the low extent of boiling of the fluids which is only seen in type I fluid inclusions. Boiling is generally associated with, and promotes significant metal precipitation from hydrothermal

solution (e.g. Wilkinson, 2001; Canet et al., 2011). This premise further supports that boiling, if any at all, did not play a very big role, especially considering that metal precipitation is not that significant, hence the low economic potential of this deposit.

Mineralisation in this system, as previously mentioned, is not associated with the typical alteration zonation, as is expected in porphyry Cu-style mineralisation systems. This could be an indication that these zones may just be very under-developed, as is inferred to be the case for this mineralizing system. Furthermore, the fluid/rock ratios of the hydrothermal fluids were likely relatively low. This is evidenced from the low degree of alteration that is largely localised to areas directly adjacent to the veins and also from the dominantly propylitic alteration present, which suggests temperatures between ~200 and 350 °C (Robb, 2005). These temperatures correspond with the combined minimum trapping temperatures of the type I and II fluid inclusions. Phyllic or sericitic alteration is inferred to be weakly to moderately developed (Tables B1 to B9), suggesting a wide range in temperatures between ~200 and 400 °C (Bodnar et al., 2014). These temperatures also largely correspond with the combined minimum trapping temperatures of type I and II fluid inclusions. Even with both alteration types present, the typical zonation of alteration zones (potassic through phyllic to propylitic zonation) is still absent, both in thin section and at outcrop scale.

The thicknesses and vein mineralogy (Tables 5.2, 5.3), as identified petrographically, do not seem to have affected whether an alteration assemblage formed or not, as the same hydrothermal vein mineralogy or composition gave rise to different alteration assemblages of varying thicknesses. Additionally, according to Table 5.2, most of the hydrothermal veins sampled cross-cut the monzonite, and therefore host rock mineralogy also did not seem to have a first-order control on whether or not a hydrothermal alteration halo developed and its associated thickness. On the basis of the aforementioned inferences, what can be inferred to control the vein mineralogy and metal precipitation has to be related to the fluid composition and its evolution over space and time, the temperature of the fluids and the host rocks, fluid/rock interactions (pH and Eh controls), as well as the extent of fluid mixing (Robb, 2005).

The primary variable is most likely the extent of fluid/rock interaction which is the interaction between a hydrothermal fluid and the surrounding wall-rock, and represents yet another process that promotes metal precipitation (Robb, 2005). Metal precipitation from hydrothermal solutions is promoted due to the changes that fluid/rock interaction induces in the prevailing fluid characteristics, particularly with respect to the pH and redox state of the mineralizing fluids (Robb, 2005). Higher fluid/rock ratios would produce a more variable alteration assemblage over time, particularly “downdip” of the fluid source, and would also have a large effect on the surrounding country rock, thereby producing a larger and more variable alteration halo mineral assemblage. Fluid/rock interaction, as mentioned before, was likely relatively low as evidenced from the overall low degree of alteration, as well as the absence of the typical zonation of alteration zones.

Zonation within the veins themselves is also not very well developed. Petrographically, only one vein demonstrated crustiform banding (YZN34b – quartz-pyrite-tourmaline-calcite vein, Fig. 5.2b) in thin section, thereby displaying some degree of zonation and pattern of mineral precipitation. However, since this only represents one example of zonation within the hydrothermal veins, not much can be concluded with regards to the potential fluid flow and evolution in a particular direction. The compositional changes in hydrothermal veins recorded in Chapter 5 give an idea of the fluid evolution and therefore potential fluid flow direction. Overall, generalised observation from the compositional changes along the hydrothermal veins is that they tend to be more pyrite-rich toward the S and E, and more quartz- and jasper-rich toward the N and W. The above observations may directly reflect the evolution of the hydrothermal fluids in these directions. It could potentially point to a source for the fluids more toward the SE where there is more Fe and S, and becoming more dilute and silica-rich further away from the source toward the NW. However, in order to confidently prove this, the compositions of the fluids at various locations need to be analysed by LA-ICP-MS of the fluid inclusions. Nevertheless, based on the compositional changes, the locus or focal point of hydrothermal fluid flow is inferred to be at Schaap Eiland, and can be thought of as the area where the hydrothermal fluids originated and flowed outward from. Schaap Eiland and Freddie se Klip, as mentioned in Chapter 5, represent the only two localities where pyrite within quartz-pyrite-bearing hydrothermal veins can be found as thick stringers (Fig. 5.17). Additionally, the massive and thick gossanous hydrothermal veins along the channel at Schaap Eiland (Figs. A9, C1) are inferred to represent remnants of pyrite mineralisation. These observations are related to the precipitation of low-grade pyrite from the second hydrothermal event (stage 2), which is also inferred to be the main ore-forming event.

Hydrothermal veining is inferred to be sub-solidus, and therefore indicates that hydrothermal veining was a later event that occurred when the rocks of the Yzerfontein Pluton were relatively cool. Mineralisation in the Yzerfontein Pluton therefore most likely took place at shallow crustal levels, particularly for type I inclusions in quartz-bearing hydrothermal veins, as mineralisation by mechanisms such as open-space filling usually takes place at these depths (Robb, 2005). As has been described in chapter 5, open-space filling is one of the most common textures seen in many of the quartz-bearing vein assemblages, where crystals grow from the margins inward. This not only suggests a shallow crustal level of fluid precipitation, but it also tends to suggest that fluid and/or metal precipitation took place within an extensional environment, as these are tension veins. Hydrothermal fluid flow within an extensional environment, most likely related to the NW-SE-oriented Colenso Fault (e.g. Kisters et al., 2002; Kisters and Belcher, 2018), is supported by the fact that most of the veins, as seen from their orientations in the field (Table C1), are oriented in a WNW-ESE, through NW-SE to NNW-SSE direction. As for the type II inclusions, they appear to have been trapped/formed in relatively deep levels in the crust, reflecting higher associated temperatures and pressures. The high trapping temperature of calcite is therefore consistent with its position in the paragenetic sequence. This suggests that the type II inclusions came

from a fluid that was present earlier in the paragenetic sequence and fluid flow, and that the hydrothermal fluids became less saline over time through the paragenetic sequence.

Type I and II fluid inclusions have once again been plotted on a salinity vs. homogenization temperature diagram (after Wilkinson, 2001), however, this time around it is to diagrammatically constrain the type of deposit to which the fluid inclusions belong. From Fig. 8.11, type I inclusions plot in overlapping fields of lode Au and epithermal deposits (majority of the samples plotting in the field for epithermal deposits), whereas the type 2 inclusions plot in the field of Sn-W deposits. On the one hand, epithermal systems are often thought to be associated with porphyry Cu systems, and, in many respects, are the shallow-level version of porphyry Cu systems where there is a greater degree of mixing between magmatic and meteoric fluids, with the latter dominating (Robb, 2005). Sn-W systems, on the other hand, are not too far off from porphyry Cu-Au deposits, in that the former are usually associated with S-type granites that are considered to develop further from a trench system or an arc system, and the latter are associated with I-type granites closer to the trench system. In fact, in some settings, Sn-W deposits are also regarded as porphyry-type deposits (Robb, 2005). Therefore, as the two types of fluid inclusions plot within these two categories it fits within the model proposed, starting with early, high salinity magmatic fluids (represented by type II fluid inclusions) that were not voluminous and didn't give rise to much mineralisation, and passing into shallower, lower salinity meteoric fluids (represented by type I fluid inclusions) that dominated the hydrothermal system and represent a more epigenetic type of alteration.

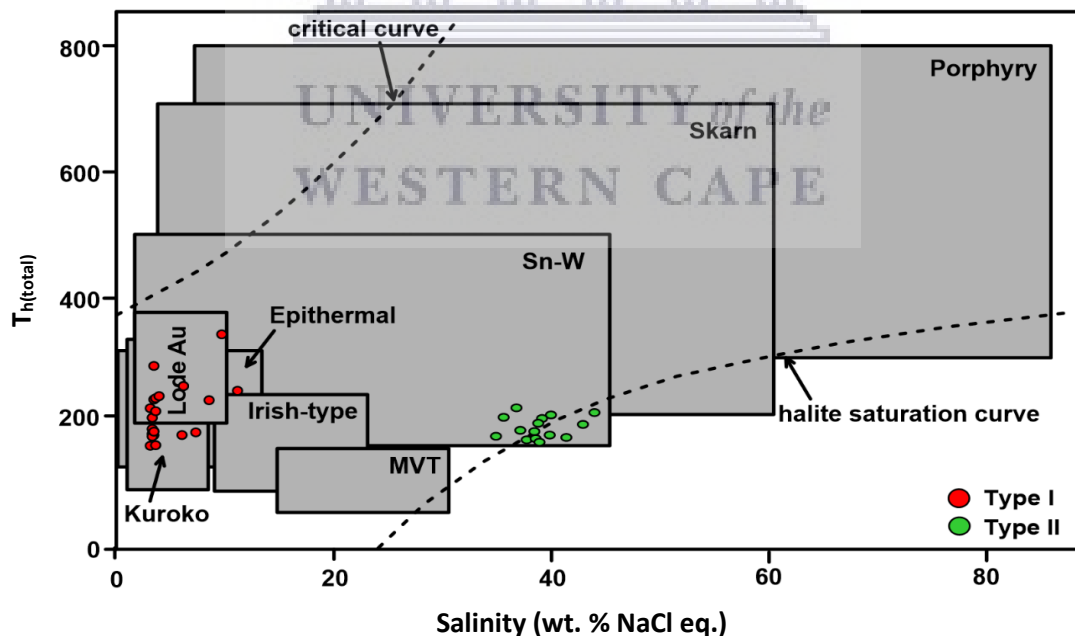


Figure 8.11: Plot of salinity vs. homogenization temperature for type I and II fluid inclusions showing the typical ranges in salinity and homogenization temperatures of fluid inclusions from different types of deposits (after Wilkinson, 2001).

From all the observations and inferences made in this section, a general paragenetic model was constructed for the hydrothermal fluids traversing the rocks of the Yzerfontein Pluton

(Fig. 8.12). The diagram illustrates the possible environment for the precipitation of the hydrothermal fluids. Since zonation of alteration zones was not observed, and a potassic alteration zone seems to be absent, the extent and outline of alteration zones were not incorporated. However, the range of pressures and depths corresponding to the temperatures over which phyllic and propylitic alteration occur are indicated, along with the corresponding minerals that are found within these alteration zones, as evidenced from the petrographic analysis of the hydrothermal veins and alteration haloes. The diagram is simplified and generalised, and predominantly accounts for the hydrothermal assemblages of the samples analysed by microthermometry, as these samples are the only ones which have pressure, temperature and depth data available.



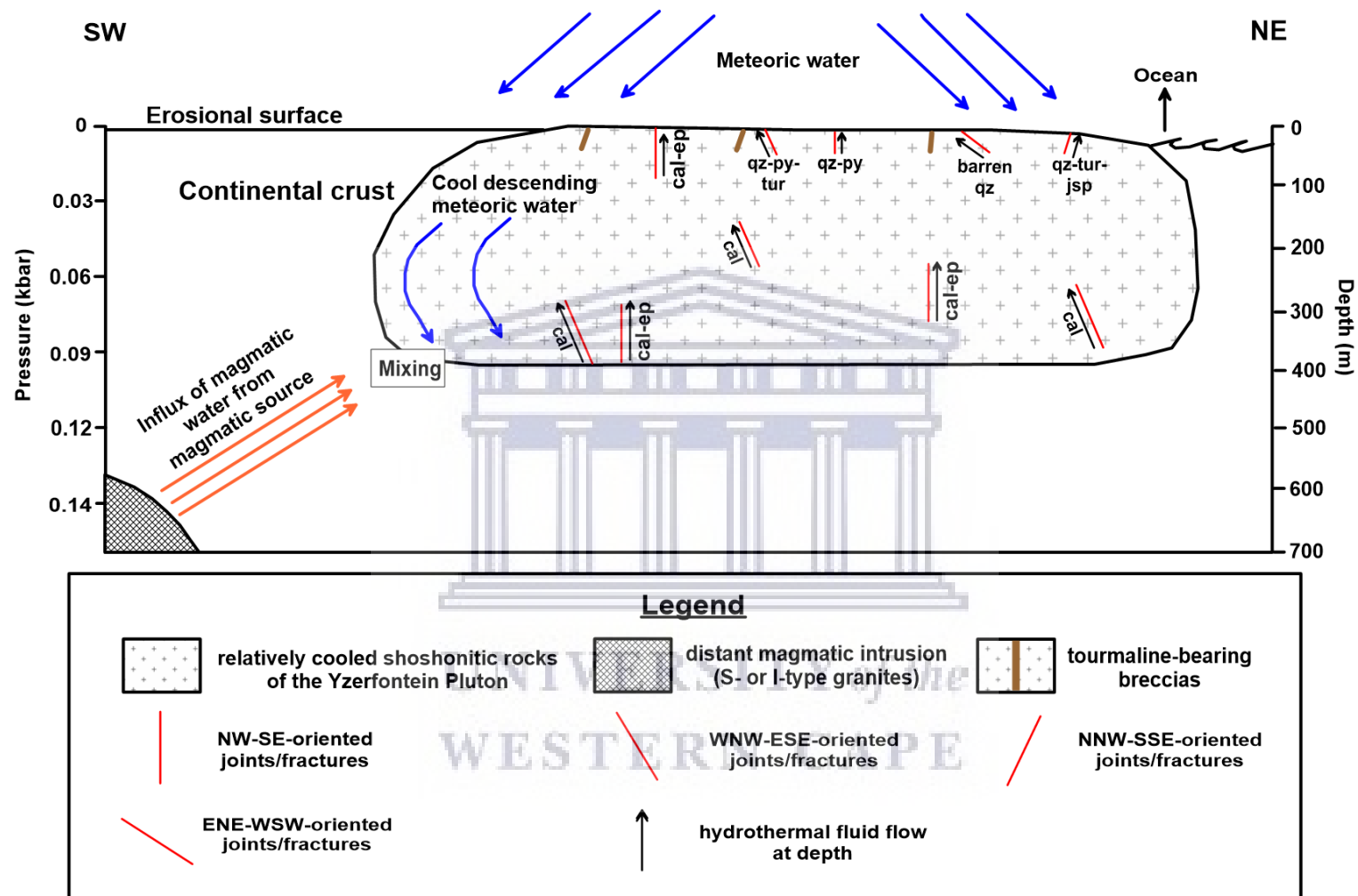


Figure 8.12: Simplified paragenetic model for hydrothermal fluid flow along pre-existing joints and fractures of the Yzerfontein Pluton. Note, this is only a general and simplified model, and therefore the depths are only approximate. The fluids were likely trapped at depth close to the time the intrusion crystallised. Since then, the pluton has, of course, been subjected to uplift and erosion, exposing this pluton to the surface and brining these veins which trapped fluids at depth, to the surface. Abbreviations: Cal = Calcite, Ep = Epidote, Jsp = Jasper, Py = Pyrite, Qz = Quartz, Tur = Tourmaline (after Whitney and Evans, 2010).

Chapter 9: Concluding Remarks

The Yzerfontein Pluton is inferred to be a composite pluton comprised of various mafic, intermediate and felsic rocks that are related by fractional crystallisation. The geochemical analysis of major and trace elements allowed for a detailed reconstruction of the petrogenesis of the host rocks of the Yzerfontein Pluton. The Sr-Nd isotopes suggest a highly fractionated and slightly enriched mantle source for the rocks of the Yzerfontein Pluton. Additionally, a subduction-related history for the rocks is inferred from the relative enrichment in LILE, such as Cs, Rb, Sr, Ba, and Pb, and the depletion of HFSE, such as Th, U, Nb and Hf (Fig. 6.5) (Gill, 1981; Wilson, 1989; McCulloch and Gamble, 1991; Gribble et al., 1996; Janoušek et al., 2000). The mafic to intermediate rocks are highly fractionated within the HREE ((Gd/Lu)_N ratios of 2.57 – 4.57) relative to the LREE ((La/Sm)_N ratios of 1.90 – 3.84), whereas the felsic rocks are highly fractionated within the LREE ((La/Sm)_N ratios of 3.64 – 5.07) relative to the HREE ((Gd/Lu)_N ratios of 1.81 – 2.49).

This study presents new data with regards to the hydrothermal veining that crosscuts the rocks of the Yzerfontein Pluton. It focuses on providing a detailed account of the field relationships and petrography of the hydrothermal veins, as well as a detailed paragenetic sequence for the minerals which precipitated from the veins. The petrographic and field investigation of the hydrothermal veins has revealed at least 7 different vein assemblages, which include quartz-dominated veins, tourmaline-dominated veins, breccias and brecciated veins, jasper-dominated veins, epidote-dominated veins, calcite-dominated veins, and, lastly, barren quartz veins. Field observations additionally show that hydrothermal veins demonstrate a change in composition along their length, being more pyrite-rich toward the S and E, and more quartz and jasper-rich toward the N and W. The paragenetic sequence of veins was constructed based on various overgrowth and crosscutting relationships. According to the sequence, the precipitation of quartz preceded the formation of all other precipitating mineral species. Precipitation of quartz was followed by the precipitation of pyrite, calcite, tourmaline, jasper and epidote. Associated with these hydrothermal veins are hydrothermal alteration haloes which reflect the occurrence of propylitic alteration associated with the formation of chlorite, epidote, calcite and zoisite, as well as phyllic or sericitic alteration which is mainly associated with the formation of sericite and chlorite. It is inferred that these veins must have formed in a dominantly extensional environment, as indicated by open-space filling of many quartz-bearing veins analysed (Robb, 2005).

New data is presented in this study from the analysis of fluid inclusions and stable isotopes. The integrated study of fluid inclusions and stable isotope geochemistry helped in constraining temperatures and pressures of type I and type II fluid inclusions, as well as their minimum trapping or formational conditions. Inclusions are mainly primary, aqueous fluid inclusions that were further classified into type I and type II fluid inclusions. From the low minimum trapping temperature of type I inclusions (186°C), as well as the low pressure (0.56 kbar) and salinities (3.06 – 11.34 wt. % NaCl_{equiv.}), they were inferred to have a meteoric origin,

as is also suggested by the stable isotope findings. For type II inclusions, the minimum trapping temperatures are much higher (260 – 379°C), as well as the pressures (1.39 – 5.55 kbar) and salinities (35.37 – 44.48 wt. % NaCl_{equiv.}), constraining the origin of type II inclusions to a dominantly meteoric origin. They have potentially experienced mixing with a magmatic fluid which may have been derived from felsic rocks such as the S-type granites and/or I-type granites of the CGS. Overall, the deposit is construed as an under-developed, sub-economic to poorly mineralised porphyry Cu-Au-deposit that did not experience extensive alteration. The fluid inclusion microthermometry and the stable isotope results ultimately aided in constructing a simplified paragenetic model for the hydrothermal veins.

Future considerations

Future work can include more details on the petrogenesis aspect of the study, focussing on aspects that have not been investigated previously. An example would be to assess the effects of crustal assimilation on the rocks of the Yzerfontein Pluton in order to assess its possible role on the evolution of the rocks.

Most of the shortcomings of the present study are related to the limited dataset obtained from stable isotope analysis, and, to some extent, fluid inclusion microthermometry. Future work should envisage to analyse more samples of hydrothermal veins for their stable isotope values, as well as their fluid inclusion properties (temperature, pressure, composition, etc.), as this could help to improve or add to the present results. Additionally, the determination of mineral geobarometers would significantly aid in constraining the crystallisation temperatures of the minerals associated with the hydrothermal veins and alteration haloes. This would, in turn, allow for more accurate isotopic values to be calculated from isotope fractionation equations. Moreover, having a larger fluid inclusion microthermometry dataset available would help to confidently constrain the role of boiling and phase separation, as well as the role of mixing of fluids of different origin. These processes were accounted for as far as possible, however, a larger dataset could potentially indicate better trends, particularly on salinity vs. homogenization temperature diagrams. It could also help to accurately determine whether processes such fluid miscibility or fluid immiscibility played a role in defining the fluid properties of the two fluid inclusion types.

The integration of microthermometry with Raman spectroscopy and LA-ICP-MS of fluid inclusions is suggested as it would help to constrain the overall P-T-v-X conditions of the fluids, which is essentially useful when describing the evolution of the fluids. Raman spectroscopy can be performed on fluid inclusions in order to confirm and quantify the composition of gaseous phases, as well as any other phases present within the different fluid inclusion types. LA-ICP-MS is a very important tool as it allows for the quantitative analysis of individual fluid inclusions. It involves the accurate and complete assessment of fluid inclusions in terms of the cationic species contained within them. Lastly, another suggestion is to study the tourmaline-bearing breccias and the tourmaline nodules occurring in the rocks of the Yzerfontein Pluton in order to determine their chemical characteristics and to assess their

relationship with the tourmaline nodules found along the Yzerfontein-Helderberg zone in more detail.



UNIVERSITY *of the*
WESTERN CAPE

References

- Adams, S.F. (1920). A microscopic study of vein quartz. *Economic Geology* 15 (8), 623-664.
- Adriaans, L. (2018). *Geology, geochemistry and Sr-Nd isotope analysis of the Vredenburg Batholith and Cape Columbine Granites Paternoster/Vredenburg, South Africa: Implications on their petrogenesis, tectonic setting, and sources*. MSc thesis (unpublished), University of the Western Cape, Cape Town, 87pp.
- Allsopp, H.L., Kolbe, P. (1965). Isotopic age determinations on the Cape granite and intruded Malmesbury sediments, Cape Peninsula, South Africa. *Geochimica et Cosmochimica Acta* 29, 1115-1130.
- Bacon, C.R., Druitt, T.H. (1988). Compositional evolution of the zoned calcalkaline magma chamber of Mount-Mazama, Crater Lake, Oregon. *Contributions to Mineralogy and Petrology* 98, 224-256.
- Bakker, R.J. (2018). AqSo_NaCl: Computer program to calculate p-T-V-x properties in the H₂O-NaCl fluid system applied to fluid inclusion research and pore fluid calculation. *Computers and Geosciences* 115, 122-133.
- Bateman, P.C. (1992). Plutonism in the central part of the Sierra Nevada batholith, California. U.S. Geological Survey Professional Paper 1483, 186pp.
- Belcher, R.W. (2003). *Tectonostratigraphic evolution of the Swartland region and aspects of orogenic lode-gold mineralization in the Pan-African Saldania Belt, Western Cape, South Africa*. PhD thesis (unpublished), University of Stellenbosch, Stellenbosch, 330pp.
- Belcher, R.W., Kisters, A.F.M. (2003). Lithostratigraphic correlations in the western branch of the Pan-African Saldania belt, South Africa: the Malmesbury Group revisited. *South African Journal of Geology* 106, 327-342.
- Ben Othman, D., Polve, M., Alègre, C.J. (1984). Nd-Sr isotopic composition of granulites and constraints on the evolution of the lower continental crust. *Nature* 307, 510-515.
- Bodnar, R.J., Lecumberri-Sanchez, P., Moncada, D., Steele-MacInnis, M. (2014). Fluid Inclusions in Hydrothermal Ore Deposits. In: Holland, H.D., Turekian, K.K. (Ed.). *Treatise on Geochemistry* (2nd Ed.). Elsevier, Oxford, 119-142.
- Boiron, M.C., Essarraj, S., Sellier, E., Cathelineau, M., Lespinasse, M., Poty, B. (1992). Identification of fluid inclusions in relation to their host microstructural domains in quartz by cathodoluminescence. *Geochimica et Cosmochimica Acta* 56, 175-185.
- Browning, C., Macey, P.H. (2015). Lithostratigraphy of the George Pluton units (Cape Granite Suite), South Africa. *South African Journal of Geology*, 118, 323-330.

Buggisch, W., Kleinschmidt, G., Krumm, S. (2010). Sedimentology, geochemistry and tectonic setting of the Neoproterozoic Malmesbury Group (Tygerberg Terrane) and its relation to neighbouring terranes, Saldania Fold Belt, South Africa. *Neues Jahrbuch für Geologie und Paläontologie – Abhandlungen* 257, 85-114.

Cabanis, B., Lecolle, M. (1989). The La/10-Y/15-Nb/8 diagram: A tool for discrimination volcanic series and evidencing continental crust magmatic mixtures and/or contamination [La diagramme La/10-Y/15-Nb/8: un outil pour la discrimination des series volcaniques et la mise en evidence des processus de mélange et/ou de contamination crustale]. *Comptes rendus de l'Académie des sciences* 309, 2023-2029.

Canet, C., Franco, S.I., Ledesma, R.M.P., González-Partida, E., Villanueva-Estrada, R.E. (2011). A model of boiling for fluid inclusion studies: Application to the Bolaños Ag–Au–Pb–Zn epithermal deposit, Western Mexico. *Journal of Geochemical Exploration* 11, 118-125.

Chemale, J.F., Scheepers, R., Gresse, P.G., Van Schmus, W.R. (2011). Geochronology and sources of late Neoproterozoic to Cambrian granites of the Saldania Belt. *International Journal of Earth Sciences* 100, 431-444

Clayton, R.N., O'Neil, J.R., Mayeda, T.K. (1972). Oxygen isotope exchange between quartz and water. *Journal of Geophysical Research* 77, 3057-3067.

Clemens, J.D., Buick, I.S., Frei, D., Lana, C., Villaros, A. (2017a). Post-orogenic shoshonitic magmas of the Yzerfontein pluton, South Africa: the 'smoking gun' of mantle melting and crustal growth during Cape granite genesis? *Contributions to Mineralogy and Petrology* 172:72.

Clemens, J.D., Regmi, K., Nicholls, I.A., Weinberg, R., Maas, R. (2016). The Tynong pluton, its mafic synplutonic sheets and igneous microgranular enclaves: the nature of the mantle connection in I-type granitic magmas. *Contributions to Mineralogy and Petrology* 171:35.

Clemens, J.D., Stevens, G., Frei, D., Joseph, C.S.A. (2017b). Origins of cryptic variation in the Ediacaran–Fortunian rhyolitic ignimbrites of the Saldanha Bay Volcanic Complex, Western Cape, South Africa. *Contributions to Mineralogy and Petrology* 172:99.

Coleman, D.S., Glazner, A.F., Miller, J.S., Bradford, K.J., Frost, T.P., Joye, J.L., Bachl, C.A. (1995). Exposure of a Late Cretaceous layered mafic-felsic magma system in the central Sierra Nevada batholith, California. *Contributions to Mineralogy and Petrology* 120, 129-136.

Coplen, T.B., Kendall, C., Hopple, J. (1983). Comparison of stable isotope reference samples. *Nature* 302, 236-238.

Cox, K.G., Bell, J.D., Pankhurst, R.J. (1979). *The Interpretation of Igneous Rocks*. Chapman & Hall, London, 450pp.

Craig, J.R., Vaughan, D.J. (1994). *Ore microscopy and ore petrography* (2nd Ed.). John Wiley & Sons, New York, 434pp.

Da Silva, L.C., Gresse, P.G., Scheepers, R., McNaughton, N.J., Hartmann, L.A., Fletcher, I. (2000). U–Pb SHRIMP and Sm–Nd age constraints on the timing and sources of the Pan-African Cape Granite Suite, South Africa. *Journal of African Earth Sciences* 30, 795-815.

DePaolo, D. (1981). A neodymium and strontium isotopic study of the Mesozoic calc-alkaline granitic batholiths of Sierra Nevada and Peninsular Ranges, California. *Journal of Geophysical Research* 68, 470-488.

De La Roche, H., Leterrier, J., Grandclaude, P., Marchal, M. (1980). A Classification of volcanic and plutonic rocks using R1 – R2 diagram and major element analysis – its relationships with current nomenclature. *Chemical Geology* 29, 183-210.

Diamond, L. (2003a). Systematics of H₂O inclusions. In: Samson, I., Anderson, A., Marshall, D. (Eds.). *Fluid Inclusions: Analysis and Interpretation*, Mineralogical Association of Canada, Short Course 32, pp. 55-79.

Djouka-Fonkwé, L.M., Kyser, K., Clark, A.H., Urqueta, E., Oates, C.J., Ihlenfeld, C. (2012). Recognizing Propylitic Alteration Associated with Porphyry Cu–Mo Deposits in Lower Greenschist Facies Metamorphic Terrain of the Collahuasi District, Northern Chile—Implications of Petrographic and Carbon Isotope Relationships. *Economic Geology* 107, 1457-1478.

Dong, G., Morrison, G., Jaireth, S. (1995). Quartz textures in epithermal veins, Queensland; classification, origin and implication. *Economic Geology* 90 (6), 1841-1856.

Dye, M. (2015). *Mineralogical characterization and paragenesis of the Cripple Creek deposit, Colorado*. MSc thesis (unpublished), Colorado School of Mines, Colorado, 115pp.

Earle, S. (2015). *Physical Geology* (1st Ed.). BCcampus Open Textbook Project, Vancouver, 621pp.

Ersoy, Y., Helvacı, C. (2010). FC–AFC–FCA and mixing modeler: A Microsoft® Excel® spreadsheet program for modelling geochemical differentiation of magma by crystal fractionation, crustal assimilation and mixing. *Computers and Geosciences* 36, 383-390.

Ewart, A., Griffin, W.L. (1994). Application of proton-microprobe data to trace-element partitioning in volcanic-rocks. *Chemical Geology* 117, 251-284.

Farina, F., Stevens, G., Villaros, A. (2012). Multi-batch, incremental assembly of a dynamic magma chamber: the case of the Peninsula pluton granite (Cape Granite Suite, South Africa). *Mineralogy and Petrology* 106, 193-216.

Foley, S.F., Jackson, S.E., Fryer, B.J., Greenough, J.D., Jenner, G.A. (1996). Trace element partition coefficients for clinopyroxene and phlogopite in an alkaline lamprophyre from Newfoundland by LAM-ICP-MS. *Geochimica et Cosmochimica Acta* 60, 629-638.

Fourie, D. (2010). *An isotope study of the felsic units of the Bushveld Large Igneous Province, South Africa*. MSc thesis (unpublished), University of Cape Town, Cape Town, 108pp.

Frelinger, S.N., Ledvina, M.D. Kyle, J.R., Zhao, D. (2015). Scanning electron microscopy cathodoluminescence of quartz: Principles, techniques and applications in ore geology. *Ore Geology Reviews* 65, 840-852.

Frimmel, H.E. (2009). Configuration of Pan-African orogenic belts in southwestern Africa. In: Gaucher, C., Sial, A.N., Halverson, G.P., Frimmel, H.E. (Eds.). *Neoproterozoic-Cambrian tectonics, global change and evolution: a focus on southwestern Gondwana*, Developments in Precambrian geology 16, Elsevier, Amsterdam, pp. 145-151.

Frimmel, H.E., Basei, M.A.S., Correa, V.X., Mbangula, N. (2013). A new lithostratigraphic subdivision and geodynamic model for the Pan-African western Saldania Belt, South Africa. *Precambrian Research* 231, 218-235.

Frimmel, H.E., Basei, M.A.S., Gaucher, C. (2011). Neoproterozoic geodynamic evolution of SW Gondwana: a southern African perspective. *International Journal of Earth Sciences* 100, 323-354.

Frost, B.R., Barnes, C.G., Collins, W.J., Arculus, R.J., Ellis, D.J., Frost, C.D. (2001). A geochemical classification for granitic rocks. *Journal of Petrology* 42, 2033-2048.

Frost, T.P., Mahood, G.A. (1987). Field, chemical, and physical constraints on mafic-felsic magma interaction in the Lamarck Granodiorite, Sierra Nevada, California. *Geological Society of America Bulletin* 99, 272-291.

Fujimaki, H., Tatsumoto, M., Aoki, K.-i. (1984). Partition coefficients of Hf, Zr, and REE between phenocrysts and groundmasses. *Journal of Geophysical Research* 89, 662-672.

Gill, J.B. (1981). *Orogenic Andesites and Plate Tectonics*. Springer-Verlag, Berlin, 390pp.

Goldstein, R.H. (2001). Fluid inclusions in sedimentary and diagenetic systems. *Lithos* 55, 159-193.

Goldstein, R.H., Reynolds, T.J. (1994). *Systematics of fluid inclusions in diagenetic minerals*. Society for Sedimentary Geology, Short Course 31, 199pp.

Gresse, P.G., Scheepers, R. (1993). Neoproterozoic to Cambrian (Namibian) rocks of South Africa: a geochronological and geotectonic review. *Journal of African Earth Sciences* 16, 375-393.

Gresse, P.G., Von Veh, M.W., Frimmel, H.E. (2006). Namibian (Neoproterozoic) to early Cambrian successions. In: Johnson, M.R., Anhaeusser, C.R., Thomas, R.J. (Eds.). *The geology of South Africa*. Geological Society of South Africa, Johannesburg/Council for Geoscience, Pretoria, pp. 395-420.

Greyling, L.N. (2009). *Fluid evolution and characteristics of mineralizing solutions in the Central African Copperbelt*. PhD thesis (unpublished), University of the Witwatersrand, Johannesburg, 266pp.

Gribble, R.F., Stern, R.J., Bloomer, S.H., Stüben, D., O'Hearn, T., Newman, S. (1996). MORB mantle and subduction components interact to generate basalts in the southern Mariana Trough back-arc basin. *Geochimica et Cosmochimica Acta* 60, 2153-2166.

Hammond, N.Q., Robb, L., Foya, S., Ishiyama, D. (2011). Mineralogical, fluid inclusion and stable isotope characteristics of Birimian orogenic gold mineralization at the Morila Mine, Mali, West Africa. *Ore Geology Reviews* 39, 218-229.

Harris, C., Faure, K., Diamond, R.E., Scheepers, R. (1997). Oxygen and hydrogen isotope geochemistry of S- and I-type granitoids: the Cape Granite Suite, South Africa. *Chemical Geology* 143, 95-114.

Harris, C., Vogeli, J. (2010). Oxygen isotope composition of garnet in the Peninsula granite, Cape Granite Suite, South Africa: constraints on melting and emplacement mechanisms. *South African Journal of Geology* 113, 385-396.

Harris, N.B.W., Pearce, J.A., Tindle, A.G. (1986). Geochemical characteristics of collisional-zone magmatism. In: Coward, M.P., Reis, A.C. (Eds.). *Collision Tectonics*. Geological Society London Special Publication 19, pp. 67-81.

Hartnady, C.J.H., Newton, A.R. and Theron, J.N. (1974). The stratigraphy and structure of the Malmesbury Group in the southwestern Cape. *Bulletin of the Precambrian Research Unit* 15, 193-213.

Hastie, A.R., Kerr, A.C., Pearce, J.A., Mitchell, S.F. (2007). Classification of altered volcanic island arc rocks using immobile trace elements: development of the Th-Co discrimination diagrams. *Journal of Petrology* 48, 2341-2357.

Hekinian, R. (1982). Petrology of the Ocean Floor. *Elsevier Oceanography Series* 33, 329-331.

Hoefs, J. (1987). *Stable Isotope Geochemistry* (3rd ed.). Springer-Verlag, Berlin, 285pp.

Hoefs, J. (2018). *Stable Isotope Geochemistry* (8th ed.). Springer-Verlag, Berlin, 437pp.

Holmes, A., Cahen, L. (1957). African Geochronology. *Overseas Geology and Mineral Resources* 5, 3-39.

Hunt, J.A., Baker, T., Cleverley, J., Davidson, G.J., Fallick, A.E., Thorkelson, D.J. (2011). Fluid inclusion and stable isotope constraints on the origin of Wernecke Breccia and associated iron oxide-copper-gold mineralization, Yukon. *Canadian Journal of Earth Science* 48, 1425-1445.

Ineson, P.R. (1989). *Introduction to practical ore microscopy*. Longman Group Limited, New York, 181pp.

Janoušek, V., Bowes, D.R., Rogers, G., Farrow, C.M., Jelinek, E. (2000). Modelling diverse processes in the petrogenesis of a composite batholith: the Central Bohemian Pluton, Central European Hercynides. *Journal of Petrology* 41, 511-543.

Janoušek, V., Moyen, J.F., Martin, H., Erban, V., Farrow, C. (2016). *Geochemical modelling of igneous processes – principles and recipes in R language*. Springer-Verlag, Berlin, New York, 346pp.

Jiang, S.Y. (1998). Stable and radiogenic isotope studies of tourmaline: An overview. *Journal of the Czech Geological Society* 43, 75-90.

Jordaan, L.J. (1990). *The Geology and Geochemistry of Mafic and Intermediate Igneous Rocks associated with the Cape Granites*. MSc thesis (unpublished), University of Stellenbosch, Stellenbosch, 216pp.

Jordaan, L.J., Scheepers, R., Barton, E.S. (1995). The geochemistry and isotopic composition of the mafic and intermediate igneous components of the Cape Granite Suite, South Africa. *Journal of African Earth Sciences* 21, 59-70.

Keller, C.B., Schoene, B., Barboni, M., Samperton, K.M., Husson, J.M. (2015). Volcanic-plutonic parity and the differentiation of the continental crust. *Nature* 523, 301-307.

Kisters, A.F.M., Agenbach, C., Frei, D. (2015). Age and tectonic significance of the volcanic Bloubergstrand member in the Pan-African Saldania Belt, South Africa. *South African Journal of Geology* 18, 213-224.

Kisters, A.F.M., Belcher, R.W. (2018). The stratigraphy and structure of the western Saldania Belt, South Africa and geodynamic implications. In: Siegesmund, S., Basei, M.A.S., Oyhantçabal, P., Oriolo, S. (Eds.). *Geology of Southwest Gondwana*. Regional Springer Book Series, pp. 387-410.

Kisters, A.F.M., Belcher, R.W., Armstrong, R.A., Scheepers, R., Rozendaal, A. and Jordaan, L.S. (2002). Timing and kinematics of the Colenso Fault: The Early-Paleozoic shift from collisional to extensional tectonic in the Pan-African Saldania Belt, South Africa. *South African Journal of Geology* 105, 257-270.

Kotzer, T.G., Kyser, T.K., King, R.W., Kerrich, R. (1993). An empirical oxygen- and hydrogen isotope geothermometer for quartz-tourmaline and tourmaline-water. *Geochimica et Cosmochimica Acta* 57, 3421-3426.

Le Bas, M.J., Streckeisen, A.L. (1991). The IUGS systematics of igneous rocks. *Journal of the Geological Society* 148, 825-833.

Le Maitre, R.W., Streckeisen, A., Zanettin, B., Le Bas, M.J., Bonin, B., Bateman, P., Belleni, G., Dudek, A., Efremova, S., Keller, J., Lamere, J., Sabine, P.A., Schmid, R., Sorensen, H., Wolley, A.R. (2002). *Igneous rocks: a classification and glossary of terms, recommendations of the International Union of Geological Sciences, subcommission of the systematics of igneous rocks*. Cambridge University Press, Cambridge, 236pp.

Legros, H., Marignac, C., Mercadier, J., Cuney, M., Richard, A., Wang, R.C., Charles, N., Lespinasse, M.Y. (2016). Detailed paragenesis and Li-mica compositions as recorders of the

magmatic-hydrothermal evolution of the Maoping W-Sn deposit (Jiangxi, China). *Lithos* 264, 108-124.

Lugmair, G.W. Marti, K. (1978). Lunar initial $^{143}\text{Nd}/^{144}\text{Nd}$: differential evolution of the lunar crust and mantle. *Earth and Planetary Science Letters* 39, 349-357.

MacKenzie, W.S., Donaldson, C.H., Guilford, C. (1982). *Atlas of igneous rocks and their textures*. Longman Group, England, 170pp.

Maske, S. (1957). *The diorites of Yzerfontein, Darling, Cape Province*. MSc thesis (unpublished), University of Stellenbosch, Stellenbosch, 68pp.

Matsumura, R. (2014). *The petrogenesis of the Nelshoogte pluton: The youngest and most compositionally variable TTG pluton in the Barberton Granite-Greenstone Terrain*. MSc thesis (unpublished), University of Stellenbosch, Stellenbosch, 108pp.

McCulloch, M.T., Gamble, J.A. (1991). Geochemical and geodynamical constraints on subduction zone magmatism. *Earth and Planetary Science Letters* 102, 358-374.

McDonough, W.F., Sun, S.S. (1995). The composition of the Earth. *Chemical Geology* 120, 223-253.

McKenzie, D., O'Nions, R.K. (1991). Partial melt distributions from inversion of rare earth element concentrations. *Journal of Petrology* 32, 1021-1091.

Middlemost, E.A.K. (1994). Naming materials in the magma igneous rock system. *Earth-Science Reviews* 37, 215-224. Maske, S. (1957). The diorites of Yzerfontein, Darling, Cape Province. *Annals University Stellenbosch* 33, 1-11.

Miková, J., Denková, P. (2007). Modified chromatographic separation scheme for Sr and Nd isotope analysis in geological silicate samples. *Journal of Geosciences* 52, 221-226.

Nagasawa, H., Schnetzler, C.C. (1971). Partitioning of rare earth, alkali and alkaline earth elements between phenocrysts and acidic igneous magma. *Geochimica et Cosmochimica Acta* 35, 953-968.

Nandedkar, R.H., Ulmer, P., Müntener, O. (2014). Fractional crystallization of primitive, hydrous arc magmas: an experimental study at 0.7 GPa. *Contributions to Mineralogy and Petrology* 167:1015.

O'Connor, J.T. (1965). A classification for quartz-rich igneous rocks based on feldspar ratios. *U.S. Geological Survey Professional Paper B525*, 79-84.

Pandit, D. (2014). Chloritization in Paleoproterozoic granite ore system at Malanjhand, Central India: mineralogical studies and mineral fluid equilibria modelling. *Current Science* 106, 565-581.

Pearce, J.A. (1996). Sources and settings of granitic rocks. *Episodes* 19, 120-125.

Pearce, J.A. (2008). Geochemical fingerprinting of oceanic basalts with applications to ophiolite classification and the search for Archean oceanic crust. *Lithos* 100, 14-48.

Pearce, J.A. (2014). Immobile element fingerprinting of ophiolites. *Elements* 10, 101-108.

Plumlee, G.S., Whitehouse-Veaux, P.H. (1994). Mineralogy, paragenesis and mineral zoning of the Bulldog Mountain Vein System, Creede District, Colorado. *Economic Geology* 89, 1883-1905.

Rabie, L.P. (1948). Geological Map of the Morreesburg-Wellington area. University of Stellenbosch (printed but not issued).

Rabie, L.P. (1974). Geological map of the Morreesburg-Wellington area. *Annals of the University of Stellenbosch*, 49 A(5).

Randive, K.R., Hari, K.R., Dora, M.L., Malpe, D.B., Bhondwe, A.A. (2014). Study of fluid inclusions: methods, techniques and applications. *Gondwana Geological Magazine* 29, 19-28.

Robb, L. (2005). *Introduction to Ore-Forming Processes*. Blackwell Science, Malden, United Kingdom, 373pp.

Roedder, E. (1984). Fluid inclusions. *Reviews in Mineralogy* 12, Mineralogical Society of America, 646pp.

Rogers, A.F. (1918). The occurrence of cristobalite in California. *Journal of Science* 45, 222-226.

Rogers, A.W. (1896). A summary of work done in the south western districts. *Annual Report of the Geological Commission of the Cape of Good Hope* 1, 13-15.

Rollinson, H.R. (1993). *Using geochemical data: Evaluation, presentation, interpretation*. Longman Scientific and Technical, New York, 352pp.

Rowe, C.D., Backeberg, N.R., Van Rensburg, T., MacLennan, S.A., Faber, C., Curtis, C., Viglietti, P.A. (2010). Structural geology of Robben Island: implications for the tectonic environment of Saldanian deformation. *South African Journal of Geology* 113, 57-72.

Rozendaal, A., Bruwer, L. (1995). Tourmaline nodules: indicators of hydrothermal alteration and Sn-Zn-(W) mineralization in the Cape Granite Suite, South Africa. *Journal of African Earth Sciences* 21, 142-155.

Rozendaal, A., Gresse, P.G., Scheepers, R., Le Roux, J.P. (1999). Neoproterozoic to Early Cambrian crustal evolution of the Pan-African Saldania Belt, South Africa. *Precambrian Research* 97, 303-323.

Rozendaal, A., Scheepers, R. (1994). Metallogenesis and exploration potential of the Neoproterozoic Saldania Belt in the southwestern Cape Province, South Africa. *Exploration and Mining Geology* 3, 419-438.

Rozendaal, A., Scheepers, R. (1995). Magmatic and related mineral deposits of the Pan-African Saldania belt in the Western Cape Province, South Africa. *Journal of African Earth Sciences* 21, 107-126.

Samson, I., Anderson, A., Marshall, D.D. (2003). *Fluid inclusions: analysis and interpretation*. Mineralogical Association of Canada, Canada, 374pp.

Sander, M.V., Black, J.E. (1988). Crystallization and recrystallization of growth-zoned vein quartz crystals from epithermal systems; implications for fluid inclusion studied. *Economic Geology* 83 (5), 1052-1060.

Scheepers, R. (1982). *The U, Th and Mo distribution in selected leucogranites of the Cape Granite Suite*. MSc thesis (unpublished). University of Stellenbosch, Stellenbosch, 134pp.

Scheepers, R. (1995). Geology, geochemistry and petrogenesis of Late Precambrian S-, I- and A-type granitoids in the Saldania belt, Western Cape Province, South Africa. *Journal of African Earth Sciences* 21, 35-58.

Scheepers, R. (2000). Granites of the Saldania mobile belt, South Africa: radioelements and P as discriminators applied to metallogeny. *Journal of Geochemical Exploration* 68, 69-86.

Scheepers, R., Armstrong, R. (2002). New U-Pb SHRIMP zircon ages of the Cape Granite Suite: implications for the magmatic evolution of the Saldania Belt. *South African Journal of Geology* 105, 241-256.

Scheepers, R., Poujol, M. (2002). U-Pb zircon age of Cape Granite Suite ignimbrites: characteristics of the last phases of the Saldanian magmatism. *South African Journal of Geology* 105, 163-178.

Scheepers, R., Schoch, A.E. (1988). Geology and geochemistry of the Klipberg alkali feldspar granite and associated hydrothermally altered rocks in the Darling batholith, south-western Cape Province. *South African Journal of Geology* 91, 211-225.

Scheepers, R., Schoch, A.E. (2006). The Cape granite suite. In: Johnson, M.R., Anhaeusser, C.R., Thomas, R.J. (Eds.). *The geology of South Africa*. Geological Society of South Africa, Johannesburg/Council for Geoscience, Pretoria, pp. 421-432.

Schidlowski, M. (1987). Application of stable isotopes to early biochemical evolution on earth. *Annual Review of Earth and Planetary Science* 15, 47-72.

Schnetzer, C.C., Philpotts, J.A. (1970). Partition coefficients of rare-earth elements between igneous matrix material and rock-forming mineral phenocrysts—II. *Geochimica et Cosmochimica Acta* 34, 331-340.

Schoch, A.E. (1972). *The Darling Granite Batholith*. MSc thesis (unpublished), University of Stellenbosch, Stellenbosch, 144pp.

Schoch, A.E., Burger, A.J. (1976). U-Pb zircon age of the Saldanha quartz porphyry, Western Cape Province. *Transactions of the Geological Society of South Africa* 79, 239-241.

Schoch, A.E., Leygonie, F.E., Burger, A.J. (1975). U-Pb Ages for Cape granites from the Saldanha batholith: a preliminary report. *Transactions Geological Society South Africa* 78, 97-100.

Scholtz, D.L. (1946). On the younger Precambrian granite plutons of the Cape Province. *Proceedings of the Geological Society of South Africa* 49, 35-82.

Shao, T., Xia, Y., Ding, X., Cai, Y., Song, M. (2019). Zircon saturation in terrestrial basaltic melts and its geological implications. *Solid Earth Sciences* 4, 27-42.

Slabber, N. (1995). *The geology and geochemistry of the Bridgetown Formation of the Malmesbury group, Western Cape province*. MSc thesis (unpublished), University of Stellenbosch, Stellenbosch, 99pp.

South African Committee for Stratigraphy (SACS). (1980). *Stratigraphy of South Africa. Part 1* (Comp. L. E. Kent). Lithostratigraphy of the Republic of South Africa, SW Africa/Namibia, and the Republics of Bophuthatswana, Transkei and Venda. *Handbook of the Geological Survey of South Africa* 8, 696pp.

Steele-MacInnis, M., Lecumberri-Sanchez, P., Bodnar, R.J. (2012). HokieFlincs_H2O-NaCl: A Microsoft Excel spreadsheet for interpreting microthermometric data from fluid inclusions based on the PVTX properties of H₂O–NaCl. *Computers & Geosciences* 49, 334-337.

Steiger, R.H., Jäger, E. (1977). Subcommittee on geochronology: convention on the use of decay constants in geo- and cosmochronology. *Earth and Planetary Science Letters* 36, 359-362.

Stevens, G., Villaros, A., Moyen, J-F. (2007). Selective peritectic garnet entrainment as the origin of geochemical diversity in S-type granites. *Geology* 35, 9-12.

Stix, J., Gorton, M.P. (1990). Variations in trace element partition coefficients in sanidine in the Cerro Toledo Rhyolite, Jemez Mountains, New-Mexico - Effects of composition, temperature, and volatiles. *Geochimica et Cosmochimica Acta* 54, 2697-2708.

Streckeisen, A. L. (1974). Classification and nomenclature of plutonic rocks. *Geologische Rundschau* 63, 773-786.

Sun, S.S., Eadington, P.J. (1987). Oxygen isotope evidence for the mixing of magmatic and meteoric waters during tin mineralization in the Mole Granite, New South Wales, Australia. *Economic Geology* 82, 43-52.

Tanaka, T., Togashi, S., Kamioka, H., Amakawa, H., Kagami, H., Hamamoto, T., Yuhara, M., Orihashi, Y., Yoneda, S., Shimizu, H., Kunimaru, T., Takahashi, K., Yanagi, T., Nakano, T., Fujimaki, H., Shinjo, R., Asahara, Y., Tanimizu, M., Dragusanu, C. (2000). JNdi-1: a neodymium isotopic reference in consistency with LaJolla neodymium. *Chemical Geology Short Communication* 168, 279-281.

Taylor, H.P. (1974). The application of oxygen and hydrogen isotope studies to problems of hydrothermal alteration and ore deposition. *Economic Geology* 69, 843-883.

Taylor, H.P. (1997). O and H isotope relationships in hydrothermal mineral deposits. In H.L. Barnes (ed.), *Geochemistry of Hydrothermal Ore Deposits*. John Wiley and Sons, pp. 229-302.

Taylor, J., Nicoli, G., Stevens, G., Frei, D., Moyen, J.F. (2014). The processes that control the leucosome compositions in metasedimentary granulites: Perspectives from the Southern Marginal Zone migmatites, Limpopo Belt, South Africa. *Journal of Metamorphic Geology* 32, 713-742.

Theron, J.N., Gresse, P.G., Siegfried, H.P. and Rogers, J. (1992). The geology of the Cape Town Area. Explanation of Sheet 3318. *Geological Survey of South Africa*, 140pp.

Todd, V.R., Shaw, S.E., Hammarstrom, J.M. (2003). Cretaceous plutons of the Peninsular Ranges batholith, San Diego and westernmost Imperial Counties, California: Intrusion across a Late Jurassic continental margin. In: Johnson, S.E., Patterson, S.R., Fletcher, J.M., Girty, G.H., Kimbrough, D.L., Martin-Barajas, A. (Eds.). *Tectonic Evolution of Northwestern Mexico and the Southwestern USA*, Geological Society of America Special Papers 374, pp. 185-235.

Vennemann T.W., O'Neil J.R. (1993). A simple and inexpensive method of hydrogen isotope and water analyses of minerals and rocks based on zinc reagent. *Chemical Geology* 103, 227-234.

Verma, S.P., Verma S.K. (2013). First 15 probability-based multidimensional tectonic discrimination diagrams for intermediate magmas and their robustness against postemplacement compositional changes and petrogenetic processes. *Turkish Journal of Earth Sciences* 22, 931-995.

Villaros, A. (2010). *Petrogenesis of the S-type Granite with particular emphasis on source processes: the example of the S-type Granite of the Cape Granite Suite*. PhD thesis (published), University of Stellenbosch, Stellenbosch, 208pp.

Villaros, A., Buick, I.S., Stevens, G. (2012). Isotopic variations in S-type granites: an inheritance from a heterogeneous source? *Contributions to Mineralogy and Petrology* 163, 243-257.

Villaros, A., Stevens, G., Buick, I.S. (2009). Tracking S-type granite from source to emplacement: Clues from garnet in the Cape Granite Suite. *Lithos* 112, 217-235.

Von Veh, M.W. (1982). *Aspects of the structure, tectonic evolution and sedimentation in the Tygerberg Terrane, southwestern Cape Province*. Precambrian Research Unit, University of Cape Town, Bulletin 32, 97pp.

Watson, E.B., Harrison, T.M. (1983). Zircon saturation revisited: temperature and composition effects in a variety of crustal magma types. *Earth and Planetary Sciences Letters* 64, 295-304.

Whalen, J.B., Chappell, B.W. (1988). Opaque mineralogy and mafic mineral chemistry of I- and S-type granites of the Lachlan fold belt, southeast Australia. *American Mineralogist* 73, 281-296.

Whitney, D.L., Evans, B.W. (2010). Abbreviation for names of rock-forming minerals. *American Mineralogist* 95, 185-187.

Wilkinson, J.J. (2001). Fluid inclusions in hydrothermal ore deposits. *Lithos* 55, 229-272.

Wilson, M. (1989). *Igneous Petrogenesis: A Global Tectonic Approach*. Unwin Hyman, London, 466pp.

Winter, J.D. (2001). *An Introduction to Igneous and Metamorphic Petrology*. Prentice Hall, Upper Saddle River, New Jersey, 697pp.

Xia, Y., Xu, X., Zhao, G., Liu, L. (2015). Neoproterozoic active continental margin of the Cathaysia block: Evidence from geochronology, geochemistry, and Nd–Hf isotopes of igneous complexes. *Precambrian Research* 269, 195-216.

Yu, G.Y., Li, S.D., Wang, Y.C., Wang, K.Y. (2019). Fluid evolution and ore genesis of the Qibaoshan Polymetallic Ore Field, Shandong Province, China: Constraints from fluid inclusions and H–O–S isotopic compositions. *Minerals* 9:394.

Zheng, Y.F. (1993). Calculation of oxygen isotope fractionation in hydroxyl-bearing silicates. *Earth and Planetary Science Letters* 120, 247-263.

Zindler, A., Hart, S.R. (1986). Chemical geodynamics. *Annual Review of Earth and Planetary Science* 14, 493-571.

UNIVERSITY of the
WESTERN CAPE

Appendix A – Geological maps and sample locations



UNIVERSITY *of the*
WESTERN CAPE

Geological Maps

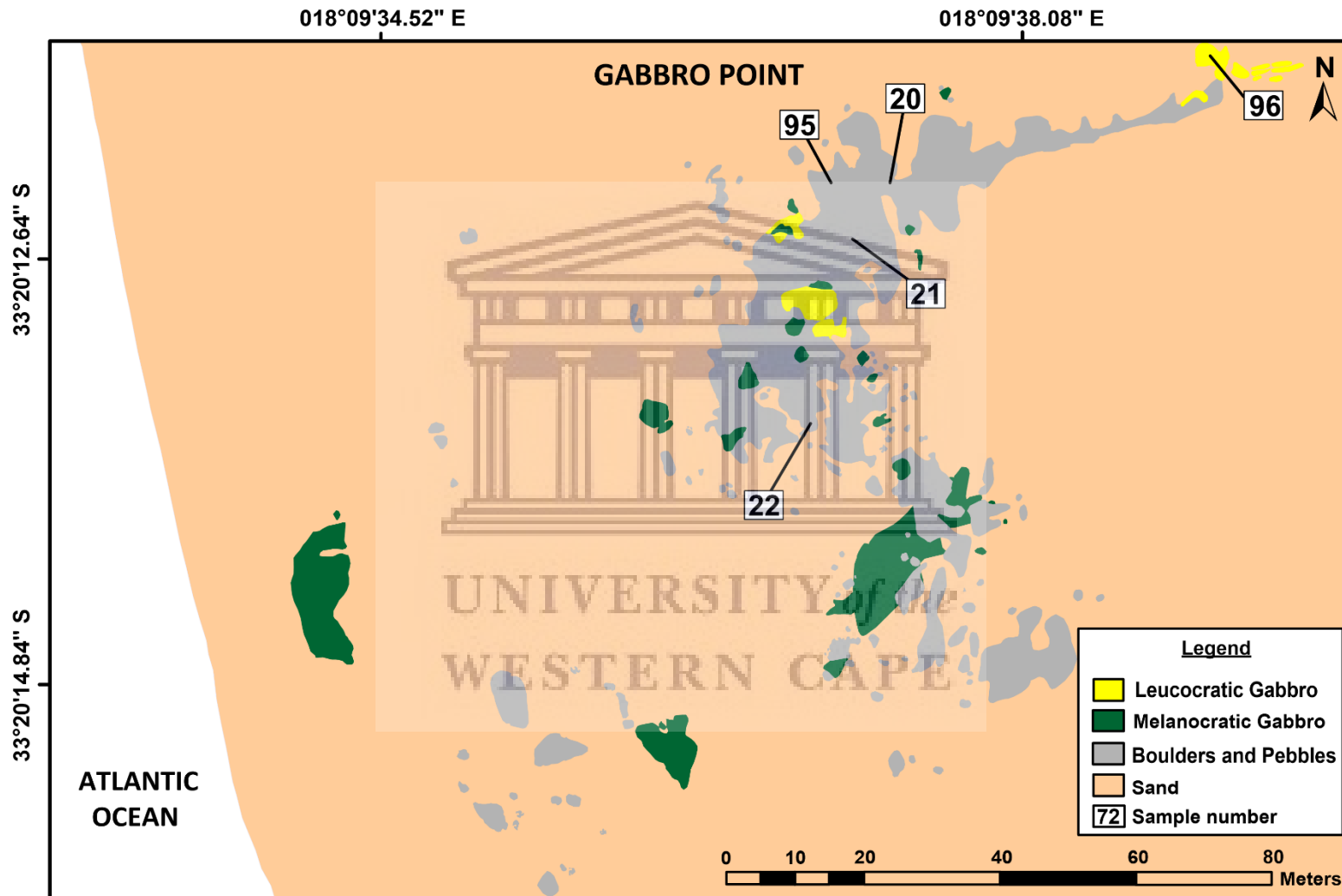


Figure A1: Geological map of the major rock types of the Yzerfontein Pluton occurring at Gabbro Point (after Jordaan, 1990).

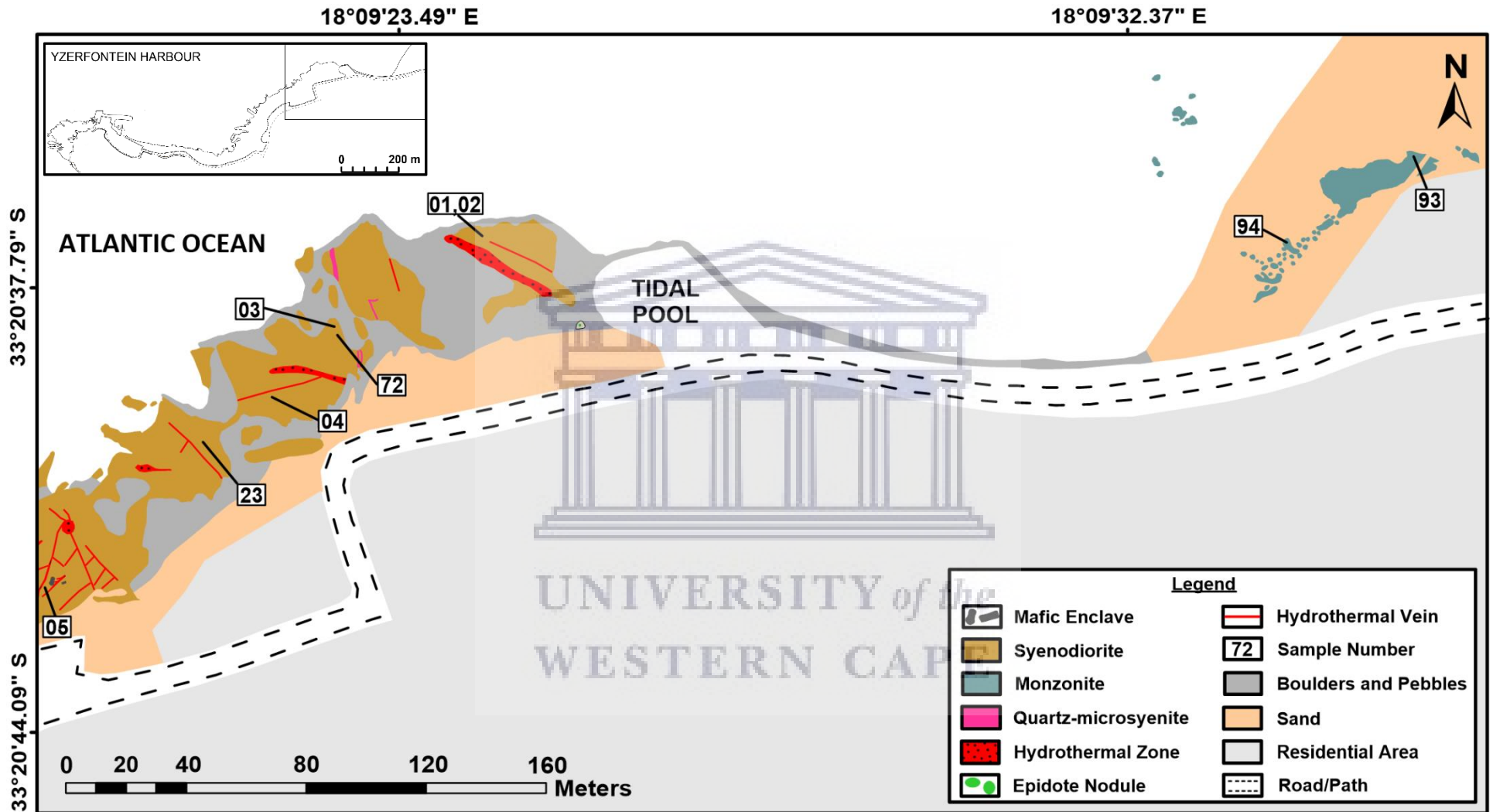


Figure A2: Geological map of the major rock types of the Yzerfontein Pluton occurring NE of the Visitors Center (after Jordaan, 1990).

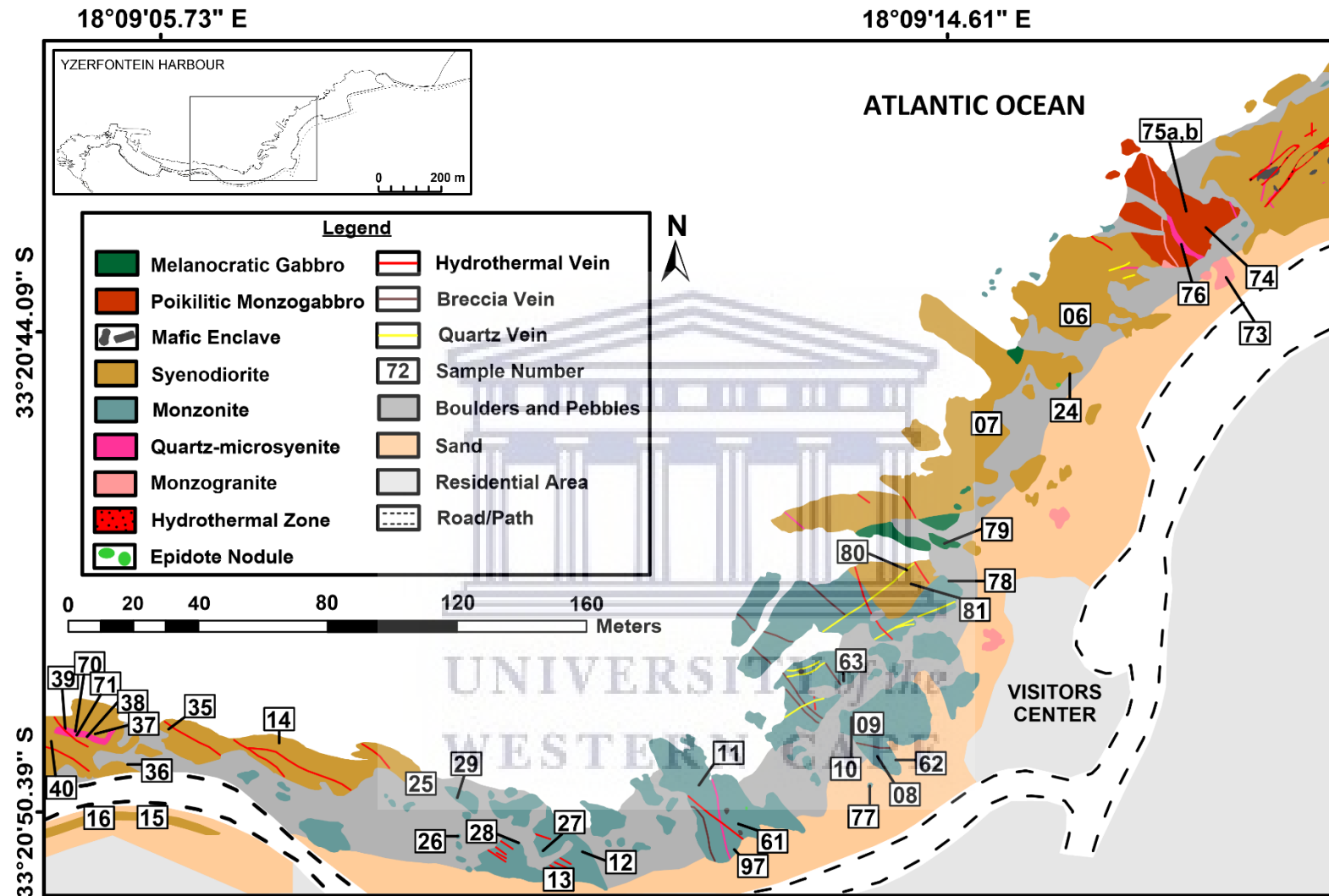


Figure A3: Geological map of the major rock types of the Yzerfontein Pluton occurring north, west and SW of the Visitors Center (after Jordaan, 1990).

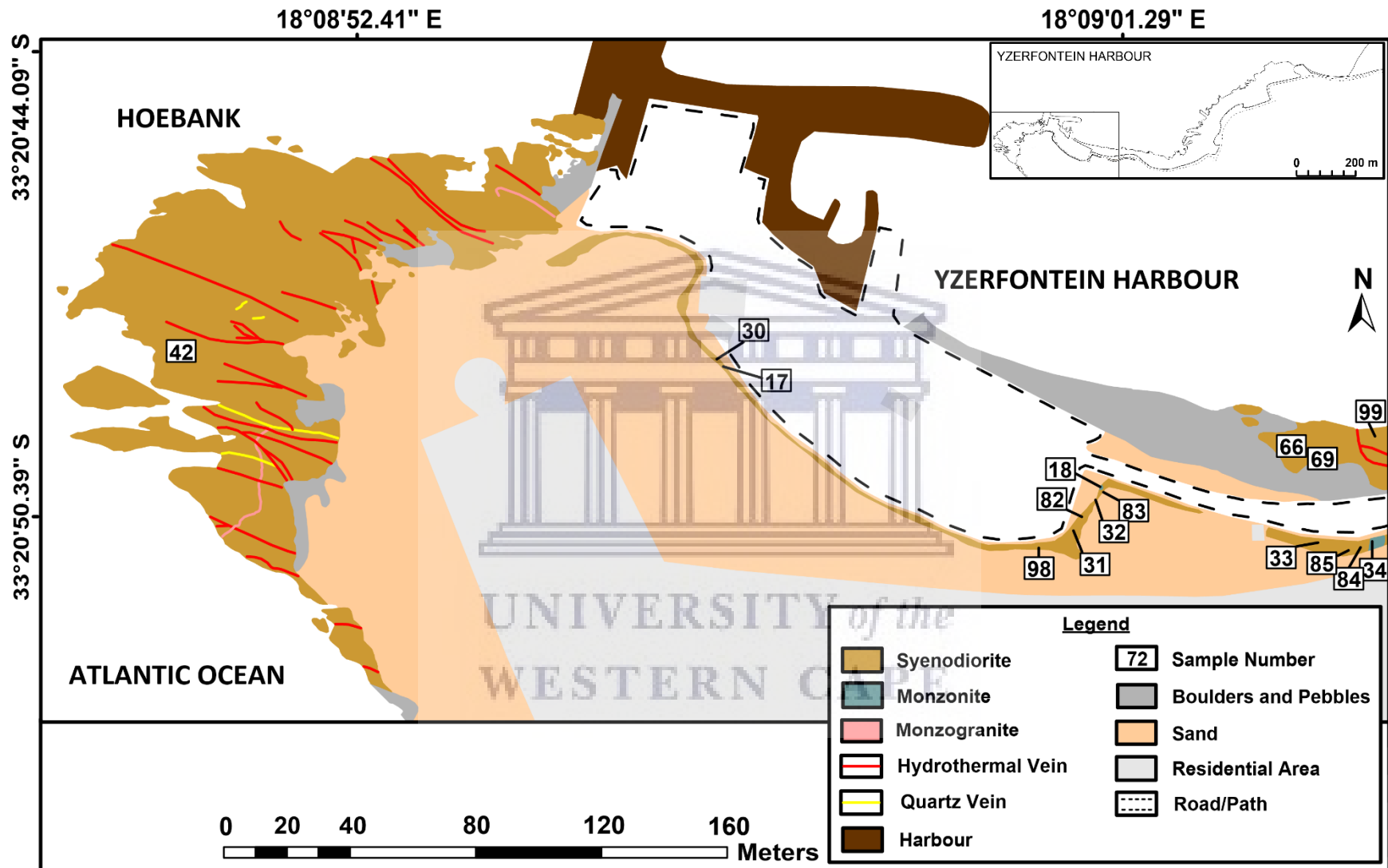


Figure A4: Geological map of the major rock types of the Yzerfontein Pluton occurring at the Yzerfontein Harbour and Hoëbank (after Jordaan, 1990).

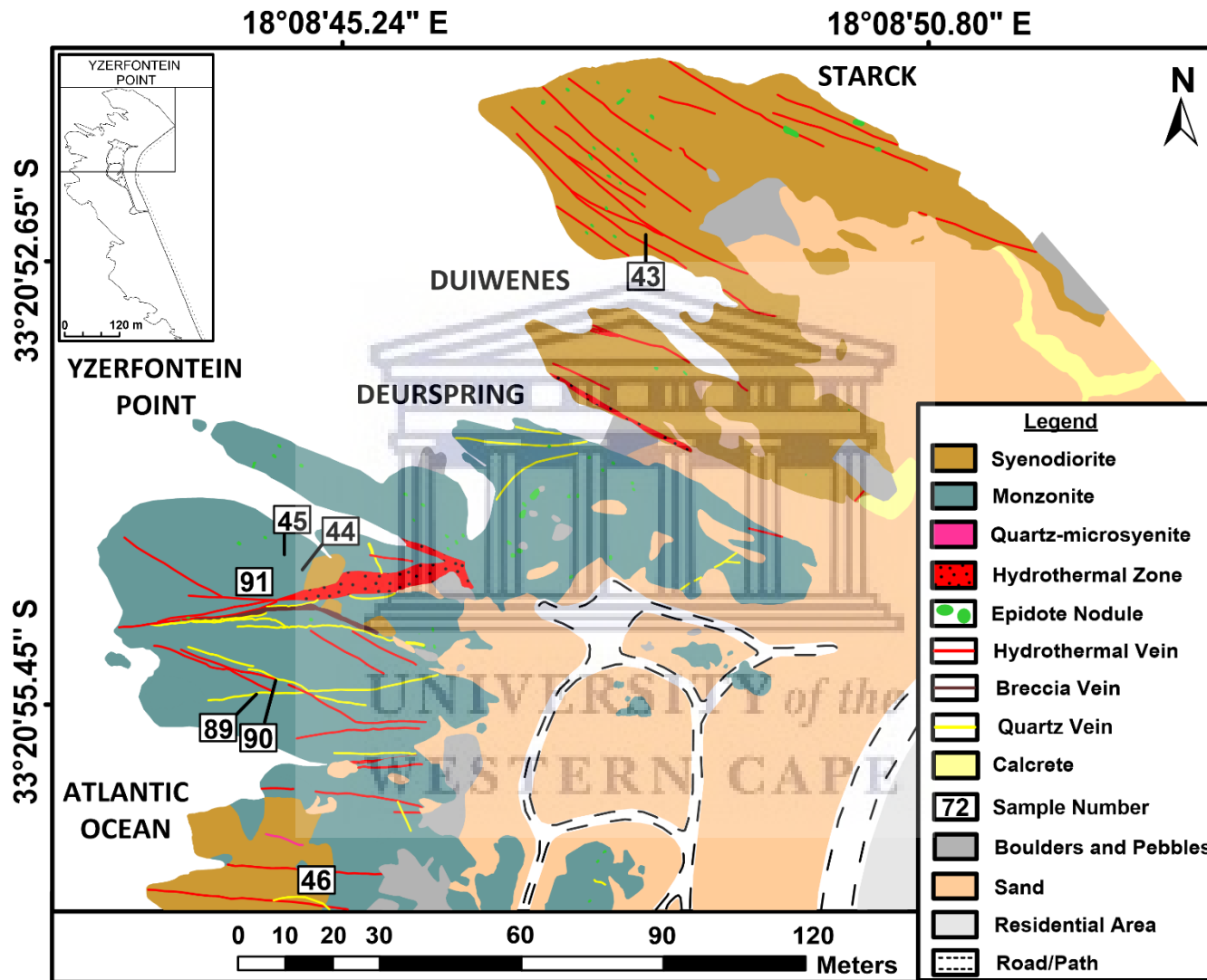


Figure A5: Geological map of the major rock types of the Yzerfontein Pluton occurring at Starck, Duiwenes, Deurspring and Yzerfontein Point (after Jordaan, 1990).

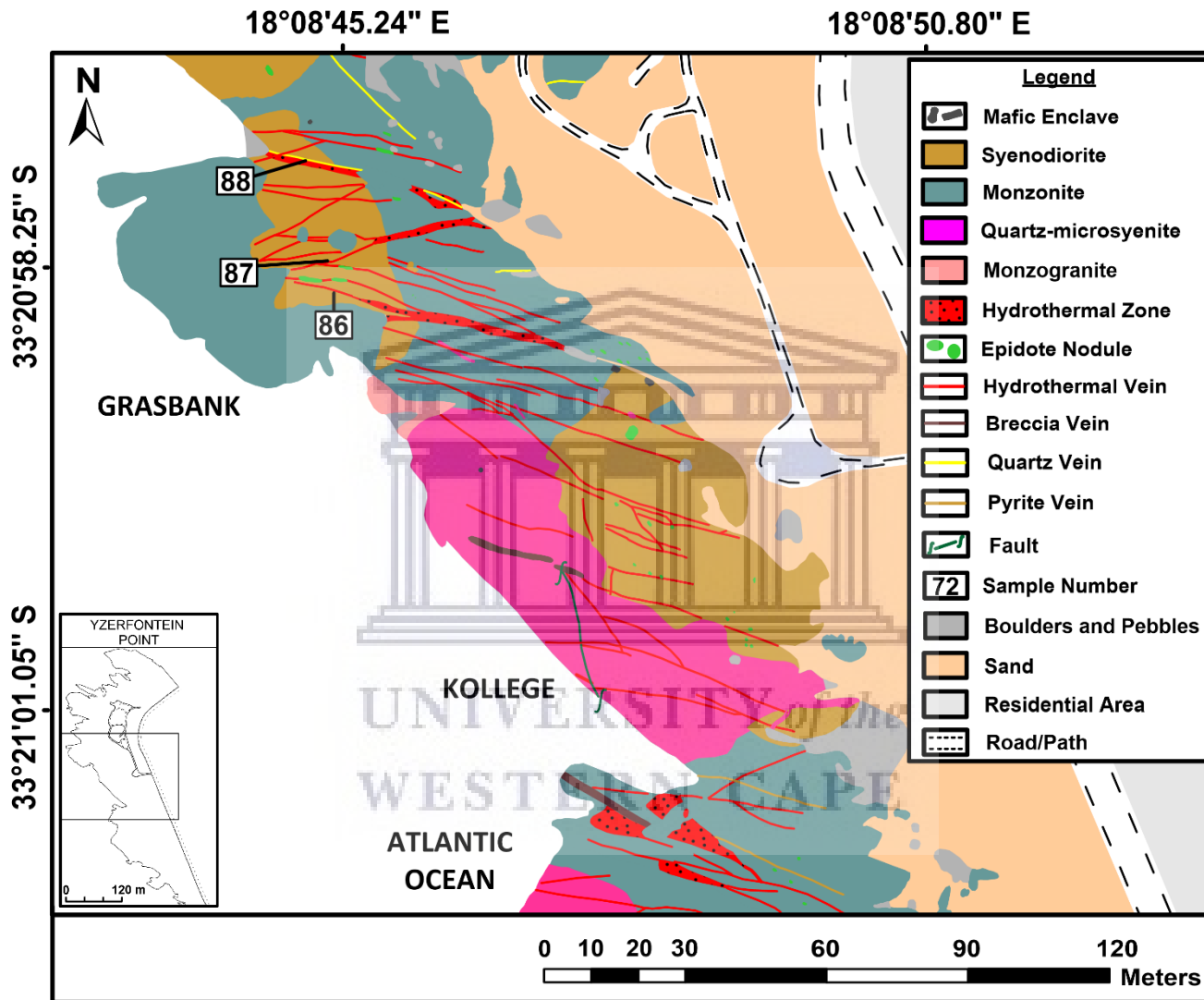


Figure A6: Geological map of the major rock types of the Yzerfontein Pluton occurring at Grasbank and Kollege (after Jordaan, 1990).

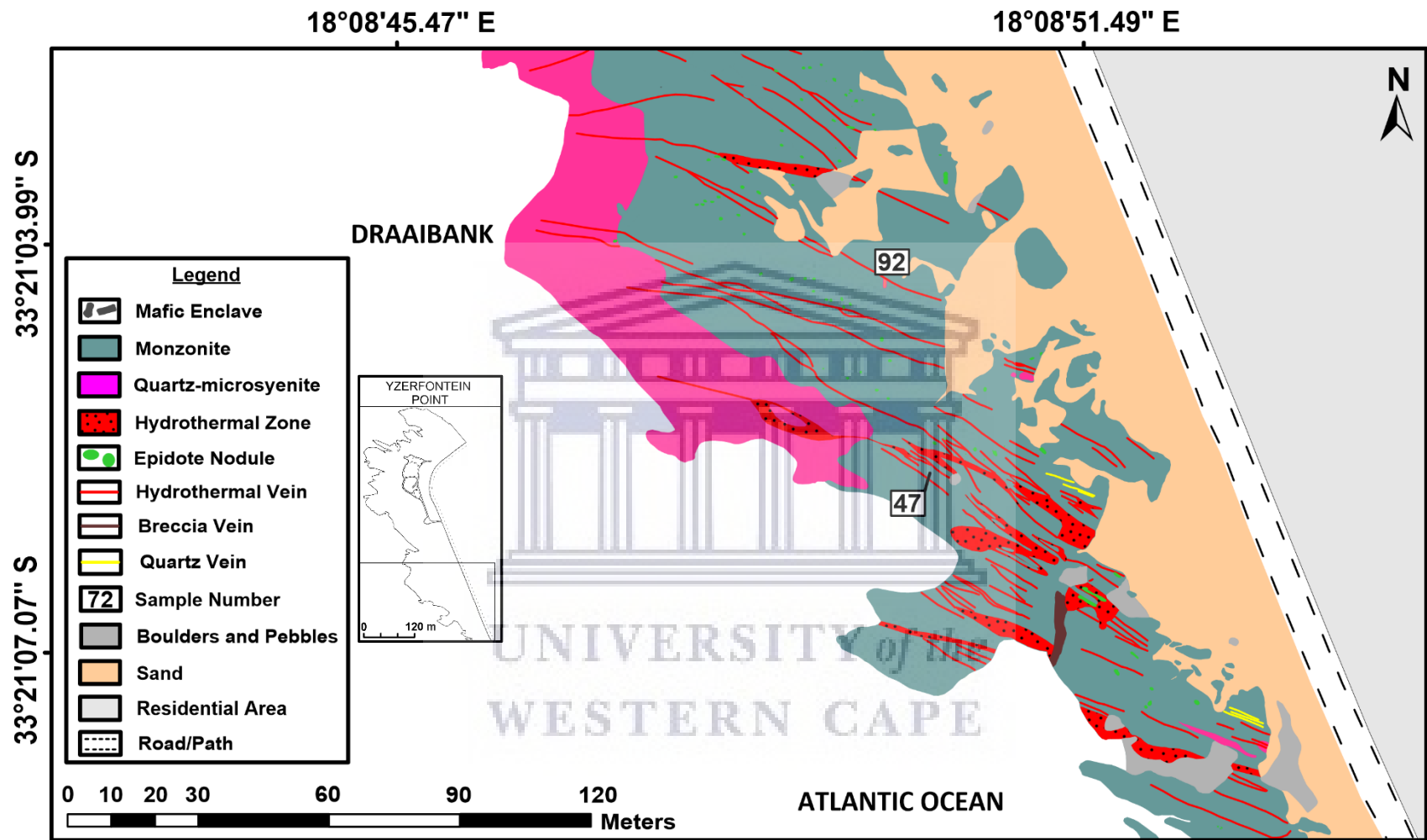


Figure A7: Geological map of the major rock types of the Yzerfontein Pluton occurring at Draaibank (after Jordaan, 1990).

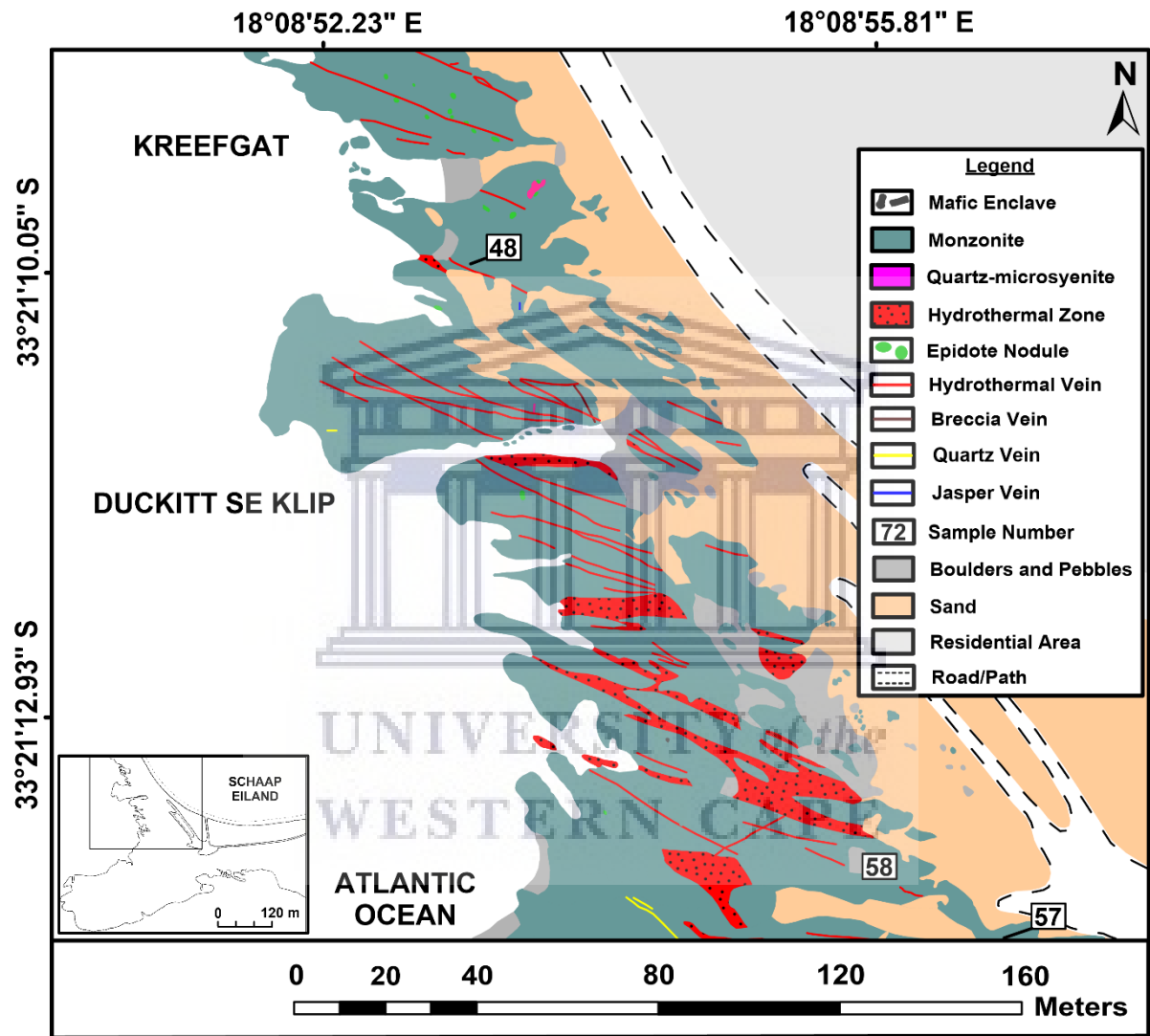


Figure A8: Geological map of the major rock types of the Yzerfontein Pluton occurring at Kreefgat and Duckitt se Klip (after Jordaan, 1990).

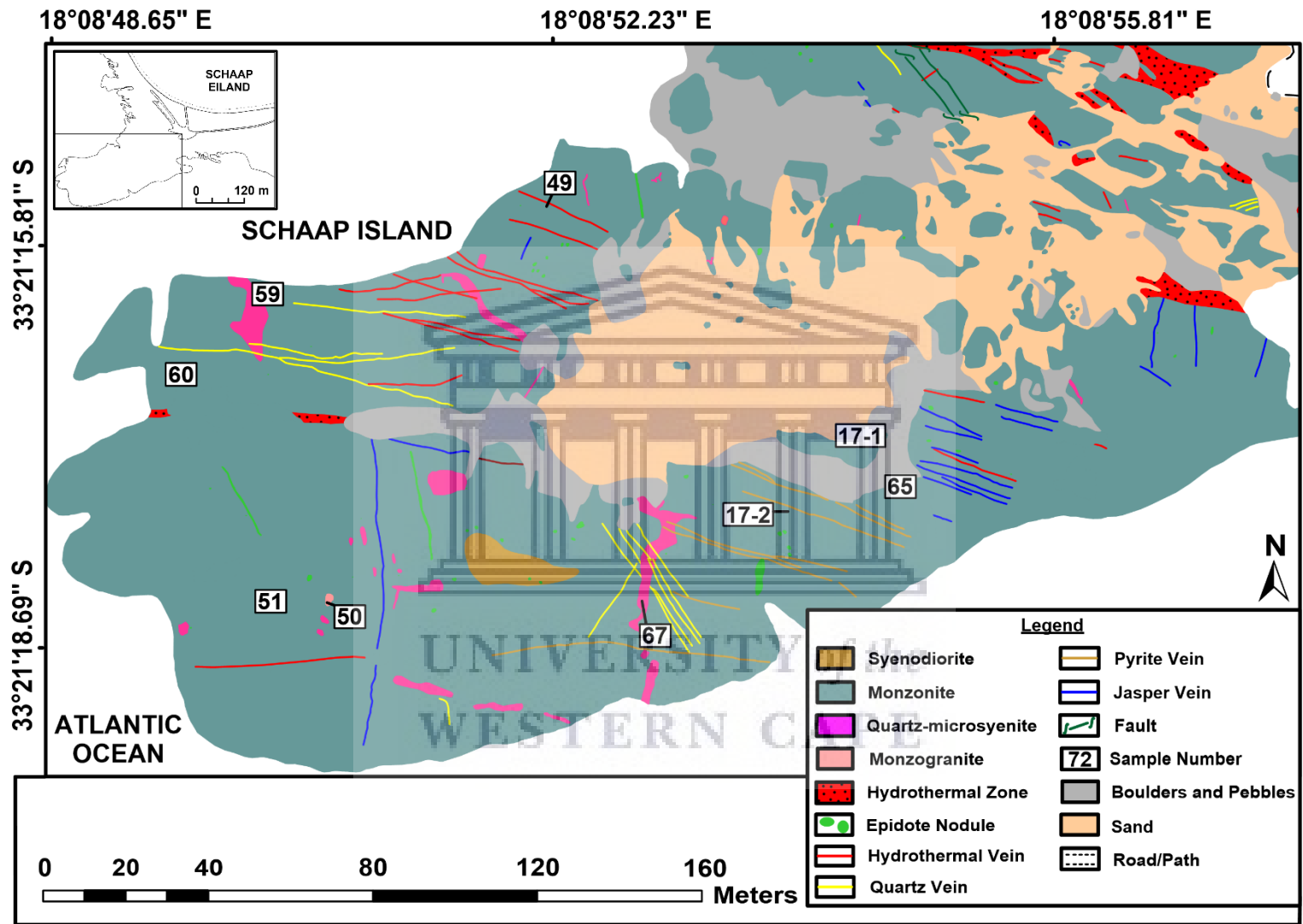


Figure A9: Geological map of the major rock types of the Yzerfontein Pluton occurring at Schaap Eiland (after Jordaan, 1990).

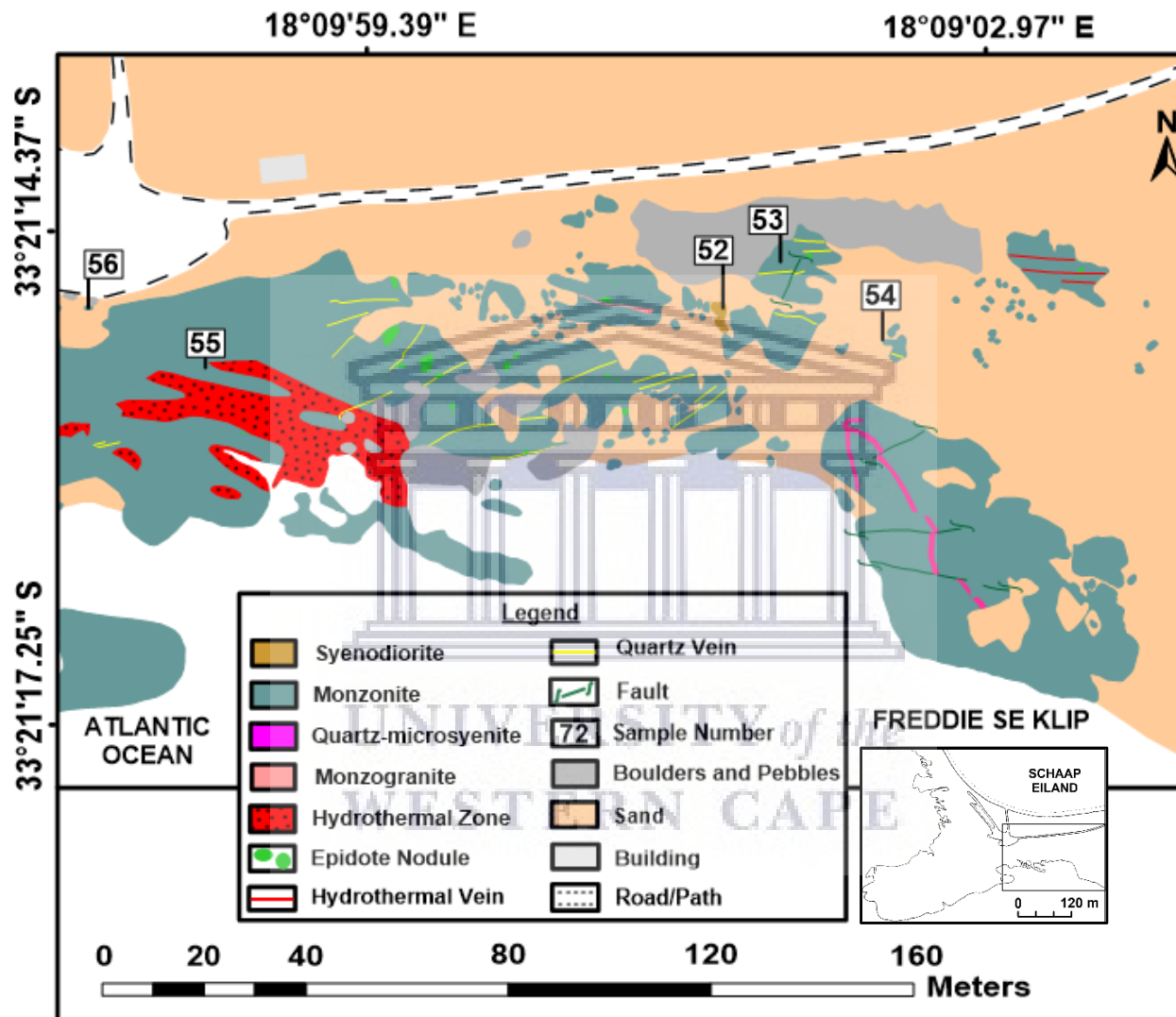


Figure A10: Geological map of the major rock types of the Yzerfontein Pluton occurring at Freddie se Klip (after Jordaan, 1990).

Sample Locations

Table A1: GPS location of samples (rock and vein types) collected in the study area and the type of analyses performed on selected samples.

Sample ID	GPS Location	Rock type/vein type	Type of analyses
YZN01	33°20'38.17"S; 18° 9'24.49"E	Syenodiorite	Petrography, Geochemistry
YZN02	33°20'38.18"S; 18° 9'24.46"E	Syenodiorite	Petrography, Geochemistry
YZN03	33°20'39.38"S; 18° 9'22.66"E	Syenodiorite	Petrography, Geochemistry
YZN04	33°20'40.27"S; 18° 9'21.72"E	Syenodiorite	Petrography, Geochemistry
YZN05	33°20'42.39"S; 18° 9'19.19"E	Syenodiorite	Geochemistry
YZN06	33°20'44.30"S; 18° 9'16.24"E	Syenodiorite	Geochemistry
YZN07	33°20'45.50"S; 18° 9'15.17"E	Syenodiorite	Petrography, Geochemistry
YZN08	33°20'49.12"S; 18° 9'13.74"E	Monzonite	
YZN09	33°20'48.77"S; 18° 9'13.65"E	Syenite	Petrography, Geochemistry
YZN10	33°20'48.71"S; 18° 9'13.48"E	Monzonite	Petrography, Geochemistry
YZN11	33°20'49.87"S; 18° 9'11.92"E	Monzonite	Petrography, Geochemistry
YZN12	33°20'50.59"S; 18° 9'10.38"E	Monzonite	Petrography, Geochemistry
YZN13	33°20'50.87"S; 18° 9'10.11"E	Monzonite	Petrography, Geochemistry
YZN14	33°20'49.65"S; 18° 9'06.82"E	Syenodiorite	Petrography, Geochemistry
YZN15	33°20'50.43"S; 18° 9'05.52"E	Syenodiorite	Petrography, Geochemistry
YZN16	33°20'50.34"S; 18° 9'04.52"E	Syenodiorite	Petrography, Geochemistry
YZN17	33°20'49.09"S; 18° 8'56.40"E	Syenodiorite	Petrography, Geochemistry
YZN18	33°20'50.28"S; 18° 9'00.61"E	Monzonite	Petrography, Geochemistry
YZN17-1	33°21'16.68"S; 18° 8'54.84"E	Jasper-dominated vein	Petrography
YZN17-2	33°21'17.22"S; 18° 8'54.00"E	Quartz-dominated vein Epidote-dominated vein	Petrography
YZN20	33°20'12.10"S; 18° 9'37.30"E	Melanocratic Gabbro	Petrography, Geochemistry
YZN21	33°20'12.40"S; 18° 9'37.00"E	Leucocratic Gabbro	Petrography, Geochemistry
YZN22	33°20'13.40"S; 18° 9'36.70"E	Leucocratic Gabbro	Geochemistry
YZN23	33°20'40.80"S; 18° 9'21.20"E	Syenodiorite	Petrography, Geochemistry
YZN24	33°20'45.00"S; 18° 9'16.20"E	Syenodiorite	Petrography, Geochemistry
YZN25	33°20'50.00"S; 18° 9'08.70"E	Epidote-dominated vein	Petrography
YZN26	33°20'50.40"S; 18° 9'09.20"E	Monzonite	

Table A1 (continued)

Sample ID	GPS Location	Rock type/vein type	Type of analyses
YZN27	33°20'50.60"S; 18° 9'09.90"E	Quartz-dominated vein	Petrography
YZN28	33°20'50.50"S; 18° 9'09.70"E	Monzonite	
YZN29	33°20'50.20"S; 18° 9'09.20"E	Monzonite	Geochemistry
YZN30	33°20'49.00"S; 18° 8'56.40"E	Syenodiorite Epidote-dominated vein	Petrography, Geochemistry
YZN31	33°20'50.60"S; 18° 9'00.40"E	Syenodiorite	Petrography, Geochemistry
YZN32	33°20'50.40"S; 18° 9'00.60"E	Syenodiorite	Petrography, Geochemistry
YZN33	33°20'50.60"S; 18° 9'03.00"E	Syenodiorite	
YZN34	33°20'50.70"S; 18° 9'03.50"E	Monzonite Quartz-dominated vein	Petrography, Geochemistry
YZN35	33°20'49.50"S; 18° 9'05.70"E	Syenodiorite	
YZN36	33°20'49.70"S; 18° 9'05.20"E	Epidote-dominated vein	Petrography
YZN37	33°20'49.50"S; 18° 9'04.70"E	Syenodiorite	
YZN38	33°20'49.50"S; 18° 9'04.60"E	Quartz-microsyenite Epidote-dominated vein	Petrography, Geochemistry
YZN39	33°20'49.40"S; 18° 9'04.40"E	Quartz-microsyenite	Petrography, Geochemistry
YZN40	33°20'49.60"S; 18° 9'04.20"E	Syenodiorite	Petrography, Geochemistry
YZN42	33°20'48.80"S; 18° 8'49.60"E	Syenite	Petrography, Geochemistry
YZN43	33°20'52.50"S; 18° 8'48.80"E	Syenodiorite	Petrography, Geochemistry
YZN44	33°20'54.70"S; 18° 8'45.60"E	Barren quartz vein	Petrography, Stable Isotopes, Fluid Inclusions
YZN45	33°20'54.60"S; 18° 8'45.50"E	Jasper-dominated vein	Stable Isotopes
YZN46	33°20'56.60"S; 18° 8'45.60"E	Syenite	Petrography, Geochemistry
YZN47	33°21'06.20"S; 18° 8'50.30"E	Monzonite	
YZN48	33°21'09.70"S; 18° 8'52.60"E	Monzonite	Geochemistry
YZN49	33°21'15.70"S; 18° 8'52.00"E	Monzonite	
YZN50	33°21'17.60"S; 18° 8'50.40"E	Monzogranite Epidote-dominated vein	Petrography, Geochemistry
YZN51	33°21'17.60"S; 18° 8'49.90"E	Monzonite	Petrography, Geochemistry
YZN52	33°21'14.90"S; 18° 9'01.80"E	Syenodiorite	Petrography, Geochemistry
YZN53	33°21'14.69"S; 18° 9'02.21"E	Monzonite	
YZN54	33°21'15.15"S; 18°09'02.77"E	Monzonite	Fluid Inclusions
YZN55	33°21'15.20"S; 18° 8'58.90"E	Monzonite	

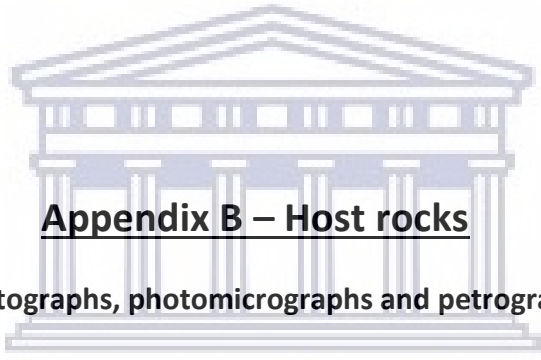
Table A1 (continued)

Sample ID	GPS Location	Rock type/vein type	Type of analyses
YZN56	33°21'15.10"S; 18° 8'58.00"E	Monzonite	
YZN57	33°21'14.60"S; 18° 8'56.00"E	Monzonite	
YZN58	33°21'14.14"S; 18° 8'54.86"E	Monzonite	
YZN59	33°21'15.97"S; 18° 8'49.87"E	Jasper-dominated vein	Petrography
YZN60	33°21'16.39"S; 18° 8'49.24"E	Quartz-dominated vein	Petrography, Stable Isotopes, Fluid Inclusions
YZN61	33°20'50.25"S; 18° 9'12.41"E	Quartz-dominated vein	Petrography, Stable Isotopes
YZN62	33°20'49.16"S; 18° 9'13.96"E	Tourmalinite breccia	Petrography, Stable Isotopes
YZN63	33°20'48.36"S; 18° 9'13.45"E	Tourmaline-dominated vein	Stable Isotopes
YZN65	33°21'16.95"S; 18° 8'55.13"E	Monzonite	
YZN66	33°20'49.57"S; 18° 9'02.64"E	Syenodiorite	Petrography
YZN67	33°21'17.57"S; 18° 8'52.86"E	Quartz-microsyenite	Petrography
YZN69	33°20'49.71"S; 18° 9'03.09"E	Epidote-dominated vein	Petrography
YZN70	33°20'49.47"S; 18° 9'04.49"E	Quartz-microsyenite	Petrography, Geochemistry
YZN71	33°20'49.51"S; 18° 9'04.50"E	Quartz-microsyenite	Petrography, Geochemistry
YZN72	33°20'39.54"S; 18° 9'22.76"E	Syenodiorite	
YZN73	33°20'43.72"S; 18° 9'18.11"E	Monzogranite	Petrography, Geochemistry
YZN74	33°20'43.21"S; 18° 9'17.65"E	Poikilitic Monzogabbro	
YZN75a	33°20'43.04"S; 18° 9'17.36"E	Poikilitic Monzogabbro	Petrography, Geochemistry
YZN75b	33°20'43.04"S; 18° 9'17.36"E	Poikilitic Monzogabbro	Geochemistry
YZN76	33°20'43.36"S; 18° 9'17.41"E	Quartz-microsyenite	Petrography, Geochemistry
YZN77	33°20'49.49"S; 18° 9'13.73"E	Tourmalinite breccia	
YZN78	33°20'47.44"S; 18° 9'14.81"E	Brecciated qz-tur-jsp	Petrography
YZN79	33°20'47.09"S; 18° 9'14.78"E	Melanocratic Gabbro	Geochemistry
YZN80	33°20'47.31"S; 18° 9'14.25"E	Barren quartz vein	
YZN81	33°20'47.45"S; 18° 9'14.30"E	Epidote-dominated vein	Petrography
YZN82	33°20'50.52"S; 18° 9'00.49"E	Epidote-dominated vein	Stable Isotopes, Fluid Inclusions
YZN83	33°20'50.32"S; 18° 9'00.67"E	Epidote-dominated vein	Petrography
YZN84	33°20'50.81"S; 18° 9'03.41"E	Epidote-dominated vein	
YZN85	33°20'50.87"S; 18° 9'03.32"E	Tourmaline-dominated vein	

Table A1 (continued)

Sample ID	GPS Location	Rock type/vein type	Type of analyses
YZN86	33°20'58.67"S; 18° 8'45.58"E	Jasper-dominated vein	Fluid Inclusions
YZN87	33°20'58.40"S; 18° 8'45.55"E	Jasper-dominated vein	
YZN88	33°20'57.55"S; 18° 8'45.44"E	Jasper-dominated vein	
YZN89	33°20'55.33"S; 18° 8'45.20"E	Jasper-dominated vein	
YZN90	33°20'55.29"S; 18° 8'45.33"E	Quartz-dominated vein	Fluid Inclusions
YZN91	33°20'54.76"S; 18° 8'45.22"E	Quartz-dominated vein	
YZN92	33°21'04.64"S; 18° 8'50.10"E	Monzonite	Geochemistry
YZN93	33°20'36.74"S; 18° 9'35.69"E	Monzonite	Petrography, Geochemistry
YZN94	33°20'38.02"S; 18° 9'34.05"E	Monzonite	Petrography
YZN95	33°20'12.08"S; 18° 9'36.94"E	Melanocratic Gabbro	Petrography, Geochemistry
YZN96	33°20'11.67"S; 18° 9'39.18"E	Leucocratic Gabbro	Petrography, Geochemistry
YZN97	33°20'50.51"S; 18° 9'12.36"E	Epidote-dominated vein	
YZN98	33°20'50.68"S; 18° 8'59.91"E	Calcite-dominated vein	Stable Isotopes
YZN99	33°20'49.49"S; 18° 9'04.03"E	Tourmaline-dominated vein	

Abbreviations: Jsp = Jasper, Qz = Quartz, Tur = Tourmaline (after Whitney and Evans, 2010).

The logo of the University of the Western Cape, featuring a classical building with a pediment and columns.

Appendix B – Host rocks

Additional field photographs, photomicrographs and petrographic descriptions

UNIVERSITY *of the*
WESTERN CAPE

Additional field photographs

Melanocratic Gabbro



Figure B1: Outcrop of melanocratic gabbro hosting a mafic enclave at Gabbro Point. Scale: Hammer with length = 33 cm.

Poikilitic Monzogabbro and Monzogranite

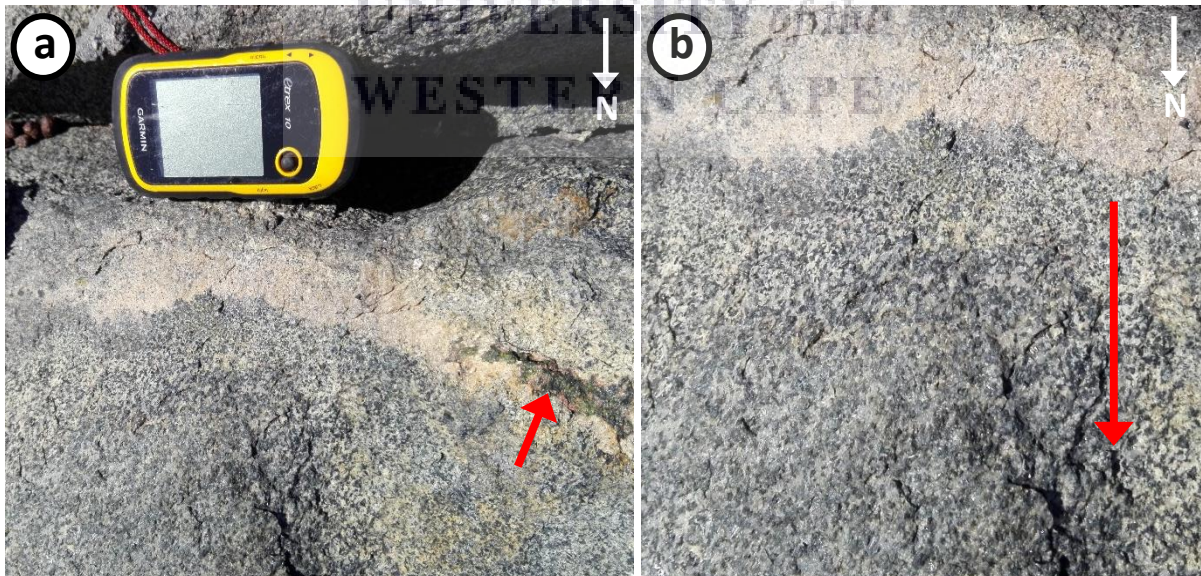


Figure B2: Monzogranite dyke cross-cutting the poikilitic monzogabbro. (a) Monzogranite dyke associated with patches of minerals including tourmaline, epidote and chlorite (indicated by the red arrow). (b) An enlargement of a section in (a) showing a gradual increase in grain size in the poikilitic monzogabbro. The red arrow denotes the direction in which the grain size increases; size of dyke: length = 0.35 – 0.40 m and width = 2.5 – 6.0 cm. Scale: GPS with length = 10 cm and width = 5.2 cm.

Poikilitic Monzogabbro



Figure B3: A portion of the poikilitic monzogabbro outcrop showing the presence of various compositional phases over a short distance of 1.5 m (measured in a NW-SE direction). Scale: GPS with length = 10 cm and width = 5.2 cm.

Syenodiorite



Figure B4: Outcrop of syenodiorite north of the Visitors Center hosting a large zone of micromonzogabbro enclaves. Note the plagioclase-rich rims on the outer margins of the enclaves. Scale: GPS with length = 10 cm and width = 5.2 cm.

Syenodiorite and Monzogranite



Figure B5: Portion of a monzogranite dyke cross-cutting the syenodiorite at Hoëbank. Locally, the dyke contains large K-feldspar phenocrysts as well as tourmaline nodules (0.1 – 0.5 cm in size) with jaspilitic haloes (0.1 – 0.2 cm in thickness); size of dyke: length = 2.5 – 3.0 m and width = 3.5 – 4.0 cm. Scale: Thumb with width = 1.5 cm.

UNIVERSITY of the
WESTERN CAPE

Additional photomicrographs

Leucocratic Gabbro

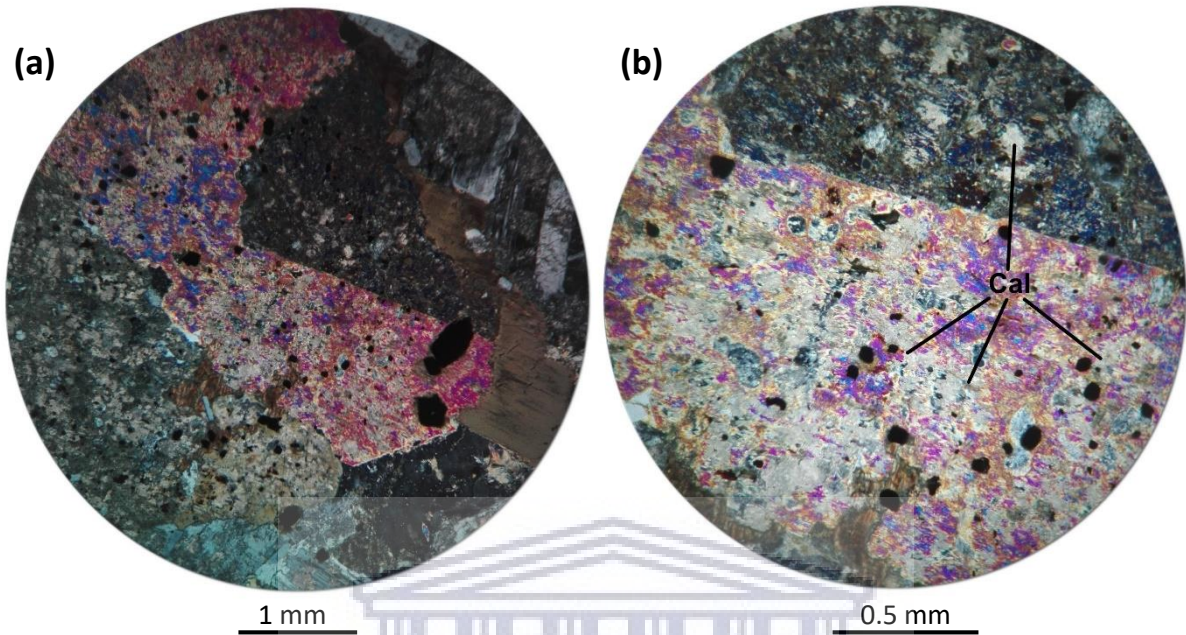


Figure B6: Thin section photomicrographs of the leucocratic gabbro in XPL showing (a) large secondary hornblende grains associated with secondary calcite at YZN21. (b) An enlargement of (a) exemplifying the presence or formation of calcite in epidote. Cal = Calcite.

Melanocratic Gabbro

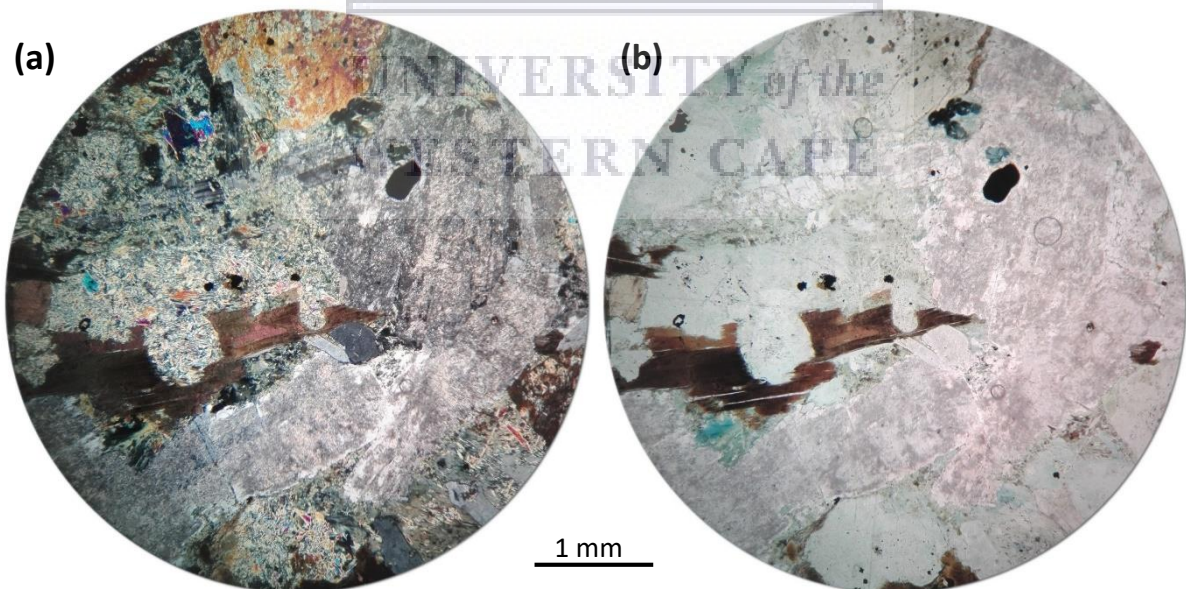
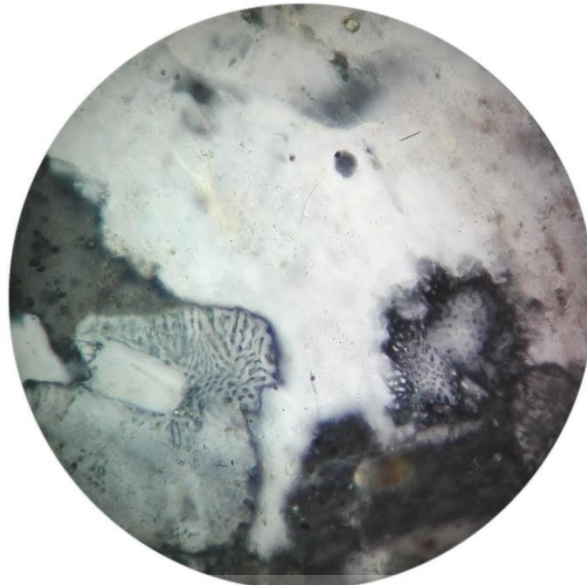


Figure B7: Thin section photomicrographs of the melanocratic gabbro in (a) XPL and (b) PPL illustrating the formation of embayments in biotite as adjacent aggregates of actinolite overgrows the biotite in YZN95.

Weakly altered syenodiorite



0.25 mm

Figure B8: Thin section photomicrograph of the syenodiorite in XPL illustrating the formation of a microgranophyric texture as a result of the intergrowth between quartz and orthoclase in YZN23.

Weakly altered syenodiorite

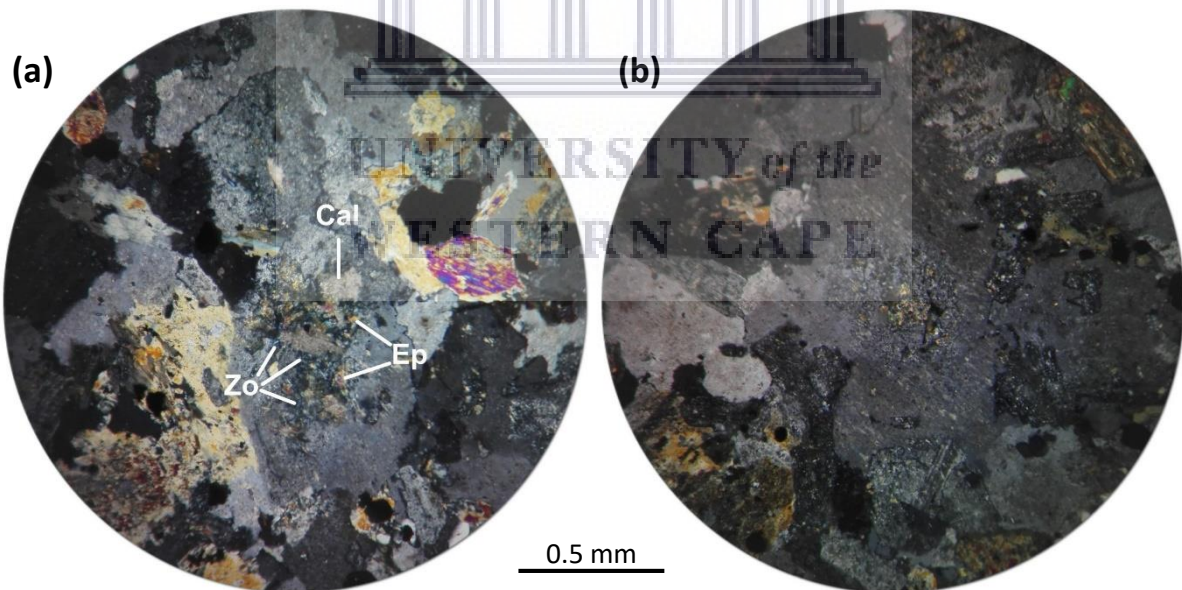


Figure B9: (a) and (b) Thin section photomicrographs of the syenodiorite in XPL showing the formation of secondary epidote, calcite and zoisite (saussurite) at the centre of orthoclase grains at YZN30. Cal = Calcite, Ep = Epidote, Zo = Zoisite.

Monzonite

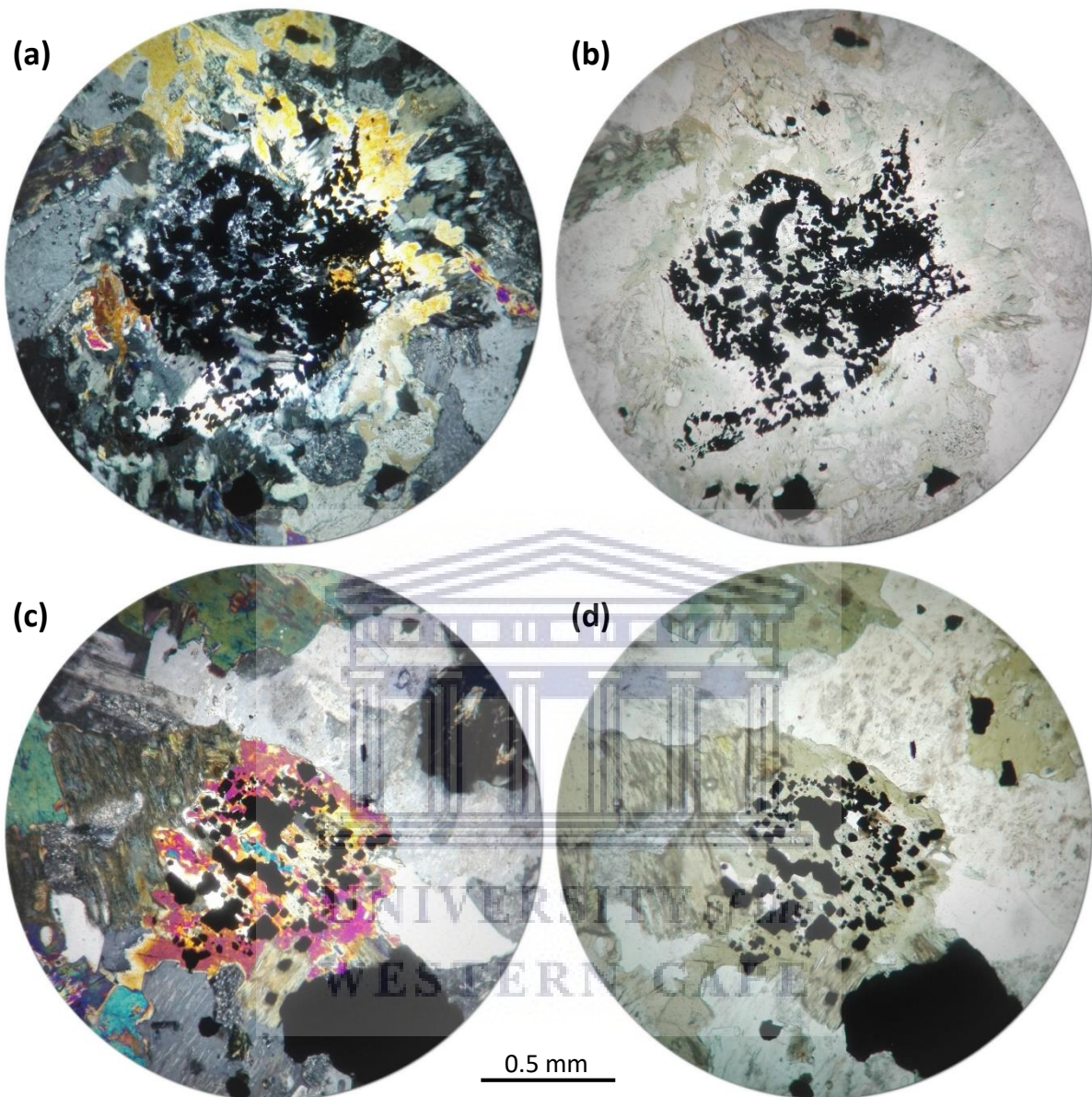


Figure B10: Thin section photomicrographs of the monzonite in PPL and XPL showing the accumulation of clumps of magnetite at the centre of partly altered augite grains in (a) and (b) YZN93 and (c) and (d) YZN94.

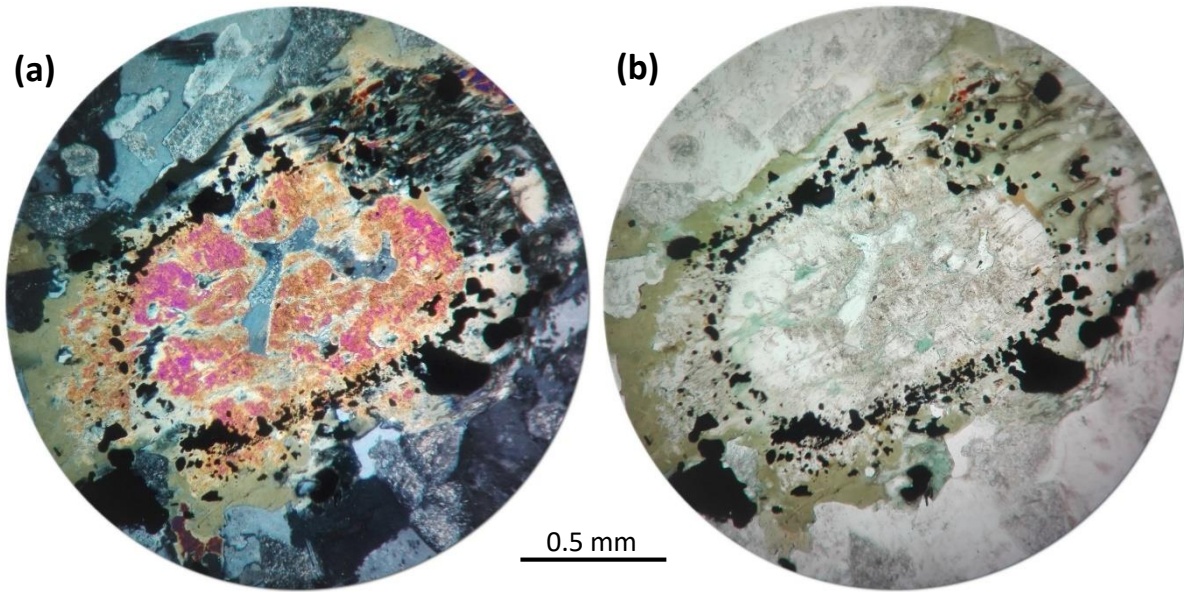


Figure B11: Thin section photomicrographs of the monzonite in (a) XPL and (b) PPL showing accumulations of tiny magnetite grains mimicking the shape of a partly altered augite grain at the boundary between the reaction rim of hornblende and the unaltered core of augite at YZN93.



Petrographic descriptions

Mafic rocks

Leucocratic Gabbro

Table B1: Summary of petrographic observations for the samples of leucocratic gabbro.

Rock type	Leucocratic Gabbro
Sample(s)	YZN21, YZN96
Mineralogy and modal abundance	Ser (~36%), Pl (~24%), Tr-Act (~20%), Bt (~7%), Hbl (~6%), Opaque minerals (~3%), Aug (~2%), Cal (~1%), Ap (<1%), Chl (<1%)
Grain size	Ser (<1.0 mm), Pl (0.1 – 5.5 mm), Tr-Act (<1.0 – 5.0 mm), Bt (0.1 – 5.0 mm), Hbl (1.0 – 1.7 mm), Opaque minerals (<1.0 – 1.0 mm), Aug (1.0 – 2.5 mm), Cal (<0.1 mm), Ap (<1.0 – 0.6 mm), Chl (<1.0 mm)
Texture(s)	Pl: lamellar-, carlsbad-, and complex twinning Tr-Act: acicular texture Bt: poikilitic texture
Alteration	Moderate sericitization and uralitization, incipient chloritization

Abbreviations: Ap = Apatite, Aug = Augite, Bt = Biotite, Cal = Calcite, Chl = Chlorite, Hbl = Hornblende, Pl = Plagioclase, Ser = Sericite, Tr-Act = Tremolite-Actinolite. Mineral abbreviations adapted from Whitney and Evans (2010).

Melanocratic Gabbro

Table B2: Summary of petrographic observations for the samples of melanocratic gabbro.

Rock type	Melanocratic Gabbro
Sample(s)	YZN20, YZN95
Mineralogy and modal abundance	YZN20 – Tr-Act (~20%), Ser (~18%), Hbl (~15%), Aug (~15%), Pl (~10%), Opx (~9%), Bt (~6%), Chl (~3%), Opaque minerals (~2%), Cal (~1%), Ap (<1%), Ep (<1%) YZN95 – Tr-Act (~27%), Ser (~24%), Hbl (~20%), Pl (~16%), Bt (~6%), Chl (~3%), Opaque minerals (~2%), Cal (~1%), Ap (<1%), Ep (<1%)
Grain size	Tr-Act (<0.1 – 4.0 mm), Ser (<0.1 mm), Hbl (1.0 – 4.2 mm), Aug (0.1 – 8.0 mm), Pl (1.5 – 7.0 mm), Opx (1.0 – 2.0 mm), Bt (0.1 – 3.5 mm), Chl (<0.1 – 2.0 mm), Opaque minerals (0.1 – 1.0 mm), Cal (0.1 – 0.6 mm), Ap (0.1 – 1.0 mm), Ep (<1.0 mm)
Texture(s)	Tr-Act: acicular texture Hbl: simple twinning Pl: lamellar and complex twinning Bt: embayed
Alteration	Moderate to strong uralitization, moderate sericitization, weak chloritization, incipient epidotization

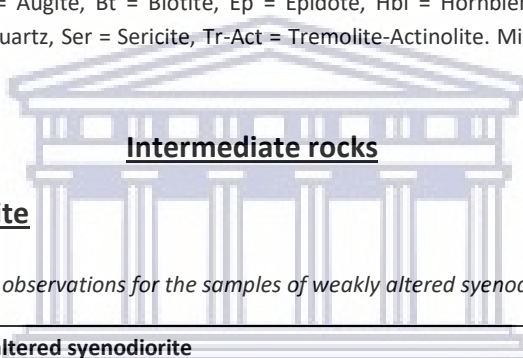
Abbreviations: Ap = Apatite, Aug = Augite, Bt = Biotite, Cal = Calcite, Chl = Chlorite, Ep = Epidote, Hbl = Hornblende, Opx = Orthopyroxene, Pl = Plagioclase, Ser = Sericite, Tr-Act = Tremolite-Actinolite. Mineral abbreviations adapted from Whitney and Evans (2010).

Poikilitic Monzogabbro

Table B3: Summary of petrographic observations for the samples of poikilitic monzogabbro.

Rock type	Poikilitic monzogabbro
Sample(s)	YZN75a
Mineralogy and modal abundance	Pl (~25%), Or (~16%), Ser (~15%), Opx (~13%), Tr-Act (~10%), Aug (~8%), Bt (~6%), Hbl (~4%), Opaque minerals (~3%), Qz (<1%), Ap (<1%), Ep (<1%)
Grain size	Pl (0.1 – 2.2 mm), Or (0.2 – 3.5 mm), Ser (<0.1 mm), Opx (0.5 – 2.0 mm), Tr-Act (<0.1 – 2.0 mm), Aug (0.5 – 2.0 mm), Bt (0.1 – 2.0 mm), Hbl (0.5 – 1.6 mm), Opaque minerals (<0.1 – 0.8 mm), Qz (0.1 – 0.5 mm), Ap (0.1 – 0.2 mm), Ep (<0.1 – 0.1 mm)
Texture(s)	Pl: lamellar-, tapered- and multiple twinning Or: poikilitic texture; microperthitic texture Opx: simple twinning Aug: simple twinning Tr-Act: mesh texture; acicular texture Bt: poikilitic texture; embayed
Alteration	Weak to moderate sericitization and uralitization, incipient epidotization

Abbreviations: Ap = Apatite, Aug = Augite, Bt = Biotite, Ep = Epidote, Hbl = Hornblende, Opx = Orthopyroxene, Or = Orthoclase, Pl = Plagioclase, Qz = Quartz, Ser = Sericite, Tr-Act = Tremolite-Actinolite. Mineral abbreviations adapted from Whitney and Evans (2010).



Intermediate rocks

Weakly altered Syenodiorite

Table B4: Summary of petrographic observations for the samples of weakly altered syenodiorite.

Rock type	Weakly altered syenodiorite
Sample(s)	YZN01, YZN02, YZN03, YZN04, YZN07, YZN14, YZN23, YZN40, YZN52
Mineralogy and modal abundance	Or (~32%), Pl (~28%), Aug (~10 – 12%), Chl (~7 – 9%), Ser (~5%), Tr-Act (~5%), Opx (~4%), Hbl (~2%), Opaque minerals (~2%), Bt (~0 – 2%), Qz (~1%), Ap (<1%), Ep (~1%)
Grain size	Or (0.1 – 5.0 mm), Pl (<1.0 – 3.0 mm), Aug (<1.0 – 4.7 mm), Chl (<1.0 mm), Ser (<1.0 mm), Tr-Act (<0.1 – 1.5 mm), Opx (0.2 – 1.4 mm), Hbl (0.1 – 1.3 mm), Opaque minerals (<0.1 – 1.0 mm), Bt (<0.1 – 2.0 mm), Qz (<0.1 – 1.0 mm), Ap (<0.1 mm), Ep (<0.1 mm)
Texture(s)	Pl: lamellar-, tapered- and complex twinning Or: Carlsbad twinning; poikilitic texture; microperthitic texture; microgranophyric texture Aug: simple twinning; embayed Tr-Act: acicular texture Bt: poikilitic texture
Alteration	Weak sericitization, uralitization and chloritization, incipient epidotization

Abbreviations: Ap = Apatite, Aug = Augite, Bt = Biotite, Chl = Chlorite, Ep = Epidote, Hbl = Hornblende, Opx = Orthopyroxene, Or = Orthoclase, Pl = Plagioclase, Qz = Quartz, Ser = Sericite, Tr-Act = Tremolite-Actinolite. Mineral abbreviations adapted from Whitney and Evans (2010).

Moderately altered Syenodiorite

Table B5: Summary of petrographic observations for the samples of moderately altered syenodiorite.

Rock type	Moderately altered syenodiorite
Sample(s)	YZN15, YZN16, YZN17, YZN24, YZN30, YZN31, YZN32, YZN43, YZN66
Mineralogy and modal abundance	Or (~35%), Pl (~17%), Hbl (~15%), Ep (~9%), Ser (~6%), Chl (~5%), Cal (~4%), Tr-Act (~3%), Qz (~3%), Opaque minerals (~2%), Ap (<1%), Zo (<1%)
Grain size	Or (0.1 – 3.2 mm), Pl (0.1 – 1.6 mm), Hbl (0.1 – 1.9 mm), Ep (0.1 – 0.3 mm), Ser (<0.1 mm), Chl (0.1 – 2.8 mm), Cal (<0.1 – 0.2 mm), Tr-Act (<0.1 mm), Qz (0.5 – 1.0 mm), Opaque minerals (<0.1 – 0.6 mm), Ap (0. – 5.0 mm), Zo (<0.1 mm)
Texture(s)	Pl: lamellar twinning Or: poikilitic texture; microperthitic texture Tr-Act: acicular texture Chl: scaly texture
Alteration	Moderate uralitization, weak to moderate saussuritization, weak sericitization and chloritization

Abbreviations: Ap = Apatite, Cal = Calcite, Chl = Chlorite, Ep = Epidote, Hbl = Hornblende, Or = Orthoclase, Pl = Plagioclase, Qz = Quartz, Ser = Sericite, Tr-Act = Tremolite-Actinolite, Zo = Zoisite. Mineral abbreviations adapted from Whitney and Evans (2010).

Monzonite

Table B6: Summary of petrographic observations for the samples of monzonite.

Rock type	Monzonite
Sample(s)	YZN10, YZN11, YZN12, YZN13, YZN18, YZN34, YZN51, YZN93, YZN94
Mineralogy and modal abundance	Pl (~30%), Or (~28%), Ser (~9%), Hbl (~7%), Aug (~6%), Chl (~5%), Qz (~4%), Opx (~3%), Tr-Act (~3%), Ep (~3%), Opaque minerals (~1%), Ap (<1%), Tur (<1%), Cal (<1%)
Grain size	Pl (0.2 – 1.9 mm), Or (0.1 – 2.5 mm), Ser (<0.1 mm), Hbl (0.1 – 1.2 mm), Aug (0.2 – 3.0 mm); Chl (0.3 – 4.0 mm), Qz (0.2 – 1.0 mm), Opx (1.0 – 3.0 mm), Tr-Act (<0.1 – 0.4 mm), Ep (<0.1 – 0.2 mm), Opaque minerals (<0.1 – 1.0 mm), Ap (<0.1 – 0.1 mm), Tur (0.4 – 1.8 mm), Cal (0.2 – 0.5 mm)
Texture(s)	Pl: lamellar twinning Or: Carlsbad twinning; poikilitic texture; microperthitic texture Tr-Act: acicular texture Chl: scaly texture
Alteration	Weak sericitization, uralitization, chloritization and epidotization

Abbreviations: Ap = Apatite, Aug = Augite, Cal = Calcite, Chl = Chlorite, Ep = Epidote, Hbl = Hornblende, Opx = Orthopyroxene, Or = Orthoclase, Pl = Plagioclase, Qz = Quartz, Ser = Sericite, Tr-Act = Tremolite-Actinolite, Tur = Tourmaline. Mineral abbreviations adapted from Whitney and Evans (2010).

Syenite

Table B7: Summary of petrographic observations for the samples of syenite.

Rock type	Syenite
Sample(s)	YZN09, YZN42, YZN46
Mineralogy and modal abundance	YZN09 - Or (~55%), Ser (~10%), Aug (~9%), Pl (~8%), Chl (~5%), Opx (~4%), Qz (~3%), Hbl (~2%), Opaque minerals (~2%), Tr-Act (~1%), Ep (<1%) YZN42, YZN46 - Or (~60%) Pl (~16%), Hbl (~9%), Tr-Act (~4%), Ser (~3%), Chl (~2%), Ep (~2%), Opaque minerals (~2%), Qz (~1%), Tur (<1%), Cal (<1%)
Grain size	YZN09 - Or (0.2 – 3.0 mm), Ser (<0.1 mm), Aug (0.1 – 1.8 mm), Pl (0.2 – 0.1 mm), Chl (1.0 – 3.0 mm), Opx (0.5 – 2.0 mm), Qz (0.1 – 0.7 mm), Hbl (0.2 – 1.2 mm), Opaque minerals (<0.1 – 0.8 mm), Tr-Act (<0.1 – 0.4 mm), Ep (<0.1 – 0.2 mm) YZN42, YZN46 - Or (0.1 – 5.0 mm), Pl (0.2 – 2.3 mm), Hbl (0.1 – 2.0 mm), Tr-Act (<0.1 – 1.0 mm), Ser (<0.1 mm), Chl (0.1 – 3.0 mm), Ep (<0.1 – 0.2 mm), Opaque minerals (<0.1 – 1.0 mm, Qz (1.0 – 2.0 mm), Tur (0.1 – 1.5 mm), Cal (<0.1 – 0.2 mm)
Texture(s)	Pl: lamellar twinning Or: Carlsbad twinning; poikilitic texture Opx: simple twinning Tr-Act: acicular texture Chl: scaly texture Tur: acicular texture
Alteration	Weak sericitization, uralitization, chloritization and epidotization

Abbreviations: Aug = Augite, Cal = Calcite, Chl = Chlorite, Ep = Epidote, Hbl = Hornblende, Opx = Orthopyroxene, Or = Orthoclase, Pl = Plagioclase, Qz = Quartz, Ser = Sericite, Tr-Act = Tremolite-Actinolite, Tur = Tourmaline. Mineral abbreviations adapted from Whitney and Evans (2010).

Felsic rocks

Quartz-microsyenite

Table B8: Summary of petrographic observations for the samples of quartz-microsyenite.

Rock type	Quartz-microsyenite
Sample(s)	YZN38, YZN39, YZN67, YZN70, YZN71, YZN76
Mineralogy and modal abundance	Or (~38%), Ser (~24%), Pl (~18%), Qz (~11%), Tr-Act (~5%), Hbl (~2%), Ep (~1%), Chl (<1%), Opaque minerals (<1%), Tur (<1%), Zo (<1%)
Grain size	Or (<0.1 – 1.5 mm), Ser (<0.1 mm), Pl (0.1 – 2.0 mm), Qz (<0.1 – 1.0 mm), Tr-Act (<0.1 – 2.0 mm), Hbl (0.1 – 0.8 mm), Ep (<0.1 – 0.2 mm), Chl (0.1 – 0.8 mm), Opaque Minerals (<0.1 – 0.2 mm), Tur (0.1 – 1.2 mm), Zo (<0.1 – 1.0 mm)
Texture(s)	Pl: lamellar twinning Or: lamellar twinning Tr-Act: acicular texture; felty texture Hbl: simple twinning
Alteration	Moderate sericitization, weak uralitization, and incipient saussuritization and chloritization

Abbreviations: Chl = Chlorite, Ep = Epidote, Hbl = Hornblende, Or = Orthoclase, Pl = Plagioclase, Qz = Quartz, Ser = Sericite, Tr-Act = Tremolite-Actinolite, Tur = Tourmaline, Zo = Zoisite. Mineral abbreviations adapted from Whitney and Evans (2010).

Monzogranite

Table B9: Summary of petrographic observations for the samples of monzogranite.

Rock type	Monzogranite
Sample(s)	YZN50, YZN73
Mineralogy and modal abundance	Or (~30%), Pl (~29%), Qz (~20%), Ser (~10%), Hbl (~4%), Tr-Act (~3%), Ep (~2%), Chl (~1%), Opaque minerals (<1%), Tur (<1%), Zo (<1%)
Grain size	Or (<0.1 – 2.0 mm), Pl (0.1 – 1.7 mm), Qz (<0.1 – 1.0 mm), Ser (<0.1 mm), Hbl (0.1 – 1.8 mm), Tr-Act (<0.1 – 1.0 mm), Ep (<0.1 – 0.5 mm), Chl (0.1 – 1.2 mm), Opaque Minerals (<0.1 – 0.2 mm), Tur (0.2 – 0.9 mm), Zo (<0.1 – 0.2 mm)
Texture(s)	Pl: lamellar twinning Or: Carlsbad twinning; micropertthitic texture Tr-Act: acicular texture Hbl: simple twinning Chl: scaly texture
Alteration	Weak sericitization, uralitization, chloritization and epidotization

Abbreviations: Chl = Chlorite, Ep = Epidote, Hbl = Hornblende, Or = Orthoclase, Pl = Plagioclase, Qz = Quartz, Ser = Sericite, Tr-Act = Tremolite-Actinolite, Tur = Tourmaline, Zo = Zoisite. Mineral abbreviations adapted from Whitney and Evans (2010).



The logo of the University of the Western Cape, featuring a classical building with a pediment and columns.

Appendix C – Hydrothermal veins

**Additional field photographs, field measurements and observations, and
photomicrographs**

UNIVERSITY *of the*
WESTERN CAPE

Additional field photographs

Quartz-dominated veins



Figure C1: Thick quartz-pyrite-tourmaline vein occurring at Schaap Eiland. Vein cross-cuts the monzonite and trends WNW-ESE. Alteration haloes are not visible around the vein in Fig. C1 due to weathering and erosion of the host rock adjacent to the veins by wave action. Scale: Compass with length = 17cm.

Jasper-dominated veins



Figure C2: NW-SE-trending quartz-tourmaline-jasper vein cross-cutting the syenodiorite at Hoëbank. Note how the vein is folded towards the end, showing a dextral (clockwise) sense of movement. Scale: Pencil with length = 14.4 cm.

Field measurements and observations

Table C1: Thickness and orientation of hydrothermal veins encountered in different localities across the study, as well as the thickness of alteration haloes associated with each type of vein.

Location	Vein Composition	Vein thickness cm	Alteration halo composition	Alteration halo thickness cm	Occurrence Rock Type	Orientation dip-direction/dip angle
NE to N of Visitors Center						
33°20'42.0"S; 18°09'19.1"E	Qz-Tur	0.04 – 0.1	Tur + Lm	0.1 – 0.12	Syenodiorite	058/86
33°20'42.0"S; 18°09'19.1"E	Qz-Ep	0.04 – 0.1	Chl + Ep	0.03 – 0.05	Syenodiorite	002/72
33°20'41.9"S; 18°09'19.5"E	Sheeted Qz-Tur-Jsp	25 – 45	Jsp + Tur + minor Lm	3 – 7	Syenodiorite	120/84; 126/82; 122/82
33°20'42.6"S; 18°09'18.9"E	Qz-Py	0.1 – 0.8	Chl + Ep	<0.1 – 1	Syenodiorite	350/74
33°20'42.5"S; 18°09'19.1"E	Qz-Py	<0.1	Chl + Lm	0.1 – 1.2	Syenodiorite	295/76
33°20'42.6"S; 18°09'18.8"E	Qz-Ep	0.1 – 1	Chl + Jsp	1.4 – 1.5	Syenodiorite	226/88
33°20'42.6"S; 18°09'18.5"E	Qz-Py	0.2 – 0.3	Chl	0.1	Syenodiorite	326/87
33°20'42.9"S; 18°09'17.9"E	Qz-Py	0.1	Chl	<0.1	Monzogabbro	156/74
33°20'43.1"S; 18°09'17.3"E	Qz-Ep	0.1 – 0.2	Chl + Ser	0.8 – 1	Monzogabbro	281/73
33°20'43.2"S; 18°09'17.2"E	Tur	1 – 1.2	Chl + Lm	0.1 – 0.5	Monzogabbro	006/77
33°20'43.2"S; 18°09'17.2"E	Qz-Py	0.1 – 0.2	Chl	0.1 – 0.2	Monzogabbro	286/80
33°20'43.4"S; 18°09'17.0"E	Qz-Py	0.08 – 0.1	Chl + minor Jsp	0.1	Syenodiorite	307/81
33°20'43.4"S; 18°09'17.0"E	Qz-Ep	0.1	Chl + Ep	0.2 – 0.7	Syenodiorite	291/80
33°20'43.5"S; 18°09'17.0"E	Qz-Py	0.1	Tur + Chl	0.5 – 0.6	Syenodiorite	340/77
33°20'44.2"S; 18°09'17.0"E	Sheeted Qz-Tur-Jsp	90 – 100	Jsp + minor Chl	1 – 5	Syenodiorite	340/80, 333/81
33°20'44.3"S; 18°09'16.3"E	Qz-Ep	0.1 – 0.15	Chl + Ser	0.7 – 1	Syenodiorite	320/88
W to SW of Visitors Center						
33°20'46.2"S; 18°09'15.0"E	Qz-Py-Tur	0.1 – 0.5	Tur + Lm + minor Chl and Jsp	0.3 – 0.45	Monzonite	340/85
33°20'48.7"S; 18°09'13.6"E	Qz-Py-Tur	2 – 4	Tur + Chl + Jsp	1 – 2	Monzonite	349/83
33°20'48.7"S; 18°09'13.6"E	Py-Tur	0.1 – 0.3	Tur	<0.1	Monzonite	003/86
33°20'48.7"S; 18°09'13.6"E	Barren Qz	0.3 – 7	None		Monzonite	063/88
33°20'47.8"S; 18°09'14.9"E	Qz-Py-Tur	1 – 3	Tur + Chl + Jsp + Ep	1 – 2	Monzonite	310/85
33°20'47.3"S; 18°09'14.5"E	Qz-Ep	0.1	Chl + Ep + Ser	0.1 – 0.12	Monzonite	243/86
33°20'47.3"S; 18°09'14.5"E	Qz-Py-Tur	1.2 – 1.4	Tur + Chl	0.8 – 1	Monzonite	348/85
33°20'47.4"S; 18°09'14.3"E	Barren Qz	10 – 25	None		Monzonite	060/86
33°20'47.9"S; 18°09'14.0"E	Qz-Py-Tur	0.1 – 0.2	Tur + Chl	0.1	Monzonite	001/88
33°20'48.3"S; 18°09'14.4"E	Qz-Py-Tur	0.2 – 0.3	Tur + Chl	0.1 – 0.2	Monzonite	006/85
33°20'48.3"S; 18°09'14.4"E	Qz-Py-Tur	0.2 – 0.3	Tur + Chl	0.1 – 0.2	Monzonite	272/75
33°20'48.3"S; 18°09'14.4"E	Qz-Py-Tur	0.1 – 0.2	Tur + Chl	0.1 – 0.2	Monzonite	001/85
33°20'50.5"S; 18°09'11.5"E	Tur-Jsp	0.5 – 1	Chl + Jsp	0.4 – 0.8	Monzonite	315/78
33°20'50.7"S; 18°09'10.2"E	Tur-Jsp	0.1 – 2.2	Chl + Jsp	0.2 – 0.4	Monzonite	310/80

Table C1 (continued)

Location	Vein Composition	Vein thickness cm	Alteration halo composition	Alteration halo thickness cm	Occurrence Rock Type	Orientation dip-direction/dip angle
33°20'50.2"S; 18°09'12.8"E	Qz-Tur	0.4 – 1.4	Tur + Jsp	0.8 – 1.5	Monzonite	142/75
33°20'50.0"S; 18°09'12.6"E	Qz-Tur	0.4 – 1.5	Jsp	0.4 – 0.7	Monzonite	309/75
33°20'50.2"S; 18°09'12.6"E	Tur	0.05 – 0.15	Jsp	2 – 4.2	Monzonite	340/78
Yzerfontein Harbour						
33°20'50.1"S; 18°09'00.8"E	Tur	0.05 – 0.2	Jsp	0.1 – 0.4	Syenodiorite	348/80
33°20'50.1"S; 18°09'00.8"E	Qz-Py-Tur	0.9 – 2.2	Tur + Chl + Jsp + Lm	4 – 5.5	Syenodiorite	349/81
33°20'50.1"S; 18°09'00.8"E	Tur	0.05 – 0.1	Lm	0.04 – 1.2	Syenodiorite	303/81
33°20'50.1"S; 18°09'00.8"E	Qz-Tur	0.1 – 2	Jsp	1 – 1.9	Syenodiorite	326/78
33°20'50.7"S; 18°09'11.0"E	Tourmalinite breccia	2 – 10.5	Jsp	0.5	Syenodiorite	316/78
33°20'50.7"S; 18°09'10.7"E	Tourmalinite breccia	0.5 – 5	Jsp	3.5 – 4.5	Syenodiorite	288/89
33°20'50.6"S; 18°09'10.3"E	Tourmalinite breccia	0.5 – 4	Chl + Jsp	2 – 2.3	Syenodiorite	240/88
33°20'50.0"S; 18°09'00.4"E	Ep-Cal	0.1 – 0.2	Chl + Ep	3.2 – 7	Syenodiorite	305/70
33°20'50.3"S; 18°09'00.7"E	Qz-Py-Tur	0.05 – 0.1	Minor Chl + Ep	0.1 – 0.2	Syenodiorite	325/55
33°20'49.6"S; 18°09'07.0"E	Tur	1.5 – 3.5	Jsp	1 – 1.5	Syenodiorite	329/75
33°20'49.6"S; 18°09'07.0"E	Py-Tur	2 – 6.5	Tur + Chl	1.6 – 2.1	Syenodiorite	327/77
33°20'49.6"S; 18°09'05.2"E	Tur	3 – 15	Lm	3.1 – 3.2	Syenodiorite	340/75
33°20'50.8"S; 18°09'03.4"E	Qz-Ep	5	Chl + Jsp	1.5 – 5	Syenodiorite	206/50
Hoëbank						
33°20'47.3"S; 18°08'52.0"E	Brecciated Py-Tur	0.65 – 2	Chl + Jsp + Lm	0.1 – 0.2	Monzonite	022/64
33°20'47.4"S; 18°08'52.2"E	Qz-Py-Tur	0.3 – 0.5	Tur + Chl + Lm + minor Jsp	0.7 – 1	Monzonite	296/80
33°20'47.4"S; 18°08'49.7"E	Qz-Tur-Jsp	0.2 – 0.3	Tur + Chl + Jsp + minor Lm	0.3 – 1	Monzonite	300/81
33°20'47.4"S; 18°08'49.7"E	Qz-Ep	0.1 – 0.3	Ep + Chl	0.8 – 1	Monzonite	033/88
33°20'48.3"S; 18°08'49.6"E	Qz-Tur-Jsp	0.4 – 0.55	Tur + Chl + Jsp	0.5 – 0.7	Monzonite	350/80
33°20'48.3"S; 18°08'49.6"E	Tur-Jsp	0.14 – 0.15	Chl + Jsp	0.5 – 0.6	Monzonite	325/80
33°20'48.5"S; 18°08'50.1"E	Qz-Tur	1.8 – 2.1	Chl	<0.1	Monzonite	349/81
33°20'49.1"S; 18°08'49.7"E	Qz-Py-Tur	<0.1	Jsp	0.1	Monzonite	323/81
33°20'49.1"S; 18°08'49.7"E	Qz-Tur-Jsp	2 – 3.4	Tur + Jsp + Chl	0.1 – 0.16	Monzonite	320/78
33°20'49.0"S; 18°08'49.6"E	Qz-Py	0.2 – 0.3	Chl + Lm	1.2 – 2.7	Monzonite	326/80
33°20'49.0"S; 18°08'49.6"E	Qz-Tur	<0.1	Tur + Jsp	0.3 – 1	Monzonite	232/85
Spruitgat						
33°20'56.4"S; 18°08'45.8"E	Qz-Ep	0.1 – 0.2	Ser + minor Ep	2 – 3	Monzonite	002/86
33°20'56.4"S; 18°08'45.8"E	Qz-Tur	0.1 – 0.2	Tur + Jsp	0.2 – 0.3	Monzonite	347/84

Table C1 (continued)

Location	Vein Composition	Vein thickness cm	Alteration halo composition	Alteration halo thickness cm	Occurrence Rock Type	Orientation dip-direction/dip angle
Grasbank						
33°20'57.2"S; 18°08'45.4"E	Qz-Tur	0.2 – 0.4	Tur + Jsp	0.3 – 0.4	Syenodiorite	350/79
33°20'57.2"S; 18°08'45.4"E	Qz-Ep	0.1 – 0.3	Ep + Ser	0.5 – 3	Syenodiorite	280/83
33°20'58.2"S; 18°08'45.7"E	Qz-Tur-Jsp-Cal	3 – 3.9	Chl + Ep	1.4 – 1.5	Syenodiorite	202/78
33°20'57.5"S; 18°08'45.4"E	Qz-Tur-Jsp	2.1 – 2.2	Chl + Ep + Lm	0.5 – 1	Syenodiorite	020/80
Yzerfontein Point						
33°20'55.3"S; 18°08'45.2"E	Qz-Py-Jsp	0.5 – 1.0	Tur + minor Lm	0.6 – 3.5	Monzonite	045/72
33°20'55.3"S; 18°08'45.3"E	Qz-Tur	0.3 – 0.4	Tur + Jsp	0.4 – 0.6	Monzonite	357/72
Draaibank						
33°21'08.7"S; 18°08'52.6"E	Qz-Py-Tur	0.4 – 0.5	Tur + Chl	0.1 – 0.2	Monzonite	352/82
33°21'08.7"S; 18°08'52.6"E	Qz-Tur-Jsp	<0.1	Tur + Jsp	0.2 – 0.6	Monzonite	283/81
33°21'08.6"S; 18°08'52.5"E	Qz-Py-Jsp	0.4 – 0.6	Chl	0 – 0.1	Monzonite	350/75
33°21'08.6"S; 18°08'52.5"E	Qz-Tur-Jsp	<0.1	Tur + Jsp	0.05 – 0.25	Monzonite	278/81
Schaap Eiland						
33°21'17.0"S; 18°08'51.3"E	Qz-Py-Tur	1.5 – 2.2	Chl + minor Lm	1 – 1.5	Monzonite	295/80
33°21'17.0"S; 18°08'51.2"E	Qz-Tur	0.3 – 0.4	Tur + Lm	1.1 – 1.25	Monzonite	309/78
33°21'17.1"S; 18°08'53.5"E	Qz-Py	2.6 – 4	Chl + Lm	1 – 2.2	Monzonite	292/86
33°21'16.7"S; 18°08'51.0"E	Py-Tur	0.1 – 5.2	Tur + Chl	1 – 2	Monzonite	100/74
33°21'16.9"S; 18°08'51.3"E	Qz-Py-Tur	2 – 3.5	Tur + Chl + Lm	1.7 – 1.8	Monzonite	290/79
33°21'16.3"S; 18°08'50.2"E	Qz-Tur	0.2 – 0.6	Tur + Jsp	1 – 2	Monzonite	343/77
33°21'17.4"S; 18°08'52.8"E	Py-Tur	0.4 – 5	Tur + Chl	0.2 – 0.6	Monzonite	348/76
33°21'17.4"S; 18°08'52.8"E	Py-Jsp	0.6 – 1.7	Chl + Lm	0.2 – 1.8	Monzonite	310/78
33°21'15.0"S; 18°08'59.4"E	Barren Qz	3.0 – 10.2	None		Monzonite	080/88
Freddie se Klip						
33°21'16.2"S; 18°09'03.5"E	Qz-Py-Tur	0.2 – 1.3	Chl + Ser	0.1 – 0.2	Monzonite	153/55
33°21'15.6"S; 18°08'02.5"E	Qz-Py	1 – 2	Chl	0.5 – 0.7	Monzonite	291/84
33°21'15.6"S; 18°08'02.5"E	Qz-Ep	0.1 – 0.3	Chl	0.2 – 0.3	Monzonite	160/85

Abbreviations: Cal = Calcite, Chl = Chlorite, Ep = Epidote, Jsp = Jasper, Lm = Limonite, Py = Pyrite, Qz = Quartz, Ser = Sericite, Tur = Tourmaline (after Whitney and Evans, 2010).

Additional photomicrographs

Jasper-dominated veins

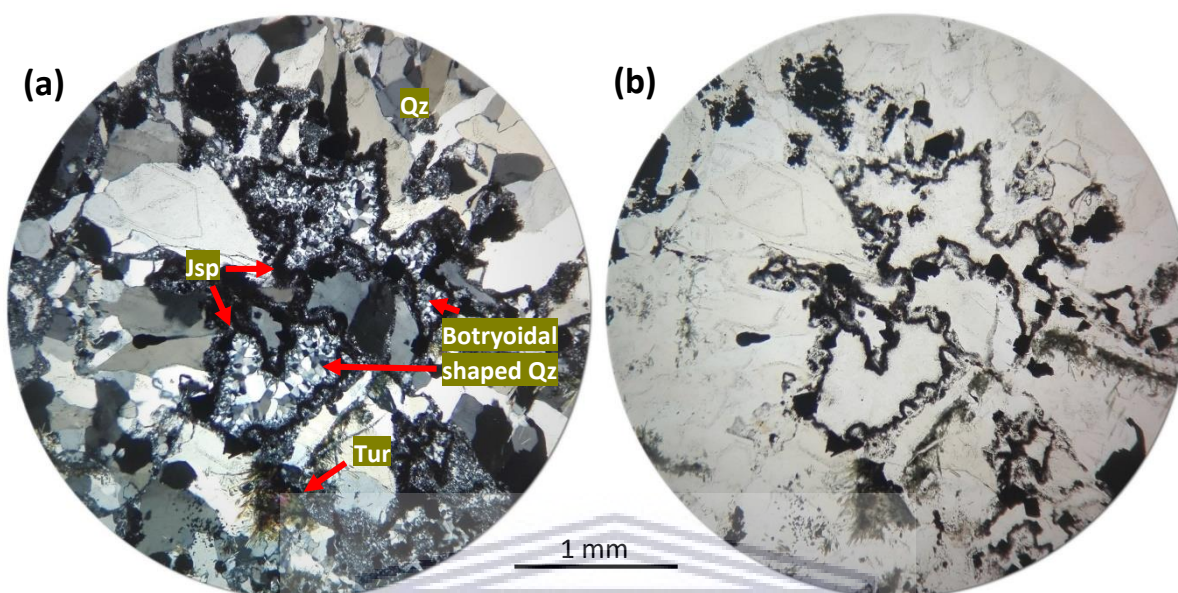


Figure C3: Thin section photomicrographs displaying a globular-like texture in a quartz-pyrite-tourmaline-jasper vein at YZN59 in (a) XPL and (b) PPL. This texture is resembled by botryoidal-shaped quartz aggregates rimmed by thin jasper bands. Tur = Tourmaline.

Jasper-dominated veins

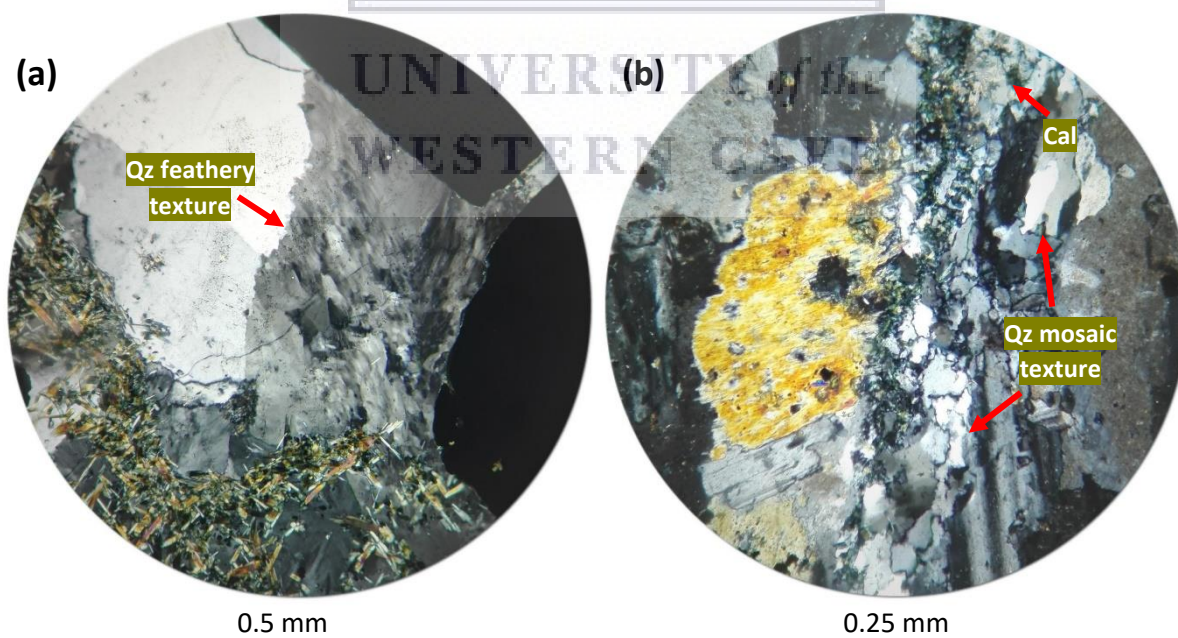
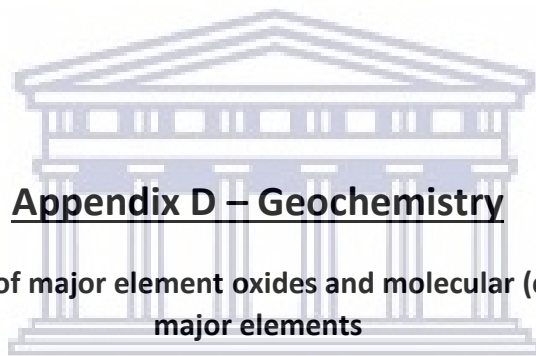


Figure C4: Thin section photomicrographs displaying primary and recrystallisation textures in quartz. (a) Feathery texture in a large quartz grain in XPL in a quartz-pyrite-tourmaline-epidote vein at YZN69. (b) Multiple interlocking quartz grains displaying a mosaic texture in XPL in a quartz-calcite-tourmaline-epidote vein at YZN30. Cal = Calcite, Qz = Quartz.



Appendix D – Geochemistry

Element concentrations of major element oxides and molecular (cationic) proportions of major elements

UNIVERSITY *of the*
WESTERN CAPE

Table D1: Element concentrations of major element oxides for the rocks of the Yzerfontein Pluton.

Sample	YZN01	YZN02	YZN03	YZN04	YZN05	YZN06	YZN07A	YZN07B	YZN09	YZN10	YZN11	YZN12	YZN13	YZN14	YZN15	YZN16	
Si	25.43	28.84	25.92	25.67	23.89	25.12	25.51	25.52	26.85	26.26	25.75	26.85	26.94	25.67	26.02	26.87	
Ti	0.50	0.40	0.46	0.52	0.56	0.51	0.50	0.49	0.46	0.49	0.52	0.53	0.53	0.49	0.43	0.46	
Al	7.81	8.03	7.72	8.10	7.69	8.17	8.28	8.28	7.94	7.93	7.87	8.14	8.09	7.50	7.62	7.95	
Fe	6.34	4.68	5.85	6.49	7.69	6.67	6.31	6.26	5.82	6.19	6.63	5.97	5.73	6.13	5.55	5.55	
Mn	0.11	0.09	0.10	0.12	0.15	0.13	0.13	0.13	0.09	0.12	0.12	0.12	0.11	0.12	0.13	0.10	
Mg	2.88	1.93	2.85	2.48	3.04	2.36	2.23	2.20	2.18	2.32	2.37	2.06	2.17	3.09	3.05	2.28	
Ca	4.72	2.18	4.49	4.38	5.74	4.72	4.39	4.28	2.44	4.09	4.33	3.13	3.04	4.82	4.53	3.29	
Na	2.07	2.66	2.08	2.25	2.40	2.37	2.58	2.69	2.55	2.32	2.34	2.24	2.56	2.26	2.48	2.59	
K	4.03	2.91	4.26	3.58	2.73	3.80	3.85	3.77	3.89	3.54	3.30	3.74	3.52	4.03	3.65	3.96	
P	0.23	0.14	0.19	0.23	0.29	0.25	0.23	0.24	0.18	0.18	0.22	0.19	0.20	0.20	0.18	0.17	
Sample	YZN17	YZN18	YZN20	YZN21	YZN22	YZN23	YZN24	YZN29	YZN30	YZN31	YZN32	YZN34	YZN38	YZN39	YZN40	YZN42	
Si	25.85	26.35	22.86	23.01	21.53	25.43	24.72	27.49	25.94	26.47	26.31	25.96	30.49	29.97	26.02	25.92	
Ti	0.48	0.50	0.55	0.40	0.37	0.52	0.55	0.52	0.49	0.49	0.52	0.52	0.33	0.33	0.48	0.49	
Al	7.89	7.81	4.34	9.25	6.91	7.99	7.98	7.99	7.91	7.89	7.92	7.81	8.21	8.25	8.14	8.05	
Fe	6.18	5.95	8.34	6.32	8.09	6.29	6.98	5.50	6.22	5.53	5.90	6.29	2.39	2.84	5.76	6.05	
Mn	0.12	0.10	0.18	0.12	0.15	0.12	0.13	0.10	0.13	0.09	0.11	0.12	0.03	0.04	0.12	0.12	
Mg	2.41	2.44	7.59	4.17	7.31	2.41	2.49	2.01	2.37	2.32	2.37	2.62	1.00	0.91	2.07	2.36	
Ca	3.63	4.04	8.68	5.55	6.28	4.24	4.77	2.81	3.31	3.73	3.68	4.20	1.19	1.64	3.64	2.61	
Na	2.44	2.49	1.47	2.54	1.67	2.43	2.57	2.36	2.49	2.57	2.45	2.42	3.17	3.19	2.56	2.61	
K	4.11	3.34	0.56	1.74	0.98	3.80	3.33	3.59	3.98	3.69	3.71	2.99	4.26	4.48	4.35	4.57	
P	0.21	0.19	0.16	0.24	0.28	0.23	0.26	0.17	0.21	0.18	0.19	0.19	0.07	0.07	0.21	0.21	
Sample	YZN43	YZN46	YZN48	YZN50	YZN51	YZN52	YZN70	YZN71	YZN73	YZN75a	YZN75b	YZN76	YZN79	YZN92	YZN93	YZN95	YZN96
Si	25.94	27.14	26.70	32.09	25.57	26.87	29.94	29.42	31.64	24.36	23.82	29.96	24.89	25.91	26.27	22.00	23.17
Ti	0.48	0.44	0.50	0.24	0.50	0.43	0.31	0.33	0.20	0.55	0.58	0.26	0.46	0.47	0.47	0.38	0.42
Al	8.08	8.38	7.62	7.16	7.46	8.14	8.50	8.61	8.11	7.79	7.58	8.31	7.08	8.03	7.89	7.22	7.87
Fe	5.93	5.08	5.72	2.79	6.41	5.18	3.11	2.97	2.42	7.28	8.15	3.20	6.53	6.37	5.87	7.92	6.71
Mn	0.12	0.09	0.12	0.05	0.13	0.11	0.02	0.06	0.03	0.14	0.15	0.05	0.12	0.16	0.11	0.15	0.12
Mg	2.23	1.83	2.52	0.77	2.87	1.88	0.66	1.13	0.51	3.27	3.20	0.84	4.11	2.03	2.72	7.00	5.21
Ca	3.49	2.53	3.98	0.63	4.92	3.37	1.09	1.84	0.66	5.45	6.00	1.13	5.69	3.59	4.00	5.47	5.83
Na	2.57	2.54	2.11	2.26	2.33	2.61	4.03	3.41	3.20	2.39	2.29	3.77	1.89	2.25	2.40	1.71	2.20
K	3.99	4.41	3.45	5.06	3.33	3.94	3.64	4.47	4.57	2.65	2.51	4.18	3.11	3.88	3.47	1.57	1.88
P	0.21	0.18	0.16	0.07	0.19	0.17	0.08	0.08	0.06	0.28	0.30	0.08	0.21	0.21	0.20	0.27	0.27

Note: Whole-rock major element oxides converted to element concentrations using oxide to element factors proposed by Willis and Duncan (2000).

Table D2: Molecular (cationic) proportions of major elements (moles of elements per 100g of rock) for the rocks of the Yzerfontein Pluton.

Sample	YZN01	YZN02	YZN03	YZN04	YZN05	YZN06	YZN07A	YZN07B	YZN09	YZN10	YZN11	YZN12	YZN13	YZN14	YZN15	YZN16	
Si	0.91	1.03	0.92	0.91	0.85	0.89	0.91	0.91	0.96	0.94	0.92	0.96	0.96	0.91	0.93	0.96	
Ti	0.01	0.01	0.01	0.01	0.01	0.01	0.01	0.01	0.01	0.01	0.01	0.01	0.01	0.01	0.01	0.01	
Al	0.29	0.30	0.29	0.30	0.29	0.30	0.31	0.31	0.29	0.29	0.29	0.30	0.30	0.28	0.28	0.29	
Fe	0.11	0.08	0.10	0.12	0.14	0.12	0.11	0.11	0.10	0.11	0.12	0.11	0.10	0.11	0.10	0.10	
Mn	0.002	0.002	0.002	0.002	0.003	0.002	0.002	0.002	0.002	0.002	0.002	0.002	0.002	0.002	0.002	0.002	
Mg	0.12	0.08	0.12	0.10	0.13	0.10	0.09	0.09	0.09	0.10	0.10	0.08	0.09	0.13	0.13	0.09	
Ca	0.12	0.05	0.11	0.11	0.14	0.12	0.11	0.11	0.06	0.10	0.11	0.08	0.08	0.12	0.11	0.08	
Na	0.09	0.12	0.09	0.10	0.10	0.10	0.11	0.12	0.11	0.10	0.10	0.10	0.11	0.10	0.11	0.11	
K	0.10	0.07	0.11	0.09	0.07	0.10	0.10	0.10	0.10	0.09	0.08	0.10	0.09	0.10	0.09	0.10	
P	0.01	0.00	0.01	0.01	0.01	0.01	0.01	0.01	0.01	0.01	0.01	0.01	0.01	0.01	0.01	0.01	
Fe+Mg	0.23	0.16	0.22	0.22	0.26	0.22	0.20	0.20	0.19	0.21	0.22	0.19	0.19	0.24	0.22	0.19	
A/CNK	0.68	1.00	0.68	0.74	0.62	0.69	0.71	0.72	0.89	0.74	0.73	0.86	0.85	0.63	0.66	0.78	
Mg#	51.10	48.65	52.77	46.73	47.60	44.84	44.83	44.69	46.22	46.29	45.09	44.17	46.48	53.68	55.80	48.57	
Sample	YZN17	YZN18	YZN20	YZN21	YZN22	YZN23	YZN24	YZN29	YZN30	YZN31	YZN32	YZN34	YZN38	YZN39	YZN40	YZN42	
Si	0.92	0.94	0.81	0.82	0.77	0.91	0.88	0.98	0.92	0.94	0.94	0.92	1.09	1.07	0.93	0.92	
Ti	0.01	0.01	0.01	0.01	0.01	0.01	0.01	0.01	0.01	0.01	0.01	0.01	0.01	0.01	0.01	0.01	
Al	0.29	0.29	0.16	0.34	0.26	0.30	0.30	0.30	0.29	0.29	0.29	0.29	0.30	0.31	0.30	0.30	
Fe	0.11	0.11	0.15	0.11	0.14	0.11	0.12	0.10	0.11	0.10	0.11	0.11	0.04	0.05	0.10	0.11	
Mn	0.002	0.002	0.003	0.002	0.003	0.002	0.002	0.002	0.002	0.002	0.002	0.002	0.001	0.001	0.002	0.002	
Mg	0.10	0.10	0.31	0.17	0.30	0.10	0.10	0.08	0.10	0.10	0.10	0.11	0.04	0.04	0.09	0.10	
Ca	0.09	0.10	0.22	0.14	0.16	0.11	0.12	0.07	0.08	0.09	0.09	0.10	0.03	0.04	0.09	0.07	
Na	0.11	0.11	0.06	0.11	0.07	0.11	0.11	0.10	0.11	0.11	0.11	0.11	0.14	0.14	0.11	0.11	
K	0.11	0.09	0.01	0.04	0.03	0.10	0.09	0.09	0.10	0.09	0.09	0.08	0.11	0.11	0.11	0.12	
P	0.01	0.01	0.01	0.01	0.01	0.01	0.01	0.01	0.01	0.01	0.01	0.01	0.00	0.00	0.01	0.01	
Fe+Mg	0.21	0.21	0.46	0.28	0.45	0.21	0.23	0.18	0.21	0.19	0.20	0.22	0.08	0.09	0.19	0.21	
A/CNK	0.74	0.73	0.31	0.79	0.62	0.71	0.68	0.88	0.78	0.74	0.76	0.74	0.99	0.91	0.75	0.83	
Mg#	47.21	48.56	67.66	60.26	67.48	46.82	45.05	45.71	46.69	49.02	47.98	48.91	49.09	42.42	45.30	47.24	
Sample	YZN43	YZN46	YZN48	YZN50	YZN51	YZN52	YZN70	YZN71	YZN73	YZN75a	YZN75b	YZN76	YZN79	YZN92	YZN93	YZN95	YZN96
Si	0.92	0.97	0.95	1.14	0.91	0.96	1.07	1.05	1.13	0.87	0.85	1.07	0.89	0.92	0.94	0.78	0.82
Ti	0.01	0.01	0.01	0.01	0.01	0.01	0.01	0.01	0.00	0.01	0.01	0.01	0.01	0.01	0.01	0.01	0.01
Al	0.30	0.31	0.28	0.27	0.28	0.30	0.32	0.32	0.30	0.29	0.28	0.31	0.26	0.30	0.29	0.27	0.29
Fe	0.11	0.09	0.10	0.05	0.11	0.09	0.06	0.05	0.04	0.13	0.15	0.06	0.12	0.11	0.11	0.14	0.12
Mn	0.002	0.002	0.002	0.001	0.002	0.002	0.0004	0.001	0.001	0.003	0.003	0.001	0.002	0.003	0.002	0.003	0.002

Table D2 (continued)

Sample	YZN43	YZN46	YZN48	YZN50	YZN51	YZN52	YZN70	YZN71	YZN73	YZN75a	YZN75b	YZN76	YZN79	YZN92	YZN93	YZN95	YZN96
Mg	0.09	0.08	0.10	0.03	0.12	0.08	0.03	0.05	0.02	0.13	0.13	0.03	0.17	0.08	0.11	0.29	0.21
Ca	0.09	0.06	0.10	0.02	0.12	0.08	0.03	0.05	0.02	0.14	0.15	0.03	0.14	0.09	0.10	0.14	0.15
Na	0.11	0.11	0.09	0.10	0.10	0.11	0.18	0.15	0.14	0.10	0.10	0.16	0.08	0.10	0.10	0.07	0.10
K	0.10	0.11	0.09	0.13	0.09	0.10	0.09	0.11	0.12	0.07	0.06	0.11	0.08	0.10	0.09	0.04	0.05
P	0.01	0.01	0.01	0.00	0.01	0.01	0.00	0.00	0.00	0.01	0.01	0.00	0.01	0.01	0.01	0.01	0.01
Fe+Mg	0.20	0.17	0.21	0.08	0.23	0.17	0.08	0.10	0.06	0.26	0.28	0.09	0.29	0.20	0.22	0.43	0.33
A/CNK	0.77	0.89	0.75	1.02	0.64	0.79	0.98	0.90	1.04	0.65	0.61	0.94	0.59	0.79	0.74	0.69	0.67
Mg#	46.36	45.31	50.31	38.67	50.73	45.40	32.92	46.76	32.48	50.77	47.40	37.55	59.15	42.29	51.57	66.98	64.09

Table D3: Limits of detection for the trace elements of samples analysed in the year 2015.

Values in ppm	Sc	V	Cr	Co	Ni	Cu	Zn	Rb	Sr	Y	Zr	Nb	Mo	Cs	Ba	La	Ce
Quantification Limits	0.333	0.194	3.698	0.229	3.593	2.441	4.072	0.238	0.282	0.056	0.159	0.058	0.367	0.158	1.041	0.082	0.107
Values in ppm	Pr	Nd	Sm	Eu	Gd	Tb	Dy	Ho	Er	Tm	Yb	Lu	Hf	Ta	Pb	Th	U
Quantification Limits	0.051	0.332	0.193	0.069	0.226	0.039	0.125	0.050	0.094	0.043	0.280	0.039	0.118	0.039	0.200	0.076	0.072

Note: Samples analysed in 2015: YZN01, YZN02, YZN03, YZN04, YZN05, YZN06, YZN07A, YZN07B, YZN09, YZN10, YZN11, YZN12, YZN13, YZN14, YZN15, YZN16, YZN17, YZN18.

Table D4: Limits of detection for the trace elements of samples analysed in the year 2017.

Values in ppm	Sc	V	Cr	Co	Ni	Cu	Zn	Rb	Sr	Y	Zr	Nb	Mo	Cs	Ba	La	Ce
Instrument DL	0.035	0.023	0.226	0.010	0.266	0.034	0.175	0.022	0.004	0.002	0.005	0.016	0.011	0.006	0.024	0.002	0.003
Method DL	0.354	0.226	2.257	0.098	2.656	0.344	1.754	0.216	0.044	0.024	0.049	0.164	0.108	0.250	0.243	0.022	0.032
Values in ppm	Pr	Nd	Sm	Eu	Gd	Tb	Dy	Ho	Er	Tm	Yb	Lu	Hf	Ta	Pb	Th	U
Instrument DL	0.003	0.009	0.010	0.003	0.009	0.003	0.005	0.003	0.006	0.001	0.010	0.005	0.007	0.002	0.011	0.005	0.005
Method DL	0.034	0.092	0.098	0.034	0.092	0.034	0.053	0.031	0.065	0.013	0.104	0.046	0.068	0.021	0.107	0.052	0.054

Note: Samples analysed in 2017: YZN20, YZN21, YZN22, YZN23, YZN24, YZN29, YZN30, YZN31, YZN32, YZN34, YZN38, YZN39, YZN40, YZN42, YZN43, YZN46, YZN48, YZN50, YZN51, YZN52.

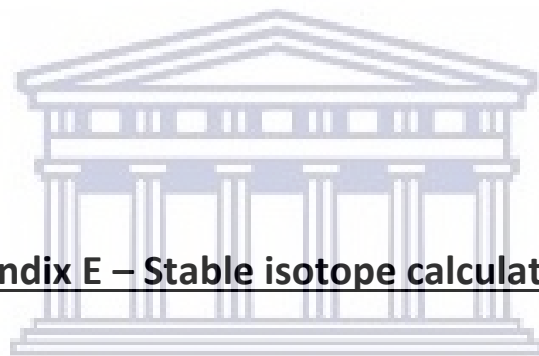
Table D5: Limits of detection for the trace elements of samples analysed in the year 2018.

Values in ppm	Sc	V	Cr	Co	Ni	Cu	Zn	Rb	Sr	Y	Zr	Nb	Mo	Cs	Ba	La	Ce
Instrument DL	0.085	0.018	0.593	0.008	0.529	0.045	0.073	0.033	0.002	0.001	0.001	0.001	0.013	0.015	0.011	0.001	0.001
Method DL	0.576	0.172	6.862	0.135	6.149	0.350	1.827	0.340	0.044	0.015	0.039	0.032	0.069	0.144	0.299	0.019	0.914
Values in ppm	Pr	Nd	Sm	Eu	Gd	Tb	Dy	Ho	Er	Tm	Yb	Lu	Hf	Ta	Pb	Th	U
Instrument DL	0.001	0.003	0.007	0.001	0.003	0.001	0.002	0.001	0.046	0.001	0.005	0.001	0.001	0.002	0.020	0.001	0.001
Method DL	0.012	0.074	0.073	0.016	0.051	0.030	0.035	0.009	0.017	0.066	0.025	0.006	0.025	0.016	0.050	0.010	0.027

Note: First set of samples analysed in 2018: YZN70, YZN71, YZN73, YZN75a, YZN75b, YZN76, YZN79, YZN92, YZN93, YZN95, YZN96.



Appendix E – Stable isotope calculations



UNIVERSITY *of the*
WESTERN CAPE

Table E1: Equations used for the determination of various isotopic parameters for mineral-mineral and mineral-fluid pairs.

Equation no.	Phases	Formula	Description	Reference
7.1	qz-tur	$1000 \ln \alpha_{(qz-tur)} = 1.0 \left(\frac{10^6}{T^2} \right) + 0.39$	Oxygen isotope fractionation between qz and tur	Kotzer et al. (1993)
7.2	qz-H ₂ O	$1000 \ln \alpha_{(qz-H_2O)} = \left(\frac{3.38 \times 10^6}{T^2} \right) - 3.40$	Oxygen isotope fractionation between qz and H ₂ O	Clayton et al. (1972)
7.3	tur-H ₂ O	$1000 \ln \alpha_{(tur-H_2O)} = \left(\frac{4.21 \times 10^6}{T^2} \right) + \left(\frac{-6.99 \times 10^3}{T} \right) + 2.14$	Oxygen isotope fractionation between tur and H ₂ O	Zheng (1993)
7.4	tur-H ₂ O	$1000 \ln \alpha_{(tur-H_2O)} = -14.2 \left(\frac{10^6}{T^2} \right) + 4.7$	Hydrogen isotope fractionation between tur and H ₂ O	Jiang (1998)
7.5	qz-tur	$\alpha_{(qz-tur)} = \frac{1000 + \delta_{qz}}{1000 + \delta_{tur}}$	Determination of the fractionation factor between qz and tur	Rollinson (1993)

Abbreviations: Cal = Calcite, Qz = Quartz, Tur = Tourmaline (after Whitney and Evans, 2010).

UNIVERSITY of the
WESTERN CAPE

Oxygen isotope geothermometer for the quartz-tourmaline pair:

The general relationship for the oxygen isotope fractionation factor between quartz and tourmaline, $\alpha_{(qz-tur)}$, is given by equation 7.1 (Kotzer et al., 1993) (Table B1). The exact value of this fractionation factor can be determined using equation 7.5 (Rollinson, 1993). Therefore, in order to determine the oxygen isotope geothermometer for YZN61a, the quartz and tourmaline $\delta^{18}\text{O}$ isotopic ratios (Table A1) are used to firstly determine the value of the fractionation factor:

$$\alpha_{(qz-tur)} = \frac{1000 + \delta_{qz}}{1000 + \delta_{tur}}$$
$$\alpha_{(qz-tur)} = \frac{1000 + 14.70}{1000 + 8.94} = 1.005708962$$

Given the $\delta^{18}\text{O}$ isotopic values of quartz and tourmaline (Table A1),

$$1000 \ln \alpha_{(qz-tur)} = 1.0 \left(\frac{10^6}{T^2} \right) + 0.39$$
$$1000 \ln 1.005708962 = 1.0 \left(\frac{10^6}{T^2} \right) + 0.39$$
$$5.30 = \left(\frac{1000000}{T^2} \right)$$
$$T^2 = \left(\frac{1000000}{5.30} \right)$$
$$T = 435 \text{ K} \cong 162^\circ\text{C}$$

Oxygen isotope fractionation between quartz and tourmaline:

The $\delta^{18}\text{O}$ isotopic value of tourmaline can be determined by making use of equation 7.1 (Kotzer et al, 1993):

$$1000 \ln \alpha_{(qz-tur)} = 1.0 \left(\frac{10^6}{T^2} \right) + 0.39$$

This equation can be rewritten as follows:

$$\delta^{18}\text{O}_{(tur)} = \delta^{18}\text{O}_{(qz)} - \left(\frac{1.0 \times 10^6}{T^2} \right) - 0.39$$

At 300 °C, given the $\delta^{18}\text{O}$ isotopic value of quartz (Table A1 – YZN44),

$$\delta^{18}\text{O}_{(tur)} = 11.17 - \left(\frac{1.0 \times 10^6}{(573)^2} \right) - 0.39$$
$$\delta^{18}\text{O}_{(tur)} = 7.73 \text{ ‰}$$

Oxygen isotope fractionation between quartz and water:

The $\delta^{18}\text{O}$ isotopic value of water can be determined by making use of equation 7.2 (Clayton et al., 1972):

$$1000 \ln \alpha_{(qz-H_2O)} = \left(\frac{3.38 \times 10^6}{T^2} \right) - 3.40$$

This equation can be rewritten as follows:

$$\delta^{18}O_{(H_2O)} = \delta^{18}O_{(qtz)} - \left(\frac{3.38 \times 10^6}{T^2} \right) + 3.40$$

At 300 °C, given the $\delta^{18}O$ isotopic value of quartz (Table A1 – YZN44),

$$\delta^{18}O_{(H_2O)} = 11.17 - \left(\frac{3.38 \times 10^6}{(573)^2} \right) + 3.40$$

$$\delta^{18}O_{(H_2O)} = 4.28 \text{ ‰}$$

Oxygen isotope fractionation between tourmaline and water:

The $\delta^{18}O$ isotopic value of water can also be determined by making use of equation 7.3 (Zheng, 1993):

$$1000 \ln \alpha_{(tur-H_2O)} = \left(\frac{4.21 \times 10^6}{T^2} \right) + \left(\frac{-6.99 \times 10^3}{T} \right) + 2.14$$

This equation can be rewritten as follows:

$$\delta^{18}O_{(H_2O)} = \delta^{18}O_{(tur)} - \left(\frac{4.21 \times 10^6}{T^2} \right) - \left(\frac{-6.99 \times 10^3}{T} \right) - 2.14$$

At 300 °C, given the $\delta^{18}O$ isotopic value of tourmaline (Table A1 – YZN61a),

$$\delta^{18}O_{(H_2O)} = 8.94 - \left(\frac{4.21 \times 10^6}{(573)^2} \right) - \left(\frac{-6.99 \times 10^3}{573} \right) - 2.14$$

$$\delta^{18}O_{(H_2O)} = 6.18 \text{ ‰}$$

Hydrogen isotope fractionation between tourmaline and water:

The δD isotopic value of water was determined by making use of equation 7.4 (Jiang, 1998):

$$1000 \ln \alpha_{(tur-H_2O)} = -14.2 \left(\frac{10^6}{T^2} \right) + 4.7$$

This equation can be rewritten as follows:

$$\delta D_{(H_2O)} = \delta D_{(tur)} + \left(\frac{14.2 \times 10^6}{T^2} \right) - 4.7$$

At 300 °C, given the δD isotopic value of tourmaline (Table A1 – YZN61a),

$$\delta D_{(H_2O)} = -34.5 + \left(\frac{14.2 \times 10^6}{(573)^2} \right) - 4.7$$

$$\delta D_{(H_2O)} = 4.05 \text{ ‰}$$

Appendix F – Fractional crystallisation modelling



UNIVERSITY *of the*
WESTERN CAPE

i.) Principal component analysis (PCA)

For the purpose of modelling fractional crystallisation, principal component analysis (PCA) was first performed (using the *GCDkit*[®] software) in order to determine which major elements are responsible for the most differentiation (Janoušek et al., 2016). According to Janoušek et al. (2016), PCA is a quantitative method that shows the directions in a geochemical space in which the geochemical data has the highest variance, which, in turn, could be directly related to the fractionation of particular mineral species (Janoušek et al., 2016). In other words, it can help to infer which minerals played a primary and secondary role in driving the compositional variation within the various rock compositions, i.e. mafic, intermediate and felsic. The directions are referred as the first, second, third, etc. principal components, with the first component (i.e. component 1, and usually the longest vector) reflecting the strongest differentiation within the dataset, and the other component showing a secondary effect (i.e. component 2, and usually the second longest arrow). In other words, each component is associated with a proportion of the total variance of the geochemical dataset (Janoušek et al., 2016).

Fig. 8.2 illustrates the result of performing PCA on the Yzerfontein Pluton dataset. This is done by plotting the major elements on what is referred to as “biplots of PCA” (Janoušek et al., 2016). PCA was performed separately on each of the rock compositions (mafic, intermediate and felsic) in order to determine which of the components played a bigger role in defining the differentiation in each of the rock compositions. With reference to Fig. 8.2, for each of the rock compositions, the first row of figures (Fig. 8.2a, c, e) shows the major direction of differentiation (displayed by the blue vectors), and the corresponding major element that is responsible for the differentiation. The sample numbers are also shown in these plots. In Fig. 8.2b, d and f, the corresponding symbols are displayed for the sample numbers shown in Fig. 8.2a, c and e, reflecting the rock types at those particular positions.

Indeed, for each rock suite it shows that different components were responsible for defining the variation within them. Fig. 8.2a illustrates that for the mafic rocks, component 1 is positively correlated with MgO, which suggests that MgO is responsible for the highest variance (or most differentiation) in the mafic rocks, and therefore driving most of the compositional variation. Secondary to MgO is Al₂O₃, which is negatively correlated with component 1 and component 2. Also having a secondary effect in producing the compositional variation in the mafic rocks is SiO₂, which is positively correlated with component 2, and, to some extent, CaO, which is positively correlated with component 1. Fe₂O₃ does not seem to have played a very big role. A vector for TiO₂ was generated, but since the vector projected very close to the origin where the vectors originate, it was excluded from the diagram. From these observations, it suggests that there may have been fractionation of ferromagnesian minerals, such as the pyroxenes, and potentially hornblende and olivine (probably the more Mg-rich end-member) during the early stages of the melt, and they are therefore mainly responsible for the differentiation of the mafic rocks. Furthermore, the observations also suggest that plagioclase, if it played a role, must not have been very

significant. Based on the petrography, these observations definitely hold true, at least in terms of the melanocratic gabbro and poikilitic monzogabbro which have a high abundance of pyroxene relative to the felsic minerals (Tables B1 to B3).

Fig. 8.2c illustrates that, for the intermediate rocks, component 1 is positively correlated with SiO_2 , which suggests that SiO_2 is responsible for the highest variance in the intermediate rocks, thus driving most of the compositional variation. Secondary to SiO_2 is CaO and Fe_2O_3 , which is positively and negatively correlated with component 2, respectively. According to Fig. 8.2c, MgO did not play a very big role in the differentiation of the intermediate rocks. Overall, it once again suggests that there may have been fractionation of pyroxenes in the intermediate rocks. Additionally, it also suggests fractionation of the more anorthite-rich end-member of plagioclase, which, as opposed to the mafic rocks, may have played a more significant role in the differentiation of the intermediate rocks. Crystallisation of alkali-feldspar appears to have played a small role compared to the other minerals, as seen from the projection of the K_2O vector. These observations are certainly consistent with the petrography of the intermediate rocks (Tables B4 to B7).

Lastly, Fig. 8.2e illustrates that for the felsic rocks, component 1 is positively correlated with SiO_2 . From the size of the SiO_2 vector relative to the other vectors, it must have played a very significant role in defining the compositional variation in the felsic rocks. Al_2O_3 and Na_2O played a secondary role in the differentiation of the felsic rocks, with slightly smaller contributions from CaO and K_2O . It appears that MgO and Fe_2O_3 did not play a very big role. This may suggest that, at this point in the fractionating sequence, most of the pyroxenes and hornblende had crystallised out of the melt to form the mafic and intermediate rocks, producing a remaining melt that is more felsic in composition relative to the primary melt. These observations indicate that fractionation of the feldspars were dominantly responsible for the differentiation within the felsic rocks. Orthoclase is likely the main alkali feldspar that fractionated, as illustrated by the projection of the K_2O vector, indicating that this mineral plays a bigger role in the felsic rocks compared to that in the other compositions. Overall, observations from PCA plots are consistent with the petrographic observations, in that the mafic rocks have a higher mafic mineral content and lower feldspar content (Tables B1 to B3) relative to the intermediate and felsic rocks (Tables B4 to B9), which show a gradual decrease in mafic mineral content as the feldspar content increases (likely fractionation-related).

ii.) Major and trace element correlation

The second statistical method that was applied to the Yzerfontein Pluton dataset is correlation of major and trace elements. This method was applied to the data as it effectively illustrates which major or trace elements share the greatest correlation, which is an indication as to which minerals could have played a major role in the differentiation of the various rock types. This method can therefore help to confirm and further corroborate the observations and inferences made during PCA of the various rock compositions. Matrix of correlation coefficients was performed on the major elements and trace elements, respectively, for each

of the rock compositions (mafic, intermediate and felsic) in order to produce correlation scatterplots (Fig. F1 to F3). The symbols in these plots are different and have been defined on the legend for each of the figures.

In terms of the mafic rocks, the strongest correlations are between Al_2O_3 and CaO , MgO and K_2O , MgO and Na_2O , Al_2O_3 and Na_2O , SiO_2 and K_2O , and lastly SiO_2 and MgO (Fig. F1a). Firstly, the good correlations between Al_2O_3 and CaO , and SiO_2 and MgO could indicate that pyroxenes have played a big role in the differentiation of the mafic rocks, particularly clinopyroxene and to a lesser extent orthopyroxene. The good correlation between SiO_2 and MgO could also be due to potential fractionation of Mg-rich olivine. Secondly, strong correlations between Al_2O_3 and CaO , MgO and Na_2O , Al_2O_3 and Na_2O , and SiO_2 and MgO suggests that crystallisation of hornblende played a role. Thirdly, strong correlations between Al_2O_3 and CaO , and Al_2O_3 and Na_2O suggests that crystallisation of plagioclase took place, however, as previously mentioned in the PCA, it did not play a very significant role in the differentiation of the mafic rocks. Lastly, the good correlation between MgO and K_2O , SiO_2 and K_2O , and SiO_2 and MgO could suggest that biotite also crystallised and therefore may have played a smaller role in the differentiation of the mafic rocks.

Moving on to the trace elements, extremely strong correlations are seen between Rb and La, Th and Zr, Zr and Nb, and Cr and Ni (Fig. F1b). The strongest correlation between Cr and Ni is expected, as they are highly partitioned into mafic minerals such as orthopyroxene, clinopyroxene and hornblende in basaltic liquids (Rollinson, 1993). This further testifies to the significant role played by these minerals in the fractionation of the mafic rocks. The strong correlations between Zr and Nb and Rb and La, as well as Th and Zr may be related to biotite and zircon fractionation, respectively. Additionally, what some of these elements have in common, is that they may reflect a crustal contribution in the origin of the mafic rocks, particularly in terms of Rb, Th, Zr, and Nb (Rollinson, 1993). Nb and Th also have a relatively strong correlation, and are both crust-related elements, suggesting a crustal influence. Ba and Eu also share a good correlation, which, to some extent, may be related to plagioclase fractionation. All the observations made in the major and trace element correlation of mafic rocks are consistent with petrographic observations made in Chapter 4.

With regards to the major element correlations in the intermediate rocks, the strongest correlations are between SiO_2 and Fe_2O_3 , SiO_2 and CaO , Al_2O_3 and MgO , MgO and CaO , and Fe_2O_3 and CaO (Fig. F2a). These relationships indicate the fractionation of pyroxene, possibly more so of clinopyroxene than orthopyroxene as illustrated by the strong correlations between SiO_2 and CaO , MgO and CaO , and Fe_2O_3 and CaO . These correlations are also indicative that hornblende may potentially have played a subordinate role in the compositional variation. The strong correlation between SiO_2 and CaO may also suggest that plagioclase may have played a significant role during fractionation, particularly the anorthite-rich end-member.

In terms of the trace elements, the intermediate rocks show some similar correlations to the mafic rocks. Good correlations are seen between Zr and Nb, Th and Nb, Th and Zr, Ba and Eu, Cr and Ni, and V and Eu (Fig. F2b). As mentioned before, trace elements such as Zr, Th and Nb may reflect a crustal influence. The strong correlation between these elements therefore suggests a strong crustal contribution. The strong correlation between Ba and Eu may suggest plagioclase fractionation, whereas the Cr and Ni correlation infers fractionation of mafic minerals such as the pyroxenes and potentially hornblende. These observations, in terms of both the major and trace element correlations of the intermediate rocks, are mostly consistent with the petrographic observations made in Chapter 4.

Relative to the mafic and intermediate rocks, the felsic rocks show different major and trace element correlations. For the major elements, the highest correlation is observed between Na₂O and K₂O, followed by Al₂O₃ and Na₂O, SiO₂ and Al₂O₃, and SiO₂ and CaO (Fig. F3a). All these relationships are indicative of feldspar fractionation. The compositional variation, based on the strongest correlation, is mostly dominated by an alkali feldspar, most likely orthoclase. Secondary to that is plagioclase, possibly more so the albite-rich end-member than the anorthite-rich end-member, as inferred from the Al₂O₃ and Na₂O correlation that is higher than the Al₂O₃ and CaO correlation. There is also a good correlation between MgO and CaO, which could suggest that clinopyroxene (to some extent), or more likely hornblende, have played a role. However, it is not as significant as the role played by the feldspars. In this section, though the studied samples of felsic composition do not contain primary pyroxenes, secondary amphiboles such as hornblende and tremolite-actinolite formed as a result of uraltization are a clear indication that primary pyroxenes were once present (Tables B8, B9).

With regards to the trace elements, the strongest correlations are apparent between Sr and Ba, and Th and La, which is followed by good correlations between Th and Nb, Nb and La, Zr and Ni, Rb and Th, Rb and La, and Rb and Nb (Fig. F3b). The strong correlation between Sr and Ba is directly associated with plagioclase fractionation, as these two elements are strongly compatible with, and highly partitioned into plagioclase, but more so Sr than Ba (Rollinson, 1993). Rb acts as an incompatible element and is highly partitioned into alkali feldspar (Rollinson, 1993). Its strong correlation with the other trace elements is certainly an indication that the felsic rocks contain high concentrations of alkali feldspar, and that they are more fractionated, reflecting the significant influence of this mineral to the overall compositional variation in the felsic rocks. This suggestion is also supported by isotopic data, which indicates that the sample of quartz-microsyenite (YZN70) has the highest ⁸⁷Rb/⁸⁶Sr ratio (1.3852) compared to the other rocks, reflecting its high alkali feldspar content, as is also corroborated by petrographic observations of the felsic rocks (Tables 6.3, B8, B9). Overall, then, the major and trace element correlations of the felsic rocks are consistent with their petrographic observations, at least in terms of the pyroxenes and plagioclase. Additionally, for all three rock compositions (mafic, intermediate and felsic), it is largely apparent that the minerals inferred to have fractionated based on the major element trends correlate with those inferred to have fractionated based on trace element trends.

iii.) Rayleigh-type fractionation

Since the mineral species that may have played a role in the compositional variation seen in each of the rock compositions of the Yzerfontein Pluton are known to some extent, they can be modelled for fractional crystallisation via Rayleigh-type fractionation. Rayleigh fractionation is modelled rather than equilibrium crystallisation, as the latter is not regarded as a common process in mafic magmas (Rollinson, 1993; Keskin, 2002). Additionally, researchers generally prefer modelling Rayleigh fractionation, as the Rayleigh law is ideal when it comes to describing the process of fractional crystallisation (Keskin, 2002). Fractionation vectors will be modelled for each of the rock compositions using compatible-compatible binary log-log trace element plots. Modelling fractionation vectors is an effective method for identifying which minerals controlled the compositional variation within a magma (Janoušek et al., 2016). The trace-element concentrations were plotted on a binary log-log plot in the *GCDkit*[®] software (Fig. 8.3). An effective approach to constructing these diagrams was to select compatible trace elements that display a sharp decrease in concentration with continued fractional crystallisation of a magma (Janoušek et al., 2016). It then required selection of the minerals for which fractionation vectors should be generated, as well as the partition coefficients of the selected compatible trace elements for particular melt compositions (Table 8.1). Once the partition coefficients and the trace element concentrations were prepared, it was possible to generate fractionation vector diagrams by making use of a code into which certain parameters had to be entered (such as the fraction of melt remaining during crystallisation (F), and the coordinates of the sample from which the vectors have to project).

The most primitive (least fractionated) samples were selected as the position for the vectors to project from. Once again, the rock compositions were separated in order to determine which minerals were fractionated and therefore played a role in the compositional variation seen in the mafic, intermediate and felsic rocks, respectively. For each of the rock compositions, $F = 0.3$. In other words, the vectors reflect the effects of 70% fractionation of the minerals in each rock suite. A vector for olivine was generated on the plot for mafic rocks, in particular, in order to account for the potential crystallisation of olivine in the mafic rocks. A vector for hornblende was also generated for all rock compositions in order to account for its potential fractionation in these rocks. Biotite, even though it did not play a very big role in the fractionation of the rocks (as was shown from the petrographic examination of the rocks (Tables B1 to B9), as well as from the PCA and correlation of major elements and trace elements of the three different rock compositions) have also been accounted for on the Rayleigh fractionation plots; the plots are shown in Fig. 8.3.

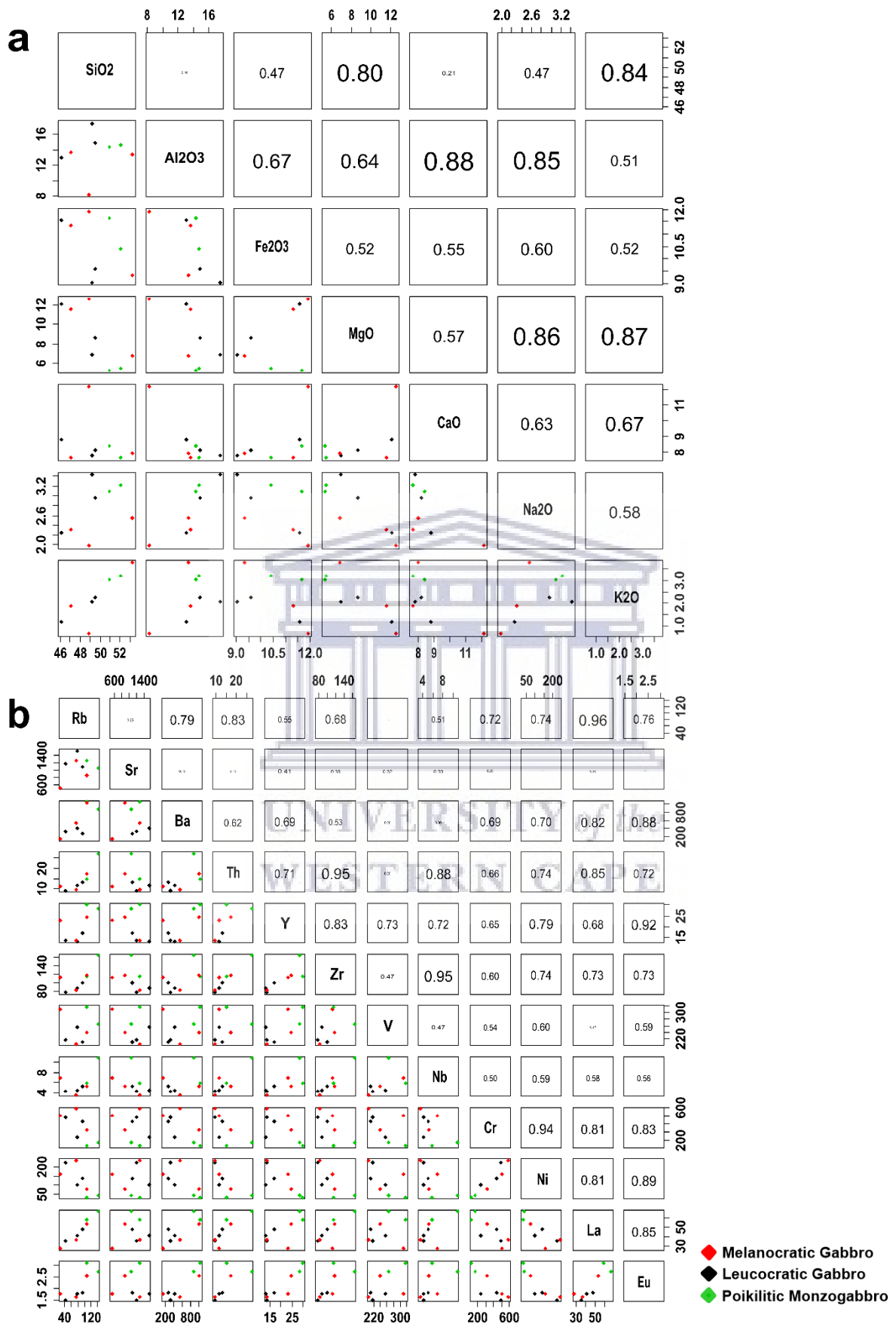


Figure F1: Correlation diagrams for selected major and trace elements for the mafic rocks of the Yzerfontein Pluton.

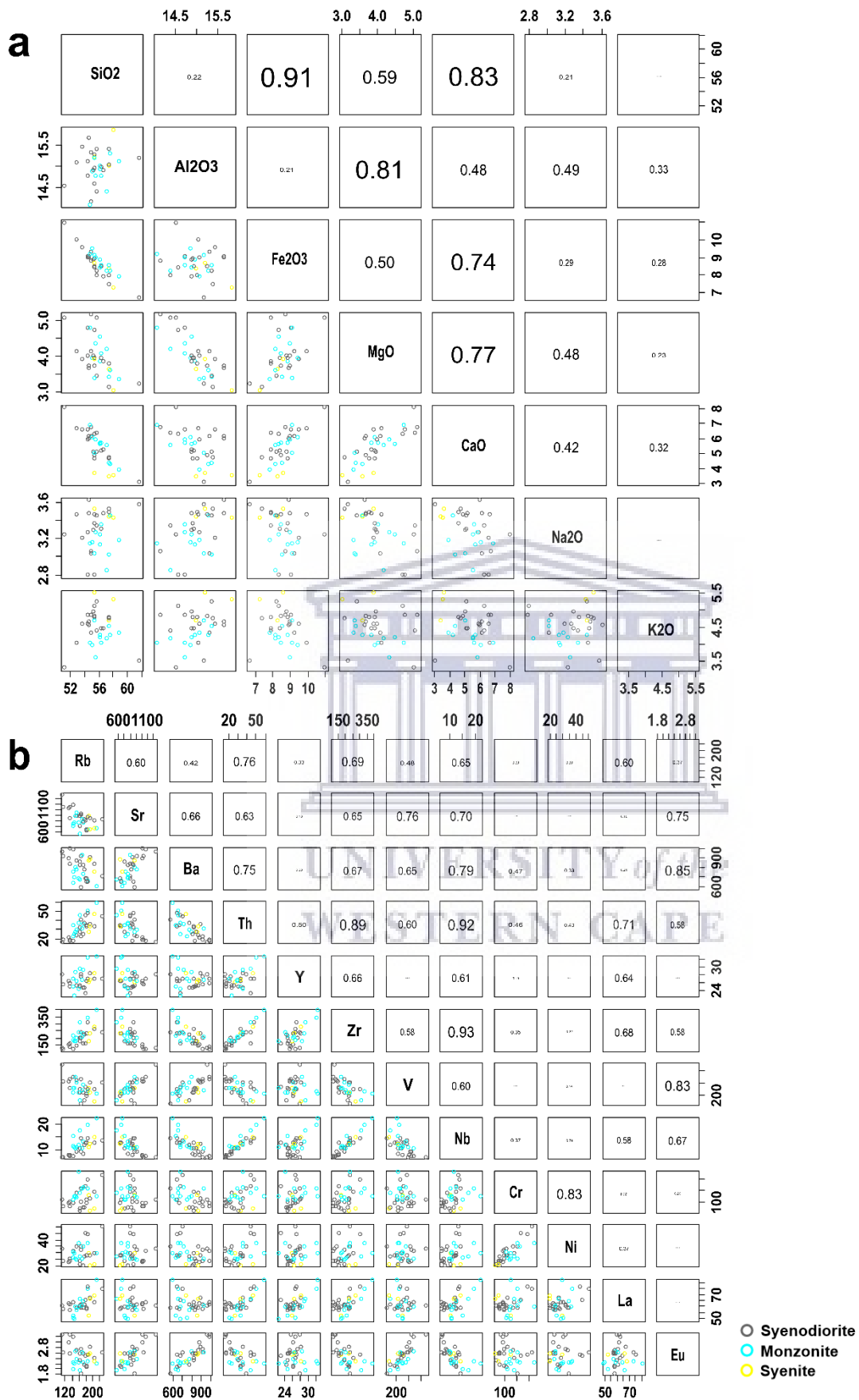


Figure F2: Correlation diagrams for selected major and trace elements for the intermediate rocks of the Yzerfontein Pluton.

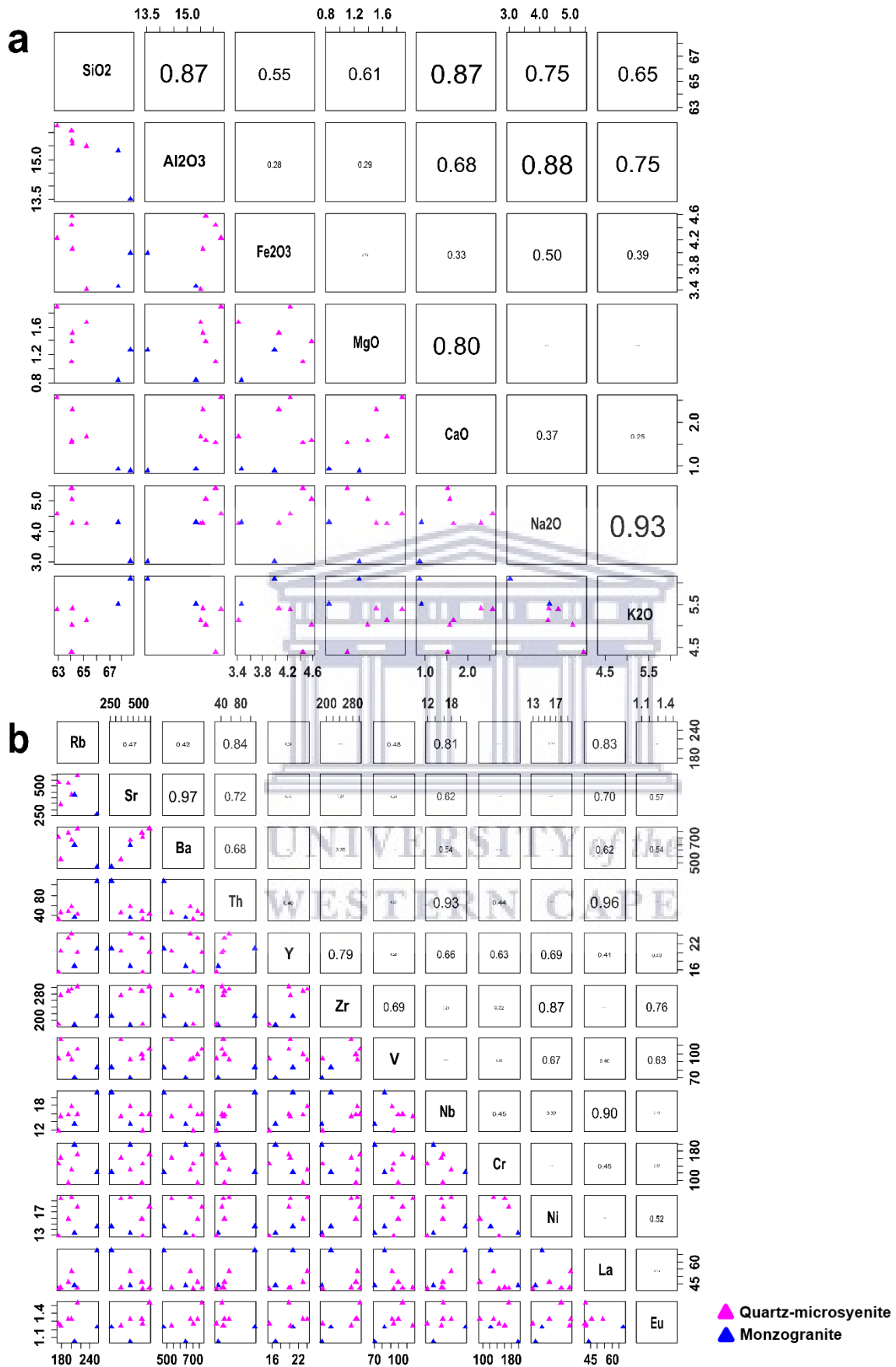


Figure F3: Correlation diagrams for selected major and trace elements for the felsic rocks of the Yzerfontein Pluton.